

PHOTOIONIZATION OF STRONGLY CORRELATED
MANY-ELECTRON ATOMS AND MOLECULES: A
HYBRID-BASIS CLOSE-COUPPLING INTERFACE TO
QUANTUM CHEMISTRY PACKAGES

CARLOS ANTONIO MARANTE VALDES

A Thesis submitted for the degree of Doctor



Departamento de Química
Facultad de Ciencias
Universidad Autónoma de Madrid

Supervisors:
Luca Argenti & Fernando Martín

Madrid, June 2017

Eternally grateful to my family, because it could not be better.

ABSTRACT

The theoretical description of observables in attosecond experiments requires a good representation of the system's ionization continuum. For polyelectronic molecules, however, this is still a challenge, due to the complicated short-range structure of correlated electronic wave functions. Whereas quantum chemistry packages (QCP) implementing sophisticated methods to compute bound electronic molecular states are well-established, comparable tools for the continuum are not widely available yet. To tackle this problem, we have developed a new approach, XCHEM, that by means of a hybrid Gaussian-B-spline basis (GABS), interfaces existing QCPs with close-coupling scattering methods.

We illustrate the performance of the GABS hybrid basis for the hydrogen atom by solving both the time-independent and the time-dependent Schrödinger equation for a few representative cases. The results are in excellent agreement with those obtained with a purely B-spline basis, with analytical results, when available, and with recent above-threshold ionization spectra from the literature. In the latter case, we report fully differential photoelectron distributions which offer further insight into the process of above-threshold ionization at different wavelengths.

To illustrate the viability of the XCHEM approach, we report results for the multichannel ionization of the helium atom and of the hydrogen molecule that are in excellent agreement with existing accurate benchmarks.

We also present a theoretical study of the multichannel photoionization of Ne in the vicinity of the autoionizing states lying between the $2s^22p^5$ and $2s2p^6$ ionization thresholds. The calculated total photoionization cross sections are in very good agreement with absolute measurements and with independent benchmark calculations performed at the same level of theory. From these cross sections, we have extracted resonance positions, total autoionization widths, Fano profile parameters and correlation parameters for the lowest three autoionizing states of $^1P^o$ symmetry. The values of these parameters are in good agreement with those reported in earlier theoretical and experimental work. We have also evaluated partial photoionization cross sections, and, from them, partial autoionization widths and Starace parameters for the same resonances, not yet available in the literature. We have found that the three lowest resonances preferentially decay into the $2p^{-1}\epsilon d$ continuum rather than into the $2p^{-1}\epsilon s$ one, in agreement with previous expectations, and that in the vicinity of the resonances the partial $2p^{-1}\epsilon s$ cross section can be larger than the $2p^{-1}\epsilon d$ one, in contrast with the accepted idea that the latter should amply dominate in the whole energy range. With the ma-

trix elements obtained within XCHEM, we used the two-photon finite-pulse model for resonant transitions to compute the side bands modulation, and reproduce a very recent RABITT experiment in Ne with very good agreement.

These findings, together with the versatility of QCPs to describe a broad range of chemical systems, indicate that this is a valid approach to study the ionization of polyelectronic systems in which correlation and exchange symmetry play a major role.

RESUMEN

La descripción teórica de los observables en los experimentos de attosegundo, requiere de una buena representación del continuo de ionización del sistema. Para moléculas polyelectrónicas, sin embargo, esto es aún un reto debido a la complicada estructura a corto radio de la función de onda electrónica producto de la correlación. Mientras que los códigos de química cuántica (QCPs) cuentan con métodos sofisticados para calcular los estados ligados, no existen herramientas equivalentes para calcular el continuo electrónico. Para resolver este problema, hemos desarrollado un nuevo método, XCHEM, que a través de una base híbrida de gaussianas con B-splines (GABS), combina QCPs con métodos close-coupling para describir la dispersión electrónica.

Mostramos el desempeño de la base GABS para el átomo de hidrógeno, resolviendo la ecuación de Schrödinger dependiente y no dependiente del tiempo para varios casos representativos. Los resultados comparan muy bien con otros obtenidos solo utilizando B-splines, fórmulas analíticas y otros cálculos recientes publicados en la literatura.

Para ilustrar las capacidades del método XCHEM, también reportamos resultados para la ionización multicanal del átomo de helio y la molécula de hidrógeno, que muestran un acuerdo excelente comparando con los resultados obtenidos con otros códigos muy precisos utilizados como referencia.

También presentamos un estudio teórico de la fotoionización multicanal del átomo de Ne cerca de las resonancias que se encuentran entre los umbrales de ionización $2s^22p^5$ y $2s2p^6$. Las secciones eficaces de fotoionización comparan muy bien con valores experimentales y otros cálculos teóricos realizados con el mismo nivel de correlación electrónica. De dichas secciones eficaces, se extrajeron las energías de las resonancias, sus anchos, el parámetro de Fano y el de correlación, estando en correspondencia con los valores medidos reportados en la literatura. Además, se calcularon las secciones eficaces parciales, y de ellas, los parámetros de Starace y los anchos parciales, no reportados aún en la literatura. Con los elementos de matrix calculados, usamos el two-photon finite-pulse model for resonant transitions para calcular la modulación de las bandas laterales en un experimento RABITT muy reciente, obteniendo muy buenos resultados.

Estos resultados, junto a la versatilidad de los QCPs para describir un gran número de moléculas, apuntan a que el método XCHEM resulta válido para estudiar la ionización de sistemas polyelectrónicos, en los que la correlación electrónica juega un papel fundamental.

PUBLICATIONS

This thesis is based on the following papers:

1. **Hybrid Gaussian-B-spline basis for the electronic continuum: Photoionization of atomic hydrogen.** C. Marante, L. Argenti, F. Martín. *Phys. Rev. A* **90**, 012506 (2014).
2. **Dressing effects in the attosecond transient absorption spectra of doubly excited states in helium.** L. Argenti, A. Jiménez-Galán, C. Marante, C. Ott, T. Pfeifer, F. Martín. *Phys. Rev. A* **91**, 061403(R) (2015).
3. **Angular dependence of photoemission time delay in helium.** S. Heuser, A. Jiménez-Galán, C. Cirelli, C. Marante, M. Sabbar, R. Boge, M. Lucchini, L. Gallmann, I. Ivanov, A. S. Kheifets, J. M. Dahlström, E. Lindroth, L. Argenti, F. Martín, U. Keller. *Phys. Rev. A* **94**, 063409 (2016).
4. **Hybrid-basis close-coupling interface to quantum chemistry packages for the treatment of ionization problems.** C. Marante, M. Klinker, I. Corral, J. González-Vázquez, L. Argenti, F. Martín. *J. Chem. Theory Comput.* **13**, 499-514 (2017).
5. **Photoionization using the XCHEM approach: Total and partial cross sections for atomic Ne and resonance parameters above the $2s^22p^5$ threshold.** C. Marante, M. Klinker, T. Kjellson, I. Corral, E. Lindroth, J. González-Vázquez, L. Argenti, F. Martín. *submitted* (2017).

CONTENTS

Index	i
I INTRODUCTION	1
1 INTRODUCTION	3
1.1 Atomic and molecular dynamics triggered by ultrashort light pulses	3
1.1.1 Theoretical approaches	4
1.2 Motivation and outline of the thesis	8
II THEORETICAL METHODS	11
2 MOLECULAR ELECTRONIC STRUCTURE <i>ab initio</i> METHODS	13
2.1 The Hartree-Fock approximation	14
2.2 Configuration interaction	16
2.3 Complete active space self consistent field method	17
3 SCATTERING THEORY	19
3.1 The close coupling method	19
3.2 Asymptotic boundary conditions	21
3.3 Analytic properties of the S matrix	23
3.3.1 Levinson-Seaton Theorem	25
3.4 Autoionizing states	25
3.4.1 A discrete state in the continuum	25
3.4.2 Resonances as eigenstates of the quenched Hamiltonian	29
4 PHOTOIONIZATION CROSS SECTION	33
4.1 One-photon amplitude	34
4.2 Two-photon amplitudes	36
4.2.1 Application to the RABITT technique	36
4.3 Cross section near an autoionizing state	38
5 THE XCHEM APPROACH	41
5.1 The XCHEM close coupling	41
5.2 The GABS basis	43
5.3 Parent ions	46
5.4 Augmentation	48
5.5 Scattering and Augmented states equivalence	49
5.6 Scattering States Numerical Methods	50
5.6.1 LU factorization and null space of \mathbf{U} matrix	53
5.6.2 Matrix inversion method	54
5.6.3 Eigenstates as a basis for the scattering states	54
5.6.4 Normalization of scattering states	55
III RESULTS	57
6 GABS BASIS PERFORMANCE: HYDROGEN ATOM IN A LASER FIELD	59

6.1	Spectral resolution of the Hamiltonian	59
6.2	Dipole transition matrix elements	61
6.3	Time-dependent Schrödinger equation	62
6.4	Bound and continuum states of hydrogen	63
6.5	Radiative transitions	68
6.6	Time-dependent results	73
7	PHOTOIONIZATION OF POLY-ELECTRONIC SYSTEMS USING XCHEM	87
7.1	One-electron parent ions	87
7.1.1	Photoionization of He	87
7.1.2	Photoionization of H ₂	90
7.2	Poly-electronic parent ions: the photoionization of Ne	95
7.2.1	Photoionization of Ne at MCI level	97
7.2.2	Photoionization of Ne at XCI level	100
7.2.3	Effect of intermediate resonances in the modulation of the SBs in RABITT experiments	108
IV	CONCLUSIONS & PERSPECTIVES	115
8	CONCLUSIONS & PERSPECTIVES	117
9	CONCLUSIONES & PERSPECTIVAS	121
V	APPENDICES	125
A	X_{lm} ASSOCIATED TO THE MOLECULAR ABELIAN POINT GROUPS	127
B	MATRIX ELEMENTS BETWEEN EXTENDED CHANNEL FUNCTIONS REPRESENTED WITH GABS BASIS FUNCTIONS	129
C	DIPOLE TRANSITION GAUGES	133
D	SINGULAR PART OF THE DIPOLE MATRIX ELEMENTS BETWEEN CON- TINUUM STATES	137
E	ANALYTICAL DIPOLE MATRIX ELEMENTS IN HYDROGEN	139
F	ANALYTICAL APPROXIMATION TO THE OUTER CONTINUUM- CONTINUUM TRANSITION INTEGRAL	145
G	RELATION BETWEEN D_{2h} AND SPHERICAL SCATTERING CHANNELS IN THE PHOTOIONIZATION OF NE	149
	BIBLIOGRAPHY	151

Part I

INTRODUCTION

INTRODUCTION

1.1 ATOMIC AND MOLECULAR DYNAMICS TRIGGERED BY ULTRASHORT LIGHT PULSES

Advances in generating controlled few-cycle laser pulses and novel ultrashort extreme ultraviolet (XUV) and X-ray sources, from free-electron laser (FEL)-based to attosecond high harmonic generation (HHG)-based facilities, have opened completely new avenues for imaging and controlling electronic and nuclear dynamics in molecules, with exciting applications in physics, chemistry and biology [1, 2, 3, 4, 5, 6, 7, 8]. The advent of x-ray free-electron lasers (XFEL) [9], has extended the domain of inquiry to non-linear processes promoted by intense ionizing radiation ($> 10^{15} \text{ PW/cm}^2$), while advances in the technology of table-top HHG sources of femtosecond and sub-femtosecond extreme ultraviolet (XUV) pulses have opened the way to observe the dynamics in the attosecond time scale [10], a whole new branch of science devoted to the study of electronic motion at its natural timescale [11]. Recently, attosecond technology has been incorporated in FEL [12, 13, 14] to generate intense XUV pulses with high spatial and temporal coherence as well as short duration, with which matter can be interrogated in the non-linear regime in a time-resolved way [15]. Finally, HHG technology has now reached the water window (3-4 nm wavelength) [16], thus making it possible to study ultrafast correlated processes in biological samples in their natural media.

The common feature to all these light sources is their ability to ionize a molecule by absorption of just a single photon. Thus, theoretical studies devoted to understand ultrafast phenomena induced by such energetic electromagnetic radiation must necessarily deal with the problem of describing the ionization continuum. This also applies to ultrafast dynamics induced by IR or visible pulses in which the probing step leads to ionization of the system [17, 18, 19, 20]. Although description of the ionization continuum is rather straightforward for atomic systems, for which a large number of accurate computational tools are available [21, 22, 23, 24, 25], this is not the case for molecules, for which the number of available codes is much scarcer and often limited to study ionization under significant restrictions, e.g., by assuming a single-active electron (SAE) or a mean-field approximation [26, 27, 28]. However, electron correlation, a hallmark of electronic motion in bound atomic and molecular systems [29], plays an even more prominent role when absorption of XUV and X-ray light leads to emission of photoelectrons [24, 25, 30]. In ionization, correlation gives rise to salient features

such as Auger resonances [31, 32, 33], associated to the formation of transiently bound, often multiply excited configurations [34, 35], whose decay is due to the coupling between different ionization channels (configuration interaction in the continuum) [36], and satellite peaks associated to orbital relaxation [37, 38, 39] and to the failure of the SAE approximation [40, 41]. Multiply-excited autoionizing states, shape resonances, and collective excitations play a fundamental role in the chemistry of the interstellar medium, in the highest layer of the earth atmosphere [42], as well as for most of the processes leading to radiation damage [43].

Nowadays most of these ultrashort light sources can be combined with sophisticated detection techniques like cold-target recoil-ion mass spectrometry (COLTRIMS) [44], velocity-map imaging (VMI) [45], time-of-flight photoelectron spectrometry [46], and high-resolution XUV spectrometry [47], allowing for the study of photoelectron emission from atoms, molecules and surfaces with a level of detail that would have been unthinkable only two decades ago. In addition to FELs and HHG generated pulses, third-generation synchrotron facilities [48, 49, 50, 51] allow one to measure the ionization spectrum of atoms and molecules in stationary conditions with much higher resolution than before, across a wide energy range. This can also be done in association with synchronized laser pulses [52].

1.1.1 Theoretical approaches

Although a plethora of theoretical methods is available to accurately describe the ionization continuum of atoms (see, e.g., [21, 22, 23, 24, 25] and references therein), this is not the case for molecules, for which existing methods are usually designed to describe specific problems, usually in regions of the photoelectron spectrum where autoionization and electron correlation play a minor role. In contrast, for bound molecular states, electron correlation can be accurately handled by using a variety of quantum chemistry packages (QCP) based on *ab initio* methods [53, 54, 55, 56, 57, 58, 59]. With proper adjustments, these methods can also provide an accurate description of molecular resonances (hole, shake-up and multiply excited states), for which electron correlation is even more important [60, 61, 62, 63]. So, extending the applicability of these codes to the ionization continuum of molecules seems the natural way to proceed in order to get a similar good description of electron correlation in the continuum region of the molecular spectrum. However, in general, this is a very challenging task. Indeed, most QCPs make use of Gaussian or Slater-type basis functions centered on the various atomic locations, which is advantageous to accelerate convergence in comparison with single-center expansions but turns into a serious disadvantage when dealing with the electronic continuum. This is because Gaussian and Slater-type functions decrease exponentially and therefore are not appropriate to describe the oscillatory behavior of the continuum wave function in the asymptotic region (which is essential to impose the proper boundary conditions of scattering states).

The problem cannot be solved by just increasing the number of basis functions, since this procedure rapidly runs into linear dependencies, thus allowing for the description of typically no more than one or two radial oscillations[64, 65, 66, 67]. For Gaussian functions, the standard in most QCPs due to their easiness for the evaluation of multi-center two-electron integrals, the situation is worse than for Slater functions, since they decrease more rapidly.

Previous work [34, 68, 69, 70, 71, 72] has shown that continuum states of simple diatomic molecules can be accurately described by using more appropriate functions, such as B-splines [73, 69, 74] or finite-element discrete-variable-representation functions (FE-DVR) [75]. However, extension of these methods to larger molecules would be very involved, since, e.g., an efficient evaluation of bi-electronic integrals and consideration of molecular symmetry would require the implementation of new algorithms, mimicking the path that standard QCPs have followed for decades.

It is therefore clear that theoretical efforts aimed at improving the description of ionization processes in molecules are necessary and timely to provide the support that these sophisticated experiments require. Current quantum-chemistry multiconfigurational methods have nowadays reached a considerable level of sophistication in the treatment of ground and electronically *bound* excited states [76], and are able to account for electron correlation with a great level of accuracy. The variational principle is at the heart of conventional multi-reference calculations, however, it cannot be applied as such to the calculation of states embedded in the ionization continuum. For this reason, systematic inclusion of correlation in the *ab initio* description of autoionizing and scattering states in polyelectronic molecules remains a challenge. A common approach used by several authors [77, 78, 27, 51, 28] to describe the electronic continuum in molecules makes use of the static-exchange approximation (SEA) [79, 80], in which the coupling between continuum states associated to different parent ions is neglected. The SEA meets the minimal requirements for the treatment of the continuum, and hence it is often used as the starting point of more sophisticated treatments based on the close-coupling (CC) approximation [81], where inter-channel coupling is included. In this sense, the SEA can be regarded as the equivalent for ionization of what Hartree-Fock is for the description of bound states. The SEA is adequate to describe primary photoemission from valence shells or core orbitals in which the photoelectron emerges with energies of the order of ~ 10 eV or more, since in these conditions the SAE picture still holds. However, the SEA is not appropriate to describe ionization processes in which more than one electron participates, e.g., autoionization arising from multiply-excited states, ionization with simultaneous excitation of one or more of the remaining electrons (shake ups), etc.

Another important requirement for the description of the electronic continuum is to disentangle, across a continuous range of energies, the asymptotic distribution of the ejected electron associated to any given molecular parent ion. This

can be done by *augmenting* the parent-ion states with electrons distributed in a large set of orbitals capable of reproducing the periodic oscillations characteristic of asymptotically-free states. The primitive Gaussian functions normally used in QCPs rapidly exhibit numerical linear dependencies that prevent the description of more than a few radial oscillations, and hence they are not well suited to describe a free electron except for the smallest energies and in a short radial region. This limitation can be partially circumvented going beyond usual Gaussian Type Orbitals (GTOs), by using Polynomial Spherical GTOs (PSGTO) [82, 83], but the continuum wave function quality still worsens when the photon energy increases and not only the outermost valence shells are involved in the photoionization. Radial basis suitable for this task, such as B-splines [69, 74] and finite-element discrete-variable-representation functions (FE-DVR) [75], have been employed in ad-hoc codes for the electronic continuum of small systems [34, 68, 69, 70, 71, 72], mainly for diatomic molecules. These codes, however, are not easy to extend to more complicated molecules, and their treatment of short-range electronic correlation is still rudimentary if compared with standard QCPs.

The single photoionization of an atomic or molecular species A by means of the absorption of one photon γ ,



converts the initial state $|i\rangle$ of the N -electron target to one of the energetically accessible states of the parent ion $|a\rangle$ of the $(N - 1)$ -electron parent ion, $E_a - E_i \leq \hbar\omega_\gamma$, and liberates a photoelectron with asymptotic linear momentum \vec{k} and spin projection σ . This process, therefore, involves the transition from a bound to a scattering state of the N -electron system. This latter circumstance remains true irrespective of whether the single ionization event involves the exchange of one or several photons, possibly with different frequencies, or of whether these photons come in the form of pulses rather than in stationary conditions. Although more complex fragmentation processes, such as multiple ionization and dissociative ionization, may follow valence and inner-valence ionization of atomic and molecular species with XUV light, single ionization with (or without) electronic excitation normally dominates. Furthermore, multiple ionization processes tend to take place through a sequence of single ionization steps when this mechanism is permitted. Therefore, single ionization can describe a broad range of phenomena. In the present work we will limit our attention to this process.

The interaction between matter and radiation is mediated by a one-body operator. To a first approximation, therefore, photoionization amplitudes can be estimated already at the SAE level. In polyelectronic targets, the interaction of the photoelectron originating from a given orbital and the other electrons in the system can be described in terms of an effective potential [84, 85], or within the Hartree [86], Hartree-Fock [87, 88, 89, 90, 25], or DFT approximations [91, 92, 51, 28]. This approach normally yields accurate photoelectron distributions at high photoelectron energies, but fails to reproduce experiments at

energies a few eV above the ionization thresholds, where exchange and correlation effects are important [93, 92]. It has been recently shown that antisymmetry needs to be taken explicitly into account to obtain qualitatively reliable results [94]. Shape resonances are also normally not well reproduced, and SAE approaches, of course, cannot account for processes associated to interchannel coupling, such as inelastic scattering and autoionizing states, particularly when the latter are populated through multiple excitations from the ground state.

The first few correlated bound electronic states of atoms and molecules, and the radiative transitions between them, can be computed quite accurately with existing QCPs. Correlated states in the electronic continuum, on the other hand, are much more challenging to obtain for three reasons. First, as mentioned above, they require the representation of oscillatory electronic wave functions up to large distances, which is challenging for the Gaussian basis sets used in QCPs. Second, the calculation of bound and scattering states requires different algorithms. For bound states, the energy is an unknown quantity that is determined through diagonalization, and degeneracy is an issue only for selected subsets of the configuration space. For ionization states, on the other hand, energy is given and, as a rule, each level is multiply or, possibly, infinitely degenerate. Simply restricting the hamiltonian to a finite basis and diagonalizing it, therefore, is not an option. Third, the scattering states required to reproduce given experimental conditions must fulfill well defined asymptotic boundary conditions.

The common practice in most theoretical approaches is to limit the Hilbert space to a subspace of configurations accounting for the most relevant dynamics of the photoionization problem. This can be realized by dividing the position space in two regions: an inner one, in which the target and parent-ion states lie, and an outer one, which contains the appropriate asymptotic solutions of the scattering states. The main differences among the available implementations based on this space partition lie in the theory level employed to compute the wave function in the inner part, and how it matches the long-range part of the wave function in the outer region. To compute the target and parent-ion states, any of the tools accounting for electron correlation in bound states can be used, e.g., multi-configuration Hartree-Fock (MCHF), configuration interaction (CI), coupled cluster, etc (see [95, 96, 97]).

To overcome the above limitations, we have developed an approach that matches the capability of state-of-the-art techniques for the calculation of correlated excited states, provided by widely available packages such as MOLCAS [53], MOLPRO [54], Columbus [55, 56], Dalton [57], GAMESS [58] and Gaussian [59], with well-established techniques for the description of the electronic continuum. We do so by using a hybrid Gaussian-B-spline basis (GABS) [98]. There are other approaches based on a similar philosophy, in which a short-range part represented by GTOs is complemented with other functions more appropriate for the scattering description, like Finite Element (FE) representation of the radial coordinate [94, 99], Discrete Variable Representation (DVR) [100, 101, 102], and plane

waves [30]. Other efforts have been made within the framework of Density Functional Theory (DFT), using for instance a multicenter expansion in B-splines [91]. We want to notice that there is another research group that use a formalism very similar to ours, merging available QCPs with scattering methods, although they use the R-matrix formalism to solve the scattering problem ([103, 104]). Their basis functions is also a hybrid one Gaussian and B-splines basis, but their Gaussian functions are regular GTOs whereas we use PSGTOs, which gives us more flexibility by reducing the maximum orbital angular momentum needed in the single-center expansion around the center of mass of the system. In fact we use (as will be apparent later in the thesis) the PSGTOs functions to connect the polycentric GTOs functions with the B-splines. Other groups have implemented the calculation of integrals involving B-splines and GTOs, but this has the inconvenient that, it is computationally very costly. Despite the existence of all these models, ours has its own advantages. Increasing the number of electrons for a fixed number of scattering channels does not make the computational cost of the full dimensional problem significantly higher. This means that the effort made to compute the helium atom would be similar to that needed to compute the water molecule for instance. Although this points to the fact that the computation of very small systems would not be very efficient, our real target, small and medium-size molecules, would be easily achievable without serious penalties. Another benefit of our implementation is the capability to obtain from a multichannel scattering problem either time independent observables, e.g., resonance energies and widths, or time dependent ones, expanding for the latter the wave function in the box of eigenstates, a very convenient way to carry out the time propagation and to extract observables from it. An additional advantage is that resonances, like doubly excited states, arise naturally from the close-coupling expansion without the need of an *ad hoc* inclusion, if one of them plays a key role in the dynamics. Our model can also support core holes, which will be the object of future studies.

1.2 MOTIVATION AND OUTLINE OF THE THESIS

The main objective of this thesis is to introduce a new formalism, XCHEM, that will allow us to compute accurately the molecular continuum states for the single-ionization problems. This new approach is based on the merging of available QCPs with state-of-the-art scattering numerical methods. The QCPs provide us with the low lying bound spectrum of the system and the parent-ion states, which can be computed with a high level of electronic correlation thanks to the sophisticated quantum chemistry methods that have been implemented in those computational packages. The matching of the short-range radial domain with the long-range domain for the ejected electron, is achieved using the hybrid Gaussian-B-splines (GABS) basis.

Hence, we focus on the test of every component of the XCHEM method to ensure the reliability of its results. First we study the photoionization of the hydrogen atom, triggered by different kinds of ultrashort pulses, using the GABS basis to understand better its performance. The other benchmark systems were the He atom and the H_2 molecule, for which we study the photoionization cross sections and the resonance parameters of several resonant series. This is the first step towards more complex systems, because in both cases the parent ions left behind have only one electron.

The next system we studied, the Ne atom, permitted us the study a real polyelectronic system (polyelectronic parent ions) for which a large amount of data had been published. Therefore, we used this published results together with independent atomic codes to assess the quality of XCHEM results. After checking throughout the thesis that the observables computed with XCHEM gave very good results, we aimed to compute new parameters not available in the literature yet, for the Ne photoionization of Ne. Specifically, the Starace parameters and the partial widths for the decay of the $2s2p^63p$, $2s2p^64p$ and $2s2p^65p$ resonances to the $2s^22p^5\epsilon s$ and $2s^22p^5\epsilon d$ scattering channels. We have also applied a two-photon transition perturbative model, in which matrix elements computed with XCHEM have been used to reproduce the modulation of the side bands in a RABITT experiment.

This thesis is structured as follows. In Chapter (2), we give an overview of the *ab initio* methods used to compute the molecular (and atomic) electronic bound spectrum, which will be useful to calculate the parent-ion states we included in our CC expansions. Chapter (3) focuses on the time-independent scattering theory for molecules, where we highlight the seek of the multichannels scattering wave function in form of a CC expansion, and the properties of the scattering S matrix to compute the properties of the autoionizing states. Chapter (4) gives an overview on the photoionization theory. We explain in this chapter the theory behind the one- and two-photon absorption processes, also when a discrete state is embedded in the continuum. The theoretical foundations of the Reconstruction of Attosecond Bursts by Interference of Two-photon Transitions (RABITT) spectroscopy is provided. In Chapter (5), we explain the XCHEM approach, through which we merge the QCPs with the scattering methods to compute accurate scattering states. We give the basis and space partitioning details, together with the explanation of several methods we have implemented to compute numerically the scattering wave function. Chapter(6) shows the results we obtained using the GABS basis to study the photoionization of the hydrogen atom, perturbatively and solving the time-dependent Schrödinger equation (TDSE) in the presence of different attosecond pulses. Chapter (7) shows the performance of the XCHEM method for the photoionization and multichannel scattering problem for different systems: He, H_2 and Ne. We focused on the computation of the resonances parameters as well as the cross sections, and for Ne, we reproduced part of a very recent RABITT experiment. Finally in Chapter (8), we give the conclusions of the

thesis and some perspectives to continue with this work. Throughout this thesis, unless otherwise stated, we will use atomic units.

Part II

THEORETICAL METHODS

MOLECULAR ELECTRONIC STRUCTURE *AB INITIO* METHODS

The Schrödinger equation is the keystone of the quantum chemistry because it gives access to the complete information of the system via the wave functions. Electrons play the key role on the chemical properties of a given molecular system, but if the molecule is not isolated, after its excitation through an external perturbation, or when the molecule is in contact with a heat reservoir, the nuclei can be excited as well, and this excess energy be transferred to its degrees of freedom, that makes the molecule to vibrate, rotate, or undergo fragmentation processes. In such a situations, not only the electronic dynamics is relevant, the nuclear motion is important too. Then our aim is to find an approximate solution, as accurate as possible, of the Schrödinger equation. Let's consider the general case of a molecule made up of M nuclei and N electrons, the full non-relativistic time-independent Hamiltonian is given by:

$$H(\mathbf{r}, \mathbf{R}) = \sum_{i=1}^N \left(-\frac{1}{2} \nabla_i^2 - \sum_{A=1}^M \frac{Z_A}{R_{Ai}} \right) + \sum_{i>j=1}^N \frac{1}{r_{ij}} - \frac{1}{2M_A} \sum_{A=1}^M \nabla_A^2 + \sum_{A>B=1}^M \frac{Z_A Z_B}{R_{AB}}, \quad (2.1)$$

where $r_{ij} = |\mathbf{r}_i - \mathbf{r}_j|$, \mathbf{r}_i and \mathbf{r}_j being the position of the i -th and j -th electrons (with respect to the center of mass), respectively, \mathbf{R}_A is the position of A nucleus and M_A is the ratio of the mass of nucleus A to the mass of an electron. The first three terms in the right-hand-side of Eq. (2.1) correspond to the electronic Hamiltonian $H_{elec}(\mathbf{r}; \{\mathbf{R}_A\})$ and depends parametrically on the nuclei positions:

$$H_{elec}(\mathbf{r}; \{\mathbf{R}_A\}) = \sum_{i=1}^N \left(-\frac{1}{2} \nabla_i^2 - \sum_{A=1}^M \frac{Z_A}{R_{Ai}} \right) + \sum_{i>j=1}^N \frac{1}{r_{ij}}. \quad (2.2)$$

Since nuclei are much heavier than electrons ($M_A \gg 1$), they move more slowly. Hence, it would be a good approximation to consider the electrons moving in the field of fixed nuclei. This is the Born-Oppenheimer approximation, and within this approximation, the kinetic energy of the nuclei can be neglected and the repulsion between them can be considered constant. Actually, for the purposes of this thesis, we are not interested in the nuclear motion, we use the fixed nuclear approximation (FNA). Then we will focus on the electronic Hamiltonian (2.2) plus the nuclei repulsion term, that only adds a constant value to the electronic energy.

Besides the spatial coordinate, to completely describe an electron it is necessary to specify its spin ζ . We denote the spatial and spin coordinates collectively by \mathbf{x} ($\mathbf{x} \equiv \{\mathbf{r}, \zeta\}$). The wave function of the N -electron system is then a function of these variables: $\Psi(\mathbf{x}_1, \dots, \mathbf{x}_N) \equiv \Psi(\mathbf{X})$. If the N electron were independent, we could look for a solution of Eq. (2.2) of the form of molecular orbitals products (Hartree products):

$$\Psi(\mathbf{X}) = \prod_{i=1}^N \phi_i(\mathbf{x}_i), \quad (2.3)$$

(note that we have dropped the parametric dependence on the nuclei positions, which is implicitly assumed), but the presence of the bielectronic terms make this solution to fail, unless these interaction are averaged and accounted as an effective potential. Furthermore, the Hartree products do not satisfy the Pauli exclusion principle, which states that since electrons are fermions, the electronic wave function has to be antisymmetric by exchange of two electrons. This is solved writing $\Psi(\mathbf{X})$ as a Slater determinant

$$\Psi(\mathbf{X}) = \frac{1}{\sqrt{N!}} \begin{vmatrix} \phi_1(\mathbf{x}_1) & \phi_2(\mathbf{x}_1) & \dots & \phi_N(\mathbf{x}_1) \\ \phi_1(\mathbf{x}_2) & \phi_2(\mathbf{x}_2) & \dots & \phi_N(\mathbf{x}_2) \\ \vdots & \vdots & \ddots & \vdots \\ \phi_1(\mathbf{x}_N) & \phi_2(\mathbf{x}_N) & \dots & \phi_N(\mathbf{x}_N) \end{vmatrix}, \quad (2.4)$$

which enforce the antisymmetrization of the wave function. The normalized Slater determinants can be written in a more compact notation, only showing the diagonal components of the determinant assuming the electrons to be labeled in order $\mathbf{x}_1, \mathbf{x}_2, \dots, \mathbf{x}_N$:

$$\Psi(\mathbf{X}) = |\phi_i \phi_j \dots \phi_k\rangle \quad (2.5)$$

2.1 THE HARTREE-FOCK APPROXIMATION

This is usually the first step towards more accurate approximations and is equivalent to the molecular orbital approximation, in which electrons are assumed to occupied some definite orbitals. Following this picture, the ground state of the N -electron system is described by a single Slater determinant

$$|\Psi_0\rangle = |\phi_1 \phi_2 \dots \phi_N\rangle. \quad (2.6)$$

According to the variational principle, the best wave function of this functional form is the one which gives the lowest possible energy

$$E_0 = \langle \Psi_0 | H_{elec} | \Psi_0 \rangle \quad (2.7)$$

The integral from Eq. (2.7) can be further simplified using the Slater-Condon rules. These rules permit to reduce the integral of N -electron wave functions constructed as Slater determinants into sums over integrals of individual molecular

orbitals. It follows that for a one-body operator, the matrix elements for two wave functions differing by more than two orbitals vanish. The wave function (2.6) is optimized (E_0 minimized) through the choice of the spin orbitals, and the optimal set of spin orbitals is determined by solving iteratively the Hartree-Fock equation. These are eigenvalue equations of the form

$$f(1)|\phi_i\rangle = \epsilon_i|\phi_i\rangle, \quad (2.8)$$

where $f(1)$, called the Fock operator, is an effective one-electron operator given by

$$f(i) = -\frac{1}{2}\nabla_i^2 - \sum_{A=1}^M \frac{Z_A}{R_{Ai}} + V_{HF}(i), \quad (2.9)$$

where $V_{HF}(i)$ is the average potential experienced by the i -th electron due to the presence of the other electrons. This way, the electronic repulsion terms are replaced by a mean field, and the complicated many-electron problem by a one-electron problem. The procedure to solve Eq. (2.8) is called the self-consistent-field (SCF) method, and the basic idea behind it, is making an initial guess for the spin orbitals in order to calculate the average field $V_{HF}(i)$, solve the eigenvalue equation and from the new set of spin orbitals start the process again until some convergence criteria is met (the mean field no longer changes). Using a basis set of K spatial functions, leads to a set of $2K$ spin orbitals, and then solving the Hartree-Fock equations we obtain N occupied spin orbitals and $2K - N$ virtual ones. The Hartree-Fock potential is given by

$$V_H(1) = \sum_{i=1} (J_i(1) - K_i(1)), \quad (2.10)$$

where the first term in the right-hand-side corresponds to the energy due to the Coulomb interaction between an electron in spin orbital i and an electron in spin orbital j

$$J_i(1)|\phi_j(1)\rangle = \langle\phi_i(2)|\frac{1}{r_{12}}|\phi_i(2)\rangle|\phi_j(1)\rangle, \quad (2.11)$$

and the second term in Eq. (2.10) corresponds to the exchange energy which is a pure quantum effect arising from the exchange of two electrons:

$$K_i(1)|\phi_j(1)\rangle = \langle\phi_i(2)|\frac{1}{r_{12}}|\phi_j(2)\rangle|\phi_i(1)\rangle. \quad (2.12)$$

The energy of an occupied spin orbital ϵ_i , represents the amount of energy (with opposite sign) that is required to remove an electron from that spin orbital. In the Hartree-Fock approximation, the total energy of the system departs from the actual energy by an amount which is given exclusively by the electronic correlation E_{corr} :

$$E_{corr} = E_{exact} - E_{HF}, \quad (2.13)$$

where E_{exact} corresponds to the exact energy of the system and E_{HF} to the Hartree-Fock energy obtained with a complete basis set. Part of this correlation is

due to the Coulomb interaction which makes the electrons repelling each others. In fact, the electron creates a Coulomb hole around its position because this electrostatic repulsion reduces the probability to find another electron in the same region of the space. Although the Coulomb correlation is the largest contribution to the electron correlation, it is not the only one. Indeed, because it implies that two fermions of same spin cannot occupy the same position simultaneously, the Pauli exclusion principle accounts for the correlation between electrons of same spin. Then, any electron create a second type of hole, called Fermi hole. It is common also to distinguish the electron correlation into dynamic and static correlation. The former arise from the fact that the electrons are not moving independently (the motion of one affects all the others). It is associated with instant correlation between electrons, mainly between opposite-spin electrons. The static correlation refers to the situation where a single Slater determinant is not sufficient to describe the ground state (e.g., when the ground state is degenerate).

2.2 CONFIGURATION INTERACTION

It has been observed that the system is better described when the total wave function is expressed as a linear combination of determinants, in particular when there are degenerate states. The additional determinants beyond the Hartree-Fock wave function, correspond to electronic configurations in which electrons are promoted into virtual orbitals, hence, such a determinants represent excited states. The configuration interaction (CI) method exploits this idea, allowing the electrons to move more freely since they can occupy virtual orbitals. In this scheme, the total wave function is written as:

$$|\Phi_0\rangle = c_0|\Psi_0\rangle + \sum_i \sum_\alpha c_i^\alpha |\Psi_{i\alpha}\rangle + \sum_{i<j} \sum_{\alpha<\beta} c_{ij}^{\alpha\beta} |\Psi_{ij}^{\alpha\beta}\rangle + \dots, \quad (2.14)$$

where the latin letters i and j are the occupied spin orbitals in the reference Hartree-Fock wave function, and the greek letters α and β are the virtual spin orbitals. The number of indexes determines the order of the excitation (e.g., double excitations $\Psi_{ij}^{\alpha\beta}$: an electron in the i -th (j -th) orbital is promoted to the virtual α -th (β -th)orbital). The CI calculation can take advantage of the symmetry properties of the system since it is known that only states of same symmetry will couple. Then, the linear combination in (2.14) can be reduced to a basis of states with the same spatial and spin symmetry, also called configuration state functions (CSFs). According to the Slater-Condon rules, Hamiltonian matrix elements between determinants that differ by more than two spin orbitals are zeros. Then, the Hartree-Fock determinant Ψ_0 only couples with doubly-excited states $\Psi_{ij}^{\alpha\beta}$ (because due to the Brillouin's theorem we have $\langle\Psi_0|H|\Psi_i^\alpha\rangle = 0$) and the singly-excited states Ψ_i^α with some singly-, doubly- and triply-excited states. The expansion coefficients in Eq. (2.14) can be determined by solving $H\Phi_0 = E\Phi_0$. The configuration interaction method does not contain approximations and exact solutions to the

total wave function can be found if all the configurations are taken into account. Such situation is referred as a full CI calculation. Unfortunately this is very costly, because the number of determinants required in the expansion grows factorially with the number of electrons and orbitals. Then the CI expansion needs to be truncated to a certain order of excitations, good enough to describe the problem of interest. For a large number of scenarios, including single- and double-excitations is sufficient.

2.3 COMPLETE ACTIVE SPACE SELF CONSISTENT FIELD METHOD

The multiconfigurational self-consistent field (MCSCF) method is a CI method where, besides the coefficients in the determinant expansion, the spin orbitals are also optimized by using an iterative like self consistent field procedure. Obviously, the SCF procedure is much more complex and harder to converge than the Hartree-Fock method. By including the orbital optimization in the SCF, the MCSCF allows the spin orbitals to be partially occupied and then to describe quasi-degenerating effects which are part of the non-dynamical correlation. However, the relaxation of this orbital does not permit to recover any dynamical correlation which depends mainly on the number of CSFs included.

In a more general aspect, the computational cost and accuracy of a MCSCF calculation is determined by the choice (number and type) of the electronic configurations used in the linear expansion. This basis of configurations constitutes the active space and has to be defined manually for each calculation. It is the main disadvantage of the method since the choice of the active space cannot always be deduced from simple chemical considerations and often requires practical experience. A very common option is the complete active space (CAS), which divides the included orbitals in two categories: the inactive and the active ones. The formers are fixed to a specific occupation number (0 or 2) while the active spin orbitals are used to generate all possible CSFs. The number N_s of singlet CSFs is given by the combination of N electrons in K basis functions:

$$N_s = \frac{K!(K+1)!}{\left(\frac{N}{2}\right)!\left(\frac{N}{2}+1\right)!\left(K-\frac{N}{2}\right)!\left(K-\frac{N}{2}+1\right)!} \quad (2.15)$$

This number N_s can be considerably reduced by considering the molecular symmetry. The choice of the active space depends as much on the molecule as on the problem to be studied. The multireference configuration interaction (MRCI) is formally equivalent to the standard CI except that it makes use of a MCSCF wave function as reference instead of the Hartree-Fock one. Thus, a preliminary MCSCF calculation has to be performed.

The CASSCF step represents an additional computational effort but the use of better reference determinants can make the convergence faster in the MRCI. Despite of this, CASSCF/MRCI is rather expensive compared to other *ab initio*

methods. Its use is limited to rather small systems. A further limitation comes from the fact that most of the commercial programs that implement the method do not give the possibility to choose explicitly the electronic configurations to be included in the CI expansion. Due to this technical limitation and to the variational principle, the system will always decay to the lowest energy state of specified symmetry. Then, optimization of higher energy states of same symmetry is a nontrivial task.

SCATTERING THEORY

3.1 THE CLOSE COUPLING METHOD

In this chapter we will consider the time-independent multichannel scattering theory, for the inelastic collision of an electron with a molecular ionic target

$$A_a^+ + e_{\vec{k}\sigma}^- \rightarrow A_b^+ + e_{\vec{k}'\sigma'}^- \quad (3.1)$$

A common procedure to build a complete set of scattering states at a given energy E is the close-coupling approach (CC). In CC, the configuration space is expressed in terms of the linear combination of antisymmetrized products of bound states of the parent ion A^+ and states of the asymptotically free electron with a well defined angular momentum [105]. Indeed, when separated by large distances, the parent ion and the electron do not interact and these states are therefore sufficient to enumerate all the possible initial or final single-ionization states of the system. When the parent ion and the electron are spatially close, they can exchange energy, angular momentum, and spin in an interaction that can be represented as a collision. To improve the description of these short-range interactions, the CC expansion is normally complemented with a set of localized N -electron functions:

$$\Psi_{\alpha E}^\Gamma(\mathbf{X}_N) = \hat{\mathcal{A}} \sum_{\beta=1}^M Y_\beta^\Gamma(\mathbf{X}_N; \hat{\mathbf{r}}_N \zeta_N) \frac{F_{\beta\alpha}^\Gamma(r_N)}{r_N} + \sum_{\gamma=1}^m \aleph_\gamma^\Gamma(\mathbf{X}_N) c_{\gamma\alpha}, \quad (3.2)$$

where α labels the linearly independent solutions of the Schrödinger equation. $\mathbf{X}_N \equiv \mathbf{x}_1, \dots, \mathbf{x}_N$, with $\mathbf{x}_i \equiv \mathbf{r}_i \zeta_i$, \mathbf{r}_i and σ_i being the electron position and spin coordinates, respectively. The scattering states satisfy the time-independent Schrödinger equation

$$H_N \Psi_{\alpha E} = E \Psi_{\alpha E}, \quad (3.3)$$

where E is the total energy and H_N is the N -electron Hamiltonian in the FNA defined by

$$H_N = \sum_{i=1}^N \left(-\frac{1}{2} \nabla_i^2 - \sum_{k=1}^M \frac{Z_A}{R_{Ai}} \right) + \sum_{i>j=1}^N \frac{1}{r_{ij}} + \sum_{A>B=1}^M \frac{1}{R_{AB}}, \quad (3.4)$$

which describes the collision of an electron with a molecule having nuclei with nuclear charge numbers Z_A , low enough not to consider relativistic effects. The

origin of coordinates can be taken to be the center of mass of the system, and we have written $r_{ij} = |\mathbf{r}_i - \mathbf{r}_j|$ where \mathbf{r}_i and \mathbf{r}_j are the vector coordinates of the i -th and j -th electrons, respectively; and $R_{ki} = |\mathbf{R}_k - \mathbf{r}_i|$, \mathbf{R}_k being the vector coordinate of the nucleus k . It is useful to define H_N in terms of the $(N-1)$ -electron Hamiltonian H_{N-1} , in order to define the scattering amplitudes:

$$H_N = H_{N-1} - \frac{1}{2} \nabla_N^2 - \sum_k \frac{Z_k}{R_{kN}} + \sum_{i=1}^N \frac{1}{r_{iN}}, \quad (3.5)$$

The label Γ in Eq. (3.2) comprehends those conserved quantum numbers corresponding to the eigenvalues of the operators that commute with the Hamiltonian, and the irreducible representation belonging to the molecule point group symmetry. In the electrostatic approximation the conserved quantum numbers in the molecular case are the total spin S and its projection onto the z direction, Σ . The channel functions $Y_\beta^\Gamma(\mathbf{X}_N; \hat{\mathbf{r}}_N \sigma_N)$ are obtained by coupling the target eigenstates Φ_b ($H_{N-1} \Phi_b = E_b \Phi_b$) with the spin-angle functions of the scattered electron to form eigenfunctions of the square of the total spin angular momentum operator and its z -component

$$Y_\beta^\Gamma(\mathbf{X}_N; \hat{\mathbf{r}}_N \zeta_N) = \sum_{\Sigma_b \sigma} C_{S_b \Sigma_b, \frac{1}{2} \sigma}^{S \Sigma} \Phi_b(\mathbf{X}_N) Y_{\ell m}(\theta_N, \phi_N) \chi_{\frac{1}{2} \sigma}(\zeta_N), \quad (3.6)$$

where $Y_{\ell m}(\theta_N, \phi_N)$ are the spherical harmonics describing the angular distribution of the scattered electron, $\chi_{\frac{1}{2} \sigma}(\zeta_N)$ are electron spin functions and $C_{ab, cd}^{ef}$ are Clebsch-Gordan coefficients. The reduced radial functions $F_{\beta \alpha}^\Gamma(r_N)$ in Eq. (3.2) describe the radial motion of the scattered electron in the β channel, and satisfy certain asymptotic boundary conditions (see next section) that fully determine the $\Psi_{\alpha E}$ solutions of the scattering problem. The $\aleph_\gamma^\Gamma(\mathbf{X}_N)$ functions are antisymmetric, \mathcal{L}^2 integrable, and are assumed to decrease rapidly with the distance from the center of mass. The $\aleph_\gamma^\Gamma(\mathbf{X}_N)$ functions represent the short-range electronic correlation effects, which may not be suitably described by a finite CC expansion. These functions could also give rise to spurious resonances when multiconfiguration target states are used, in which case special care is needed [106].

To obtain accurate scattering amplitudes we must include in the first expansion on the right-hand side (RHS) of Eq. (3.2) all the target states of physical interest: both the initial and final parent-ion eigenstates corresponding to the scattering amplitude of interest, as well as all other target eigenstates that are expected to play an important role as intermediate states.

Substituting $\Psi_{\alpha E}^\Gamma(\mathbf{X}_N)$ in the Schrödinger equation (3.3), and projecting onto the channel functions $Y_\beta^\Gamma(\mathbf{X}_N; \hat{\mathbf{r}}_N \sigma_N)$, and onto the short-range N -electrons functions $\aleph_\gamma^\Gamma(\mathbf{X}_N)$, we obtain a system of close-coupling equations

$$\begin{cases} \langle \frac{Y_\beta^\Gamma(\mathbf{X}_N; \hat{\mathbf{r}}_N \sigma_N)}{r_N} | (H_N - E) | \Psi_{\alpha E}^\Gamma(\mathbf{X}_N) \rangle = 0, & \beta = 1, \dots, M \\ \langle \aleph_\gamma^\Gamma(\mathbf{X}_N) | (H_N - E) | \Psi_{\alpha E}^\Gamma(\mathbf{X}_N) \rangle = 0, & \gamma = 1, \dots, m, \end{cases} \quad (3.7)$$

which can be cast in the form of second-order integrodifferential coupled equations for the $F_{\beta\alpha}^\Gamma(r_N)$ reduced radial functions, subject to the orthogonality constraints $\langle F_{\beta\alpha}^\Gamma(r) | P_{n\ell_\alpha}(r) \rangle = 0$ for all n . The orthogonality constraint ensures that the reduced radial functions are orthogonal to all the orbitals $P_{n\ell_\alpha}(r)$, used to construct the target states:

$$\begin{aligned} & \left(\frac{d^2}{dr^2} - \frac{\ell_\beta(\ell_\beta + 1)}{r^2} + 2 \frac{(\sum_k Z_k - N - 1)}{r} + k_\beta^2 \right) F_{\beta\alpha}^\Gamma(r), \\ & = 2 \sum_{\gamma=1}^M \sum_{\lambda=1}^{\lambda_{\max}} d_{\beta\gamma\lambda}^\Gamma F_{\gamma\alpha}^\Gamma(r), \quad r \geq R_0, \beta = 1, \dots, M. \end{aligned} \quad (3.8)$$

For $r_N > R_0$, the radial distance beyond which all the parent-ion states are negligible, the long-range potential coefficients $d_{\beta\gamma\lambda}^\Gamma$ are given by

$$d_{\beta\gamma\lambda}^\Gamma = \left\langle \frac{Y_\beta^\Gamma(\mathbf{X}_N; \hat{\mathbf{r}}_N \sigma_N)}{r_N} \middle| \sum_{k=1}^{N-1} r_k^\lambda P_\lambda(\cos \theta_{kN}) \middle| \frac{Y_\gamma^\Gamma(\mathbf{X}_N; \hat{\mathbf{r}}_N \sigma_N)}{r_N} \right\rangle, \quad (3.9)$$

where θ_{kN} is the angle between the unit vectors $\hat{\mathbf{r}}_k$ and $\hat{\mathbf{r}}_N$, and $P_\lambda(\cos \theta)$ are the Legendre polynomial.

3.2 ASYMPTOTIC BOUNDARY CONDITIONS

To uniquely specify the scattering solutions $\Psi_{\alpha E}^\Gamma(\mathbf{X}_N)$, we need to define the asymptotic boundary conditions satisfied by the reduced radial wave functions $F_{\beta\alpha}^\Gamma(r_N)$. The M second-order differential equations (3.8) support in general $2M$ linearly independent solutions. However, the requirement that the total wave function is bounded

$$|F_{\beta\alpha}^\Gamma(r)| < \infty \quad r \rightarrow \infty; \quad F_{\beta\alpha}^\Gamma(r) \sim a_{\beta\alpha} r^{l_\beta+1} \quad r \rightarrow 0; \quad \alpha, \beta = 1, \dots, M, \quad (3.10)$$

$a_{\beta\alpha}$ being some normalization factors. The previous condition reduce the number of linearly independent solutions to the number of open channels M_0 at energy E . For simplicity let's assume all channels are open, then the asymptotic boundary conditions satisfied by the M linearly independent solutions of (3.8) can be written in the form

$$F_{\beta\alpha}^\Gamma(r) \sim \frac{1}{\sqrt{k_\beta}} [\sin \Theta_\beta(r) \delta_{\beta\alpha} + \cos \Theta_\beta(r) \mathbb{K}_{\beta\alpha}^\Gamma], \quad r \rightarrow \infty, \quad (3.11)$$

where

$$\Theta_\beta(r) = k_\beta r + \frac{Z}{k_\beta} \ln 2k_\beta r - \ell_\beta \pi / 2 + \sigma_{\ell_\beta}(k_\beta), \quad (3.12)$$

Z is the charge of the molecular parent ion and σ_{ℓ_β} is the Coulomb phase $\sigma_\ell = \arg \Gamma(\ell + 1 + i\gamma)$. In Eq. (3.11), the factor $k_\beta^{-1/2}$ normalizes the ingoing

spherical wave to unit flux, which implies that the $M \times M$ -dimensional $K_{\beta\alpha}^\Gamma$ matrix is symmetric. This matrix can be computed from the following system of integral equations [107]

$$\mathbb{K}_{\beta E' \alpha E}^\Gamma - V_{\beta E' \alpha E}^\Gamma(E) = \sum_{\gamma \neq \beta} \int d\epsilon V_{\beta E' \gamma \epsilon}^\Gamma(E) \frac{\mathcal{P}}{E - \epsilon} \mathbb{K}_{\gamma \epsilon \alpha E}^\Gamma, \quad (3.13)$$

where \mathcal{P} refers to the principal part and the effective potential $V_{\beta E' \alpha E}^\Gamma(E)$ is defined by

$$V_{\beta E' \alpha E}^\Gamma(E) \equiv \langle Y_{\beta E'}^\Gamma(\mathbf{X}_N; \hat{\mathbf{r}}_N \sigma_N) | H_N - E | Y_{\alpha E}^\Gamma(\mathbf{X}_N; \hat{\mathbf{r}}_N \sigma_N) \rangle. \quad (3.14)$$

The system of equations (3.13) can be solved, for instance, using the Kohn variational principle [108]. We will refer to the stationary scattering solution with the asymptotic boundary condition (3.11) as $\Psi_{\alpha E}^{\Gamma P}(\mathbf{X}_N)$. Other important matrices in the scattering formalism the $S_{\alpha\beta}^\Gamma$ and $T_{\alpha\beta}^\Gamma$ matrices, can be expressed in terms of the $\mathbb{K}_{\alpha\beta}^\Gamma$ mentioned above. The scattering $S_{\alpha\beta}^\Gamma$ matrix corresponds to reduced radial functions $u_{\beta\alpha}^{\Gamma\pm}(r_N)$ for the N -th electron following the asymptotic behaviour ($\Psi_{\alpha E}^{\Gamma\pm}(\mathbf{X}_N)$ for the total wave function) [109, 110]

$$\begin{aligned} u_{\beta\alpha}^{\Gamma+}(r) &= \sqrt{\frac{2}{\pi k_\beta}} [e^{-i\Theta_\beta(r)} \delta_{\beta\alpha} + e^{i\Theta_\beta(r)} S_{\beta\alpha}^\Gamma], \quad r \rightarrow \infty, \\ u_{\beta\alpha}^{\Gamma-}(r) &= \sqrt{\frac{2}{\pi k_\beta}} [e^{i\Theta_\beta(r)} \delta_{\beta\alpha} + e^{-i\Theta_\beta(r)} S_{\beta\alpha}^{*\Gamma}], \quad r \rightarrow \infty. \end{aligned} \quad (3.15)$$

Thus the scattering wave function $\Psi_{\alpha E}^{\Gamma-}$ behaves asymptotically as a combination of incoming spherical waves for all open channels (α, β , and γ in Figure 5.1) and an outgoing spherical wave in channel α

$$\begin{aligned} \langle \Psi_{\alpha E'}^{\Gamma-} | \Psi_{\beta E}^{\Gamma+} \rangle &= \delta(E' - E) S_{\alpha\beta}^\Gamma(E) \\ \langle \Psi_{\alpha E'}^{\Gamma\pm} | \Psi_{\beta E}^{\Gamma\pm} \rangle &= \delta(E' - E) \delta_{\alpha\beta} \end{aligned} \quad (3.16)$$

In terms of the $\mathbb{K}_{\alpha\beta}^\Gamma$ matrix it takes the form:

$$S_{\alpha\beta}^\Gamma = \frac{\mathbb{I} - i\pi \mathbb{K}_{\alpha\beta}^\Gamma}{\mathbb{I} + i\pi \mathbb{K}_{\alpha\beta}^\Gamma}. \quad (3.17)$$

The same reduced radial functions in Eq. (3.15) can be obtained using the $T_{\alpha\beta}^\Gamma$ matrix by making the transformation

$$T_{\alpha\beta}^\Gamma = \frac{1}{2i\pi} (\mathbb{I} - S_{\alpha\beta}^\Gamma) \quad (3.18)$$

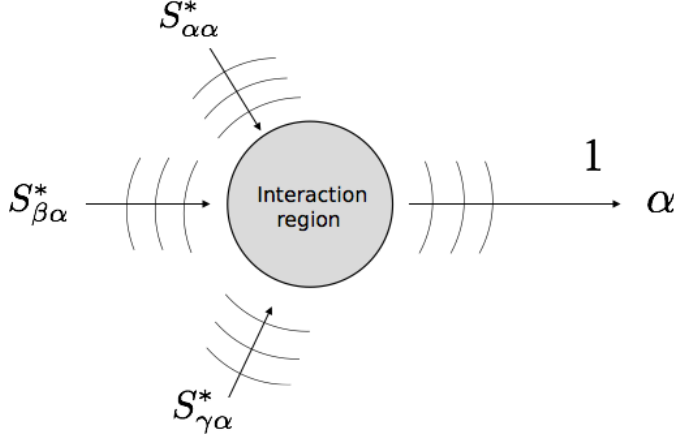


Figure 3.1: Sketch of the incoming boundary conditions that must fulfil the scattering wave function $\Psi_{\alpha E}^{\Gamma-}$ (see text for notations).

3.3 ANALYTIC PROPERTIES OF THE S MATRIX

From the first equation in 3.16, it is easy to show that the $S_{\alpha\beta}$ matrix (from now on we drop the Γ superscript for the sake of simplicity) is unitary:

$$(S_{\alpha\beta})^\dagger S_{\alpha\beta} = S_{\alpha\beta} (S_{\alpha\beta})^\dagger = \mathbb{I}. \quad (3.19)$$

This condition implies that the eigenvalues coming from the $S_{\alpha\beta}$ matrix diagonalization has module one

$$S_{\alpha\beta} = \mathbf{U} e^{2i\Delta} \mathbf{U}^\dagger, \quad (3.20)$$

where $e^{2i\Delta} = e^{2i\phi_\alpha} \delta_{\alpha\beta}$ is a diagonal matrix storing the eigenvalues (the number 2 is introduced by convenience). The $\phi_\alpha(E)$ phases are called either eigenphases or scattering phase shifts, result from the short-range departure of the polyelectronic potential, from the Coulomb potential. Hence, the eigenphases are very sensitive to the electronic correlation. In the vicinity of an isolated resonance the $S_{\alpha\beta}$ matrix can be written as [111, 112, 113]

$$S_{\alpha\beta}(E) = S(E)_{\alpha\beta}^0 - \frac{i\sqrt{\Gamma_\alpha \Gamma_\beta}}{E - E_r + \frac{i\Gamma}{2}}, \quad (3.21)$$

where E_r and Γ are the resonance energy and width respectively, Γ_α is the partial width describing the decay of the resonance into the α channel of $S(E)_{\alpha\beta}^0$, which is a background matrix slowly varying with the energy E , as well as the eigenphases $\phi_\alpha^0(E)$ arising from its diagonalization

$$\mathbf{O}^\dagger S(E)_{\alpha\beta}^0 \mathbf{O} = e^{2i\phi_\alpha^0} \delta_{\alpha\beta}. \quad (3.22)$$

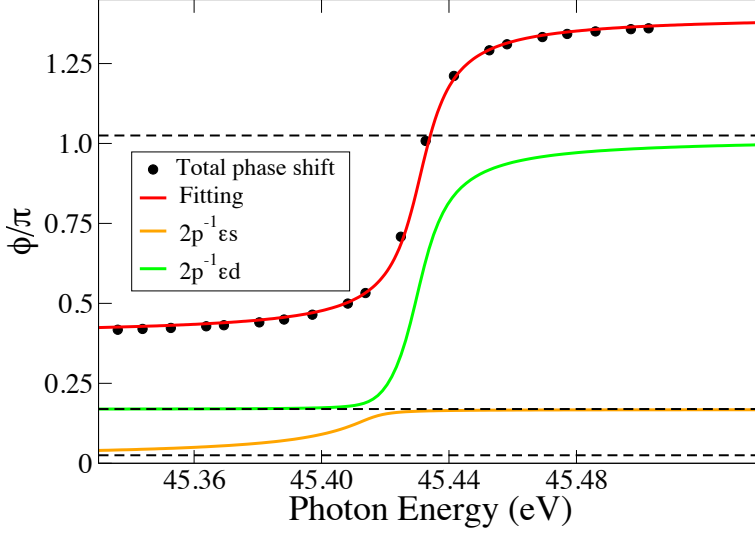


Figure 3.2: Total phase shift and eigenphases of $1P^0$ symmetry, for the two channels scattering problem in Ne, around the $2s2p^63p$ resonance. (see 7.2 for details).

The total width Γ is the sum over all the partial widths $\Gamma = \sum_{\mu} \Gamma_{\mu}$. Resonances are poles of the $S(E)_{\alpha\beta}$ matrix. If we apply to the $S(E)_{\alpha\beta}$ matrix a similarity transformation using the matrices that diagonalize $S(E)_{\alpha\beta}^0$, we obtain

$$\mathbf{O}^\dagger S(E)_{\alpha\beta} \mathbf{O} = e^{i\phi_\alpha^0} \left[\delta_{\alpha\beta} - \frac{i\sqrt{\Gamma_\alpha \Gamma_\beta}}{E - E_r + \frac{i\Gamma}{2}} \right] e^{i\phi_\beta^0}. \quad (3.23)$$

If the determinant is taken at both sides of Eq. (3.23) it yields

$$e^{2i\sum_{\mu} \phi_{\mu}} = \left[e^{2i\sum_{\mu} \phi_{\mu}^0} \right] \frac{E - E_r - \frac{i\Gamma}{2}}{E - E_r + \frac{i\Gamma}{2}}, \quad (3.24)$$

which implies that the total phase shift, built up from the sum over all the eigenphases $\phi(E) = \sum_{\mu} \phi_{\mu}(E)$, experiences a variation of π when going from well below to well above the resonance (see Figure 3.2), and fulfills the analytical form [113]:

$$\phi(E) = \phi^0(E) + \arctan \left(\frac{\Gamma}{2(E_r - E)} \right), \quad (3.25)$$

where $\phi^0(E)$ is the background of the total phase $\phi^0(E) = \sum_{\mu} \phi_{\mu}^0(E)$. From the fit of the computed total phase to Eq. (3.25), the resonance energy and width can be determined. The individual eigenphases fulfill the equation [112]:

$$2(E - E_r) = \sum_{\mu=1}^M \Gamma_{\mu} \cot(\phi_{\mu}^0 - \phi_{\mu}(E)). \quad (3.26)$$

3.3.1 Levinson-Seaton Theorem

For an electron moving in a modified potential $V(r)$, which beyond a distance r_a is described by the attractive Coulomb potential $-Z/r$, the energy eigenvalues can be expressed in terms of the quantum defect μ_n [114]:

$$E_n = -\frac{Z^2}{2(n - \mu_n)^2}. \quad (3.27)$$

The quantum defect is a measure of how different is the potential $V(r)$ with respect to the Coulomb one, in the short-range radial domain. This departure from the Coulomb potential behaviour is also responsible for the scattering phase shift $\delta(E)$, hence, it is to be expected that in the energy limit in which the bound spectrum transform into a continuum spectrum, the quantum defect and the scattering phase shift exhibit some continuity across threshold. In fact this is known as the Levinson-Seaton theorem, and states that [115]

$$\lim_{n \rightarrow \infty} \pi \mu_n = \lim_{E \rightarrow 0} \delta(E). \quad (3.28)$$

Figure 3.3 illustrates the Levinson-Seaton theorem for the He atom in $1S^e$ using different levels of theory for the calculation: SAE, SEA and fully correlated. It can be seen the fulfillment of the Levinson-Seaton theorem for every case. Such plots are useful to optimize the effective potential to be used in SAE computations [116].

3.4 AUTOIONIZING STATES

3.4.1 A discrete state in the continuum

Let's consider a time-independent hamiltonian H given by the sum of a reference hamiltonian H_0 and of a perturbation V [36]

$$H = H_0 + V \quad (3.29)$$

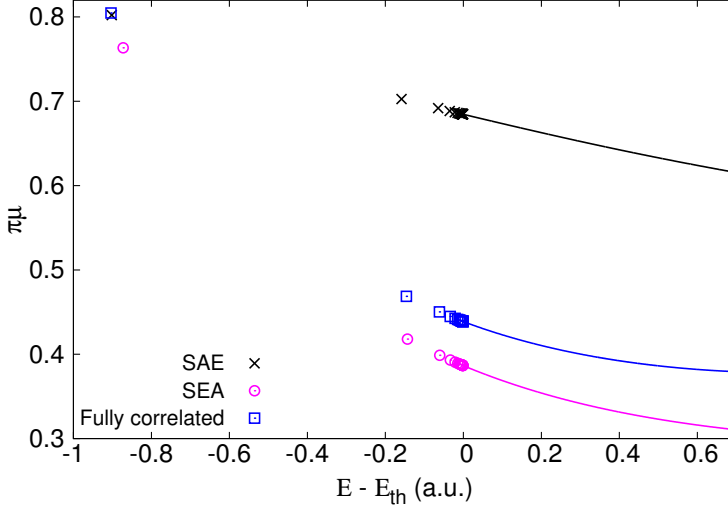


Figure 3.3: Quantum defect (times π) and scattering phase shifts vs the energy relative to the first ionization threshold in helium atom (-2 a.u.), for total $1s^e$ symmetry. The results under three different levels of theory are shown: SAE (black), SEA (magenta) and fully correlated (blue) (see [117] for details).

If H_0 has a discrete ground state $|0\rangle$ with energy E_0 , a set of continuum states $|E\rangle$ starting from a certain threshold $E_{th} > E_0$, and a second bound state $|a\rangle$ with energy $E_a > E_{th}$, then

$$H_0|0\rangle = E_0|0\rangle, \quad H_0|a\rangle = E_a|a\rangle, \quad H_0|E\rangle = E|E\rangle \quad \forall E \geq E_{th}, \quad (3.30)$$

where the eigenstates of H_0 are normalized as

$$\langle 0|0\rangle = \langle a|a\rangle = 1, \quad \langle E'|E\rangle = \delta(E' - E) \quad \forall E \geq E_{th}, \quad (3.31)$$

We assume that the only effect of the perturbation potential V is to couple the state $|a\rangle$ to the continuum states, and all the other matrix elements of V are zero

$$V_{aE} = \langle a|V|E\rangle = \langle E|V|a\rangle^*. \quad (3.32)$$

Due to this coupling, $|a\rangle$ is not stationary, and will eventually decay in the continuum to which it is coupled. Let us indicate with $|\psi_E\rangle$ an eigenstate with energy E of the complete hamiltonian (different from the ground state), then

$$(E - H)|\psi_E\rangle = 0, \quad (3.33)$$

which implies that

$$\begin{aligned} \langle a|E - H|\psi_E\rangle &= 0, \\ \langle E'|E - H|\psi_E\rangle &= 0, \quad \forall E'. \end{aligned} \quad (3.34)$$

If we expand ψ_E on the basis of the interacting states

$$|\psi_E\rangle = b_E|a\rangle + \int c_{\epsilon,E}|\epsilon\rangle d\epsilon, \quad (3.35)$$

and plug this expansion in the system (3.34), using the properties of the H_0 and V operators, we get the set of equations

$$\begin{aligned} (E - E_a)b_E - \int V_{a\epsilon}c_{\epsilon,E}d\epsilon &= 0, \\ -V_{E'a}b_E + (E - E')c_{E',E} &= 0, \quad \forall E'. \end{aligned} \quad (3.36)$$

The previous homogeneous system have a solution which is determined only up to a multiplicative constant, which is fixed by the requirement that the solution is normalized as $\langle\psi_E|\psi_{E'}\rangle = \delta(E - E')$. From the second equation in 3.36, we can say with certainty that the value of $c_{E',E}$ for $E' \neq E$ is

$$c_{E',E} = \frac{V_{Ea}}{E - E'}b_E, \quad \forall E' \neq E. \quad (3.37)$$

While the b_E coefficient is a regular function, the set of coefficients $c_{E',E}$ are not to be treated as simple functions. Since they were introduced under the sign of an integral, they should be rather regarded as distributions. For these reasons, we can expect that $c_{E',E}$ comprises a delta function, since any solution of the form

$$c_{E',E} = V_{Ea} \frac{\mathcal{P}}{E - E'} b_E + f(E) \delta(E - E') \quad (3.38)$$

is valid as well, where \mathcal{P} stands for the principal value. In order to get a solution different from the trivial one ($b_E = 0$), the function $f(E)$ must not be zero. Furthermore, we are free to use any other determination of the $(E - E')^{-1}$ expression since, by means of the formula

$$\frac{1}{E - E' \pm i0^+} = \frac{\mathcal{P}}{E - E'} 1 \mp i\pi\delta(E - E'), \quad (3.39)$$

they all amount to just a different choice for the function $f(E)$. Here we will choose the following convention

$$c_{E',E} = \frac{V_{Ea}}{E - E' + i0^+} b_E + \delta(E - E'). \quad (3.40)$$

This is the choice that leads to a normalized wave function. Replacing this expression in the first equation in (3.36) we obtain

$$[E - (E_a + \mathcal{P} \int \frac{V_{a\epsilon}V_{\epsilon a}}{E - \epsilon} d\epsilon - i\pi|V_{aE}|^2)]b_E = V_{aE}. \quad (3.41)$$

We can define an energy shift $\Delta_a(E)$ and an energy width $\Gamma_a(E)$ associated to the state $|a\rangle$ as

$$\Delta_a(E) = \mathcal{P} \int \frac{V_{a\epsilon}V_{\epsilon a}}{E - \epsilon} d\epsilon, \quad \Gamma_a(E) = 2\pi|V_{aE}|^2, \quad (3.42)$$

and hence we can introduce the complex resonance energy

$$\tilde{E}_a(E) = E_a + \Delta_a(E) - i\frac{\Gamma_a(E)}{2}. \quad (3.43)$$

Finally, Eq. (3.41) can be solved as

$$b_E = \frac{V_{aE}}{E - \tilde{E}_a} \quad (3.44)$$

and therefore

$$c_{\epsilon,E} = \delta(E - \epsilon) + \frac{V_{\epsilon a} V_{aE}}{(E - \epsilon + i0^+)(E - \tilde{E}_a)}. \quad (3.45)$$

Substituting the equations above in Eq. (3.35) we get the final real continuum states of the system

$$|\psi_E\rangle = |E\rangle + (|a\rangle + \int d\epsilon |\epsilon\rangle \frac{V_{\epsilon a}}{E - \epsilon + i0^+}) \frac{V_{aE}}{E - \tilde{E}_a} \quad (3.46)$$

If we isolate the principal part in the integral over the continuum function, Eq. (3.47) can be transformed into

$$|\psi_E\rangle = |E\rangle \frac{E - \tilde{E}_a^R}{E - \tilde{E}_a} + |\tilde{a}\rangle \frac{V_{aE}}{E - \tilde{E}_a}, \quad (3.47)$$

where $\tilde{E}_a^R = \Re(\tilde{E}_a)$ is the real part of the complex resonance energy. The state $|\tilde{a}\rangle$ is referred to as the *dressed* resonance, and is given by

$$|\tilde{a}\rangle = |a\rangle + \mathcal{P} \int d\epsilon |\epsilon\rangle \frac{V_{\epsilon a}}{E - \epsilon}. \quad (3.48)$$

For energies that are far away from the resonance, $E - \tilde{E}_a^R(E) \gg \Gamma_a(E)/2$, the new continuum states essentially coincide with the old ones, $|\psi_E\rangle \simeq |E\rangle$. It is therefore convenient to express the perturbed states in terms of a normalized distance from the position of the resonance

$$\varepsilon(E) \equiv \frac{E - \tilde{E}_a^R(E)}{\Gamma_a(E)/2}. \quad (3.49)$$

Using this notation, the perturbed continuum states become

$$|\psi_E\rangle = |E\rangle \frac{\varepsilon}{\varepsilon + i} + |\tilde{a}\rangle \frac{1}{\pi V_{Ea}(\varepsilon + i)}. \quad (3.50)$$

The quantities $\tilde{E}_a(E)$ and $\Gamma_a(E)$ are not simple parameters because they depend on the energy E . However, if the interaction matrix element V_{aE} changes smoothly enough in a large energy interval across the original energy E_a of the unperturbed state, we can approximate both $\Delta_a(E)$ and $\Gamma_a(E)$ with their values at $E = E_a$. Under these assumptions, ε is simply a linear function of the energy.

In particular, the energy distribution of the original unperturbed state $|a\rangle$ is a Lorentzian profile peaked at the shifted energy \tilde{E}_a^R

$$\frac{dP_a}{d\varepsilon} = |\langle\psi_E|a\rangle|^2 = \frac{1}{\pi(\varepsilon^2 + 1)}, \quad \int \frac{dP_a}{d\varepsilon} d\varepsilon = 1. \quad (3.51)$$

If at the time $t = 0$ the system is prepared in the state $|a\rangle$, the wave function is readily written

$$|\Psi_a(t)\rangle = \int dE |\psi_E\rangle e^{-iEt} \langle\psi_E|a\rangle, \quad (3.52)$$

and the probability that the wave function is still in the state $|a\rangle$ at any given time t is

$$\mathcal{A}_a(t) = \langle a|\Psi_a(t)\rangle = \frac{\Gamma}{2\pi} \int dE \frac{e^{-iEt}}{|E - \tilde{E}_a|^2} = e^{-i\tilde{E}_a t}, \quad (3.53)$$

where the last equality was obtained under the assumption that the resonance is sufficiently far from threshold, $|E_a^R - Et| \gg \Gamma$, enabling the extension of the integration to the whole energy interval. For positive times, the integral can be enclosed in the lower complex energy plane and the Cauchy's residue theorem applied easily.

The probability of finding the system in the state $|a\rangle$ at time t , is

$$P_a(t) = |\mathcal{A}_a(t)|^2 = e^{-\Gamma t}. \quad (3.54)$$

This is a very important result: $|a\rangle$ decays exponentially with lifetime $\tau = 1/\Gamma$.

3.4.2 Resonances as eigenstates of the quenched Hamiltonian

Resonances, can also be obtained as (non normalizable) eigenfunctions of the Hamiltonian fulfilling purely outgoing boundary conditions, known as Siegert states [118]. Siegert states have complex eigenvalues $E = E_r - i\Gamma/2$, where E_r is the resonance energy (sometimes call position) and Γ the resonance width (inverse of the lifetime) [119], and they diverge exponentially for $r \rightarrow \infty$. Despite these properties, Siegert states can still be obtained numerically with a diagonalization of the Hamiltonian in an \mathcal{L}^2 basis using complex scaling (CS) and exterior complex scaling (ECS) methods, in which the coordinate r is continued outside some scaling radius R into the complex plane by a θ angle rotation following a straight path [120, 121]. An alternative way to enforce outgoing boundary conditions in a basis that does not represent divergencies, is to introduce in the Hamiltonian a complex absorbing potential (CAP) [122, 123]

$$V_{CAP}(r) = -i\eta W(r), \quad (3.55)$$

where $W(r)$ is a smooth monotonic positive function that vanishes at the origin and η is a real positive number setting the strength of the potential. After adding

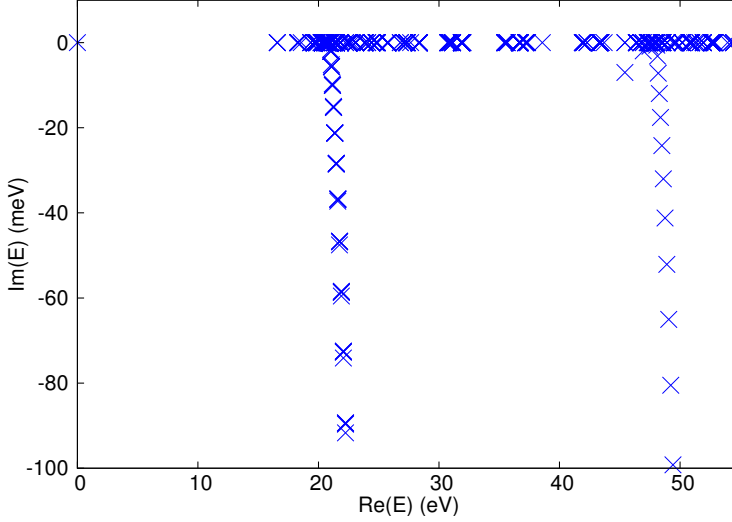


Figure 3.4: Eigenvalues of the H_Q of Ne using $V_{CAP}(r) = -i4.426 \cdot 10^{-4} \Theta(r - R)(r - R)^2$, with $R = 150$ a.u. in a box of 200 a.u.. Bound states eigenvalues remain in the real axis, those of the continuum states are rotated around the ionization thresholds defining rays, and the corresponding to the resonances have also an imaginary component and do not belong to the aforementioned rays (see 7.2 for details on the Ne calculations). The real part of the energy is referenced with respect the ground state.

the CAP to the Hamiltonian (quenched Hamiltonian $H_Q = H + V_{CAP}$), the divergence of the wave function is absorbed by the CAP and the wave function becomes square integrable. CAPs are also very useful to avoid the wave-packet reflexions at the edge of the box when solving the TDSE numerically.

Since H_Q is non-Hermitian, the eigenvalues coming from its diagonalization are complex in general (see Figure 3.4), and the eigenvectors are not orthogonal like in Hermitian matrices. In contrast with with Hermitian matrices H_Q has different right (\mathbf{C}_R) and left (\mathbf{C}_L) eigenvectors:

$$\begin{aligned} \mathbf{Q} \mathbf{H} \mathbf{C}_R &= \mathbf{C}_R \mathbb{E}, \\ \mathbf{C}_L^\dagger \mathbf{Q} \mathbf{H} &= \mathbf{E} \mathbf{C}_L^\dagger, \\ \mathbf{C}_L^\dagger \mathbf{C}_R &= \mathbf{I}. \end{aligned} \tag{3.56}$$

Whereas complex coordinate rotations are known to be equivalent to non-multiplicative complex potentials [122], multiplicative CAPs are not perfect absorbers, which means that they permit to enforce outgoing boundary conditions only in the limit of very small values of η and increasingly large absorption ranges. On the other hand, the simplicity of CAP, together with the possibility to combine them with state-of-the-art methods to treat the electronic correlation, starting the complex absorption at some radius R , is the real strength of the method. It is worth to clarify that in Figure 3.4, several eigenvalues with zero

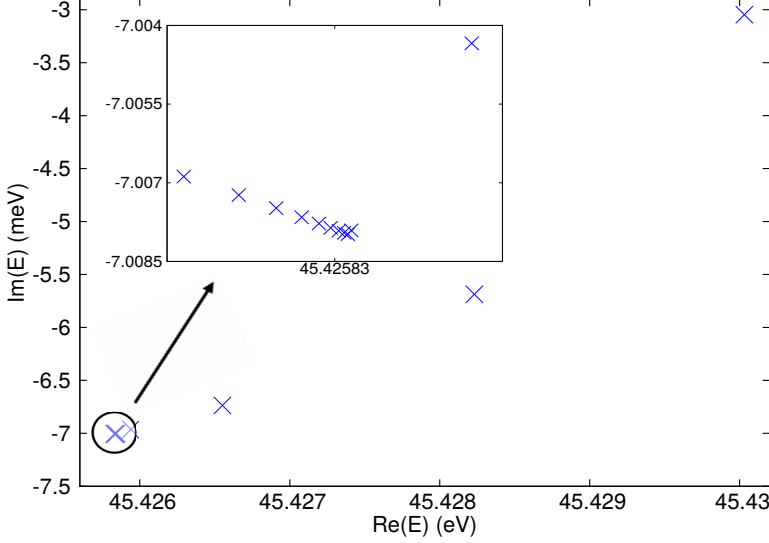


Figure 3.5: Eigenvalues of the $2s2p^6 3p$ resonance of Ne (see 7.2), computed using different CAP strengths $V_{CAP}^{(n)}(r) = -i\eta_n \cdot \Theta(r - R)(r - R)^2$, where $\eta_n = \epsilon(\delta^n - 1)/(\delta - 1)$, $\epsilon = 10^{-5}$ and $\delta = 1.47$.

imaginary part show up, when it should be rotated as the rest of continuum states, but this is due to the fact that this *bound* states belong to symmetries for which no channels are open (not defined in the CC expansion). To obtain accurate resonance energies with the CAPs method requires to carry out convergence tests varying the η parameter [124]. A practical criteria to determine the optimized CAP strength is to analyze the trajectories of the Siegert energies $E(\eta)$ in the complex plane, and identify the η values around which the density of $E(\eta)$ -points has a maximum (see Figure 3.5), what leads to the condition [125]:

$$\left| \eta \frac{dE}{d\eta} \right|_{\eta=\eta_0} = \min_{\eta} \left| \eta \frac{dE}{d\eta} \right|, \quad (3.57)$$

In an infinite basis, the RHS of Eq. (3.57) would be zero, other value higher than that is consequence of having a finite basis. One of the most common choices for $W(r)$ are of the form:

$$W(r) = \Theta(r - R)(r - R)^n, \quad (3.58)$$

where $\Theta(r - R)$ is the Heaviside step function. This definition, with $n = 2$, is the one we used in the computation of the Siegert energies.

PHOTOIONIZATION CROSS SECTION

Many processes in the interaction between matter (atoms/molecules) and radiation can be treated in terms of the exchange of a finite number of photons, often at the level of the lowest-order perturbation theory (LOPT)

$$A + \sum_i n_i \gamma_{\omega_i \hat{\epsilon}_i} \rightarrow A^* + \sum_i n'_i \gamma_{\omega'_i \hat{\epsilon}'_i}. \quad (4.1)$$

In order to derive the amplitudes of multi-photon processes in general, the starting point is the time-dependent Schrödinger equation (TDSE)

$$i \frac{\partial \psi(t)}{\partial t} = H(t) \psi(t). \quad (4.2)$$

To find a perturbative solution to Eq. (4.2), the time-dependent Hamiltonian is partitioned in a time-independent reference, or field-free part, and in an interaction part

$$H(t) = H_0 + H'(t). \quad (4.3)$$

In the dipole approximation, where the spatial variation of the external field across the system is neglected, and in velocity gauge, the time-dependent interaction operator is

$$H'_V(t) = -\vec{A}(t) \cdot \sum_i \frac{q_i \vec{p}_i}{m_i c}, \quad (4.4)$$

where q_i , m_i and \vec{p}_i are the charge, mass and canonical momentum of the i -th particle, and c is the speed of light. It is possible to convert the interaction term $H'_V(t)$ from the velocity to the length form, with the Göppert-Mayer gauge transformation, which results in

$$H'_L(t) = -\vec{E}(t) \cdot \sum_i q_i \vec{r}_i. \quad (4.5)$$

To derive the perturbative solution of the TDSE, it is convenient to change representation from the Schrödinger picture to the interaction picture. This is achieved by applying the following unitary transformation to the wave function

$$\psi_I(t) = e^{iH_0 t} \psi(t), \quad (4.6)$$

which leads to the equation

$$i \frac{\partial \psi_I(t)}{\partial t} = H'_I(t) \psi_I(t), \quad H'_I(t) = e^{iH_0 t} H'(t) e^{-iH_0 t}. \quad (4.7)$$

In the interaction representation the reference hamiltonian has formally disappeared from the TDSE equation. In absence of external perturbations, therefore, any state is stationary. We can find an iterative solution to Eq. (4.7), by taking the time integral on both side that equation from an initial time t_0 to a final time t , what gives

$$\psi_I(t) = \psi_I(t_0) + \frac{1}{i} \int_{t_0}^t H'_I(t_1) \psi_I(t_1) dt_1. \quad (4.8)$$

In this expression, which is exact, we still have the unknown wave function $\psi_I(t)$ under the integration sign on the RHS of Eq. (4.8). However, we can replace the unknown quantity with the whole RHS evaluated at $t = t_1$ we get

$$\psi_I(t) = \psi_I(t_0) + \frac{1}{i} \int_{t_0}^t H'_I(t_1) \psi_I(t_0) dt_1 + \left(\frac{1}{i}\right)^2 \int_{t_0}^t \int_{t_0}^{t_1} H'_I(t_1) H'_I(t_2) \psi_I(t_2) dt_2 dt_1. \quad (4.9)$$

The same procedure can be repeated as many times as wished, leading to the Dyson series:

$$\psi_I(t) = U(t, t_0) \psi_I(t_0) = \sum_{n=0}^{\infty} U^{(n)}(t, t_0) \psi_I(t_0), \quad (4.10)$$

where

$$U^{(n)}(t, t_0) = \left(\frac{1}{i}\right)^n \int_{t_0}^t dt_1 \int_{t_0}^{t_1} dt_2 \cdots \int_{t_0}^{t_{n-1}} dt_n H'_I(t_1) H'_I(t_2) \cdots H'_I(t_n). \quad (4.11)$$

The radiative transition amplitude between two eigenstates of the field-free hamiltonian H_0 , an initial state $|i\rangle$ and a final state $|f\rangle$ is given by

$$\mathcal{A}_{f \leftarrow i} = \langle f | U(t, t_0) | i \rangle. \quad (4.12)$$

Using the perturbative expansion in Eq. (4.10), we can write the transition amplitude as a sum of terms

$$\mathcal{A}_{f \leftarrow i} = \mathcal{A}_{f \leftarrow i}^{(0)} + \mathcal{A}_{f \leftarrow i}^{(1)} + \mathcal{A}_{f \leftarrow i}^{(2)} + \cdots, \quad \mathcal{A}_{f \leftarrow i}^{(n)} = \langle f | U^{(n)}(t, t_0) | i \rangle. \quad (4.13)$$

4.1 ONE-PHOTON AMPLITUDE

The first non-vanishing amplitude is the one that is linear in the perturber $H'(t)$. If $|i\rangle$ and $|f\rangle$ are two non-degenerate states, then

$$\mathcal{A}_{f \leftarrow i}^{(1)} = \frac{1}{i} \int_{t_0}^t dt_1 \langle f | H'_I(t_1) | i \rangle = \frac{\mathcal{O}_{fi}}{i} \int_{t_0}^t dt_1 e^{i\omega_{fi}t} F(t), \quad \omega_{fi} = \omega_f - \omega_i, \quad (4.14)$$

where $F(t)$ is the pulse profile. Then the one-photon amplitude is proportional to the Fourier transform ($\tilde{F}(\omega) = 1/(2\pi) \int dt e^{-i\omega t} F(t)$) of the field:

$$\mathcal{A}_{f \leftarrow i}^{(1)} = \frac{\sqrt{2\pi}}{i} \mathcal{O}_{fi} \tilde{F}(\omega_{fi}). \quad (4.15)$$

In the case of a monochromatic square pulse with duration T

$$F(t) = \begin{cases} F_0 \cos(\omega t + \phi) = \left(\frac{F_\omega^*}{2} e^{i\omega t} + \frac{F_\omega}{2} e^{-i\omega t}\right), & t \in [-\frac{T}{2}, \frac{T}{2}], \\ 0, & \text{otherwise,} \end{cases} \quad (4.16)$$

where $F_\omega = F_0 e^{-i\phi}$, the Fourier transform is

$$\tilde{F}(\omega_{fi}) = \sqrt{\frac{\pi}{2}} \left\{ F_\omega \frac{\sin[(\omega_{fi} - \omega)T/2]}{\pi(\omega_{fi} - \omega)} + F_\omega^* \frac{\sin[(\omega_{fi} + \omega)T/2]}{\pi(\omega_{fi} + \omega)} \right\}. \quad (4.17)$$

The function $\delta_T(\omega) \equiv \sin(\omega T/2)/(\pi\omega)$ is a well known representation of the Dirac delta distribution $\delta(\omega)$ in the limit $T \rightarrow \infty$. Taking this limit, the transition probability is thus proportional to the exposure time T and is given by

$$P_{f \leftarrow i}^{(1)} = \frac{\pi T}{2} F_0^2 |\mathcal{O}_{fi}|^2 [\delta(\omega_{fi} + \omega) + \delta(\omega_{fi} - \omega)]. \quad (4.18)$$

We can define a transition rate as the transition probability per unit time. For one-photon processes, therefore, it is proportional to the intensity of the radiation. In the dipole approximation and velocity gauge ($F_0 = A_0/c$ and $\mathcal{O} = \hat{\epsilon} \cdot \vec{P}$), we have for the absorption process

$$W_{f \leftarrow i}^{(1)} = \frac{P_{f \leftarrow i}^{(1)}}{T} = \frac{\pi A_0^2}{2c^2} |\langle f | \hat{\epsilon} \cdot \vec{P} | i \rangle|^2 \delta(\omega_{fi} - \omega). \quad (4.19)$$

The cross section is defined as the ratio between the rate with which the final state is populated to the incoming flux of photons $\Phi_\gamma = \omega A_0^2/(8\pi c)$, which results in

$$\sigma_{f \leftarrow i} = \frac{4\pi^2}{c\omega} |\langle f | \hat{\epsilon} \cdot \vec{P} | i \rangle|^2 \delta(\omega_{fi} - \omega). \quad (4.20)$$

The cross section has the dimension of an area and does not depend on the laser intensity anymore. The delta function in Eq. (4.20) indicates that the cross section is a distribution rather than a normal function; therefore, it is really meaningful only when convoluted with smooth test functions. Indeed, in a real experiment we observe at best very sharp peaks in a spectrum, not literal delta functions. In the case in which the final state is a continuum state $|\psi_E\rangle$, normalized as a delta function $\langle \psi_{E'} | \psi_E \rangle = \delta(E' - E)$, the square of their matrix elements with discrete states is to be interpreted as a density in energy:

$$\frac{d\sigma_{f \leftarrow i}}{dE} = \frac{4\pi^2}{c\omega} |\langle \psi_E | \hat{\epsilon} \cdot \vec{P} | i \rangle|^2 \delta(E - \omega_i - \omega). \quad (4.21)$$

Since the delta function in this case just expresses the conservation of total energy, it is customary to provide the cross section to the continuum in integral form, recovering the dimension of an area:

$$\sigma_{f \leftarrow i} = \frac{4\pi^2}{c\omega} |\langle \psi_E | \hat{\epsilon} \cdot \vec{P} | i \rangle|^2. \quad (4.22)$$

4.2 TWO-PHOTON AMPLITUDES

Let's consider now the second order term in the Dyson expansion (4.10)

$$\begin{aligned} \mathcal{A}_{f \leftarrow i}^{(2)} &= - \int_{t_0}^t dt_1 \int_{t_0}^{t_1} dt_2 e^{i\omega_f t_1} F(t_1) F(t_2) \langle f | \mathcal{O} e^{-iH_0(t_1-t_2)} \mathcal{O} | i \rangle e^{-i\omega_i t_2} \\ &= - \sum_j \mathcal{O}_{fj} \mathcal{O}_{ji} \int_{t_0}^t dt_1 e^{i\omega_{fj} t_1} F(t_1) \int_{t_0}^{t_1} dt_2 e^{i\omega_{ji} t_2} F(t_2) \end{aligned} \quad (4.23)$$

Using the same square pulse defined in Eq. (4.16), and taking the limits $t_0 \rightarrow -\infty$ and $t \rightarrow \infty$, the transition amplitude for the absorption of one photon from pulse 1 followed by one photon absorption from pulse 2 reads

$$\mathcal{A}_{f \leftarrow i}^{(2)} = - \frac{F\omega_2}{2} \frac{F\omega_1}{2} \sum_j \mathcal{O}_{fj} \mathcal{O}_{ji} \int_{-\infty}^{\infty} dt_1 e^{i(\omega_{fj}-\omega_2)t_1} \int_{-\infty}^{t_1} dt_2 e^{i(\omega_{ji}-\omega_1)t_2}. \quad (4.24)$$

The derivation of the expressions for the other second-order processes: two-photon emission, one absorption and one emission and vice versa, is straightforward. The second integral in Eq. (4.24) can be easily solved using the parametric integral

$$\int_{-\infty}^t d\tau e^{i\omega\tau} = \lim_{\eta \rightarrow 0^+} \int_{-\infty}^t d\tau e^{i(\omega-i\eta)\tau} = \frac{ie^{i\omega t}}{-\omega + i0^+}, \quad (4.25)$$

where $(x + i0^+)^{-1}$ is another important and ubiquitous distribution in physics. Introducing Eq. (4.25) in Eq. (4.24) we get

$$\mathcal{A}_{f \leftarrow i}^{(2)} = -2i\pi \frac{F\omega_2}{2} \frac{F\omega_1}{2} \langle f | \mathcal{O} G_0^+(\omega_i + \omega_1) \mathcal{O} | i \rangle \delta_T(\omega_{fi} - \omega_1 - \omega_2), \quad (4.26)$$

where we have introduced the retarded resolvent operator

$$G_0^+(E) = (E - H_0 + i0^+)^{-1}. \quad (4.27)$$

If the two photon frequencies ω_1 and ω_2 differ, we have to consider also the process in which the photon with ω_2 is absorbed before the photon with ω_1 , then the total two-photon absorption amplitude is

$$\begin{aligned} \mathcal{A}_{f \leftarrow i}^{(2)} &= -2i\pi \frac{F\omega_2}{2} \frac{F\omega_1}{2} [\langle f | \mathcal{O} G_0^+(\omega_i + \omega_1) \mathcal{O} | i \rangle + \\ &\quad + \langle f | \mathcal{O} G_0^+(\omega_i + \omega_2) \mathcal{O} | i \rangle] \delta_T(\omega_{fi} - \omega_1 - \omega_2) \end{aligned} \quad (4.28)$$

4.2.1 Application to the RABITT technique

The RABITT technique (Reconstruction of Attosecond Bursts by Interference of Two-photon Transitions) is an interferometric two-photon spectroscopy that permits to characterize the temporal profile of attosecond pulse trains (APT). In this

technique, the APT is realigned, with a controllable time-delay (τ), to a weak replica of the IR pulse used to generate it. The energy of the high-order harmonics (HH) in the train is generally sufficient to ionize a rare gas. In absence of the IR radiation, this results in the production of photoelectrons with kinetic energy $E = (2n + 1)\omega - I_p$, where I_p is the atomic ionization potential. This process is well described by the one-photon ionization equations given in 4.1. Due to the presence of the IR field, however, two photon transitions corresponding to the absorption of one XUV photon and to the exchange of one IR photon can also take place. As a result, photoelectron signals at $2n\omega - I_p$, the so-called side-bands (SB), also appear. The same SB $2n$ can be reached either through the absorption of one photon from the HH $2n - 1$ (ω_{2n-1}) and of one IR photon, or through the absorption of one photon from the HH $2n + 1$ (ω_{2n+1}) and the stimulated emission of one IR photon. The interference between these two inequivalent quantum paths results in oscillations of the intensity of the SBs as a function of the time delay, with the characteristic frequency equal to twice that of the IR. By measuring the dephasing between the oscillations of consecutive SBs, it is possible to reconstruct the whole temporal profile of the APT.

The sum of the two-photon transition amplitudes to the SBs is readily written by applying the formulas we derived earlier in this section

$$\mathcal{A}_{2n\omega}^{(2)}(E) = \{F_{\omega_{2n-1}}F_{\omega}\mathcal{M}_{2n-1} + F_{\omega_{2n+1}}F_{\omega}^*\mathcal{M}_{2n+1}\}\delta_T(E - \omega_i - 2n\omega), \quad (4.29)$$

where for the sake of brevity, we called the two-photon transition matrix elements for the absorption of the $2n - 1$ and of the $2n + 1$ harmonics as \mathcal{M}_{2n-1} and \mathcal{M}_{2n+1} , respectively:

$$\mathcal{M}_{2n-1} = \langle E | \mathcal{O}[G_0^+(\omega_i + \omega) + G_0^+(\omega_i + \omega_{2n-1})] | i \rangle \quad (4.30)$$

$$\mathcal{M}_{2n+1} = \langle E | \mathcal{O}[G_0^+(\omega_i - \omega) + G_0^+(\omega_i + \omega_{2n+1})] | i \rangle. \quad (4.31)$$

The integral transition rate to the sideband, therefore, is given by

$$\mathcal{W}_{2n\omega}^{(2)} = \frac{1}{T} \int dE |\mathcal{A}_{2n\omega}^{(2)}(E)|^2 = \frac{\pi}{8} |F_{\omega_{2n-1}}F_{\omega}\mathcal{M}_{2n-1} + F_{\omega_{2n+1}}F_{\omega}^*\mathcal{M}_{2n+1}|^2 \quad (4.32)$$

The argument of the two-photon integrals is generally called atomic phase, $\varphi_n^{At} = \arg(\mathcal{M}_n)$. If we use the APT as a reference to define the temporal scale, and thus keep it fixed with respect to the time delay τ , then the phases of the harmonics field amplitudes do not change with the time delay, while the phase of the IR, which we can here assume to be very long, is linear with the time delay:

$$F_{\omega_{2n-1}} = |F_{\omega_{2n-1}}|e^{-i\phi_{2n-1}}, \quad F_{\omega_{2n+1}} = |F_{\omega_{2n+1}}|e^{-i\phi_{2n+1}}, \quad F_{\omega} = |F_{\omega}|e^{-i(\phi_{IR} + \omega\tau)}. \quad (4.33)$$

Inserting these dependences in the expression for the transition rate to the sideband, we get

$$\begin{aligned} \mathcal{W}_{2n\omega}^{(2)} &\propto |F_{\omega_{2n-1}}F_{\omega}\mathcal{M}_{2n-1}|^2 + |F_{\omega_{2n+1}}F_{\omega}^*\mathcal{M}_{2n+1}|^2 + \\ &+ 2|F_{\omega_{2n-1}}F_{\omega}F_{\omega_{2n+1}}F_{\omega}^*\mathcal{M}_{2n-1}\mathcal{M}_{2n+1}|\cos(2\omega\tau - \Phi_{2n}), \end{aligned} \quad (4.34)$$

where

$$\Phi_{2n} = \phi_{2n+1} - \phi_{2n-1} - \phi_{IR} + \varphi_{2n-1}^{At} - \varphi_{2n+1}^{At} \quad (4.35)$$

Thus, the phase of the SBs are equal to the phase difference between consecutive harmonics minus the IR phase and minus the difference between the atomic phases. If the properties of the ionization continuum do not change much across the energy span of few ω 's, as it is generally the case for rare gases in the energy region far from the ionization threshold, on the one side, and far from autoionizing states, on the other side, then the two-photon integrals \mathcal{M}_{2n-1} and \mathcal{M}_{2n+1} are similar both in absolute value and in phase. In particular, the atomic phase can be accurately linearized across the whole energy interval: $\varphi_{2n-1}^{At} - \varphi_{2n+1}^{At} \simeq 2\omega \partial \varphi_E^{At} / \partial E$.

Both the absolute value of the IR phase and the (typically small) value of the atomic phase change are a single unknown constant. If these constants are known, then the individual differences $\phi_{2n+1} - \phi_{2n-1}$ can be determined and, from these, by means of an inverse discrete Fourier transform, the envelope of the whole train can be determined in absolute terms. If one is not particularly interested in knowing exactly where the APT is located within the IR pulse (and, hence, whether the maxima in the sidebands correspond to attosecond pulses at the zeros or at the maxima of the IR field) the absolute value of the IR phase or the energy derivative of the atomic phase are not particularly relevant. Even without knowing them, from all the values of $\Phi_{2n} - \Phi_{2n-2}$, it is still possible to determine the average shape of the envelope of an attosecond pulse in the train, and in particular its duration.

4.3 CROSS SECTION NEAR AN AUTOIONIZING STATE

Let's consider a radiative transition from the ground state $|0\rangle$ to the new continuum, mediated by the operator $\mathcal{O} = \hat{\epsilon} \cdot \vec{P}$ (velocity gauge). As we have seen in the previous sections, the cross section to the continuum is given by

$$\sigma_E = \frac{4\pi^2}{c\omega_\gamma} |\langle E | \mathcal{O} | 0 \rangle|^2. \quad (4.36)$$

In the case in which the discrete state and the continuum interact (see 3.4.1), the transition amplitude becomes

$$\langle 0 | \mathcal{O} | \psi_E \rangle = \mathcal{O}_{0E} \frac{\varepsilon}{\varepsilon + 1} + \frac{\mathcal{O}_{0\tilde{a}}}{\pi V_{Ea}(\varepsilon + i)}. \quad (4.37)$$

In the special case in which the transition amplitude to the unperturbed continuum is exactly zero $\mathcal{O}_{0\tilde{a}} = \mathcal{O}_{0a}$, and then

$$\sigma_E = \frac{4\pi^2}{c\omega_\gamma} \cdot \frac{\Gamma_a / (2\pi)}{(E - \tilde{E}_a^R)^2 + (\Gamma_a / 2)^2}. \quad (4.38)$$

In other words, the interaction with the continuum *blurred* the bound state (the delta function becomes a Lorentzian), and $|a\rangle$ acts like a door-state to an otherwise dark continuum. In the more general case, in which the radiative transition to the unperturbed continuum does not vanish, we can factor out the continuum transition amplitude:

$$\langle 0|\mathcal{O}|\psi_E\rangle = \mathcal{O}_{0E} \frac{\varepsilon + q}{\varepsilon + i}, \quad (4.39)$$

where the new parameter q has been introduced [126]

$$q = \frac{\mathcal{O}_{0\bar{a}}}{\pi V_{Ea} \mathcal{O}_{0E}}. \quad (4.40)$$

This quantity is real, provided that the two radiative transition amplitudes have the same phase, which is always the case for linearly polarized fields and targets whose Hamiltonian is invariant under time reversal. The cross section has the form of the famous Fano profile:

$$\sigma_E = \sigma_{bg}(E) \frac{(\varepsilon + q)^2}{\varepsilon^2 + 1}. \quad (4.41)$$

INTERFACE BETWEEN QUANTUM CHEMISTRY AND SCATTERING METHODS: THE XCHEM APPROACH

5.1 THE XCHEM CLOSE COUPLING

To describe a single-ionization scattering state it is convenient to distinguish between two radial ranges: a short range, $r_i < R_0$, where all N electrons are within a fixed radius R_0 from the conventional center of the parent ion and a long range, $r_N > R_0$, where one and only one electron (e.g., the N -th) is located beyond R_0 , that is $r_{i < N} < R_0$. Indeed, if the boundary value R_0 is large enough, the eigenstates of the parent ion are negligible whenever $r_i > R_0$. As a result, the complete single-ionization wave function in the second region is well represented by the close-coupling (CC) ansatz

$$r_N > R_0, \quad \Psi_{\alpha E}^-(\mathbf{x}_1, \dots, \mathbf{x}_N) = \frac{1}{N} \sum_{\beta} N_{\beta E} Y_{\beta}(\mathbf{x}_1, \dots, \mathbf{x}_{N-1}; \hat{r}_N, \zeta_N) \frac{u_{\beta, \alpha E}^-(r_N)}{r_N}, \quad (5.1)$$

where \mathbf{x}_i denotes the position and spin coordinates of electron i , \hat{r}_N and ζ_N are the angular and spin coordinates, respectively, of electron N , Y_{α} is a spin-coupled channel function (see below), $N_{\beta E}$ is a normalization factor that ensures the correct asymptotic behavior, and $u_{\beta, \alpha E}^-(r)$ is the radial function that describes the continuum electron, which is asymptotically given by Eq. (3.15)

In the present work, the spin-coupled channel function Y_{α} is given by the antisymmetrized parent ion function Φ_a coupled to the N -th electron spin function χ , and multiplied by the spherical harmonic $Y_{\ell m}$, which expresses the angular distribution of the N -th electron,

$$\begin{aligned} Y_{\alpha}(\mathbf{x}_1, \dots, \mathbf{x}_{N-1}; \hat{r}_N, \zeta_N) &= 2^{S+1} [\Phi_a(\mathbf{x}_1, \dots, \mathbf{x}_{N-1}) \otimes {}^2\chi(\zeta_N)]_{\Sigma} Y_{\ell m}(\hat{r}_N) \\ &= \sum_{\Sigma_a \sigma} C_{S_a \Sigma_a, \frac{1}{2}\sigma}^{S\Sigma} 2^{2S_a+1} \Phi_{a, \Sigma_a} {}^2\chi_{\sigma}(\zeta_N) Y_{\ell m}(\hat{r}_N). \end{aligned} \quad (5.2)$$

In Eq. (5.2) S is the total spin of the system, Σ its z projection, S_a and Σ_a are the corresponding values for the parent ion, σ is the z component of the electron spin, and $C_{S_a \Sigma_a, \frac{1}{2}\sigma}^{S\Sigma}$ is a Clebsch-Gordan coefficient. For the sake of clarity, the spin multiplicity of both the parent-ion and continuum-electron components, $2S_a + 1$ and 2, respectively, have been indicated as prefixes of the corresponding wave functions. The channel index α corresponds to the set of indexes (S, Σ, a, ℓ, m) ,

while the parent-ion index a defines entirely the state of the parent ion, except for its total spin projection. We will be mostly interested in spin-free Hamiltonians. Therefore, the total spin S and spin-projection Σ will be constant parameters across the whole scattering calculation.

Due to the natural asymptotic separation between a finite number (or a denumerable set) of channel functions $Y_\alpha(\mathbf{x}_1, \dots, \mathbf{x}_{N-1}; \hat{r}_N, \zeta_N)$ and the radial wave function of an electron in the continuum, in a scattering perspective we describe the complete function as a linear combination of “extended” channel functions $\bar{Y}_{\alpha i}$ and of localized short-range N -electron states \aleph_i :

$$\Psi_{\alpha E}^- = \sum_i \aleph_i c_{i, \alpha E} + \sum_\beta \sum_i \bar{Y}_{\beta i} c_{\beta i, \alpha E}. \quad (5.3)$$

The extended channel functions $\bar{Y}_{\alpha i}$ are defined as

$$\bar{Y}_{\alpha i} = N_{\alpha i} \hat{\mathcal{A}} Y_\alpha(\mathbf{x}_1, \dots, \mathbf{x}_{N-1}; \hat{r}_N, \zeta_N) \varphi_i(r_N) \quad (5.4)$$

where $\{\varphi_i\}$ is a set of radial functions suitable to describe the continuum and $\hat{\mathcal{A}}$ is the antisymmetrizer

$$\hat{\mathcal{A}} = \frac{1}{N!} \sum_{\mathcal{P} \in \mathcal{S}_N} (-1)^p \mathcal{P}, \quad p = \text{parity of } \mathcal{P}, \quad (5.5)$$

with \mathcal{P} the standard permutation operator that belongs to the space of N -particle permutations, \mathcal{S}_N . The channel functions Y_α are assumed to be already totally antisymmetric with respect to the permutation of the first $N - 1$ parent-ion electrons

$$\forall \mathcal{P} \in \mathcal{S}_{N-1}, \quad \mathcal{P} Y_\alpha(\mathbf{x}_1, \dots, \mathbf{x}_{N-1}; \hat{r}_N, \zeta_N) = (-1)^p Y_\alpha(\mathbf{x}_1, \dots, \mathbf{x}_{N-1}; \hat{r}_N, \zeta_N). \quad (5.6)$$

The antisymmetrizer for N particles $\hat{\mathcal{A}}^{(N)}$ can be written in terms of that for $N - 1$ particles, $\hat{\mathcal{A}}^{(N-1)}$:

$$\hat{\mathcal{A}}^{(N)} = \frac{1}{N} \left(1 - \sum_{i=1}^{N-1} \mathcal{P}_{iN} \right) \hat{\mathcal{A}}^{(N-1)}, \quad (5.7)$$

where \mathcal{P}_{iN} denotes the permutation operator between particles i and N . Therefore, the extended channel functions can also be written as

$$\bar{Y}_{\alpha i} = \frac{N_{\alpha i}}{N} \left(1 - \sum_{i=1}^{N-1} \mathcal{P}_{iN} \right) Y_\alpha(\mathbf{x}_1, \dots, \mathbf{x}_{N-1}; \hat{r}_N, \zeta_N) \varphi_i(r_N). \quad (5.8)$$

We use three different kinds of functions to build the N -electron basis: **i**) a set of localized Gaussian functions $\{G_i^L(\mathbf{x}_1)\}$ as provided by the quantum chemistry packages (QCPs) (for molecules, they would be located at the different atomic positions –multi-center expansion), **ii**) a set of diffuse even-tempered Gaussian functions $\{G_i^M(\mathbf{x}_1)\}$ and **iii**) a set of B-splines functions $\{B_i(\mathbf{x}_1)\}$ starting at $r = R_0$. Basis functions defined in **ii**) and **iii**) constitute the so called GABS basis, $\{G_i^M(\mathbf{x}_1)\} \cup \{B_i(\mathbf{x}_1)\}$ (for molecules, these functions would be located at the

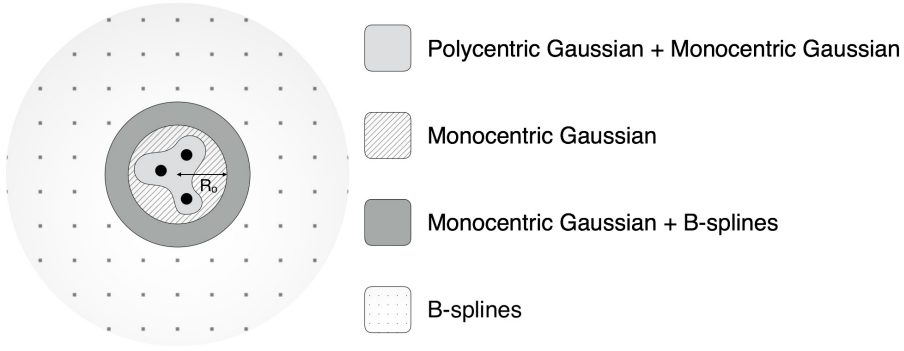


Figure 5.1: Sketch of the radial space partition and the basis functions used to describe the wavefunctions on it. (see text for details).

center of mass –single-center expansion). The $G_i^M(\mathbf{x}_1)$ functions are in principle defined in the whole interval $r \in [0, \infty)$. However, due to their fast exponential decrease, there is a distance R_1 ($R_1 > R_0$) beyond which the overlap with the B-splines is negligible (see [98] for details). The region ($r \in [R_0, R_1]$) where both subsets overlap guarantees a smooth transition from the outer to the inner region, thus providing great flexibility to the $G_i^M(\mathbf{x}_1)$ functions in the short-range region, because B-splines compensate the deficiencies of the $G_i^M(\mathbf{x}_1)$ functions in reproducing the rapid oscillations of the diffuse states (Rydberg and continuum states). From R_1 on, B-splines take over the full description of the wave function. This is how the inner part of the space partition matches almost perfectly the outermost part, in contrast with methods that make use of a rigid boundary to divide the two regions [21]. The typical thickness of the $R_1 - R_0$ transition region is tens of a.u..

5.2 THE GABS BASIS

The GABS basis is a mono-centric basis comprising a set of Gaussian functions and a set of B-splines whose support starts from a given radius R_0 (see Fig. 5.2). Due to their fast-descent character, the Gaussian functions are numerically negligible beyond a radius $R_1 > R_0$. Functions expressed in the GABS basis, therefore, are represented by purely Gaussian functions in the short range, i.e., $r < R_0$, by a combination of Gaussian and B-spline functions in the intermediate region, $R_0 < r < R_1$, and by purely B-spline functions thereafter. As shown in the next section, the simultaneous presence of Gaussian and B-splines in the intermediate region enhances greatly the flexibility of the Gaussian functions in the innermost region as well.

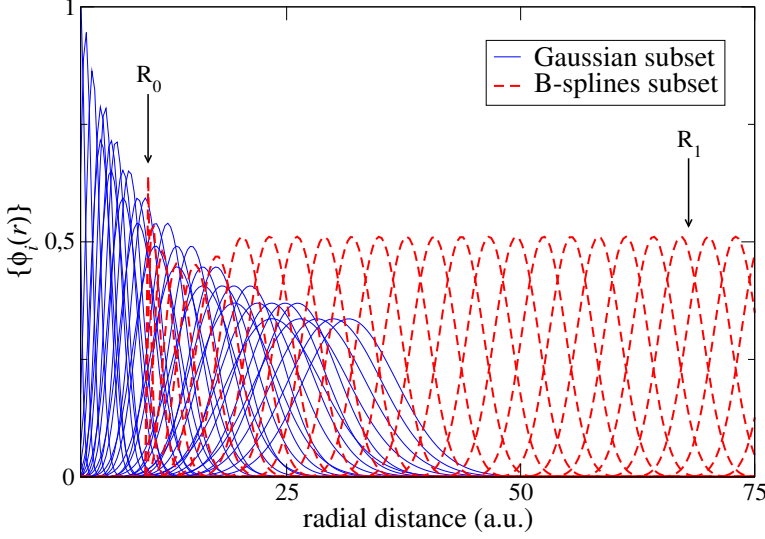


Figure 5.2: (Color online) Plot of the radial part of some Gaussian (solid lines) and B-spline (dashed lines) representatives of the mono-centric GABS basis set as a function of the distance from the origin. The first B-spline node is located at $R_0 = 10$ a.u. The basis defines three characteristic regions: (i) $r \in [0, R_0]$, where only Gaussian functions are present, (ii) $r \in [R_0, R_1]$, where Gaussian and B-spline functions overlap, and (iii) $r \in [R_1, R_{\text{box}}]$ where the Gaussian functions are negligible.

The Gaussian spatial basis functions with angular momentum ℓ and projection m are defined as

$$G_{\alpha K}^{\ell m}(\vec{r}) = N_{\alpha \ell} \frac{g_{\alpha K \ell p}(r)}{r} X_{\ell m}(\hat{r}), \quad (5.9)$$

where

$$g_{\alpha K}(r) = r^{K_{\ell p}+1} e^{-\alpha r^2}, \quad (5.10)$$

$K_{\ell p} = \ell + 2p$, with $p = 0, 1, \dots, p_{\text{max}}$, and $(K_{\ell p})_{\text{max}} \equiv K_{\text{max}}$ is a fixed parameter that defines the maximum orbital angular momentum, ℓ_{max} , the basis can represent. The lower bound on K ensures that $g_{\alpha K}(r) \sim r^{\ell+1}$ is regular at the origin.

The $X_{\ell m}$ functions ($m \geq 0$) are symmetry adapted spherical harmonics, also known as real spherical harmonics [127], defined in terms of the spherical harmonics $Y_{\ell m}$ as

$$\begin{aligned} X_{\ell 0} &= Y_{\ell 0}, \\ X_{\ell m} &= \frac{1}{\sqrt{2}} (Y_{\ell m} + (-1)^m Y_{\ell -m}), \\ X_{\ell -m} &= \frac{1}{i\sqrt{2}} (Y_{\ell m} - (-1)^m Y_{\ell -m}). \end{aligned} \quad (5.11)$$

Notice that the present definition of symmetry adapted spherical harmonics differs from other ones found in the literature ($X_{\ell m}^S$), by a phase $X_{\ell m}^S = (-1)^m X_{\ell m}$.

The symmetry adapted spherical harmonics allow us to work with the same point groups employed in the QCPs for the short-range part of the wavefunctions. We have implemented the Abelian groups: C_1 , C_s , C_2 , C_i , C_{2v} , C_{2h} , D_2 and D_{2h} (see Appendix A).

Finally, $N_{\alpha K}$ is a normalisation factor

$$u_{\alpha K}(r) = N_{\alpha K} g_{\alpha K}, \quad \int_0^\infty dr u_{\alpha K}^2(r) = 1. \quad (5.12)$$

Normally, we will use for all orbital angular momenta a single set of even-tempered exponents $\{\alpha_1, \alpha_2, \dots, \alpha_{N_\alpha}\}$, generated from the two parameters α and β according to the geometric series [128, 67],

$$\alpha_n = \alpha \beta^{n-1}. \quad (5.13)$$

There are thus $N_G^\ell = N_\alpha \lfloor (\ell_{\max} - \ell)/2 + 1 \rfloor$ such states for each angular momentum ℓ ($\lfloor x \rfloor$ is the largest integer n such that $n \leq x$). Extended Gaussian basis sets are notoriously plagued by large linear dependencies which can easily disrupt numerical accuracy. For this reason, numerically redundant linear combinations must be eliminated from the set before it can be used in calculations. To do so, for each orbital angular momentum ℓ , we diagonalize the overlap matrix $\mathbf{S}_{\alpha K, \beta K'}^\ell = \langle G_{\alpha K}^{\ell 0} | G_{\beta K'}^{\ell 0} \rangle$ and exclude those eigenfunctions whose eigenvalue is more than M_S^G times smaller than the largest eigenvalue where M_S^G is a given maximum condition number (in our case, $M_S^G = 10^6$). We refer to the N_G^ℓ remaining eigenstates as to the preconditioned Gaussian basis $\{|\mathcal{G}_1^{\ell m}\rangle, |\mathcal{G}_2^{\ell m}\rangle, \dots, |\mathcal{G}_{N_G^\ell}^{\ell m}\rangle\}$.

Splines are piecewise polynomials with maximum degree $k - 1$, \mathcal{C}^∞ everywhere, except at the positions given by a fixed non decreasing set of nodes $\{t_i\}_{i=1,2,\dots,n}$ where they are at least \mathcal{C}^{k-v_i-1} , v_i being the so-called multiplicity of the node [73]. The splines that vanish below the smallest and above the largest node form a linear space with dimension $n - k$. B-splines are those $n - k$ elements of the latter space whose support is limited to k consecutive intervals (or, alternatively, whose support comprises $k + 1$ consecutive nodes, when counted with their multiplicity). The B-splines of order k , $\{B_i^k\}_{i \in \{1,2,\dots,n-k\}}$, have the following explicit iterative expression [73],

$$\begin{aligned} B_i^1(x) &= \theta(x - t_i) \cdot \theta(t_{i+1} - x), \\ B_i^k(x) &= \frac{(x - t_i) B_i^{k-1}(x)}{t_{i+k-1} - t_i} + \frac{(t_{i+k} - x) B_{i+1}^{k-1}(x)}{t_{i+k} - t_{i+1}}, \end{aligned} \quad (5.14)$$

where $\theta(x)$ is the Heaviside step function $\theta(x) = 1$ if $x > 0$; $\theta(x) = 0$ otherwise. In the following, we shall assume that the first and last nodes are k times degenerate, while the other nodes are non degenerate. The use of B-splines in atomic and molecular physics calculations has been reviewed in [74]. When using B-splines, a large k value is desirable because higher-order polynomials give rise to better accuracy. If k is too large, however, linear dependencies start

to be an issue for B-splines as well [129]. For calculations conducted in double precision, $k = 7$ is found to be a good compromise. When the first node t_1 is located at a finite radius R_0 , it is advisable to exclude the first three B-splines to ensure \mathcal{C}^2 regularity of the wave function.

Preconditioned Gaussian functions and B-splines are separately well conditioned basis sets. When considered together, however, numerical linear dependencies may arise since the two sets overlap over an extended radial region, this issue being more pronounced when the ℓ_{\max} parameter in the Gaussian basis is large. To prevent numerical instabilities, the spline space is purged from the elements that contribute most to the numerical over-completeness of the GABS basis. We do so by diagonalizing the projector \hat{P}_G that defines the preconditioned Gaussian space in the basis of B-splines (for simplicity, we drop the angular momentum indexes)

$$\begin{aligned} \langle \mathbf{B} | \hat{P}_G | \mathbf{B} \rangle &= \mathbf{S}_{bg} \mathbf{S}_{gg}^{-1} \mathbf{S}_{gb} = \mathbf{O} \mathbf{\Lambda} \mathbf{O}^\dagger, \\ \mathbf{\Lambda}_{ij} &= \lambda_i \delta_{ij}, \quad \mathbf{O}^\dagger \mathbf{O} = \mathbf{1}, \end{aligned} \quad (5.15)$$

where

$$\mathbf{S}_{gg} = \langle \mathcal{G} | \mathcal{G} \rangle, \quad \mathbf{S}_{bg} = \langle \mathbf{B} | \mathcal{G} \rangle, \quad \mathbf{S}_{gb} = \mathbf{S}_{bg}^\dagger, \quad (5.16)$$

$$|\mathcal{G}\rangle = (|\mathcal{G}_1\rangle, |\mathcal{G}_2\rangle, \dots, |\mathcal{G}_{N_G}\rangle) \quad (5.17)$$

$$|\mathbf{B}\rangle = (|B_1\rangle, |B_2\rangle, \dots, |B_{N_B}\rangle) \quad (5.18)$$

We exclude from the basis the eigenfunctions whose eigenvalue differs from 1 less than an assigned threshold ϵ_P^B (in our case, $\epsilon_P^B = 10^{-8}$). The remaining eigenstates form a preconditioned B-spline basis that will be called $\{|\mathcal{B}_1^\ell\rangle, |\mathcal{B}_2^\ell\rangle, \dots, |\mathcal{B}_{N_{B_p}}^\ell\rangle\}$.

This procedure is carried out separately for each orbital angular momentum, since the set of Gaussian functions depends on ℓ . We will use the symbol χ_n^ℓ (or χ_n , if the angular momentum is clear from the context) to indicate the elements of the resulting regularized GABS basis, $\{\chi_n^\ell\} = \{\mathcal{G}_i^\ell\} \cup \{\mathcal{B}_j^\ell\}$. As anticipated at the beginning of this section, although the support of the Gaussian functions is in principle the whole $[0, \infty)$ semi-axis, in practice the Gaussian functions are negligible beyond a certain radius R_1 . As a consequence, the B-splines whose support is located beyond R_1 already belong to the null space of the projector and can be kept unchanged throughout the regularization procedure. This means that, beyond a certain index, the regularized GABS functions are pure B-splines. In particular, local operators expressed in this part of the GABS basis retain a sparse character (see Fig. 5.3).

5.3 PARENT IONS

The parent-ion wave functions are calculated using multi-configurational methods, i.e. the wave function of every parent ion, a vector in the Configuration

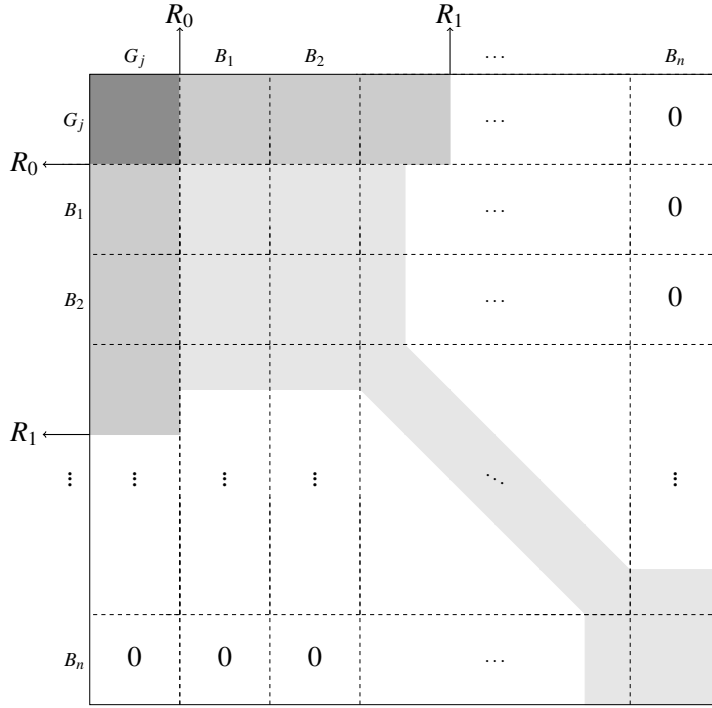


Figure 5.3: (Color online) Typical structure of an operator matrix in GABS representation. Shaded and white areas represent blocks containing nonzero and zero elements, respectively.

Interaction (CI) picture, is represented by a linear combination of Configuration State Functions (CSFs) as

$$|\Phi_a(\mathbf{x})\rangle = \sum_i c_{ia} |q^{2S_a+1} \Xi_i(\mathbf{x})\rangle, \quad (5.19)$$

where $|q^{2S_a+1} \Xi_i(\mathbf{x})\rangle$ represents an $(N-1)$ -electron CSF with multiplicity $2S_a+1$ and symmetry q . These CSFs can be related to Slater determinants using the Graphical Unitary Group Approach (GUGA) [130], avoiding the possibility of spin contamination, so that the eigenfunction a can be converted into combinations of Slater determinants (D_i), as

$$|\Phi_a(\mathbf{x})\rangle = \sum_i c'_{ia} |D_i(\mathbf{x})\rangle, \quad (5.20)$$

where the orbitals included in the Slater determinants are constructed as a linear combination of localized Gaussian functions

$$\phi_i^L(\mathbf{x}_1) = \sum_j R_{ji}^L G_j^L(\mathbf{x}_1), \quad (5.21)$$

being R_{ji}^L the expansion coefficient for the orbital i in the localized Gaussian basis function G_j^L . It is important to remember that Gaussian basis functions are centered on the different nuclei of the molecule, which requires the evaluation of polycentric integrals to calculate the properties of the system. For reasons that will become apparent later, in the latter equation we have included a superscript L to explicitly indicate that all these functions are localized.

The optimization of the orbitals and CI vectors can be done using standard quantum chemistry methods. Specifically, we use the Complete Active Space Self Consistent Field (CASSCF) where the orbitals are divided into inactive, active and virtual subspaces. The inactive and virtual orbitals are doubly occupied and empty, respectively. The active orbitals define the so-called active space and the CI vector is constructed in the CSF basis considering all possible configurations for the electrons in this reduced set of orbitals, i.e. a full CI calculation inside the active space. To allow for the description of different parent ions with the same set of orbitals, parent-ion states are obtained by using the state-average formalism, SA-CASSCF [131]. The orbitals are calculated, imposing symmetry constraints, using the QCP MOLPRO [54], that allows one to average states of different symmetries. This set of orbitals is then transformed to make it compatible with the MOLCAS [132] code, and the CI vector of Eq. (5.19) is recalculated preserving the symmetry constraints. The required matrix elements, Hamiltonian and multipoles up to 5th order between the parent ions, are calculated using the RASSI module of MOLCAS. Finally, in order to further manipulate the electronic wave function, the CI vector is transformed into a linear combination of Slater Determinants using the GUGA table provided by MOLCAS, thus leading to parent-ion wave functions in the form given by Eq. (5.20).

5.4 AUGMENTATION

In order to calculate the augmented states, the virtual orbitals of the parent ion (defined as linear combinations of the localized Gaussian functions centered at the atomic positions) are removed, while the auxiliary set of Gaussian functions belonging to the GABS basis and located on the center of mass is added, i.e. we follow a strategy similar to that usually employed to describe Rydberg states [133]. As explained above, these Gaussian functions will help us to reproduce the electronic continuum close to the nuclear environment by creating a set of mainly monocentric orbitals that will connect the localized ones at short distances with B-spline functions at long distances.

The monocentric orbitals, ϕ^M , are constructed by removing linear dependencies and orthogonalizing them to the localized orbitals ϕ^L :

$$\phi_i^M(\mathbf{x}_1) = \sum_j R_{ji}^M G_j^M(\mathbf{x}_1) + \sum_j a_{ji} \phi_j^L(\mathbf{x}_1), \quad (5.22)$$

where R_{ji}^M are the linearly independent components of the orbital i in the monocentric Gaussian functions G_j^M , and a_{ji} contains the contribution of the localized orbital j to fulfill the orthonormalization requirements. For the sake of clarity, we have dropped all indexes but one in the definition of the monocentric Gaussian functions given in Eq. (5.9) and we have explicitly added the superscript M to emphasize the monocentric character of these functions.

The augmentation procedure is carried out for all chosen parent-ion states over all possible orbitals, both localized (ϕ_i^L , Eq. (5.21)) and monocentric (ϕ_i^M , Eq. (5.22)),

$$|\bar{\Phi}_{ai}(\mathbf{x})\rangle = a_i^\dagger |\Phi_a(\mathbf{x})\rangle, \quad (5.23)$$

where $\bar{\Phi}_{ai}$ describes the parent ion a augmented in the orbital i . This augmentation is easy to implement when the parent ions are described in the basis of Slater determinants (see equation (5.20)) as

$$|\bar{\Phi}_{ai}(\mathbf{x})\rangle = \sum_j c'_{ja} a_i^\dagger |D_j(\mathbf{x})\rangle. \quad (5.24)$$

This function is then projected into a basis with a well defined spin, using the GUGA table of the parent ion with an extra electron, to obtain the augmented state defined in Eq. (5.27):

$$|\bar{Y}_{ai}^{aug}(\mathbf{x})\rangle = \sum_k c''_{kai} |q^{2S+1}\Xi_k(\mathbf{x})\rangle, \quad (5.25)$$

where the elements c''_{kai} are given by

$$c''_{kai} = \sum_j c'_{ja} \langle q^{2S+1}\Xi_k(\mathbf{x}) | a_i^\dagger |D_j(\mathbf{x})\rangle, \quad (5.26)$$

and we have used the fact that $\alpha \equiv (S, \Sigma, a, \ell, m)$. Finally, all the properties between the different augmented parent ions, i.e. the Hamiltonian, overlap and dipole matrices, are obtained with the RASSI module of MOLCAS.

In summary, the key ingredients of XCHEM are the following: **i)** the space partition and the basis functions selection for its representation (GABS+multi-center Gaussian expansion), **ii)** the disjoint support of B-splines from the parent-ion wave functions included in the CC expansion, and **iii)** the interface of MOLCAS with scattering methods, which allows us to include electron correlation at the same level as that provided by *ab initio* QCPs for bound states.

5.5 EQUIVALENCE BETWEEN THE SCATTERING AND THE AUGMENTED STATES

QCPs can provide an accurate description of the parent-ion states. To account for the additional continuum electron, these states must be supplemented with

additional one-electron functions, which can be done in practice by using the so called *augmented states*, defined as

$$\bar{Y}_{\alpha i}^{aug} = \hat{P}^{S\Sigma} \hat{a}_{i\ell_\alpha m_\alpha \sigma}^\dagger \Phi_{a, \Sigma_a} \quad (5.27)$$

for an orbital with well defined ℓ_α, m_α quantum numbers, where $\hat{P}^{S\Sigma}$ is the *projector* on the functions with total spin S and spin projection Σ , $\hat{a}_{i\ell m \sigma}^\dagger$ is the creator of an electron in the spin-orbital $\phi_i(\mathbf{x}) = \phi_i(r) Y_{\ell m}(\hat{r})^2 \chi_\sigma(\zeta)$, and Φ_{a, Σ_a} is a parent-ion state with well defined total spin projection Σ_a . For simplicity in the notation, the ℓ, m and σ quantum numbers are implicit in the i index used to denote a particular spin-orbital $\phi_i(\mathbf{x})$. The creator operator is defined on the space of spin-orbitals occupation-number vectors as

$$\hat{a}_i^\dagger |n_1, n_2, \dots, 0, \dots\rangle^i = (-1)^{\sum_{j=1}^{i-1} n_j} |n_1, n_2, \dots, 1, \dots\rangle^i, \quad (5.28)$$

$$\hat{a}_i^\dagger |n_1, n_2, \dots, 1, \dots\rangle^i = 0. \quad (5.29)$$

Furthermore, the spin-orbital occupation-number vectors are identified to Slater determinants as

$$\langle \mathbf{x}_1, \mathbf{x}_2 \dots, \mathbf{x}_N | n_1, n_2, \dots \rangle = \sqrt{N!} \hat{A} \prod_{i=1}^{\infty} \phi_i^{n_i}(\mathbf{x}_{N_i}), \quad N_i = \sum_{j=1}^i n_j. \quad (5.30)$$

What is the exact relation between the augmented states and the extended channel functions introduced in the preceding subsection? In the close-coupling formalism, the anti-symmetrization of the product of an $(N-1)$ -electron determinant $|\phi_{k_1} \cdots \phi_{k_{N-1}}|$ times a given spin orbital ϕ_i is

$$\hat{A} |\phi_{k_1} \cdots \phi_{k_{N-1}} \phi_i| = \frac{1}{\sqrt{N}} |\phi_{k_1} \cdots \phi_{k_{N-1}} \phi_i|. \quad (5.31)$$

Whenever the appended spin-orbital follows all the occupied spin-orbitals in the determinant (as it is always the case when augmenting a parent ion with a virtual orbital), the following relation holds:

$$\hat{A} \Phi_a \phi_i = \frac{1}{\sqrt{N}} (-1)^{N-1} \hat{a}_i^\dagger \Phi_a. \quad (5.32)$$

Using the definition of the augmented states and of the extended channel functions, it is therefore easy to derive the following relation:

$$\bar{Y}_{\alpha i}^{aug} = (-1)^{N-1} \frac{\sqrt{N}}{N_{\alpha i}} C_{S_a \Sigma_a, \frac{1}{2}\sigma}^{S\Sigma} \bar{Y}_{\alpha i}. \quad (5.33)$$

5.6 NUMERICAL METHODS TO COMPUTE THE SCATTERING STATES

From the equations provided in the CC section (5.1) and in the appendix, the Hamiltonian (B.9) and overlap (B.3) operator matrices can be computed, and using these, the scattering states obtained. The block structure of the operators is

shown in Figure 5.4. The \aleph_j functions represent the N_e -electron localized states (obtained using a polycentric Gaussian expansion), the $Y_\alpha G_j^M$ ones involve the parent-ion wave functions augmented with the monocentric Gaussian set (which are related to the extended channel functions as explained in section 5.4), and the $Y_\alpha B_k$ functions represent the extended channel functions with B-splines B_k for the outer electron. In this notation, α runs over all channels included in the CC ansatz. The blocks that cross the wave functions exclusively expanded in terms of Gaussian functions are computed with the QCPs. To compute the other matrix elements, the equations given in the appendix have been used. Taking into account that, by construction, there is a disjoint support between B-spline functions and the polycentric Gaussian functions, the blocks corresponding to this interaction are zero. At a given distance, the operator mediated integral between B-splines and the monocentric Gaussian functions is negligible, and hence, from that distance on, these blocks will be zero as well. This last feature together with the fact that B-spline functions have a compact support lead to sparse matrices, whose structure can be exploited when operating with them. The zero blocks in Figure 5.4 are represented by a white background.

To compute the scattering solution $\Psi_{\alpha E}^-$, we require $(\hat{H} - E)\Psi_{\alpha E}^-$ to vanish when projected onto the N basis functions that are zero at the box boundary (i.e., the farthest grid point used in the definition of the B-spline basis). If the CC expansion includes M channels Y_β that are open at the energy E , the corresponding components of $\Psi_{\alpha E}^-$ generally do not all vanish at the box boundary and they must therefore include the last B-spline in the box. These two requirements lead to a $N \times (N + M)$ homogeneous system of linear equations which has M non-trivial solutions:

$$(\mathbf{H} - E\mathbf{S}) \cdot \Psi = 0. \quad (5.34)$$

To solve (5.34) using the methods we will explain below, we require the left-hand matrices to contain linearly independent rows and columns. In general, the operator blocks coming from QCPs exhibit linear dependencies. The blocks in which the bras correspond to a parent ion augmented with monocentric Gaussian functions and the kets correspond to a parent ion coupled with B-splines or vice versa can also have linear dependencies, because several of the Gaussian functions can be represented by linear combinations of B-splines. But the blocks in which both the bras and kets involve B-splines are linearly independent, due to the effective completeness of this basis [129] and the order set in the computation of these polynomials ($k < 15$). To go from the original operator matrix to the conditioned one $\mathbf{O}_p \rightarrow \tilde{\mathbf{O}}_p$, we need to build the conditioning matrix \mathbf{P}_{con} that makes the transformation:

$$\tilde{\mathbf{O}}_p = \mathbf{P}_{\text{con}}^T \mathbf{O}_p \mathbf{P}_{\text{con}}. \quad (5.35)$$

The conditioning matrix \mathbf{P}_{con} only transforms the square block \mathbf{O}_p' in \mathbf{O}_p , containing the QC matrix elements and the rows and columns in which there is a non-negligible overlap between monocentric Gaussian and B-spline functions (see Figure 5.4). To find this transformation, the N_e -electron overlap sub-matrix involving the same functions as \mathbf{O}_p' is diagonalized, $\mathbf{S}' = \mathbf{O}\mathbf{A}\mathbf{O}^T$, and those eigen-

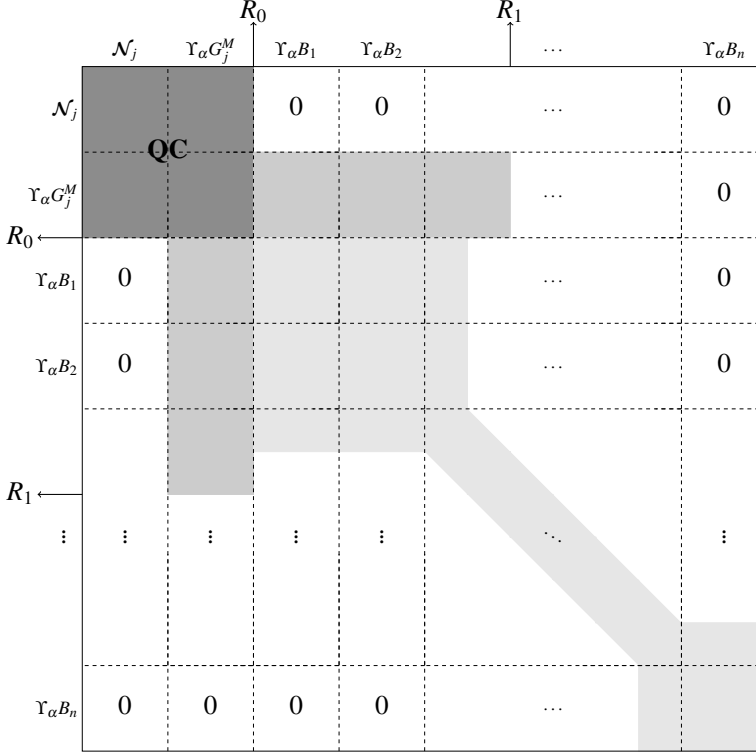


Figure 5.4: Matrix structure of the Hamiltonian operator. See text for notations. Shaded areas represent matrix blocks containing non-zero matrix elements. The QC block is obtained from the QCPs. The remaining matrix elements are evaluated by using the equations given in the Appendix.

vectors whose eigenvalues are lower than some threshold removed ($\mathbf{O} \rightarrow \tilde{\mathbf{O}}$, $\mathbf{\Lambda} \rightarrow \tilde{\mathbf{\Lambda}}$), leading to

$$\mathbf{P}_{\text{con}} = \left[\begin{array}{c|c} \tilde{\mathbf{O}}\tilde{\mathbf{\Lambda}}^{-\frac{1}{2}} & \mathbf{0} \\ \hline \mathbf{0} & \mathbf{1} \end{array} \right]. \quad (5.36)$$

After conditioning the overlap and the Hamiltonian matrices, the system of linear equations (5.34) transforms into:

$$(\tilde{\mathbf{H}} - E\tilde{\mathbf{S}}) \cdot \tilde{\Psi} = \mathbf{0}, \quad (5.37)$$

where the new solutions $\tilde{\Psi}$ are related to the original ones by $\Psi = \mathbf{P}_{\text{con}}\tilde{\Psi}$. Once the system of linear equations (5.37) is free from linear dependencies, we set to zero the M rows containing the B-splines that do not vanish at the end of the box (coincides with the number of channels). This is necessary in order to get the non-trivial solution of the system of equations.

5.6.1 LU factorization and null space of \mathbf{U} matrix

This method is based in the LU factorization of the matrix associated with the homogeneous system of linear equations:

$$\tilde{\mathbf{H}} - E\tilde{\mathbf{S}} = \mathbf{LU} = \begin{bmatrix} l_{11} & 0 & \cdots & 0 \\ l_{21} & l_{22} & \cdots & 0 \\ \vdots & & \ddots & \vdots \\ l_{n1} & l_{n2} & \cdots & l_{nn} \end{bmatrix} \begin{bmatrix} u_{11} & u_{12} & \cdots & u_{1n} \\ 0 & u_{22} & \cdots & u_{2n} \\ \vdots & & \ddots & \vdots \\ 0 & 0 & \cdots & u_{nn} \end{bmatrix}, \quad (5.38)$$

where the matrices have the dimension $n = N + M$. Due to the LU factorization, the system (5.37) is equivalent to finding the null space of the matrix \mathbf{U} .

$$\mathbf{U} \cdot \tilde{\Psi} = \begin{bmatrix} u_{11} & u_{12} & \cdots & u_{1N} & \cdots & u_{1n} \\ 0 & u_{22} & \cdots & u_{2N} & \cdots & u_{2n} \\ \vdots & \vdots & \ddots & & \cdots & \vdots \\ 0 & 0 & \cdots & u_{NN} & \cdots & u_{Nn} \\ 0 & 0 & 0 & \cdots & 0 & u_{(N+1)(N+2)} \cdots u_{(N+1)n} \\ 0 & 0 & 0 & 0 & \cdots & 0 \cdots u_{(N+2)n} \\ \vdots & \vdots & \vdots & \vdots & \vdots & \vdots \\ 0 & 0 & 0 & 0 & 0 & 0 \cdots 0 \end{bmatrix} \cdot \begin{bmatrix} \tilde{\Psi}_{11} & \tilde{\Psi}_{12} & \cdots & \tilde{\Psi}_{1M} \\ \tilde{\Psi}_{21} & \tilde{\Psi}_{22} & \cdots & \tilde{\Psi}_{2M} \\ \vdots & \vdots & \ddots & \vdots \\ \tilde{\Psi}_{N1} & \tilde{\Psi}_{N2} & \cdots & \tilde{\Psi}_{NM} \\ -1 & 0 & \cdots & 0 \\ 0 & -1 & \cdots & 0 \\ \vdots & \vdots & \ddots & \vdots \\ 0 & 0 & \cdots & -1 \end{bmatrix} = \mathbf{0}. \quad (5.39)$$

As we have set to zero M rows, we have the same number M of degrees of freedom in the solution, which will be cleared later by the asymptotic fitting of the solutions to the Coulomb wave functions that represent the scattering states at long distances (see 5.6.4). There will also be M matrix elements in the diagonal of \mathbf{U} that will be zero, which allows us to solve the system by back-substitution:

$$\begin{aligned} u_{NN}\tilde{\Psi}_{Nj} &= u_{N(N+j)} \\ u_{(N-1)(N-1)}\tilde{\Psi}_{(N-1)j} + u_{(N-1)(N)}\tilde{\Psi}_{Nj} &= u_{(N-1)(N+j)} \\ &\vdots \end{aligned} \quad (5.40)$$

We will refer to this method as HSLE.

5.6.2 Matrix inversion method

If we remove in the matrix $(\tilde{\mathbf{H}} - E\tilde{\mathbf{S}})$ the M rows containing the B-splines that do not vanish at the end of the box, and permute the columns containing those functions in order to be placed in the last M columns, Eq. (refeq:HSLEConditioned) can be written in blocks as

$$\left[\begin{array}{c|c} \mathbf{A} & \mathbf{B} \end{array} \right] \left[\begin{array}{c} \tilde{\Psi}_{\mathbf{N}} \\ -\mathbf{I} \end{array} \right] = \mathbf{0}, \quad (5.41)$$

where the matrix \mathbf{A} with $N \times N$ dimension is Hermitian, because the last B-splines in the box are placed in \mathbf{B} . Matrix $\tilde{\Psi}_{\mathbf{N}} = \{\tilde{\Psi}_{ij}\}; i = 1, \dots, N; j = 1, \dots, M$ (see Eq. (5.39)) and \mathbf{I} is an $M \times M$ identity matrix. The matrix \mathbf{A} is invertible because it is free of linear dependencies and it is Hermitian. Then a solution can be found in the form

$$\tilde{\Psi}_{\mathbf{N}} = \mathbf{A}^{-1}\mathbf{B} \quad (5.42)$$

Although this solution is straightforward it scales poorly with the matrix size (number of scattering channels and basis functions in the CC), because it requires a matrix inversion for every energy of interest. This limitation could partly be circumvented by exploiting the sparse structure of the matrices (thanks to B-splines,) using parallel routines for the matrix inversion. We will refer to this method as INVM.

5.6.3 Eigenstates as a basis for the scattering states

This method requires to compute the full Hamiltonian spectrum for the system confined to the box:

$$\mathbf{H}\Phi = \mathbb{E}\mathbf{S}\Phi, \quad (5.43)$$

where \mathbb{E} is a diagonal matrix with the eigenvalues (energies) and Φ the matrix of eigenvectors (the columns represents the eigenstates). To do so, we start from the pristine Hamiltonian and overlap matrices, without applying the (5.36) conditioner, in order to do it in a more general and independent way, Diagonalizing this time the full overlap matrix, and removing the eigenvectors whose eigenvalues are lower than some defined threshold, the new overlap matrix free of linear dependencies results in

$$\mathbf{S} = \mathbf{O}\mathbf{\Lambda}\mathbf{O}^\dagger. \quad (5.44)$$

The thresholds used to remove the linear dependencies in order to compute the eigenstates are typically higher (remove more eigenvectors) than those only used to condition the matrices for the scattering calculations, typically the values are

10^{-5} and 10^{-8} respectively, for the $\Lambda_{ii}/\max(\Lambda_{ii})$ ratio. From this spectral resolution of the overlap, a new conditioner matrix can be built $\mathbb{T} = \mathbb{O}\Lambda^{-\frac{1}{2}}$ (a rectangular matrix), allowing to transform Eq. (5.43) in:

$$\mathbb{H}\mathbb{Q} = \mathbb{E}\mathbb{Q}, \quad (5.45)$$

where the new conditioned Hamiltonian is $\mathbb{H} = \mathbb{T}^\dagger \mathbf{H} \mathbb{T}$ and the relation between the old and new eigenvectors is $\Phi = \mathbb{T}\mathbb{Q}$. Since \mathbb{Q} is orthogonal, from the spectral resolution (5.44) it is easy to show that

$$\Phi^\dagger \mathbf{S} \Phi = \mathbf{I}. \quad (5.46)$$

Using this relation, the Hermitian matrix $\mathbf{A} = [\mathbf{H} - \mathbf{E}\mathbf{S}]_{N \times N}$ in Eq. (5.41) can be expressed in terms of the Φ eigenstates:

$$\mathbf{A} = \Phi \Phi^\dagger \mathbf{A} \Phi \Phi^\dagger = \Phi (\Phi^\dagger \mathbf{S} \Phi \mathbb{E} - \mathbf{E}) \Phi^\dagger = \Phi (\mathbb{E} - \mathbf{E}) \Phi^\dagger, \quad (5.47)$$

and then the same Eq. (5.42) of the INVM method can be used with $\mathbf{A}^{-1} = \Phi (\mathbb{E} - \mathbf{E})^{-1} \Phi^\dagger$. This way the matrix inversion is straightforward, provided the full spectrum of the Hamiltonian in the box is available, which could penalize the computation. We will refer to this method as SPEC.

5.6.4 Normalization of scattering states

The radial monoelectronic function coupled to the parent ions in the scattering solution (see Eqs. (5.3) and (5.4)) appears as a linear combination of orbitals containing both Gaussian and B-spline functions

$$\phi_{\beta\alpha}(r) = \sum_i N_{\beta i} \varphi_i(r) c_{\beta i, \alpha E} \quad (5.48)$$

and is asymptotically fitted to a combination of regular, $F(r)$, and irregular, $G(r)$, Coulomb functions [134]

$$\phi_{\beta\alpha}(r) = a_{\beta\alpha} F_\beta(r) + b_{\beta\alpha} G_\beta. \quad (5.49)$$

From this fit, we can compute the scattering matrix $\mathbb{S}(E, E')$ for the elastic collision, $\mathbb{S}(E) \delta(E - E') = \langle \Psi_E^- | \Psi_{E'}^+ \rangle$ (see 3), as

$$\mathbb{S} = \frac{\mathbf{A} + i\mathbf{B}}{\mathbf{A} - i\mathbf{B}}, \quad (5.50)$$

where $A_{\beta\alpha} = \sqrt{\frac{\pi k_\beta}{2}} a_{\beta\alpha}$ and $B_{\beta\alpha} = \sqrt{\frac{\pi k_\beta}{2}} b_{\beta\alpha}$, being k_β the momentum relative to the threshold defined by the β -parent ion. Using these matrices, we can also obtain the correct scattering wave function with incoming boundary conditions through:

$$\Psi_{\alpha E}^- = \sum_\beta \Psi_{\beta E} \cdot (A_{\beta\alpha} + iB_{\beta\alpha})^{-1}, \quad (5.51)$$

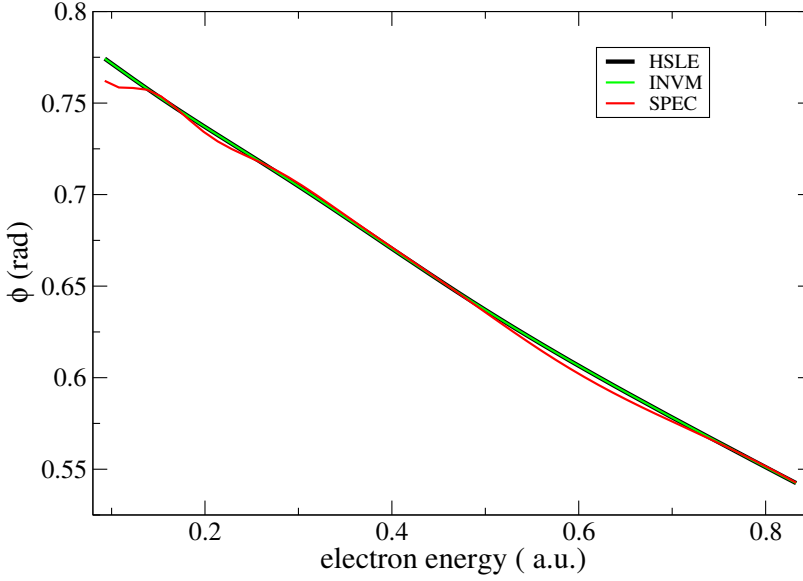


Figure 5.5: One of the Ne eigenphases of $1P^0$ symmetry, in the energy region below the $2s2p^6np$ resonant serie, obtained using three different numerical implementations to compute the scattering states: HSLE (black), INVM (green) and SPEC (red) (see text for details).

where $\Psi_{\beta E}$ are the solutions of (5.34). The eigenvalues of S have the form $e^{2i\theta_\alpha}$, where θ_α ($\alpha = 1, \dots, M$) are the so called phase-shifts or eigen-phases [135, 136], which can be used as a sensitive observable to check the accuracy of the calculation of the multichannel continuum by comparing them to independently established benchmarks.

In Figure 5.5, the performance of the three methods explained before: HSLE (5.6.1), INVM (5.6.2) and SPEC (5.6.3) is shown, plotting one of the eigen-phases of the Ne multichannel scattering problem below the $2s2p^6np$ resonant serie (see 7.2 for more details). The results using HSLE and INVM methods are indistinguishable. For the SPEC method we used a larger threshold to prevent numerical instabilities in the eigenvalues of the bound states. As a consequence, more basis functions were removed, thus decreasing the flexibility of the basis in the continuum.

Part III

RESULTS

GABS BASIS PERFORMANCE: HYDROGEN ATOM IN A LASER FIELD

6.1 SPECTRAL RESOLUTION OF THE HAMILTONIAN

Different choices for the conditions fulfilled by the state functions at the box boundary lead to different sets of eigenvalues and eigenstates of the Hamiltonian.

CONFINED EIGENSTATES One possible choice is to require that all the wave functions vanish at the box boundary. With either a purely B-spline basis or, owing to the fast-descent character of the Gaussian functions, with the hybrid GABS basis, such condition is ensured by excluding the last B-spline from the basis set. In the following, we will add a bar on top of a basis-set symbol (e.g., $\bar{\chi}$) to indicate that the last B-spline is excluded. If this is the case, the Hamiltonian is an hermitian matrix which can be diagonalized by solving the generalized secular problem

$$\bar{H}\bar{C} = \bar{S}\bar{C}\bar{E}, \quad \bar{E}_{ij} = \bar{E}_i\delta_{ij}, \quad \bar{C}^\dagger\bar{C} = \mathbf{1}, \quad (6.1)$$

where

$$\bar{S} = \langle \bar{\chi} | \bar{\chi} \rangle, \quad \bar{H} = \langle \bar{\chi} | H | \bar{\chi} \rangle. \quad (6.2)$$

We will indicate the confined (or box) eigenstates as $|\phi\rangle = |\bar{\chi}\rangle\bar{C}$. The confined bound states that do not get close to the box boundary approximate the first terms of the Rydberg series of the unconstrained Hamiltonian, while the positive-energy states represent a discrete selection of the generalized continuum eigenstates of the unconstrained Hamiltonian, up to a certain energy E_{\max} , after which the quality of the states starts to deteriorate. The basis of the box eigenstates of the Hamiltonian so obtained is equivalent to the original basis and offers some advantages when solving the TDSE numerically (see section 6.3).

PHYSICAL EIGENSTATES By requiring that the wave function vanishes at the box boundary, one is needlessly crippling the flexibility of the B-splines and of the hybrid basis alike. In fact, if the last B-spline is included, the basis is perfectly capable to represent, within the box, any eigenfunction of the Hamiltonian that is regular at the origin and whose energy does not exceed E_{\max} [74]. To see this,

let us look for a generic eigenfunction with energy E (which, in principle, can even be complex) in the following form

$$|\psi_E\rangle = |\bar{\chi}\rangle c_E + |B_N\rangle b_E, \quad (6.3)$$

where with B_N we indicate the last B-spline of the basis set. If E belongs to the box spectrum $\{\bar{E}_1, \bar{E}_2, \dots\}$, the solution is a box eigenstate and the coefficient of the last B-spline is zero, $b_E = 0$. In the other cases, we can derive the other coefficients in terms of b_E by solving the $(n-1) \times n$ homogeneous linear system

$$\langle \bar{\chi} | E - H | \psi_E \rangle = 0, \quad (6.4)$$

which, under the given hypothesis, has exactly one solution,

$$|\psi_E\rangle \propto |\bar{\chi}\rangle \bar{\mathbf{G}}_0(E) \langle \bar{\chi} | H - E | B_N \rangle b_E + |B_N\rangle b_E, \quad (6.5)$$

$$\bar{\mathbf{G}}_0(E) = (E\bar{\mathbf{S}} - \bar{\mathbf{H}})^{-1}. \quad (6.6)$$

The expression (6.5) provides valid scattering solutions for any $E \in [0, E_{\max}]$, which are as accurate as the discretized-continuum eigenstates obtained from the diagonalization of the Hamiltonian in the box (a similar treatment to the one presented here can be found, e.g., in [137]). To ensure that the analytic continuation Ψ_E of ψ_E to the whole $[0, \infty)$ real semi-axis fulfills the condition

$$\langle \Psi_E | \Psi_{E'} \rangle = \delta(E - E'), \quad (6.7)$$

the value of b_E must be determined by matching, at the box boundary, the reduced radial part $u_{\ell E}(r)$ of the wave function,

$$\psi_{E\ell m}(\vec{r}) = \frac{u_{\ell E}(r)}{r} Y_{\ell m}(\hat{r}), \quad (6.8)$$

(ℓ is the formerly implied angular momentum) with a linear combination of the analytical regular $F_\ell(\gamma, \rho)$ and irregular $G_\ell(\gamma, \rho)$ Coulomb functions with the same energy [134],

$$u_{\ell E}(r) = \sqrt{\frac{2}{\pi k}} \left[\cos \delta F_\ell(\gamma, \rho) + \sin \delta G_\ell(\gamma, \rho) \right], \quad (6.9)$$

where $k = \sqrt{2E}$, $\gamma = -Z/k$, $\rho = kr$, and δ is the phase shift. When comparing with an ionization experiment, we need to evaluate the transition amplitudes to the detector eigenstates $\psi_{E\hat{\Omega}}^-$, i.e., the states that have a well defined asymptotic energy E and direction $\hat{\Omega}$ in the far future. These are the scattering states which fulfill incoming boundary conditions [138], and have the following expression,

$$\psi_{E\hat{\Omega}}^- = \sum_{\ell m} \psi_{E\ell m} Y_{\ell m}^*(\Omega) e^{-i(\sigma_\ell + \delta_\ell - \ell\pi/2)}, \quad (6.10)$$

where σ_ℓ is the Coulomb phase shift [139] and δ_ℓ the scattering phase shift (see Chapter 3 for details).

In the case of negative energies, only those solutions to Eq. (6.5) whose analytical extension is regular at $r \rightarrow \infty$ represent valid bound eigenstates. This property can be ensured by requiring that the logarithmic derivative of the radial part of ψ_E match that of the eigenfunction of the Coulomb problem with the same (negative) energy and that is regular at infinity,

$$\frac{u'_{\ell E}(r)}{u_{\ell E}(r)} = \frac{\left[e^{-\rho} \rho^{\ell+1} U(\ell+1 - Z/\kappa, 2\ell+2, 2\rho) \right]'}{e^{-\rho} \rho^{\ell+1} U(\ell+1 - Z/\kappa, 2\ell+2, 2\rho)}, \quad (6.11)$$

where $\kappa = \sqrt{-2E}$, $\rho = \kappa r$, $U(a, b, z)$ is the confluent hypergeometric function of the second kind [134], and both the LHS and RHS of (6.11) are to be evaluated for $r = R_{\text{box}}$ (see App. E for an outline of the derivation). The boundary condition (6.11) constitutes an implicit equation for the allowed bound energies $E_{n\ell}$. If the Hamiltonian coincides with that of an hydrogenic ion, the solutions are of course $E_{n\ell} = -Z^2/2n^2$. If the Hamiltonian differs from that of the hydrogen atom by a short-range spherically symmetric potential, the boundary equation (6.11) still has infinite roots which can easily be found numerically and which represent all the bound energy levels of the system. Once the values of the bound states energies are known, it is possible to apply the same procedure used for the scattering states to find an accurate representation, within the box, of any unconfined bound state. To find the proper normalization for the bound states derived with this technique, however, it is necessary to separately evaluate the truncated integral of the regular solution of the Coulomb problem that extends the numerical wave function to infinite radii,

$$I_{\ell E}(R_{\text{box}}) = \int_{R_{\text{box}}}^{\infty} u_{\ell E}^2(r) dr. \quad (6.12)$$

6.2 DIPOLE TRANSITION MATRIX ELEMENTS

Dipole transition matrix elements are a necessary ingredient of both perturbative and non-perturbative radiative transitions. In the next section we will compare the reduced dipole transition matrix elements between selected eigenstates $\psi_{E\ell m}$ of the field-free Hamiltonian,

$$\langle \psi_{E\ell} | \mathcal{O}_1^{(g)} | \psi_{E'\ell'} \rangle = \sum_{mm'\mu} \frac{C_{\ell'\ell m', j\mu}^{\ell m}}{\sqrt{2\ell+1}} \langle \psi_{E\ell m} | \mathcal{O}_{1\mu}^{(g)} | \psi_{E'\ell' m'} \rangle, \quad (6.13)$$

where $C_{a\alpha, b\beta}^{c\gamma}$ is a Clebsch-Gordan coefficient [140], evaluated in different numerical basis as well as analytically, for three gauges g , length, velocity, and acceleration,

$$\mathcal{O}_{1\mu}^{(l)} = r_{1\mu}, \quad \mathcal{O}_{1\mu}^{(v)} = p_{1\mu}, \quad \mathcal{O}_{1\mu}^{(a)} = Z \frac{r_{1\mu}}{r^3}. \quad (6.14)$$

The *off-shell* dipole transition matrix elements in different gauges between physical eigenstates are related to each other through the identities

$$i(E - E') \langle \psi_{E\ell} \| \mathcal{O}_1^{(l)} \| \psi_{E'\ell'} \rangle = \langle \psi_{E\ell} \| \mathcal{O}_1^{(v)} \| \psi_{E'\ell'} \rangle, \quad (6.15)$$

$$(E - E') \langle \psi_{E\ell} \| \mathcal{O}_1^{(v)} \| \psi_{E'\ell'} \rangle = i \langle \psi_{E\ell} \| \mathcal{O}_1^{(a)} \| \psi_{E'\ell'} \rangle. \quad (6.16)$$

While the Hamiltonian is particularly sensitive to the rapidly-varying parts of the wave function, due to the presence of the kinetic energy operator, the kernels in (6.14) put a higher emphasis on the wave function at either short or long range. The agreement between matrix elements across different gauges and numerical representations, therefore, is an alternative valuable measure of the wave function quality beyond the numerical fulfillment of the secular equation.

If the continuum-continuum transitions are evaluated between box eigenstates instead of physical states (i.e., if the radial integrals are truncated at $r = R_{\text{box}}$), Eq. (6.16) needs to be modified,

$$\begin{aligned} (E - E') \langle \psi_{E\ell} \| \mathcal{O}_1^{(v)} \| \psi_{E'\ell'} \rangle_{r \in [0, R_{\text{box}}]} &= \\ &= i \langle \psi_{E\ell} \| \mathcal{O}_1^{(a)} \| \psi_{E'\ell'} \rangle_{r \in [0, R_{\text{box}}]} + \\ &+ \frac{i}{2} \sqrt{2\ell' + 1} C_{\ell'0,10}^{\ell 0} \frac{d u_{\ell E}}{dr} (R_{\text{box}}) \frac{d u_{\ell' E'}}{dr} (R_{\text{box}}). \end{aligned} \quad (6.17)$$

Furthermore, while Eq. (6.15) remains valid even when considered between box eigenstates, the transition matrix elements themselves do differ from those evaluated between scattering states. In App. C we derive and discuss at length the above equations. In the next section, we will use them to frame the results of our calculations.

6.3 TIME-DEPENDENT SCHRÖDINGER EQUATION

To compute the effects of intense linearly-polarized radiation pulses on a bound state ϕ_0 of a hydrogen atom, we solve the TDSE,

$$i\partial_t \psi(t) = H(t) \psi(t); \quad \psi(t_0) = \phi_{1s}, \quad (6.18)$$

by expanding the time-dependent wave function $\psi(t)$ in the basis of the box eigenstates of the field-free Hamiltonian, obtained from either the GABS or the purely B-spline basis,

$$\psi(t) = \sum_{i\ell} \phi_{i\ell} c_{i\ell}(t), \quad (6.19)$$

where axial symmetry, $m = 0$, is assumed throughout. In the present work, beyond the field-free electrostatic term H_0 , the complete Hamiltonian comprises the

time-dependent interaction with the external fields $H'(t)$ in the dipole approximation,

$$H(t) = H_0 + H'(t), \quad (6.20)$$

$$H_0 = \frac{p^2}{2} - \frac{Z}{r}, \quad (6.21)$$

$$H'(t) = \begin{cases} \alpha \vec{A}(t) \cdot \vec{p} & \text{velocity gauge} \\ \vec{E}(t) \cdot \vec{r} & \text{length gauge} \end{cases}, \quad (6.22)$$

where $\vec{A}(t)$ and $\vec{E}(t)$ are the vector potential and the electric field of the external radiation, respectively. The TDSE is integrated numerically by propagating the solution on a time-grid $t_i = t_{i-1} + dt$,

$$\psi(t + dt) = U(t + dt, t)\psi(t), \quad (6.23)$$

where $U(t + dt, t)$ is a second-order split exponential propagator,

$$U(t + dt, t) \equiv e^{-iH_0 \frac{dt}{2}} e^{-iH'(t + \frac{dt}{2}) dt} e^{-iH_0 \frac{dt}{2}}. \quad (6.24)$$

As the wave function is expressed in a spectral basis, the action on ψ of the two outer exponential factors on the RHS of (6.24) is trivial. The most time-consuming step of the propagation (6.23) is the evaluation of $\exp[-iH'(t + dt/2)dt]$ on ψ . Here, we carry it out by representing the exponential operator on the truncated Krylov basis generated by the repeated action of $H'(t + dt/2)$ on the $\exp[-H_0 dt/2]\psi(t)$ state. In the conditions examined in the present work, where fields with only moderate intensities are contemplated, this representation converges rapidly with respect to the size N_K of the Krylov space, which can generally be truncated to $N_K \leq 5$. Such a fast convergence is a consequence of the factorization between the H_0 and the H' action achieved with the splitting in (6.24).

The bound state population $P_{n\ell}$ and the asymptotic energy-resolved and angularly resolved photoelectron distribution $d^2P(E, \cos \theta)/dE d \cos \theta$ are obtained by projecting the wave packet, at any time after the external pulse is over, on a complete set of bound and scattering eigenstates of the field-free Hamiltonian, computed with the techniques described in Sec. 6.1,

$$P_{n\ell} = |\langle \psi_{n\ell 0} | \psi(t) \rangle|^2, \quad (6.25)$$

$$\frac{d^2P(E, \cos \theta)}{dE d \cos \theta} = 2\pi \left| \langle \psi_{E,\Omega}^- | \psi(t) \rangle \right|^2. \quad (6.26)$$

6.4 BOUND AND CONTINUUM STATES OF HYDROGEN

In this section we illustrate the accuracy of the GABS basis from the perspective of the spectral resolution of the field-free electrostatic hamiltonian of hydrogen

Table 6.1: Energies for the first 6 bound s and p hydrogen states, obtained using the B-splines basis and two purely Gaussian basis.

n	Analytical	B-splines	Gaussian ^a		Gaussian ^b
		$\ell = 0, 1$	$\ell = 0$	$\ell = 1$	$\ell = 0$
1	-0.5	-0.50000000	-0.49996942	*	-0.49993963
2	-0.125	-0.12500000	-0.12499618	-0.12500000	-0.12499244
3	-0.0(5)	-0.05555556	-0.05555436	-0.05555552	-0.05525990
4	-0.03125	-0.03125000	-0.03110496	-0.03111820	-0.01909004
5	-0.02	-0.02000000	-0.01593253	-0.01612874	0.04060086
6	-0.013(8)	-0.01388889	0.00422693	0.00368341	0.14949865

^a $\ell_{\max} = 20$ ^b $\ell_{\max} = 2$

by comparing the results with the analytical ones and with those obtained using both a purely B-spline basis and a purely Gaussian basis. We use B-splines of degree $k = 7$ defined on a uniform grid with node spacing $\Delta r = 0.5$ a.u. up to a maximum radius $R_{\text{box}} = 1000$ a.u., and $N_{\alpha} = 22$ Gaussian exponents $\alpha_n = \alpha\beta^{n-1}$ for the even tempered Gaussian basis, with $\alpha = 0.01$, $\beta = 1.46$.

In table 6.1, we report the energies for the bound s and p hydrogen states with principal quantum number $n \leq 6$, obtained by using two different values of ℓ_{\max} , $\ell_{\max} = 2$ and $\ell_{\max} = 20$.

As anticipated, B-splines provide essentially exact results for all the states considered, while the quality of the eigenvalues obtained with the Gaussian functions deteriorates already for $n = 4$, due to their inability to reproduce the many oscillations Rydberg satellites have. Extending ℓ_{\max} from 2 to 20 improves significantly the energy of the third and fourth states. Even with the larger even-tempered basis, however, the results still remain well off mark from the $n = 5$ state on. In the calculation with the Gaussian functions, the error on the energy of the ground state is one order of magnitude larger than for the first excited state. This circumstance is peculiar to s orbitals and is due to the well known difficulty Gaussian functions have in reproducing the cusp condition at the origin. Indeed, the energies of the $2p$ and $3p$ states reported in Table 6.1 are two orders of magnitude more accurate than those of the $2s$ and $3s$ ones computed with the same basis.

Table 6.2 reports the energy of several bound hydrogen states computed with three GABS bases that differ for the value of ℓ_{\max} and for the position of the first B-spline node.

Table 6.2: Energies for the first 15 s and p bound hydrogen states, obtained in three different GABS basis.

n	Analytical	$\ell_{\max} = 20, R_0 = 10 \text{ a.u.}$		$\ell_{\max} = 2, \ell = 0$	
		$\ell = 0$	$\ell = 1$	$R_0 = 5 \text{ a.u.}$	$R_0 = 10 \text{ a.u.}$
1	-0.5	-0.49997191	*	-0.49994231	-0.49994092
2	-0.125	-0.12499648	-0.12500000	-0.12499278	-0.12499261
3	-0.0(5)	-0.05555451	-0.05555556	-0.05555241	-0.05555337
4	-0.03125	-0.31249561	-0.03125000	-0.03124909	-0.03124907
5	-0.02	-0.01999977	-0.02000000	-0.01999954	-0.01999952
6	-0.013(8)	-0.01388876	-0.01388889	-0.01388862	-0.01388861
7	-0.01020408	-0.01020400	-0.01020408	-0.01020391	-0.01020391
8	-0.0078125	-0.00781245	-0.00781250	-0.00781239	-0.00781238
9	-0.00617284	-0.00617280	-0.00617284	-0.00617276	-0.00617276
10	-0.005	-0.00499997	-0.00500000	-0.00499994	-0.00499994
11	-0.00413223	-0.00413221	-0.00413223	-0.00413219	-0.00413219
12	-0.00347(2)	-0.00347221	-0.00347222	-0.00347219	-0.00347219
13	-0.00295858	-0.00295857	-0.00295858	-0.00295855	-0.00295855
14	-0.00255102	-0.00255101	-0.00255102	-0.00255064	-0.00255063
15	-0.00(2)	-0.00222221	-0.00222222	-0.00221182	-0.00221182

In s symmetry, all three GABS bases give excellent values across the bound spectrum with errors, for $n \geq 2$, of the order of $\sim 10^{-6}$ or lower, irrespective of ℓ_{\max} . The energy of all the p orbitals is accurate to eight decimal digits. We can better understand the origin of GABS good performance by looking at the contribution of B-splines and Gaussian functions to the radial part of the eigenstates computed with the hybrid basis. Fig. 6.1 shows these quantities for the 7s and 15s states, with the corresponding radial orbitals obtained with the B-spline basis as a reference.

The plots in Fig. 6.1 illustrate two distinctive features of the GABS basis. Firstly, B-splines complete the Gaussian basis in the outer region. As a result, the basis can represent the oscillatory behavior of highly excited bound states there. Secondly, B-splines effectively counterbalance any value that the diffuse Gaussian functions can take in the intermediate region. As a result, the diffuse Gaussian functions acquire larger flexibility in the inner region as well.

The conclusions above apply to the states in the continuum as well. In Fig. 6.2(a), we compare the radial part of the analytical ψ_{sE} generalized eigenfunction for $E = 0.1 \text{ a.u.}$ with the corresponding numerical quantity computed

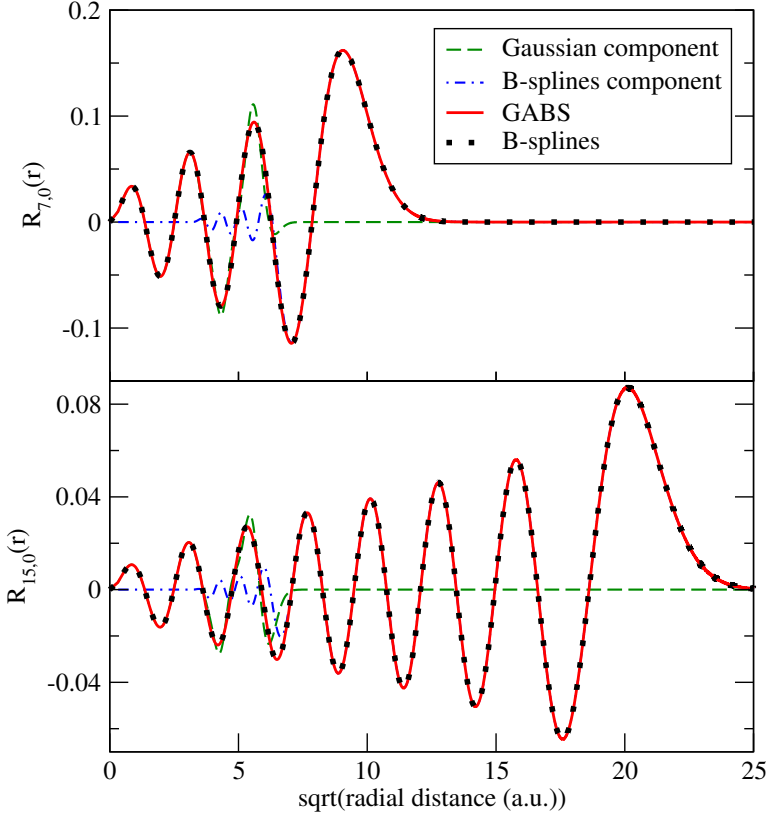


Figure 6.1: Radial part of the 7s (top panel) and 15s (bottom panel) hydrogen Rydberg states as a function of \sqrt{r} , computed with B-splines (dots) and GABS (solid line). For the latter case, the Gaussian component (dashed line) and the B-spline component (dashed-dotted line) are separately shown.

with the unconstrained-continuum method described in Sec. 6.1 using the GABS basis. The two curves are indistinguishable to the naked eye. We quantify the numerical error in Fig. 6.2(b) for three different energies: $E = 0.1$ a.u., 1 a.u., and 4 a.u. In the outer radial region ($R_1 \geq 55$ a.u.), where only B-splines contribute significantly to the wave function, the numerical error is of the order of 10^{-10} , 10^{-7} , and 10^{-4} for the three considered energies, respectively. In the intermediate radial region, between $\simeq 20$ a.u. and $\simeq 40$ a.u., where both the diffuse Gaussian functions and the B-splines contribute to the wave function, the absolute representation error has a plateau of the order of 10^{-7} for $E \leq 1$ a.u. At higher energies the error is dominated by the larger B-spline asymptotic error. Finally, in the short-range region, where the wave function is represented only in terms of Gaussian functions, for the two smallest energies the absolute error has a plateau of the order of 10^{-4} , i.e., comparable to the asymptotic B-spline representation error for $E = 4$ a.u. In contrast to the behavior observed in the intermediate region, the error in the short-range region is always dictated by the

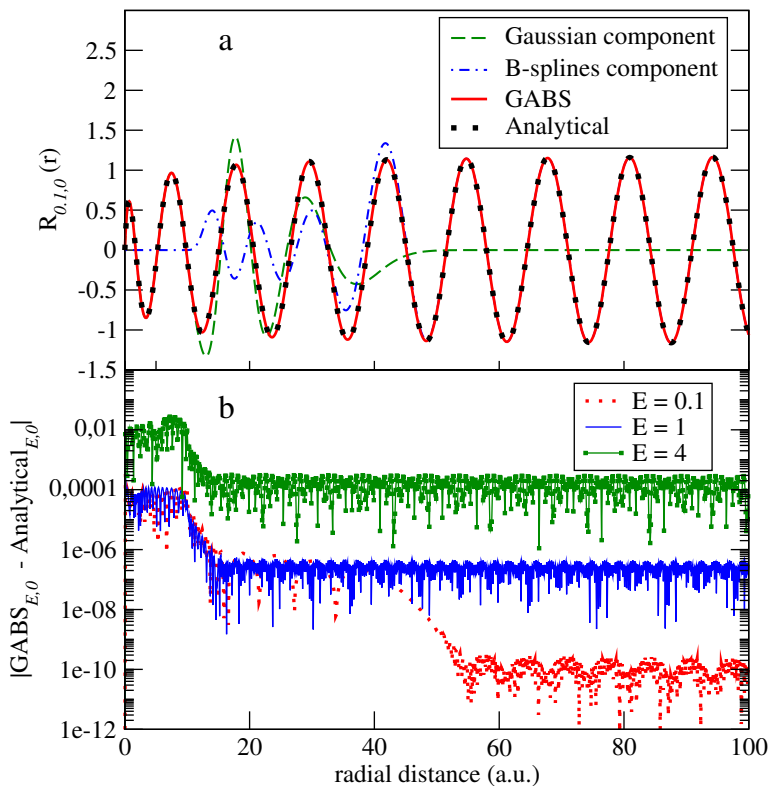


Figure 6.2: Upper panel: radial part of the ψ_{sE} hydrogen scattering state with $E = 0.1$ a.u., computed analytically (dots) and numerically using GABS (solid line) $R_0 = 1000$ a.u., $\ell_{\max} = 20$. The Gaussian (dashed line) and the B-spline (dashed-dotted line) components of the numerical function are also shown. This picture illustrates that, when assisted by the B-splines, the Gaussian functions gain the freedom of deviating substantially from the target function in the intermediate radial range, thus acquiring more flexibility at short range. Bottom panel: absolute local error of the scattering states ψ_{sE} computed with GABS for $E = 0.1$ a.u. (dots), $E = 1$ a.u. (solid line) and $E = 4$ a.u. (dotted line). See text for more details.

Gaussian functions. As a result, at the third larger energy, the error there becomes of the order of few percent units.

The quality of continuum wave functions, therefore, depends crucially on the location R_0 where the transition between the inner and the intermediate region takes place. A more comprehensive characterization of the quality of the continuum hydrogen s wave functions is provided in Fig. 6.3 in the form of the phase shift as a function of the excess energy up to $E = 5$ a.u., for several values of R_0 : 5 a.u., 10 a.u., 15 a.u., 20 a.u.. The phase shift is a sensitive probe of the accuracy of a continuum wave function. Ideally, since in the current case we are not considering the influence of potentials other than Coulomb's, the phase shift with respect to the analytical regular Coulomb function should be identically zero. Immediately above threshold, the phase shift is smaller than 10^{-4} rad for all four values

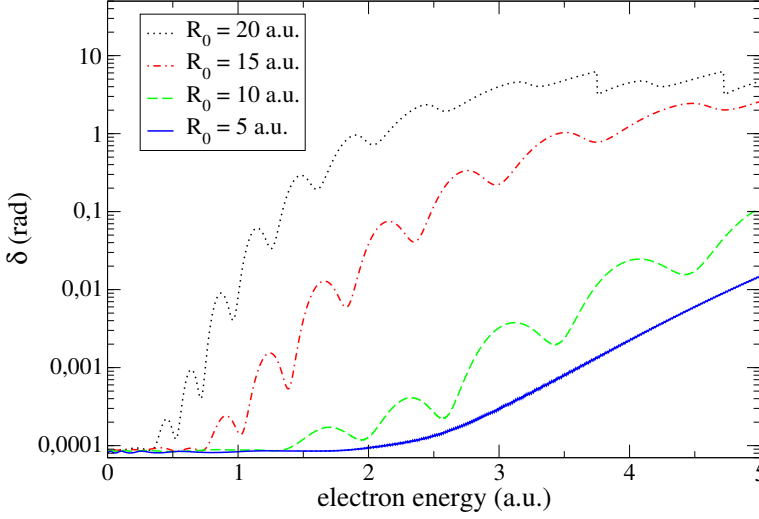


Figure 6.3: Phase shift of the numerical scattering states ψ_{sE} , computed with GABS ($R_{\text{box}} = 500$ a.u., $\ell_{\text{max}} = 20$), for several values of R_0 : 5 a.u. (solid line), 10 a.u. (dashed line), 15 a.u. (dashed-dotted line), and 20 a.u. (dots).

of R_0 . For the smallest value of R_0 , the phase shift remains essentially unaltered up to $E = 2$ a.u., to increase exponentially thereafter as a function of the energy up to $\simeq 10^{-2}$ rad at $E = 5$ a.u.. As soon as the error in the phase shift is of the order of unity, virtually any information on the potential is lost. As R_0 increases, the energy at which the phase-shift error starts blowing up decreases. Fig. 6.4 quantifies approximately the maximum energy that can be represented as a function of the value of R_0 , for a given constraint on the maximum error on the phase shift. As the figure illustrates, the maximum reliable energy value decreases linearly with R_0 . Finally, Fig. 6.5 illustrates the impact of the ℓ_{max} parameter on the asymptotic phase shift of the continuum wave functions. For $R_0 = 10$ a.u., a large ℓ_{max} value is essential to achieve a good function quality up to 5 a.u.. Reducing ℓ_{max} to 2 dramatically deteriorates the accuracy in this energy interval. For the smaller radius $R_0 = 5$ a.u., on the other hand, either values of ℓ_{max} lead to an accuracy comparable to that obtained for $R_0 = 10$ a.u. with $\ell_{\text{max}} = 20$.

6.5 RADIATIVE TRANSITIONS

Beyond energy, the other observable needed to describe the time-evolution of a system under the influence of external fields is the dipole operator. It is essential, therefore, to assess the accuracy of the dipole matrix elements in the hybrid basis.

In Table 6.3 we compare the analytical reduced matrix elements $|\langle \psi \| p_1 \| \psi' \rangle|$ for a few selected dipole transitions between bound hydrogenic states with those

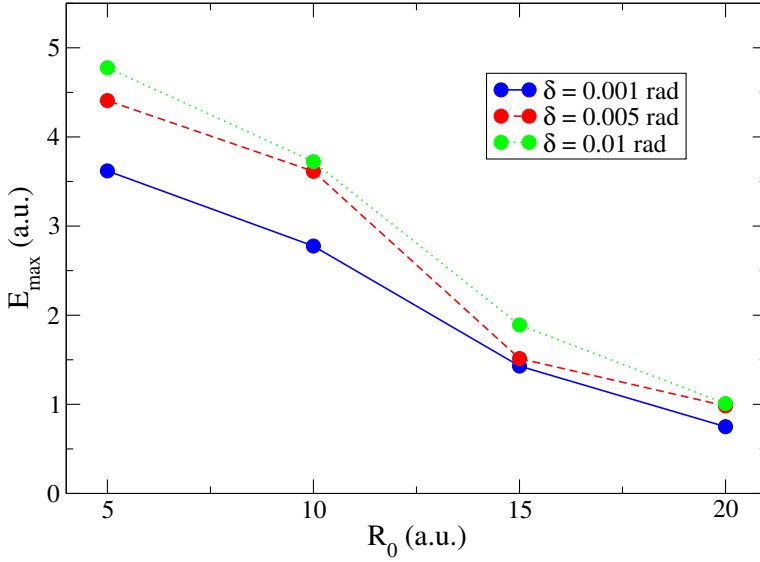


Figure 6.4: Orientative maximum representable energies as a function on R_0 , for three phase shift tolerances. The lines serve the only purpose of guiding the eye.

obtained numerically with B-splines, with GABS functions in the three gauges of length, velocity and acceleration, as well as, in velocity gauge, for two additional representative pairs of the ℓ_{\max} and R_0 parameters. The transitions matrix elements computed with the B-splines are exact for all six tabulated decimal digits. In the case of the GABS basis, the $s - p$ transitions are generally affected by an error of the order of 10^{-5} a.u. for all three gauges, which is ascribable to the cusp representation problem mentioned in the last section. Indeed, the numerical $p - d$ and $d - f$ transitions are in agreement with the analytical results within one part in a million. Finally, the last column shows that the accuracy of the bound-bound transition matrix elements is preserved even employing a much smaller value for ℓ_{\max} . Since the representation of Rydberg states is expected to be at least as accurate as that of the continuum states immediately above the threshold opening, this observation is in agreement with the small value of the phase shift close to threshold reported in Fig. 6.5 for all the three choices of R_0 and ℓ_{\max} .

In Fig. 6.6 we compare the absolute value of some selected bound-continuum reduced dipole matrix elements in velocity gauge, obtained using the GABS basis, with the analytical results (see App. E). The agreement is generally very good, with errors of the order of one part in ten thousands up to $E = 2$ a.u.. At low energies, the largest errors arise when s orbitals are involved, while for the $p - d$ transitions the errors is smaller than one part in a million up to $E = 1$ a.u. With the current choice of parameters, the error in the matrix element starts to increase progressively above $E = 2$ a.u., reaching the level of a few percent for $E = 5$ a.u.. The agreement between the dipole matrix elements in length, velocity and

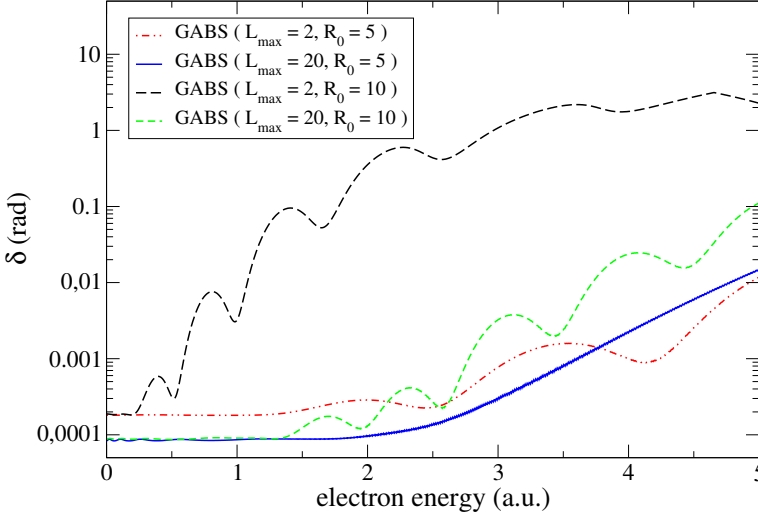


Figure 6.5: Phase shift of the numerical scattering states ψ_{sE} computed with four different sets of GABS parameters.

acceleration gauge is illustrated in the representative case of the transition from the $1s$ orbital in Fig. 6.7. The relative difference between gauges is comparable to or smaller than the relative error of the velocity results with respect to the analytical value (see Fig. 6.8). This means that the gauge agreement is consistently preserved in the whole energy range examined here.

As in the case of the phase shift, the accuracy of the bound-continuum dipole matrix elements depends crucially on the parameters of the basis (see Fig. 6.8). For $R_0 = 10$ a.u., few monomial exponents ($\ell_{\max} = 2$) are sufficient to attain acceptable accuracy up to 1 a.u.. Larger monomial expansions, however, are essential to achieve good accuracy at larger energies. With $\ell_{\max} = 20$, the transition matrix elements with the larger Gaussian box have the same accuracy as those obtained with $R_0 = 5$ a.u., and an absolute error below 1% up to 4 a.u..

In the dipole matrix elements examined so far, at least one of the wave functions is localized near the origin. To be able to represent multi-photon transitions and non-perturbative effects, however, accurate continuum-continuum matrix elements are needed as well. In Fig. 6.9 we compare the analytical results for $|\langle \psi_{\ell E} \| p_1 \| \psi_{\ell' E'} \rangle|$ taken from the literature [141] with those obtained numerically using the GABS basis in the length, velocity and acceleration gauges for three representative initial discretized-continuum states with $E \simeq 1, 2$, and 3 a.u.

A few comments are in order. First, since the integration domain of the numerical transition integrals is limited to the box, the length and the velocity gauge agree with each other but differ qualitatively from the acceleration matrix element. On the other hand, the latter gauge, which has a fast decreasing kernel, is

Table 6.3: Several bound-bound radiative transitions obtained via the analytical formula, using the B-splines basis and the GABS bases.

Trans.	Analyt.	B-splines	GABS ₁ ^a			GABS ₂ ^b	GABS ₃ ^c
			Len	Vel	Acc	Vel	Vel
1s-2p	0.483850	0.483850	0.483859	0.483855	0.483852	0.483860	0.483860
2s-3p	0.212834	0.212834	0.212847	0.212844	0.212843	0.212855	0.212855
3s-4p	0.132935	0.132935	0.132946	0.132943	0.132945	0.132952	0.132952
2p-3d	0.466297	0.466297	0.466297	0.466297	0.466297	0.466297	0.466297
3p-4d	0.260048	0.260048	0.260048	0.260048	0.260048	0.260048	0.260048
3d-4f	0.430680	0.430680	0.430680	0.430680	0.430680	*	*

^a $\ell_{max} = 20$ and $R_0 = 10$.^b $\ell_{max} = 2$ and $R_0 = 5$.^c $\ell_{max} = 2$ and $R_0 = 10$.

in excellent agreement with the analytical result. Furthermore, while in length and velocity gauge the matrix elements oscillate wildly with respect to either continuum-energy indexes, the matrix element in the acceleration gauge, a part for the characteristic peak *on-shell*, is everywhere a smooth function of the energy index. The discrepancy between length and velocity, on the one side, and acceleration, on the other side, is readily explained: we are neglecting the contribution to the integral of the part of the wave function outside the quantization box (see App. C and D). Indeed, the oscillations in, say, the velocity gauge matrix element can be shown to depend on the size of the quantization box. In fact, as the size of the box is increased, the velocity matrix elements are expected to converge weakly to the acceleration value (i.e., their integrals with any smooth test functions converge to the same value as $R_{\text{box}} \rightarrow \infty$). The acceleration gauge does not suffer from this dependence thanks to the fact that its kernel decreases rapidly with the electronic radius. The three gauges can thus be reconciled by estimating analytically the contribution to the length and velocity matrix elements coming from the region outside the quantization box (see App. D). This is what we have done in Fig. 6.10 for the illustrative case of the velocity gauge. As the picture shows, the outer contribution to the matrix elements, which is actually calculated in length gauge and converted to velocity gauge afterwards (see App. D), exactly cancels the original fast oscillations, leading to a matrix element that is a smooth function of one of the continuous energy indexes, in excellent agreement with the analytical result. The residual small discrepancies still visible in the plot are due to the approximations made in the analytical estimate of the outer contribution to the transition integral.

In conclusion, all the principal field-free and perturbative one-photon observables for the hydrogen atom can be reproduced with very high accuracy in a

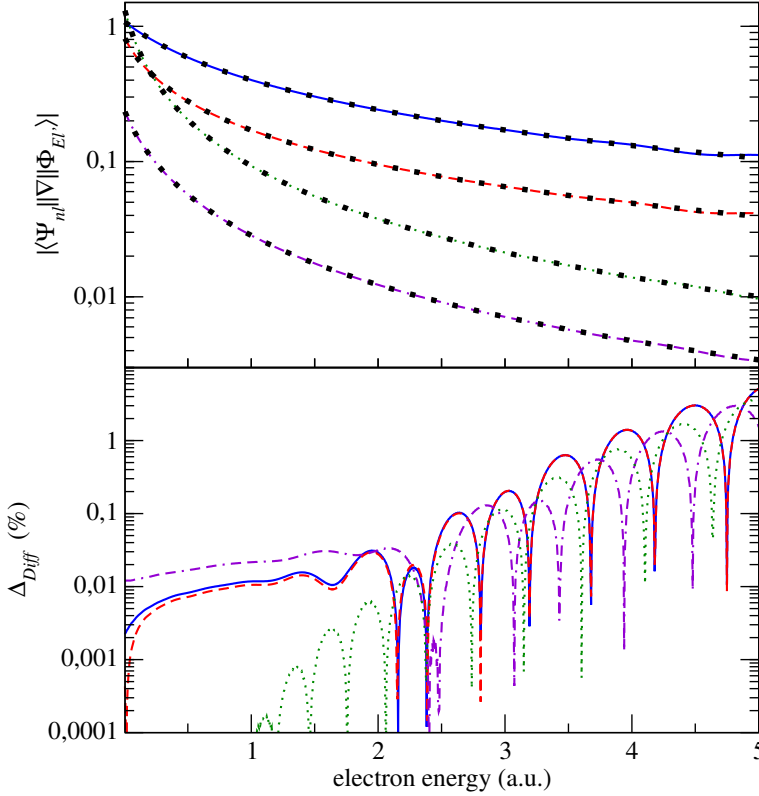


Figure 6.6: Top panel: absolute value of selected reduced dipole transition matrix elements in velocity gauge computed using the GABS basis and compared with the corresponding analytical results (full squares). Bottom panel: relative percent deviation between numerical and analytical results. The following transitions are shown: $1s - \epsilon_p$ (solid line), $2s - \epsilon_p$ (dashed line), $2p - \epsilon_s$ (dash-dotted line), $2p - \epsilon_d$ (dotted line).

wide energy range with a hybrid basis in which the wave function is represented in a radial region as large as 10 a.u. in terms of Gaussian functions alone.

It is worth stressing here that, as shown in [142], inclusion of the contribution from outside the box is essential to correctly evaluate above-threshold multi-photon ionization cross sections in length and velocity gauges in the framework of perturbation theory. This is so because, at a given photon energy, perturbation theory requires the evaluation of only those continuum-continuum dipole matrix elements that involve the electron continuum state compatible with that photon energy. In contrast, when seeking for solutions of the TDSE, inclusion of the contributions from outside the box is not necessary provided that all continuum-continuum matrix elements are consistently evaluated in the same box and the electronic wave packet does not reach the boundaries of the box before projection onto physical eigenstates is performed (see also the discussion in [143]). Thus, in the following section, where results from solving the TDSE are presented, the

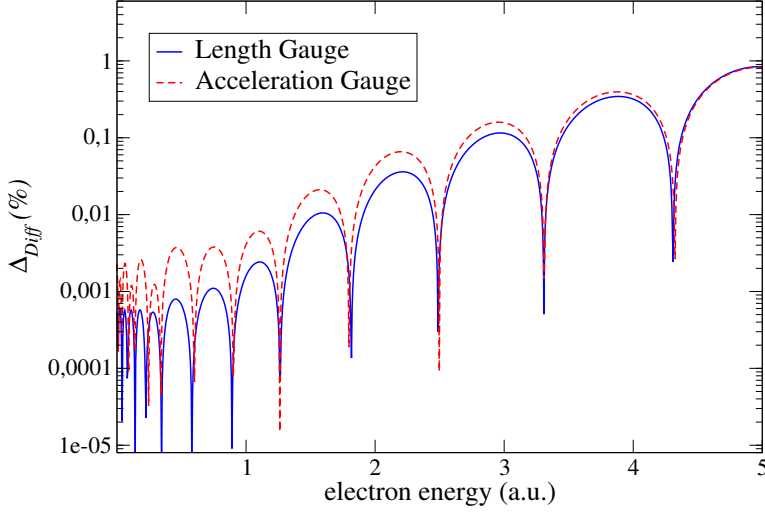


Figure 6.7: Relative percent deviation of $|(E - E_{1s})\langle\psi_{E_p}|\mathcal{O}_1^{(l)}|\psi_{1s}\rangle|$ and $|(E - E_{1s})^{-1}\langle\psi_{E_p}|\mathcal{O}_1^{(a)}|\psi_{1s}\rangle|$ from $|\langle\psi_{E_p}|\mathcal{O}_1^{(v)}|\psi_{1s}\rangle|$ (solid line and dashed line, respectively), computed with a GABS basis using $R_0 = 500$ a.u., $\ell_{\max} = 20$.

continuum-continuum dipole matrix elements will not include the corrections from outside the box.

6.6 TIME-DEPENDENT RESULTS

The ultimate test of the viability of the GABS basis for the description of laser-driven processes is to use it to reproduce fully differential photoelectron observables in non-perturbative conditions by solving the TDSE numerically. In this section, we examine the photoelectron distribution for the above-threshold ionization (ATI) [144] of the hydrogen atom from the ground state under the influence of single, intense, comparatively long ultraviolet pulses,

$$\text{H}(1s) + n\gamma_{\text{UV}} \rightarrow \text{H}^+ + e_k^-, \quad (6.27)$$

for which recent independent data to compare with are available. The methodology used to solve numerically the TDSE and to extract the asymptotic differential photoelectron observables at the end of the interaction was described in Sec. 6.3. We conduct the simulation using a purely B-spline basis, which is known to provide good reference results [145], as well as a GABS basis, with $R_0 = 10$ a.u. and $\ell_{\max} = 20$. For both basis, the angular expansion of the wave function is truncated at $\ell \leq 10$. To assess the accuracy of the solution, we use the same laser parameters employed in two recent works, one by Rodríguez *et al.* [146] ($\omega = 0.35$ a.u., $I = 1.4 \cdot 10^{13} \text{W/cm}^2$, 30-cycle \cos^2 -envelope electric laser pulse) and the other

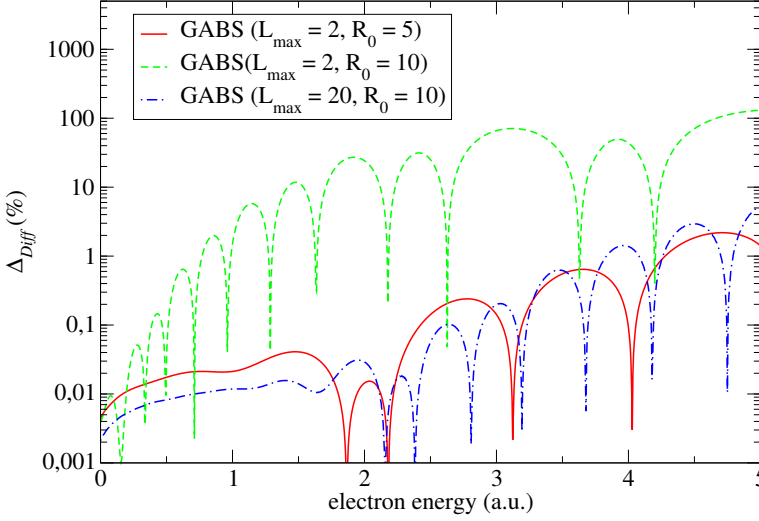


Figure 6.8: Relative percent deviation from the analytical result of the dipole transition matrix element in velocity gauge between the hydrogen ground state and the continuum, $\langle \psi_{E_p} \| \mathcal{O}_1^{(v)} \| \psi_{1s} \rangle$, computed with three representative GABS basis.

one by Grum-Grzhimailo *et al.* [147] ($\omega = 0.114$ a.u., $I = 10^{14}$ W/cm², 20-cycle \cos^2 -envelope electric laser pulse). It should be noted that we conduct the simulation in velocity gauge starting from the definition of the external vector potential as

$$\vec{A}(t) = \hat{z} A_0 \cos^2 \left(\frac{\pi t}{\tau} \right) \cos(\omega t + \varphi) \theta(\tau/2 - |t|), \quad (6.28)$$

where φ is the carrier-envelope phase (CEP), τ is the pulse duration (twice the full width at half maximum of the intensity profile), and $\theta(x)$ is the Heaviside step function. This way, the external electric field, given by $\vec{E} = -c^{-1} \partial_t \vec{A}(t)$, automatically integrates to zero, as it should [148]. On the other hand, in [146] a parametrization for the electric field similar to (6.28) is used instead,

$$\vec{E}(t) = \hat{z} E_0 \cos^2 \left(\frac{\pi t}{\tau} \right) \sin(\omega t) \theta(\tau/2 - |t|). \quad (6.29)$$

This latter expression differs from the one that can be derived from our definition (6.28) of the vector potential, due to the time-dependence of the pulse envelope. Furthermore, Eq. (6.29) is applicable in principle only for zero CEP, since the field must integrate to zero [148]. Having said that, for long pulses such as those considered in this and their work (20-30 cycles), the difference between the two parameterizations is negligible and affects only minor details of the photoelectron spectra.

SHORT WAVELENGTH In our first simulation, which reproduces the results by Rodríguez *et al.*, the laser angular frequency is $\omega = 0.35$ a.u.. Fig. 6.11 compares

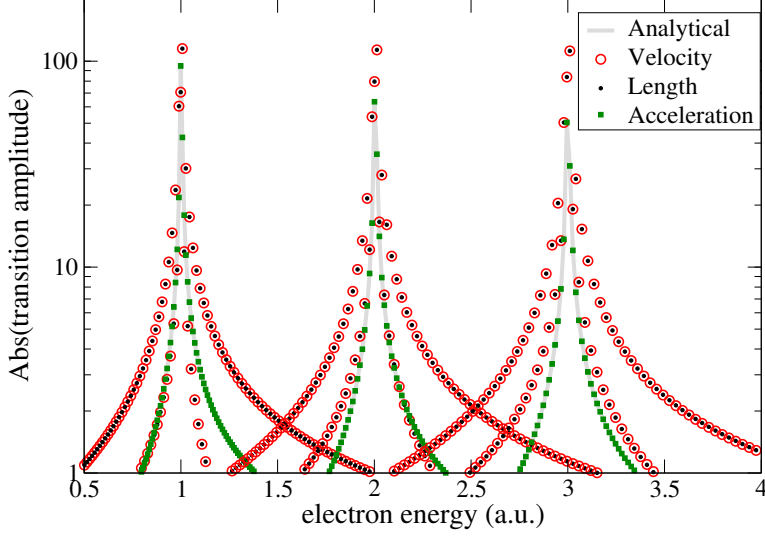


Figure 6.9: Absolute value of the reduced transition matrix elements $(E_p - E_s)\langle\psi_{E_p}|\mathcal{O}_1^l|\psi_{E_s}\rangle$ (dotted line), $\langle\psi_{E_p}|\mathcal{O}_1^v|\psi_{E_s}\rangle$ (solid line), $(E_p - E_s)^{-1}\langle\psi_{E_p}|\mathcal{O}_1^a|\psi_{E_s}\rangle$ (dashed line), computed with GABS for several scattering states by truncating the radial integral at R_{box} . Three representative energies for the s state are shown: 1 a.u. (first peak), 2 a.u. (second peak), and 3 a.u. (third peak). The numerical results are compared with the exact analytical result in velocity gauge (full squares). For the quantization box considered, the acceleration gauge has already converged to the analytical results. On the other hand, the truncated length and the velocity matrix element are in excellent agreement with each other but differ from the analytical results for a rapidly oscillating term, which results from the neglected contribution to the exact transition integral that comes from the radial region beyond the box radius.

the ATI spectra obtained using GABS and B-splines with the corresponding quantity digitized from [146].

The spectra obtained with GABS and B-splines are in excellent agreement down to the tiniest detail, indicating that the solution of the TDSE is accurate. The main peaks are in excellent agreement also with the results from the literature. Minor departures between the current prediction and the literature are visible only in the background signal, which is six orders of magnitude smaller than the dominant peak signal. We attribute these discrepancies to the different parameterizations (6.28,6.29) of the external pulse employed in the two simulations. As anticipated, these differences are entirely negligible to all practical purposes. At least two photons are needed to ionize the atom, with the first excitation step being close to the $1s - 2p$ resonance. As a consequence, the ATI process is resonantly enhanced, resulting in secondary peaks in the ATI spectrum, as discussed in [146]. In particular, the first shoulder that is visible at $E = 0.225$ a.u., on the upper-energy side of the first ATI peak, and the two peaks at $E \simeq 0.29$ a.u. and $E \simeq 0.32$ a.u. are due to the components of the two-photon transition that are resonant with the $2p$, $3p$ and $4p$ states, respectively. This can be realized by looking

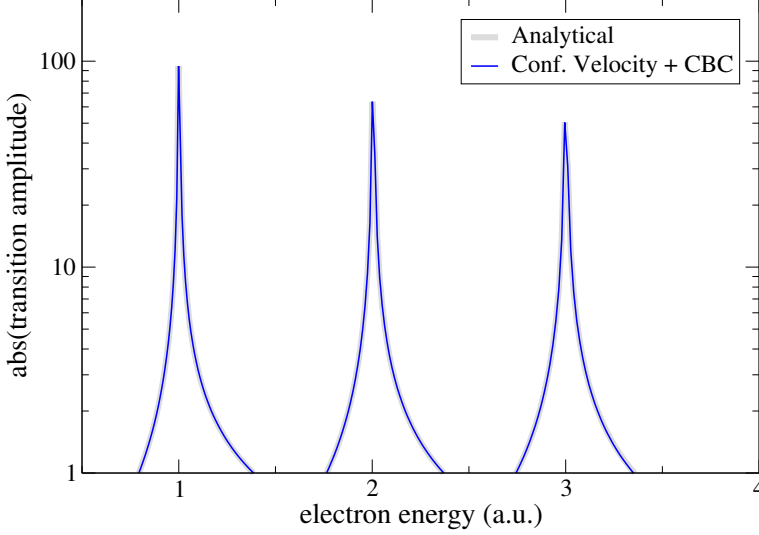


Figure 6.10: Absolute value of the reduced velocity-gauge hydrogen dipole matrix element $\langle \psi_{E_p} | \mathcal{O}_1^v | \psi_{E_s} \rangle$ from three s scattering states ($E = 1, 2, 3$ a.u.) to several p scattering states evaluated as the sum of two contributions (thin solid line): the first contribution is the numerical radial integral shown in Fig. 6.9, which is computed with the GABS basis and truncated at R_{box} , and the second contribution is the confined boundary correction (CBC) term derived in App. C. The agreement between the numerical result and the exact analytical result (thick solid line) is excellent.

at the finite-pulse version of the lowest-order two-photon transition amplitude for this process

$$\mathcal{A}_{E\ell \leftarrow 1s}^{(2)} = -i \int d\omega \tilde{F}(-\omega) \tilde{F}(E_{1s} + \omega - E) \times \langle E\ell | \mathcal{O} G_0^+(E_{1s} + \omega) \mathcal{O} | 1s \rangle, \quad (6.30)$$

where

$$\tilde{F}(\omega) = \mathcal{F}[F](\omega) = \frac{1}{\sqrt{2\pi}} \int dt F(t) e^{-i\omega t}, \quad (6.31)$$

\mathcal{O} is the transition operator in either the length or the velocity gauge, and $F(t)$ the corresponding $E(t)$ or $\alpha A(t)$ fields. Eq. (6.30) is valid for non-resonant as well as for resonant transitions (in contrast to the equivalent expression for monochromatic fields), provided that Rabi oscillations, ac-Stark shifts and depletion of the ground state population can be neglected. In the present case, the laser central frequency $\omega = 0.35$ a.u. is detuned with respect to the $1s - 2p$ transition by $\delta = \omega - \omega_{2p1s} = -0.025$ a.u. (we introduce the notation $\omega_{ij} = E_i - E_j$). At peak intensity F_0 , the variation of the ground-state population ΔP_{1s} due to Rabi oscillations is $\Delta P_{1s} = [1 + (\delta/\Omega_0)^2]^{-1} = 0.26$, where $\Omega_0 = |F_0 \mathcal{O}_{2p,1s}| \simeq 0.015$ a.u. Therefore, the system remains mostly in the ground state; hence, Eq. (6.30) is expected to provide meaningful guidance for a qualitative interpretation of the first group of peaks in the ATI spectrum. Quantitative predictions, of course,

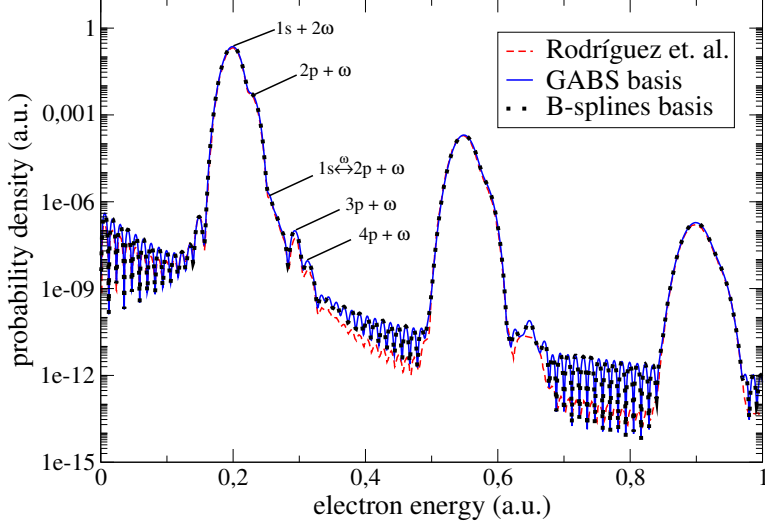


Figure 6.11: ATI photoelectron spectrum from hydrogen ground state due to a 30-cycle \cos^2 laser pulse with $\omega = 0.35$ a.u. and $I = 14 \text{ TW/cm}^2$. The present results, computed by solving the TDSE using either a purely B-spline basis (dots) or the GABS basis (solid line), are compared with the spectrum obtained under similar conditions by Rodríguez *et al.* [146]. See text for more details.

require a separate numerical solution of the TDSE for at least the $1s$ and the np essential states [146]. Indeed, the population transfer between the $1s$ and the $2p$ state is small but not negligible. Furthermore, the effective Rabi period $T_\Omega = 2\pi / \sqrt{\delta^2 + \Omega_0^2}$, which is strongly modulated across the laser pulse, is comparable to the duration of the pulse itself. As a consequence, the amplitude of the $2p$ state undergoes a sharp isolated variation which manifests in the spectrum as a broad feature around the resonant $2p$ peak, rather than in the form of the Autler-Townes doublet that characterizes complete Rabi oscillations.

Keeping in mind these caveats, let us go back to Eq. (6.30). To disentangle the resonant component from the non-resonant one, we split the retarded resolvent in an off-shell part G_0^P and an on-shell part,

$$\begin{aligned} G_0^+(\omega) &= G_0^P(\omega) - i\pi\delta(\omega - H_0), \\ G_0^P(\omega) &= \frac{P}{\omega - H_0}. \end{aligned} \quad (6.32)$$

The two-photon transition amplitude (6.30) then splits into a corresponding principal-value term $\mathcal{A}_{E \leftarrow 1s}^{(2,P)}$ and an on-shell term $\mathcal{A}_{E \leftarrow 1s}^{(2,r)}$,

$$\mathcal{A}_{E \leftarrow 1s}^{(2)} = \mathcal{A}_{E \leftarrow 1s}^{(2,P)} + \mathcal{A}_{E \leftarrow 1s}^{(2,r)}. \quad (6.33)$$

The principal-value component of the transition amplitude,

$$\mathcal{A}_{E\ell\leftarrow 1s}^{(2,P)} = -i \int d\omega \tilde{F}(-\omega) \tilde{F}(E_{1s} + \omega - E) \times \\ \times \langle E\ell | \mathcal{O} G_0^P(E_{1s} + \omega) \mathcal{O} | 1s \rangle, \quad (6.34)$$

is responsible for the main peak in Fig. 6.11, at $E = 0.2$ a.u.. This is obvious for the contribution of the virtual states, i.e., those $|\epsilon p\rangle$ states in the expansion of $G_0^P(E_{1s} + \omega)$ whose energy ϵ is far from $E_{1s} + \omega_0$, where ω_0 is the central angular frequency of the pulse,

$$P \int d\omega \tilde{F}(-\omega) \tilde{F}(E_{1s} + \omega - E) \frac{\mathcal{O}_{E\ell,\epsilon p} \mathcal{O}_{\epsilon p,1s}}{E_{1s} + \omega - \epsilon} \simeq \\ \simeq \frac{\mathcal{O}_{E\ell,\epsilon p} \mathcal{O}_{\epsilon p,1s}}{E_{1s} + \omega_0 - \epsilon} \int d\omega \tilde{F}(-\omega) \tilde{F}(E_{1s} + \omega - E) = \\ = \frac{\mathcal{O}_{E\ell,\epsilon p} \mathcal{O}_{\epsilon p,1s}}{E_{1s} + \omega_0 - \epsilon} \sqrt{2\pi} \mathcal{F}[F^2](E_{1s} - E). \quad (6.35)$$

Though less evident, the same is true for the asymmetric principal-value contribution of the non-virtual excitations. Numerical tests show that the characteristic positions and widths of the latter are comparable to those of the virtual contributions.

The picture qualitatively changes for the on-shell contribution to the transition amplitude $\mathcal{A}_{E\ell\leftarrow 1s}^{(2,r)}$. Each term in the eigenstate expansion of this component is simply half the product between the first-order transition amplitudes $\mathcal{A}_{j\leftarrow i}^{(1)}$ to go (i) from the ground $1s$ state to the resonant np state and (ii) from the resonant np state to the final state in the continuum,

$$\mathcal{A}_{E\ell\leftarrow 1s}^{(2,r)} = -\pi \sum_n \mathcal{O}_{E,np} \mathcal{O}_{np,1s} \tilde{F}(\omega_{1snp}) \tilde{F}(\omega_{npE\ell}) = \\ = \frac{1}{2} \sum_n \mathcal{A}_{E\ell\leftarrow np}^{(1)} \cdot \mathcal{A}_{np\leftarrow 1s}^{(1)} \quad (6.36)$$

where

$$\mathcal{A}_{fi}^{(1)} = -i\sqrt{2\pi} \tilde{F}(\omega_{if}) \mathcal{O}_{fi}. \quad (6.37)$$

The on-shell part of the two-photon transition amplitude is responsible for the shoulder at $E = 0.225$ a.u. and for the peaks at $E \simeq 0.29$ a.u. and $E \simeq 0.32$ a.u., which correspond to the $2p$, $3p$ and $4p$ resonant states, respectively. Notice that the amplitudes of these peaks have the characteristic $\mathcal{F}[F](E_{np} - E)$ profile of one-photon transitions; in particular, they are narrower than the non-resonant two-photon peak amplitude, which is instead proportional to $\mathcal{F}[F^2](E_{1s} - E)$, i.e., to the Fourier transform of a temporally compressed pulse. Finally, the second shoulder, starting at $E \simeq 0.25$ a.u., is the incipient signature of the wide feature with which the non-perturbative $1s - 2p$ transition, mentioned earlier in this section, manifests in the spectrum.

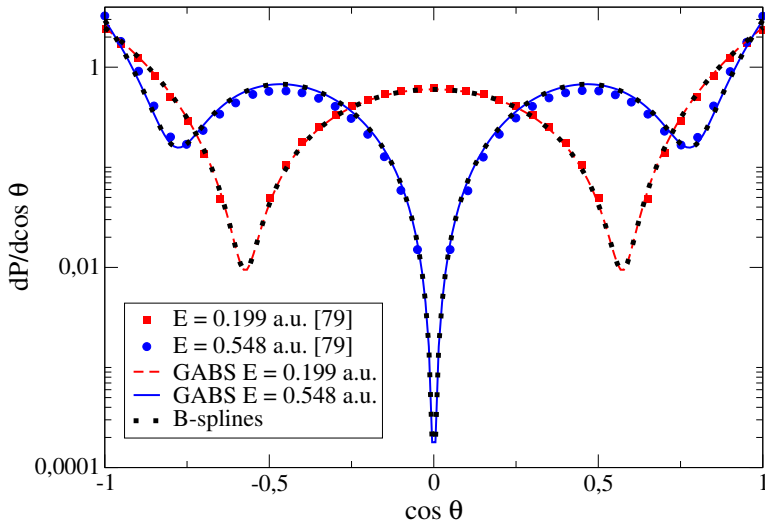


Figure 6.12: Normalized photoelectron angular distribution corresponding to the 1st and 2nd ATI peaks in Fig. 6.13(a), computed here by solving the TDSE in either a B-spline or a GABS basis, and compared to the results obtained by Rodríguez *et al.* [146] in similar conditions.

In Fig. 6.12 we compare the angular distribution of the electrons in the region of the first and second ATI peaks with those reported by Rodríguez.

Again, the agreement between the two calculations is excellent, confirming the accuracy of the observables obtained with the hybrid GABS basis. As expected, the angular distribution has a lobe structure consistent with a complex linear combination of $s + d$ amplitudes, for the first ATI peak, and $p + f$ amplitudes, for the second ATI peak. In both cases, the two amplitudes are neither in phase nor in anti-phase, hence the lack of proper nodes in the spectrum, except, in principle, for $\theta = 90^\circ$ for the second ATI peak (even in this case, though, interference from the long-range tail of the nearby ATI peaks prevents the photoelectron distribution to attain zero).

To gain further insight in the angular distribution, we show in Fig. 6.13(a) the doubly-differential photoelectron spectrum as a function of both the electron energy and the cosine of the ejection angle. To the best of our knowledge, such fully differential representation of the photoelectron distribution has not been reported before. Rodríguez's 2D differential distribution.

While the regions corresponding to the ATI peaks visible in Fig. 6.13(a) have approximately a uniform lobe structure (three, four and five maxima for the two-, three- and four-photon peaks, respectively), at a closer inspection of the fully differential plot, three additional aspects emerge. First, the ATI peaks along the polarization axis ($\cos \theta = \pm 1$) are slightly shifted to lower energies with respect to the photoelectrons ejected orthogonal to the field polarization ($\cos \theta = 0$). Sec-

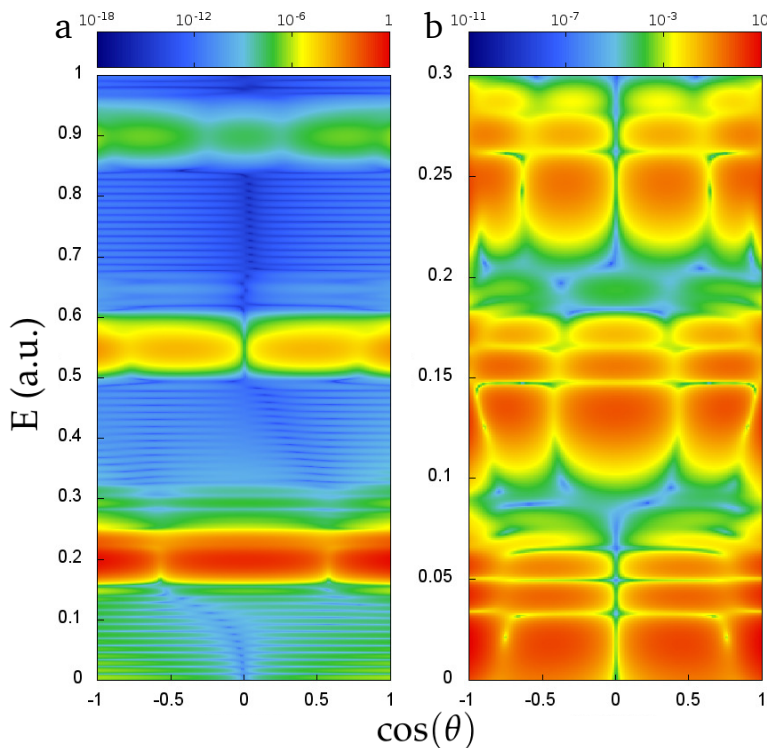


Figure 6.13: Doubly differential photoelectron distribution $d^2P/dE d\cos\theta$ for the process described in Fig. 6.11 (left panel) and Fig. 6.15 (right panel).

ond, the characteristic three-maxima angular distribution associated to the first group of peaks is slightly more pronounced for the dominant peak ($E \simeq 0.2$ a.u.) than for the two shoulders associated to the resonant $1s \rightarrow 2p \rightarrow E\ell$ transition ($E \simeq 0.225$ a.u. and 0.27 a.u.). Third, the three-maxima structure in the first group of peaks is interrupted in a narrow interval around $E \simeq 0.25$ a.u. where the two dips are less pronounced. As it turns out, this is because the energy $E = 0.25$ a.u. coincides with the position of the first side peak of $\mathcal{F}[F^2](E_{1s} - E)$ (cmp. Eq. (6.35)). The presence of secondary peaks is a typical characteristics of the Fourier transform of any pulse with a compact support; the symmetric counterpart is clearly visible at $E = 0.15$ a.u.. The side peak amplitude is in anti-phase with respect to that of the dominant peak. As a consequence, when interfering with the resonant component, it cancels part of the angular modulation, resulting in a more isotropic distribution. This peculiar phenomenon, which would not be visible if the external pulse had, say, a Gaussian envelope, illustrates well how special care is needed when assigning spectra generated using pulses that have a structured Fourier transform to start with.

The change of the angular distribution with energy is highlighted in Fig. 6.14 where we plot the normalized photoelectron angular distribution at six rep-

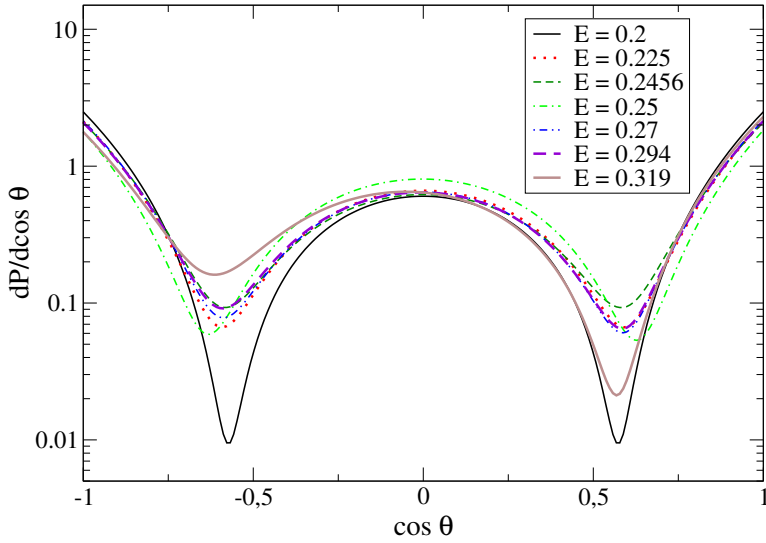


Figure 6.14: Normalized photoelectron angular distribution for several selected energies in Fig. 6.13(a). The energies 0.225, 0.294 and 0.319 a.u. correspond to the $2p$, $3p$ and $4p$ resonances respectively.

representative energies, $E = 0.2$ a.u (main peak of the non-resonant transition), $E = 0.225$ a.u. ($2p$ resonant peak), $E = 0.2456$ a.u. (side peak of the non-resonant transition, which corresponds to the least pronounced dips in the spectrum), $E = 0.25$ a.u. (intermediate energy at which the dips are pushed towards smaller angles from the polarization axis), $E = 0.27$ a.u. (second shoulder, presumably associated to the non-perturbative $2p$ resonant transition), $E = 0.294$ a.u. and $E = 0.319$ a.u. ($3p$ and $4p$ resonant peaks, respectively). Notice that, starting from $E \simeq 0.27$ a.u., the symmetry of the photoelectron distribution is progressively broken. This is more dramatic for the weakest peak, the one corresponding to the resonant $3p$ transition, for which the maxima in the upward direction is higher than that in the downward direction, while the opposite is true for the two minima. This behavior is most likely due to the interference between the weak resonant two photon amplitude and the tail of the non-resonant three-photon amplitude, which have opposite parity [149].

LONG WAVELENGTH As a second example, we test our simulations against the results reported by Grum-Grzhimailo *et al.* [147] for ionization with a 20-cycle pulse with angular frequency $\omega = 0.114$ a.u. and peak intensity $I = 10^{14}$ W/cm². In this case, five photons are needed to achieve ionization. As Fig. 6.15 shows, the agreement between the data digitized from [147] and the present calculations with GABS and the purely B-spline basis is again excellent. The photoelectron peaks obtained with either of the two latter basis are actually slightly shifted to lower energies with respect to those reported in [147]. Since a similar shift in the position of the peaks for high-intensity pulses was already observed in [147] as a

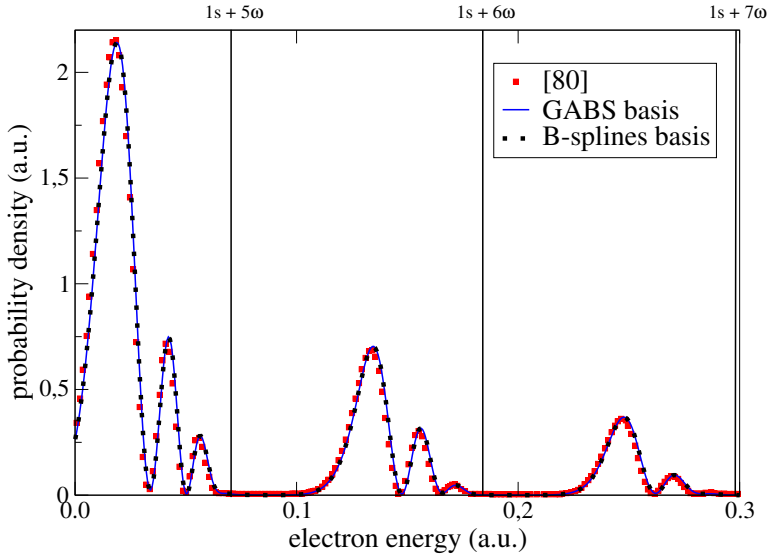


Figure 6.15: ATI photoelectron spectrum from hydrogen ground state due to a 20-cycle \cos^2 laser pulse with $\omega = 0.114$ a.u. and $I = 0.1$ PW/cm². The present results, computed by solving the TDSE using either a purely B-spline basis (black dots) or the GABS basis (solid line), are compared with the spectrum obtained under similar conditions by Grum-Grzhimailo *et al.* [147] (light full squares). See text for more details.

consequence of changing the field parameterization from Eq. (6.28) to Eq. (6.29), we assume that the shift we observe here is due to a similar effect.

The most striking features of the spectrum shown in Fig. 6.15 are: (i) the multi-peak structure of each n -photons ATI signal and (ii) the fact that the position of the dominant peak in each group is shifted to lower energies by as much as 0.07 a.u. with respect to the nominal values $n\omega_{UV} - E_0$, the latter value rather approaching the upper limit of each peak subgroup. This phenomenon was first observed around 30 years ago by Bardsley *et al.* [150] and the mechanism at its basis was identified and described by several authors shortly thereafter [151, 152, 153]. Since essentially the same phenomenon has recently received renewed interest, in association with the use of intense ultra-short extreme ultraviolet pulses [154], in the following we briefly summarize the rationale of the underlying mechanism and contextualize our results with reference to the original [153] and latest [154] works on the subject. When a discrete state ψ interacts with a moderately intense laser pulse, and as long as the laser does not resonantly couple ψ to other discrete states, the energy of ψ (i.e., the cycle-averaged rate of its phase modulation) changes by a quantity ΔE_{ψ}^{ac} called ac-Stark shift. For a monochromatic field with amplitude E_0 and angular frequency ω , the ac-Stark shift ΔE_{1s}^{ac} of the ground state

of hydrogen is given, to the lowest order of perturbation theory, by the solution to the following equation

$$\Delta E_{1s}^{ac} = \frac{E_0^2}{4} \mathcal{M}_{1s1s}(E_{1s} + \Delta E_{1s}^{ac}, \omega), \quad (6.38)$$

where

$$\mathcal{M}_{ii}(E, \omega) = \langle i | z \left[G_0^+(E + \omega) + G_0^+(E - \omega) \right] z | i \rangle. \quad (6.39)$$

The ac-Stark shift of the ground state can thus be either positive or negative depending on whether ω is, respectively, smaller or larger than the excitation energies ω_{ep1s} to the group of (discrete or continuum) $|\epsilon p\rangle$ states that are most strongly coupled to the ground state. The energy of the states in the continuum is affected by the ac-Stark effect as well. In this case, the ac-Stark shift is approximated reasonably well by the ponderomotive energy $\Delta E_{E\ell}^{ac} \simeq U_p = E_0^2/4\omega^2$, a positive quantity. Now, a careful treatment of time-dependent perturbation theory (see, e.g., Chap. 3 in [155]) shows that, in the absence of intermediate resonant states, the absorption of n photons γ_ω from an initial state $|i\rangle$ to populate a final state $|f\rangle$ takes place provided that the ac-Stark shifted energies of the two dressed states differ by $n\omega$, $\tilde{E}_f = \tilde{E}_i + n\omega$. In the case of ionization of atomic hydrogen from the ground state, this means that the field-free energy E of the final continuum state $|E\ell\rangle$ populated by the absorption of n photons is approximately given by

$$E \simeq E_{1s} + n\omega + \Delta E_{1s}^{ac} - U_p. \quad (6.40)$$

This last equation is justified on the assumption that, when the external field switches off, the population of a dressed state follows the state adiabatically. Incidentally, such assumption is not justified if the photoelectron leaves the laser focus before the pulse is over. In this latter case, the electron is accelerated by the gradient of the ponderomotive potential that is present along the cross section of the laser beam, thus acquiring the dressing energy once and for all, instead of returning it to the field. When the light that dresses the system and induces the multi-photon transition comes in the form of a short pulse, the amplitude E_0 of the electric field associated to it changes with time, $E_0 = E_0(t)$,

$$\vec{E}(t) = \hat{e} E_0(t) \sin(\omega t + \phi(t)). \quad (6.41)$$

For example, in the case of the parametrisation (6.29) mentioned in the last section, the carrier is modulated by a cosine-square envelope

$$E_0(t) = E_0 \cos^2\left(\frac{\pi t}{\tau}\right) \theta(\tau/2 - |t|). \quad (6.42)$$

In these conditions, the energy E of the final state that is populated by means of the absorption of n photons from the hydrogen ground state changes across the pulse as well,

$$E(t) \simeq E_{1s} + n\omega + \frac{E_0^2(t)}{4} \left[\mathcal{M}_{1s1s}(E_{1s}, \omega) - \frac{1}{\omega^2} \right] \quad (6.43)$$

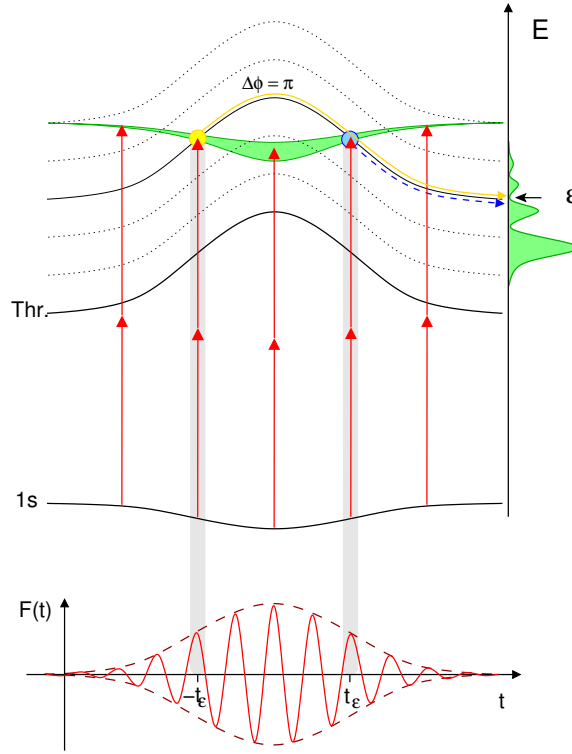


Figure 6.16: Schematic illustration of the dynamic-interference mechanism underlying the appearance of the multi-peak substructure in the non-resonant multi-photon photoelectron signals when an atom is ionized with intense isolated ultra-short pulses. The external pulse induces an ac-Stark shift of the energy levels of the atom. Depending on the value of the time-dependent intensity of the laser, the pulse promotes at different times transitions to laser-dressed states that are adiabatically connected to field-free states with different energies, thus resulting in a global shift of the photoelectron signal. Two temporally separated amplitudes contribute to each final energy. The phase difference acquired by the first amplitude with respect to the second one in the intermediate time lapse can give rise to either constructive or destructive interference thus resulting in a peak or a zero in the photoelectron spectrum, respectively. See text for more details.

(for simplicity, we disregard the dependence of \mathcal{M} on the first energy entry).

This phenomenon is qualitatively illustrated in Fig. (6.16): as the external oscillating field becomes more and more intense, the energy of any state gets shifted by a quantity that follows the laser-intensity profile and which reaches its maximum in correspondence with the peak of the pulse envelope. As the intensity of the pulse decreases again, and eventually vanishes, the energies of the dressed states return to their original field-free value, thus traversing for a second time, in the opposite direction, all the intermediate energies. As a consequence, for a symmetric pulse centered at $t = 0$, the probability amplitude to each possible

final energy ϵ , $\mathcal{A}_{\epsilon \leftarrow 1s}^{(n)}$, receives two contributions: one at a time $-t_\epsilon$ and another one at a time t_ϵ , where $E(t_\epsilon) = \epsilon$ (see Fig. 6.16),

$$\mathcal{A}_{\epsilon \leftarrow 1s}^{(n)} = \mathcal{A}_{\epsilon \leftarrow 1s}^{(n)}(-t_\epsilon) + \mathcal{A}_{\epsilon \leftarrow 1s}^{(n)}(t_\epsilon). \quad (6.44)$$

Indeed, for $t = \pm t_\epsilon$, the n -photon transition from the ground state is resonant with the dressed state that is adiabatically connected to the field-free state with energy ϵ . The two amplitudes $\mathcal{A}_{\epsilon \leftarrow 1s}^{(n)}(\pm t_\epsilon)$ have comparable magnitude, but not the same phase. This is because, in the time interval $\Delta t = 2t_\epsilon$ elapsed from the first transition to the second one, the amplitude of the final excited state acquires an additional phase with respect to the ground state, which is approximately given by $\Delta\phi_\epsilon \simeq 2n\omega t_\epsilon$ (in this latter formula, we made the simplifying assumption that the ac-Stark shifts are small when compared with the total transition energy $n\omega$). The two amplitudes, therefore, will interfere destructively whenever $2n\omega t_\epsilon = (2k+1)\pi$, thus giving rise to a node in the photoelectron spectrum,

$$P_{\epsilon \leftarrow 1s}^{(n)} \simeq 4 \left| \mathcal{A}_{\epsilon \leftarrow 1s}^{(n)}(t_\epsilon) \right|^2 \cos^2(n\omega t_\epsilon). \quad (6.45)$$

The transitions taking place close to the center of the pulse, and which thus lead to the population of the final continuum state whose energy lies farther from the field-free resonant condition, interfere all constructively. As a result, in the photoelectron spectrum we observe a dominant peak at the maximally shifted final energy, accompanied by several other peaks with progressively smaller intensities and whose energy positions approach the value predicted by the field-free resonance condition $E = E_{1s} + n\omega$.

For $\omega = 0.114$ a.u., both terms in parenthesis on the RHS of (6.43) are negative. In our simulation, at peak intensity, the ac-Stark shift of the ground and continuum states have the following approximate values,

$$\Delta E_{1s}^{ac} = -0.003 \text{ a.u.}, \quad U_p = 0.055 \text{ a.u.} \quad (6.46)$$

A closer look at Fig. 6.15 reveals that the displacement of the largest peak with respect to the nominal position in the weak-field limit is $\simeq -0.051$ a.u. for the first groups of signals (five-photon absorption) and $\simeq -0.049$ a.u. for the second one (six-photon absorption). While both values are in qualitative agreement with the prediction $\Delta E_{\max} = \Delta E_{1s}^{ac} - U_p = 0.058$ a.u., a couple of observations are pertinent nonetheless. Firstly, the observed shift changes from one group of peaks to the other. This is not unexpected since the photoionization cross section changes rapidly close to the threshold and the ac-Stark shift of continuum states, which is an order of magnitude larger than the ac-Stark shift of the ground state, may also change significantly in this energy range. In fact, the variation in the energy shift in the continuum is comparable to the ac-Stark shift of the ground state itself. Secondly, due to the short duration of the pulse, the displacement of the maximum in the spectral profile is arguably smaller than the one that would be obtained with a monochromatic laser with the same peak intensity.

The appearance of a peak substructure in the photoelectron signal for the absorption of a fixed number of photons from a short pulse has also been recently observed by Demekhin and Cederbaum [154] in the context of the ionization of the hydrogen atom by an energetic ($\omega \simeq 2$ a.u.) intense pulse ($I = 5 \cdot 10^{15} \text{ W/cm}^2$), in the region of one-photon absorption. In this case, the photoelectron signal gives rise to a group of peaks that are shifted at higher energies with respect to the nominal position of the peak in the weak-field limit, rather than at smaller energies as in the case discussed in this paper. This is because, for $\omega_{\text{UV}} \simeq 2$ a.u., the ac-Stark shift of the ground state is (i) positive and (ii) larger than the ponderomotive shift experienced by the final continuum states.

In Fig. 6.13(b), we report the fully differential photoelectron distribution corresponding to the spectrum shown in Fig. 6.15, computed with the GABS basis.

When compared with the analogous spectrum in Fig. 6.13(a), obtained with a higher laser frequency and lower pulse intensity, it is apparent that the structure is more complicated. Here, the correspondence between the number of dips in the angular distribution and the number of absorbed photons is not visible anymore. Indeed, the first group of peaks, comprised between the threshold and $E \simeq 0.08$ a.u., which results from the absorption of five photons, counts at most four local maxima. Furthermore, the downward energy shift of the signal for the photoelectrons ejected along the polarization axis with respect to those ejected perpendicularly to it, which was barely visible in Fig. 6.13(a), is here much more pronounced. This effect, which is clearly visible for the two absolute maxima in the group of peaks comprised between $E \simeq 0.09$ a.u. and $E \simeq 0.2$ a.u. (the first group of peaks is truncated by the threshold opening) constitutes an additional aspect of the dynamical-shift effect that cannot be detected in a 2D plot like Fig. 6.15. The spectral lines that are most dramatically distorted by this effect are the weakest ones within each group, i.e., at $E \simeq 0.07$ a.u. and $E \simeq 0.19$ a.u., which are also the ones closer to the nominal weak-field positions of the ATI peaks. A final peculiar aspect that we would like to highlight in Fig. 6.13(b) is the appearance of isolated narrow dips in the transition probability, e.g., for $(E, \cos \theta) \simeq (0.03 \text{ a.u.}, \pm 0.7)$, $(0.02 \text{ a.u.}, \pm 0.75)$, $(0.125 \text{ a.u.}, \pm 0.9)$. This phenomenon is associated to the fact that the transition amplitude beneath the photoelectron distribution is complex, rather than real. As a result, the loci of zeros in the $(E, \cos \theta)$ domain of its real and imaginary components are curves that generally intersect at isolated points only. Symmetry nodes, like those at $\theta = 90^\circ$ for the absorption of an odd number of photons, are a notable exception.

PHOTOIONIZATION OF POLY-ELECTRONIC SYSTEMS USING XCHEM

7.1 ONE-ELECTRON PARENT IONS

7.1.1 Photoionization of He

The helium atom is an extensively studied system for which accurate independent *ab initio* codes are available [117].

The parent-ion states of He^+ were obtained by performing a formally SA-CASSCF calculation of 5 states, where the active space consists of one electron and 5 orbitals: $1s$, $2s$, $2p_x$, $2p_y$ and $2p_z$. For this computation we used a modified version of the aug-cc-pV6Z [156] basis set, where only the s and p expansions were considered. In this way, the well known hydrogen-like orbitals were obtained for $n = 1$ and $n = 2$ shells. The orbitals were optimized with the MOLPRO package under D_{2h} symmetry constraints (2 states for symmetry A_g and 1 state for the symmetries B_{1u} , B_{2u} and B_{3u}) and exported to MOLCAS to follow the augmentation procedure using two different GUGA tables: CAS(1,5) for the case of the parent ions and CAS (2,7) for the case of the augmented parent ions.

For the monocentric GABS basis, B-splines of order 7 were used starting at $R_0 = 10$ a.u., in a box of 400 a.u., with a uniform grid of 0.5 a.u. separation between consecutive nodes. The Gaussian functions were generated using for the α_i exponents in (5.9) an even-tempered set of 22 elements, whose minimum and maximum elements are $\alpha_1 = 0.01$ and $\alpha_{22} = 28.28$. The other parameter of the Gaussian subset, K_{max} , which defines the maximum angular momentum these functions can represent, was set to $K_{max} = 3$ (see 5.2).

Using this GABS basis, we defined three different CC expansions (5.1), with total multiplicity $2S + 1 = 1$ (see Table 7.1). The first one (CC₁) contains two helium parent ions, $\text{He}^+(1s)$ and $\text{He}^+(2s)$, while the second and the third CC expansion (CC₂ and CC₃) have the extra parent ion $\text{He}^+(2p)$, and are intended to build up the channels with symmetries $^1S^e$ and $^1P^o$, respectively.

We used the CC₁ expansion to estimate the Hamiltonian spectrum in the box. Several of its Rydberg state energies converging to the $N = 1$ threshold

Table 7.1: CC expansions used for the helium atom computations. For each angular momentum, the projection m takes all the possible values.

	CC ₁ ^a	CC ₂	CC ₃
Configurations	$1s \otimes X_{\ell m}$	$1s \otimes X_{00}$	$1s \otimes X_{1m}$
	$2s \otimes X_{\ell m}$	$2s \otimes X_{00}$	$2s \otimes X_{1m}$
		$2p \otimes X_{1m}$	$2p \otimes X_{00}, X_{2m}$

^a $\ell = 0, 1, 2$.

(-2 a.u.) are shown in Table 7.2. As a reference, an *ab initio* code relying exclusively on B-splines and resembling the same correlation level imposed by the CC₁ expansion, was used. This independent method is virtually exact for the non-relativistic He, provided that no further limitations to the electronic correlation are assumed [117]. The agreement is very good, due to the fact that the Rydberg states' oscillations, dominant in the middle and long range, are mainly reproduced by the B-splines, whereas the short range part is described by the Gaussian subset, exhibits only few oscillations.

Following the procedures explained in the previous sections, we computed for the CC₂ and CC₃ expansions the scattering matrix S , and hence the eigenphases. Figure 7.10 shows the calculated scattering phase-shifts, $\theta(E)$ [see Eq. (3.25)], in the vicinity of the first two resonances of the $^1S^e$ and $^1P^o$ series below the $N = 2$ threshold (-0.5 a.u.). In this energy region, there is only one open channel for each symmetry, although there are interactions among all the channels used in the CC expansions. The presence of the resonances is clearly indicated by the jumps of π in the total phase-shift. By fitting the calculated phase-shifts to Eq.

Table 7.2: Energies (in a.u.) of several Rydberg states converging to the $N = 1$ ionization threshold of He (-2 a.u.), obtained by using B-splines only (reference calculation) and the CC₁ expansion given in Table 7.1.

State	B-splines	CC ₁
1s5s	-2.021053	-2.021047
1s3d	-2.019996	-2.019996
1s4p	-2.019821	-2.019814
1s6s	-2.014493	-2.014486
1s4d	-2.013887	-2.013879
1s5p	-2.013785	-2.013777
1s7s	-2.010582	-2.010574
1s5d	-2.010203	-2.010195

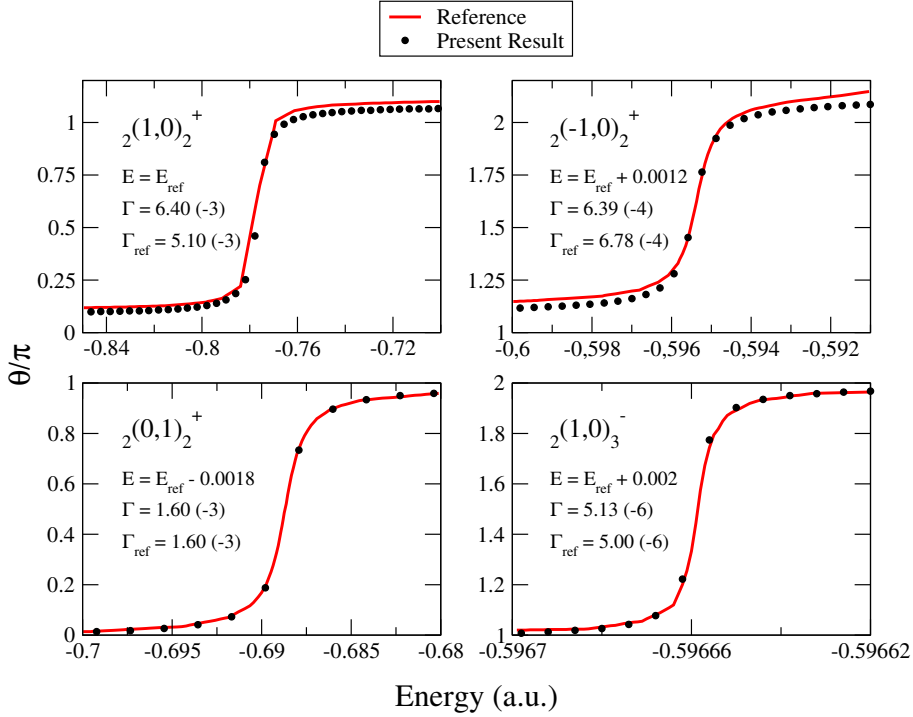


Figure 7.1: Total phase-shift energy dependence in units of π . The two top panels and the two bottom panels show the first two resonances for the $1S^e$ and $1P^o$ series, respectively, below the $N = 2$ (-0.5 a.u.) threshold. Herrick's notation [157] has been used to label these doubly excited states ${}_N(K, T)_n^A$. Three of the eigenphases have been shifted in energy to better visualize the comparison of the resonant profile with the benchmark. E_{ref} and Γ_{ref} correspond to the reference values.

(3.25), we have extracted the corresponding energy positions and autoionization widths. As can be seen, the agreement with the results of the reference calculations is very good. For the energies, the maximum absolute deviation is quite small: 0.002 a.u.. For the widths, the error is smaller than 6% , except for the first resonance of the $1S^e$ series, for which it is $\sim 20\%$.

In the energy region between the $N = 2$ and $N = 3$ thresholds, several channels are open for the CC_2 and CC_3 expansions, as can be seen in Figure 7.2. This time no resonances can be seen because we are not including any configuration with a parent ion beyond the $N = 2$ threshold. Again the calculated phase-shift curves compare very well with the reference ones. Only for those profiles corresponding to the channels in which the parent ion is left in the $\text{He}^+(1s)$ state, deviations from the reference results are larger than 5% . This is due to the fact that, in this channel, the energy of the continuum electron is high (>1.5 a.u.) and the chosen GABS basis is not flexible enough to provide an accurate representation of the corresponding rapidly oscillating continuum orbital. This situation is easily

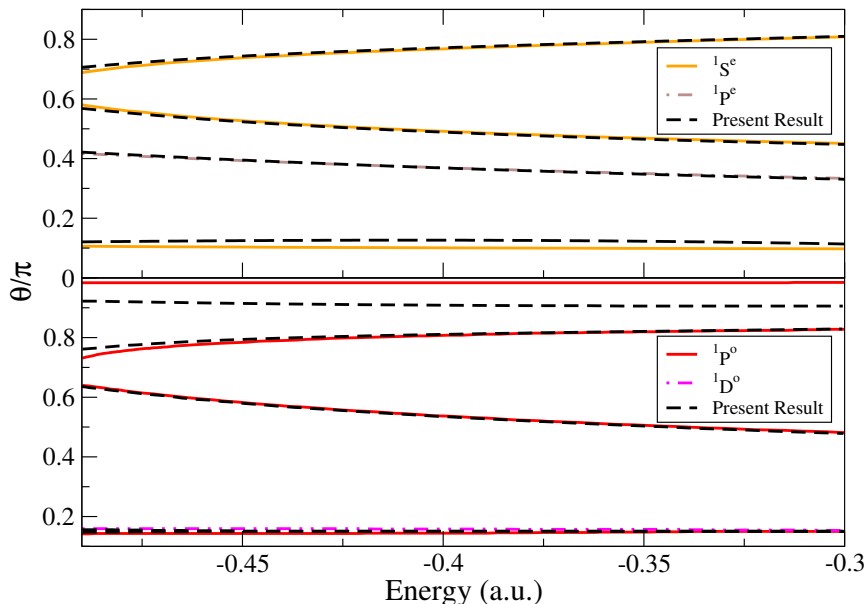


Figure 7.2: Multichannel scattering total phase-shifts above the $N = 2$ (-0.5 a.u.) threshold. The top panel shows the channels with even symmetry and the bottom panel those with odd symmetry.

solvable by improving the GABS basis, e.g., by increasing the number of K 's in the subset of monocentric Gaussian functions.

Figure 7.3 shows the photoionization cross section below the $N = 2$ threshold, obtained by using Eq. (7.5) and the CC_3 expansion. The calculated spectrum exhibits pronounced peaks corresponding to the resonances belonging to the $1P^o$ series, which display the characteristic Fano line shapes [36]. Figure 7.3 also shows the comparison between our results in velocity gauge and those from the reference calculations in velocity and length gauges. The agreement between the two gauges within the benchmark, and between the benchmark and our results again is very good.

7.1.2 Photoionization of H_2

To test our model in a molecular target, we have chosen the simplest multielectronic molecule, H_2 , for which one can compare with accurate benchmark calculations [34, 68].

In the calculations of the parent ion H_2^+ , several states were obtained by using the CASSCF methodology with an active space of 1 electron in 7 orbitals and the s and p functions from the aug-cc-pV6Z basis set [158]. The states included in

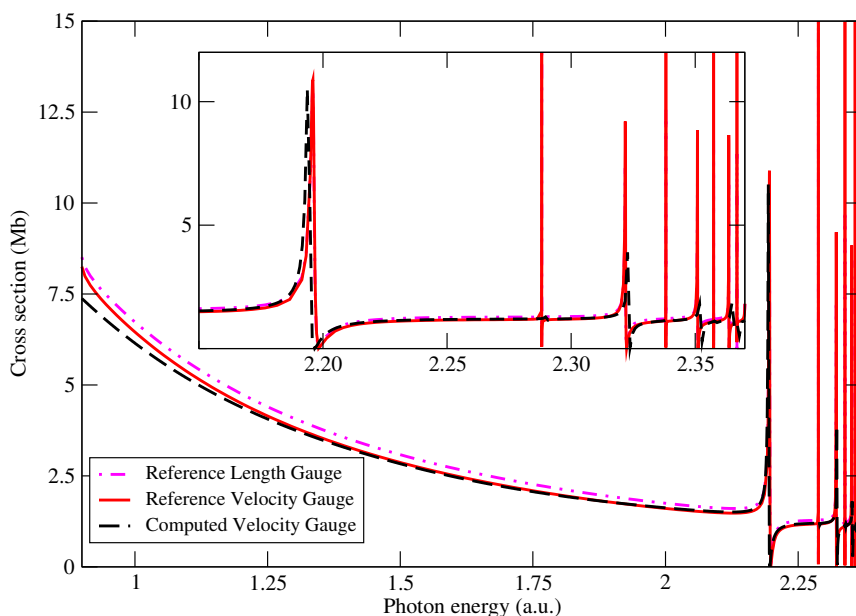


Figure 7.3: Cross section from the He ground state. The inset shows the region where the first resonances appear, having the characteristic Fano profile.

the parent-ion calculation were 2 for the symmetry A_g ($1s\sigma_g$ and $2s\sigma_g$), and 1 for each of the symmetries B_{3u} and B_{2u} ($2p\pi_u$), B_{1u} ($2p\sigma_u$), B_{2g} and B_{3g} ($3d\pi_g$). The orbitals obtained for these states are shown in Fig 7.4. As explained in section 5.3, the orbitals were optimized with the MOLPRO package using D_{2h} symmetry and exported to MOLCAS to follow the augmentation procedure. In this case the GUGA tables employed were a CAS(1,7) for the parent ion and a CAS(2,9) for the augmented states. For the GABS basis we used the same parametrization as for the helium atom (see previous section), except for the fact that this time the box length is 200 a.u..

In Table 7.3, the energies for the first three $^1\Sigma_g^+$ and the first two $^1\Sigma_u^+$ states of H_2 at equilibrium distance ($R = 1.4$ a.u.) are shown, for five different computa-

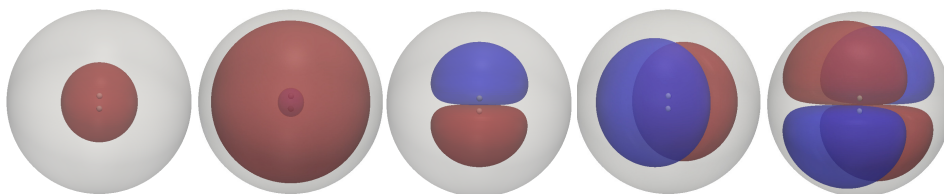


Figure 7.4: The orbitals included in the active space of the H_2^+ parent ion, from left to right: $1s\sigma_g$, $2s\sigma_g$, $2p\sigma_u$, $2p\pi_u$ and $3d\pi_g$. The sphere defining the region in which B-splines are not present is also shown.

Table 7.3: The upper part shows the energies for the first three $^1\Sigma_g^+$ and the first two $^1\Sigma_u^+$ states of H_2 at equilibrium distance. The lower part shows the dipoles computed in velocity gauge along the internuclear axis, between the $^1\Sigma_g^+$ and the of $^1\Sigma_u^+$ states.

	MRCIS	XCHEM ₁ ^a	XCHEM ₂ ^b	XCHEM ^c	B-splines ^d
Energy (a.u.)					
$^1\Sigma_g^+$	-1.1674	-1.1380	-1.1650	-1.1650	-1.1725
	-0.6908	-0.5682	-0.6905	-0.6905	-0.6911
	-0.5717	-0.0185	-0.6263	-0.6263	-0.6259
$^1\Sigma_u^+$	-0.7047	-0.5156	-0.7040	-0.7040	-0.7045
	-0.6159	0.0163	-0.6280	-0.6279	-0.6279
Dipole (a.u.)					
$1(^1\Sigma_g^+) - 1(^1\Sigma_u^+)$	0.4546	0.3643	0.4537	0.4530	-
$1(^1\Sigma_g^+) - 2(^1\Sigma_u^+)$	0.3105	0.0296	0.2145	0.2201	-
$2(^1\Sigma_g^+) - 1(^1\Sigma_u^+)$	0.0370	-0.1722	0.0382	0.0382	-
$2(^1\Sigma_g^+) - 2(^1\Sigma_u^+)$	0.1956	0.0140	0.1465	0.1468	-
$3(^1\Sigma_g^+) - 1(^1\Sigma_u^+)$	-0.1088	-0.0452	-0.1713	-0.1724	-
$3(^1\Sigma_g^+) - 2(^1\Sigma_u^+)$	-0.1595	0.0037	-0.0083	-0.0129	-

^a Only polycentric Gaussian basis.

^b Polycentric and monocentric Gaussian basis.

^c All Gaussian plus the B-splines.

^d Independent method relying exclusively on B-splines.

tional schemes. In the Multireference Configuration Interaction (MRCI), besides those active orbitals depicted below to obtain the parent-ion wave functions, the $3s\sigma_g$, $3p\pi_u$, $3p\sigma_u$ and $4d\pi_g$ were added to obtain the first bound states of the neutral H_2 . Using this approach only single excitations were allowed. Three other results are computed following the XCHEM formalism and using three different approximations: **i**) using only the multi-center Gaussian expansion, **ii**) using the multi-center and single-center Gaussian expansion and **iii**) adding the B-splines to the previous approximation. The other computation was done using exclusively B-spline functions according to the methods described in [34, 68]. The lower part shows the dipoles computed in velocity gauge along the \hat{z} direction (the internuclear axis), between the $^1\Sigma_g^+$ and the of $^1\Sigma_u^+$ states. These results show that the low lying states are not affected by the addition of the B-splines in the XCHEM formalism, and that the accuracy of its computation is equivalent to those obtained by standard QC methods.

Table 7.4: First three $^1\Sigma_u^+$ resonances energies and widths (in a.u.), for several internuclear distances. The results obtained with the (7.1) CC expansions are compared with accurate reference calculations (see acknowledgements). Numbers in parentheses represent power of ten.

R	Resonance	E_{ref}	Γ_{ref}	E	Γ
1.0	1	0.2853	8.74(−3)	0.2847	8.94(−3)
1.0	2	0.3708	1.89(−3)	0.3703	1.97(−3)
1.0	3	0.3808	2.71(−4)	0.3809	2.86(−4)
1.4	1	−3.592(−2)	1.54(−2)	−3.602(−2)	1.45(−2)
1.4	2	4.237(−2)	3.58(−3)	4.206(−2)	3.89(−3)
1.4	3	4.794(−2)	6.21(−4)	4.792(−2)	5.88(−4)
2.0	1	−0.2926	2.55(−2)	−0.2899	2.33(−2)
2.0	2	−0.2236	3.52(−3)	−0.2225	1.39(−3)
2.0	3	−0.2212	3.94(−3)	−0.2223	6.45(−3)
3.0	1	−0.4783	4.10(−2)	−0.4673	3.67(−2)
3.0	2	−0.4238	2.80(−3)	−0.4230	2.21(−3)
3.0	3	−0.4177	1.15(−2)	−0.4170	9.73(−3)

To assess the quality of our results, we performed calculations in the fixed-nuclei approximation for the first three $^1\Sigma_u^+$ resonances at several internuclear distances, and compared them with those from an independent computation based on a different formalism [34], which essentially leads to exact results. The CC expansions used to build the $^1\Sigma_u^+$ channel from a collection of H_2^+ parent-ion states is

$$\begin{aligned}
&1s\sigma_g \otimes X_{\ell 0}, \quad \ell = 0, 1, 2, 3 \\
&2p\sigma_u \otimes X_{\ell 0}, \quad \ell = 0, 1, 2, 3 \\
&(2p\pi_u)_{x,y} \otimes X_{\ell m}, \quad \ell = 1, 2, 3, m = \pm 1 \\
&2s\sigma_g \otimes X_{\ell 0}, \quad \ell = 0, 1, 2, 3 \\
&(3d\pi_g)_{x,y} \otimes X_{\ell m}, \quad \ell = 1, 2, 3, m = \pm 1.
\end{aligned} \tag{7.1}$$

The results for the resonance positions and widths are given in Table 7.4. As can be seen, there is a good agreement for almost all the resonances. The larger discrepancies show up for the second and third resonances at an internuclear distance of 2.0 a.u., for which the resonance widths are $\sim 40\%$ off. This difference can be explained by the fact that, in the vicinity of this internuclear distance, the second and third $^1\Sigma_u^+$ resonances exhibit a sharp avoided crossing [34]. As a consequence, tiny errors in the computed wave functions can lead to a different mixing of the relevant configurations and hence to large errors in the corresponding autoionization widths in this region. Apart from these two special cases, the general trend is that the shorter the internuclear distance the better the accuracy,

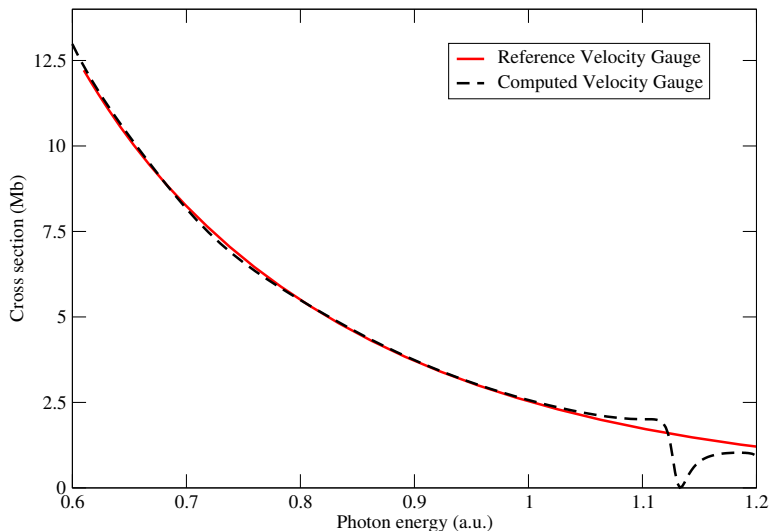


Figure 7.5: Photoionization cross section from the H_2 ground state at equilibrium distance to the $^1\Sigma_u^+$ continuum. The reference does not include the resonances (only the background), meanwhile the present computation does include the resonances, the first of which is shown.

which can be easily understood if one takes into account that we are using the same monocentric Gaussian expansion for all cases, whose representation capability decreases for an increasing separation between the nuclei.

The photoionization cross section, obtained in velocity gauge, for an H_2 molecule at the equilibrium distance $R = 1.4$ a.u. is given in Figure 7.5. Only contribution from the $^1\Sigma_u^+$ continuum is shown. The calculated cross section includes contributions from doubly-excited states associated to our choice of the parent-ion states given in Eq. (7.1). In the figure, we only show contribution from the first resonance, which appears as a pronounced dip at around a photon energy of 1.13 a.u., in excellent agreement with earlier results obtained within the fixed-nuclei approximation [69, 159]. Using the code of Ref. [34], we have also performed nearly-exact all-B-spline reference calculations for the photoionization non resonant background by including the same number of parent-ion states as in Eq. (7.1). We notice that these reference calculations do not include the contribution from the doubly-excited states. As can be seen, except for the obvious absence of the resonance in the latter calculations, the agreement with our results is excellent.

7.2 POLY-ELECTRONIC PARENT IONS: THE PHOTOIONIZATION OF NE

The first unambiguous observations of resonant states in the photoionization spectra of noble gases were reported in the 1960's [160, 161, 162, 163] and the unusual shape of the peaks observed in these experiments was explained by Fano in his seminal 1961 paper [36] as resulting from the interaction of a discrete state embedded in the continuum (see also [126]). Neon is the lightest noble atom in which the remaining cation has a truly poly-electronic character, so that photoionization dynamics is much richer than in helium. For this reason, neon has been systematically used to test new many-body theoretical methods. More recently, due to the recent advances in the generation of shorter and shorter pulses and the possibility to track electron wave packet dynamics in real time, there has been a renewed interest in this system [164, 165, 166, 167, 168] that calls for additional theoretical effort.

THE STOCK APPROACH In order to test the performance of the XCHEM approach to describe Ne photoionization, we have compared our results with those of independent numerical calculations performed with the STOCK code, for a few selected cases in which we can guarantee that the same level of electron correlation has been used. Details of the STOCK code can be found in [25]. Briefly, the method relies exclusively on B-splines as a primary basis set, and instead of explicitly imposing asymptotic boundary conditions as we do (see Eq. (3.15)), it makes use of the exterior complex scaling (ECS) formalism [169, 120], which ensures outgoing waves in the asymptotic region. For the bound states of the parent ions, STOCK uses the Multiconfiguration Hartree-Fock method (MCHF) [96], in which the atomic wave function is expanded as a linear combination of CSF:

$$|\Psi(\mathbf{x})\rangle = \sum_i c_i |^{2S+1}\Xi_i(\mathbf{x})\rangle. \quad (7.2)$$

In this method, both the coefficients $\{c_i\}$ and the radial functions $\{R_{nl}(r)\}$ used to expand the spin orbitals are varied to minimize the energy functional using a weighted average of the non-relativistic energy of a selected number of parent-ion states:

$$E[\{c_i\}, \{R_{nl}(r)\}] = \sum_j w_j \langle \Psi_j(\mathbf{x}) | H | \Psi_j(\mathbf{x}) \rangle. \quad (7.3)$$

The MCHF problem is solved using the ATSP2K package [170]. The STOCK code has been designed to describe atomic systems, so that it is computationally more efficient than the XCHEM code to describe Ne photoionization. XCHEM goal is to describe molecular systems in association with common QCPs, and hence it contemplates the D_{2h} point group (and its subgroups) but not $SO(3)$. On the other hand, in contrast with XCHEM, STOCK builds the CC expansion using as target states each and every parent ion in the CASSCF. Therefore, for a computation that includes electronic excitations of the target, the only way to have an equivalent CC expansion with XCHEM is to include all parent-ion eigenstates, which is

extremely expensive if we are only interested in describing ionization above the lowest ionization thresholds and obtaining a good description of electron correlation. Thus we have restricted the benchmarking with the STOCK code to the case in which the parent ion states in the CC expansion are described by the reference configuration (i.e., no further electronic excitations are allowed to optimize the parent-ion wave functions).

COMPUTATIONAL DETAILS In our CC expansion, we have included two parent ions corresponding to the configurations $1s^2 2s^2 2p^5$ ($^2P^o$) and $1s^2 2s^1 2p^6$ ($^2S^e$), which after augmentation with the $G_i^{SC}(\mathbf{x}_1)$ and B-spline bases, leads to CI vectors of about one million components (each component corresponds to a different configuration) for the neutral system, for the case of maximum correlation (see below). The wave functions representing the two parent ions were computed by using different levels of correlation, depending on how the 9 electrons were distributed in the space defined by the atomic orbitals. In order to create a common set of orbitals, valid for both parent ions, a State Average CASSCF calculation was performed, optimizing with respect to the energetic average of the $^2S^e$ and the (triply degenerate) $^2P^o$ states. We will show results for two levels of correlation: i) minimal CI (MCI), in which the parent ion states are obtained using a CAS(7,4) calculation. That is, including all configurations (subject to spin and symmetry restrictions) obtained by seven electrons distributed over the $2s$, $2p_x$, $2p_y$ and $2p_z$ orbitals with the $1s$ orbital being doubly occupied always, and ii) extended CI (XCI), in which the active space is extended from the MCI case, to allow also occupation of $3p$, $3d$ and $4s$ orbitals (i.e. a CAS(7,13) calculation).

At both MCI and XCI level, the parent ions are obtained using a cc-pVQZ Gaussian basis set [171, 172]. The virtual orbitals that result from the calculation are excluded from the augmentation procedure, since they are quite diffuse and would overlap with the B-splines, in contrast with one of the XCHEM assumptions.

The GABS basis consists of B-splines of order $k = 7$ starting at $R_0 = 7$ a.u. with a node separation of 0.5 a.u. in a box of 200 a.u., and a set of Gaussian functions ($G_{iK}^{\ell m}(\vec{r}) = N_{i\ell} r^{K_\ell} e^{-\alpha_i r^2} X_{\ell m}(\hat{r})$) with an even-tempered sequence of α_i exponents as that used in [173] and $K_\ell = \ell + 2k$ values with $\ell_{max} = 3$ and $k_{max} = 2$. For the parent-ions we have considered, we only need a photoelectron angular momentum up to $\ell = 2$ to describe the $^1S^e$ and $^1P^o$ total symmetries. This choice leads to the following powers of r according to the angular momentum: $K_0 = 0, 2, 4$, $K_1 = 1, 3, 5$, and $K_2 = 2, 4, 6$.

In Table 7.5, the energies of the parent ions used in the CC and the energies of the lower four states of Ne with $^1S^e$ and $^1P^o$ symmetries are shown. The agreement between the two independent computational schemes is very good. The virial theorem was also successfully checked at XCI correlation level for the neutral bound states.

Table 7.5: Bound state energies comparison between STOCK and XCHEM, for different levels of correlation. The top part shows the energy of the parent ions used in the CC expansion. The bottom part shows the first four energies of the states with $^1S^e$ and $^1P^o$ symmetries. The ratio $\kappa = -\langle i|V|i\rangle/\langle i|K|i\rangle$, where computed, is given in parentheses.

Ne ⁺ energies (a.u.)				
	STOCK		XCHEM	
Corr.	$2p^{-1}$	$2s^{-1}$	$2p^{-1}$	$2s^{-1}$
MCI	-127.8174	-126.7345	-127.8172	-126.7335
XCI	-	-	-127.9927	-126.9970
Ne energies (a.u.)				
	$^1S^e$	$^1P^o$	$^1S^e$	$^1P^o$
MCI	-128.5873	-127.9865	-128.5881	-127.9861
	-127.9123	-127.8844	-127.9120	-127.8841
	-127.8627	-127.8735	-127.8623	-127.8731
	-127.8440	-127.8533	-127.8395	-127.8530
XCI	-	-	-128.7709(1.9999)	-128.1613(2.0002)
	-	-	-128.0884(2.0002)	-128.0597(2.0003)
	-	-	-128.0381(2.0003)	-128.0487(2.0003)
	-	-	-128.0140(2.0000)	-128.0285(2.0003)

7.2.1 Photoionization of Ne at MCI level

At this level of correlation we can compare, on an equal footing, the XCHEM results with those obtained with STOCK, as explained in the previous section. Figure 7.6 shows the eigenphases computed for the scattering channels with $^1S^e$ and $^1P^o$ symmetries using both approaches at the MCI level. For the former symmetry, which is the same as for the ground state, the continuum above the lowest ionization threshold corresponds to a state in which the $2s^22p^5$ parent ion is coupled with an outer electron described by a p -wave: $2s^22p^5\epsilon p$. Above the $2s2p^6$ threshold, a new continuum emerges for the same symmetry: $2s2p^6\epsilon s$. For the $^1P^o$ symmetry, we have multiple channels both below and above the $2s2p^6$ threshold: $2s^22p^5\epsilon s$ and $2s^22p^5\epsilon d$ below the $2s2p^6$ threshold and the additional channel $2s2p^6\epsilon p$ above. Below the $2s2p^6$ threshold, the continuum contains a single resonance series: $2s2p^6ns$ and $2s2p^6np$ for the $^1S^e$ and $^1P^o$ symmetries, re-

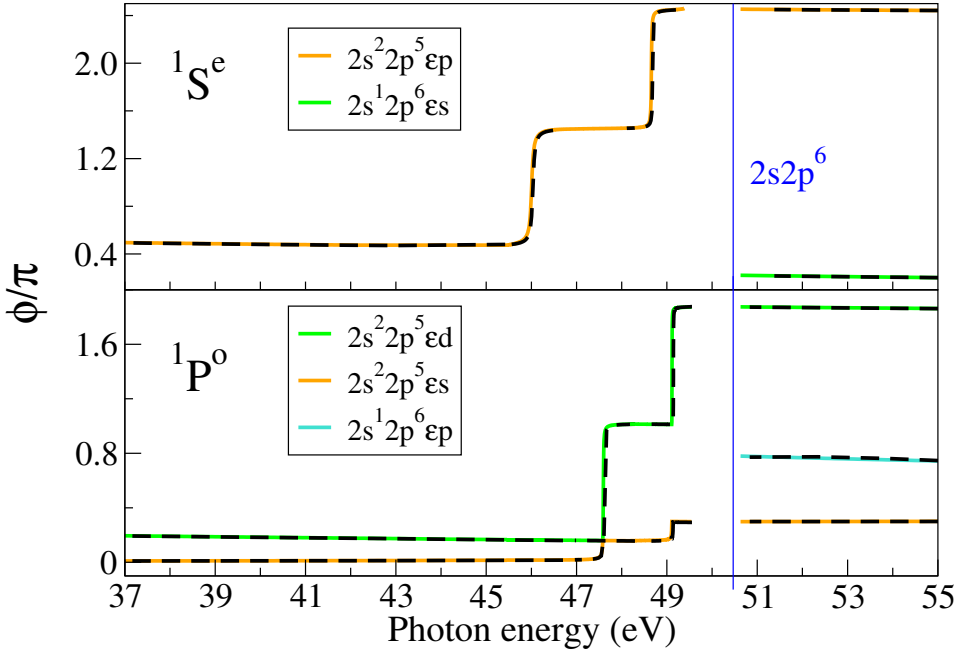


Figure 7.6: Eigenphases in units of π for the scattering channels of symmetry $1S^e$ (top panel) and $1P^o$ (bottom panel), computed using XCHEM (dashed lines) and STOCK (solid lines) at CIS level. The region shown below the $2s2p^6$ ionization threshold (vertical line) extends from well below the resonances up to the second resonance for the two resonance series $2s2p^6ns$ and $2s2p^6np$.

spectively. The agreement between the XCHEM and STOCK eigenphases is excellent, both in the resonant and non-resonant regions.

Notice the pronounced jumps in the phases when one goes through the resonances. From Eq. (3.26), we obtain for the two open channels of $1P^o$ symmetry:

$$\frac{\Gamma_1}{\Gamma_2} = -\frac{\tan(\phi_\nu(E_r) - \phi_1^0)}{\tan(\phi_\nu(E_r) - \phi_2^0)}, \quad \nu = 1, 2. \quad (7.4)$$

Eq. (7.4) can be used to compute the Γ_1/Γ_2 ratio. Notice that, in contrast with the total phase, the partial eigenphases experience a variation smaller than π radians in the vicinity of the resonances. Figure 7.6 shows, however, that in the vicinity of the $2s2p^6np$ resonances, the $2s^2 2p^5 \epsilon d$ eigenphase takes most of the π jump. This indicates that the decay of these resonances to the $2s^2 2p^5 \epsilon d$ continuum is the dominant process, as expected by propensity rules [174].

The $2s2p^6np$ resonant series also leaves its fingerprint in the photoionization cross section in the form of Fano-like peaks, due to the interference between the

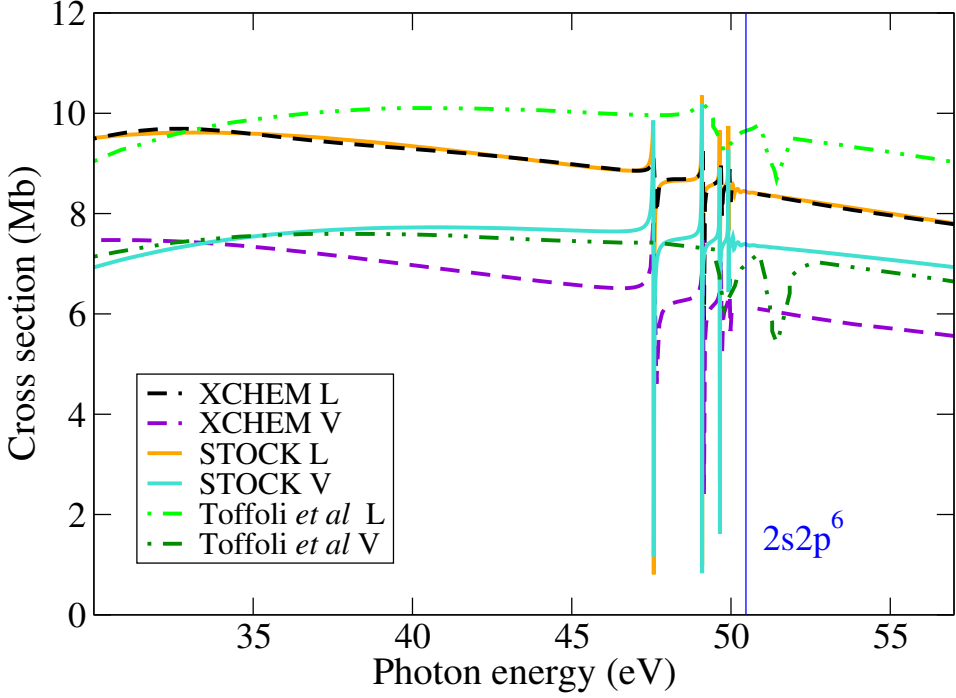


Figure 7.7: Total photoionization cross section from the ground state of Ne, computed using XCHEM (dashed lines) and STOCK (solid lines) at CIS level, for length (L) and velocity (V) gauges. Results from Toffoli et al [175], obtained by using the same level of correlation, are also shown (dashed-dotted lines). The vertical line indicates the position of the $2s2p^6$ ionization threshold.

direct and resonance mediated ionization paths [36]. The partial photoionization cross section corresponding to a channel μ is given by

$$\begin{aligned}\sigma_{\mu}^L &= \frac{4\pi^2(E - E_g)}{c} |\langle \Psi_{\mu E}^- | \hat{\epsilon} \cdot \sum \vec{r}_i | \Psi_g \rangle|^2 \\ \sigma_{\mu}^V &= \frac{4\pi^2}{c(E - E_g)} |\langle \Psi_{\mu E}^- | \hat{\epsilon} \cdot \sum \vec{p}_i | \Psi_g \rangle|^2,\end{aligned}\quad (7.5)$$

where the superscripts L and V stand for the length and velocity gauges respectively. The polarization of the incident light is $\hat{\epsilon}$, c is the speed of light and E_g the ground state energy.

Figure 7.7 shows the total photoionization cross section ($\sigma = \sum \sigma_{\mu}$), computed with XCHEM and STOCK at MCI level, for length and velocity gauges. Independent theoretical results obtained by other authors, at the same level of correlation, are also shown [175]. The results of XCHEM and STOCK in length gauge are indistinguishable to the naked eye. However, in the velocity gauge, the slopes of the corresponding non-resonant backgrounds are different, while the position and shape of the resonance peaks remain similar. Since both calculations were per-

formed at MCI level, the difference in the background can only be explained by differences in the basis functions used in those calculations: a hybrid Gaussian/B-spline basis in XCHEM and a purely B-spline one in STOCK. As explained above, in XCHEM, B-spline functions are only used beyond R_0 , which means that the short-range part description of the continuum wave function is entirely described by Gaussian functions. In contrast, in STOCK B-splines are used all the way from the origin to the asymptotic region. B-spline functions provide more flexibility than Gaussian functions, in particular, they can better describe the wave function cusp at $r = 0$. Hence it is not surprising that discrepancies are only seen in the velocity gauge, since it emphasizes the contribution of the short-range part of the wave function. This is possibly the reason why, in the velocity gauge, the non-resonant background of Ref. [175] (an all-B-spline calculation) is in better agreement with STOCK than with XCHEM. Nevertheless, the resonant peaks predicted in [175] are shifted around 2.2 eV to higher energies, thus suggesting a poorer representation of electron correlation in the resonant states.

7.2.2 Photoionization of Ne at XCI level

Figure 7.8 shows the total cross sections again, but this time computed at the XCI level with XCHEM. They are compared with the experimental values reported in [176]. The comparison is made on absolute scale (no rescaling of either the calculated or the measured cross sections). As can be seen, the agreement between theory and experiment is very good. Also, the separation between the results obtained in the length and velocity gauges is smaller than in Fig. 7.7, and more uniform across the whole energy interval. Such improved gauge agreement is a consequence of having used a larger number of excitations in the parent-ion states. Another difference with Fig. 7.7 is that the resonant peaks are displaced to lower energies, thus indicating a better description of electron correlation in the resonant states. Interestingly, the XCHEM result computed in length gauge is closer to the measured data than that obtained in velocity gauge. This fact stresses once again that the quality of the wave functions in the short-range domain, though acceptable, is not as good as in the middle and long ranges, due to the intrinsic limitations of the Gaussian expansion in the innermost region and the poor short-range electronic correlation.

Let us now analyze in more detail the resonance structures observed in the spectrum. For the multichannel case, the photoionization cross section near an isolated resonance takes the form [126]:

$$\sigma(\epsilon) = \sigma_a(\epsilon) \frac{(q + \epsilon)^2}{\epsilon^2 + 1} + \sigma_b(\epsilon), \quad (7.6)$$

where $\epsilon = \frac{2(E-E_r)}{\Gamma}$ is the reduced energy and q the Fano parameter. The smooth functions of the energy $\sigma_a(\epsilon)$ and $\sigma_b(\epsilon)$, represent the contribution of the transitions to the scattering states that do and do not interact, respectively, with the

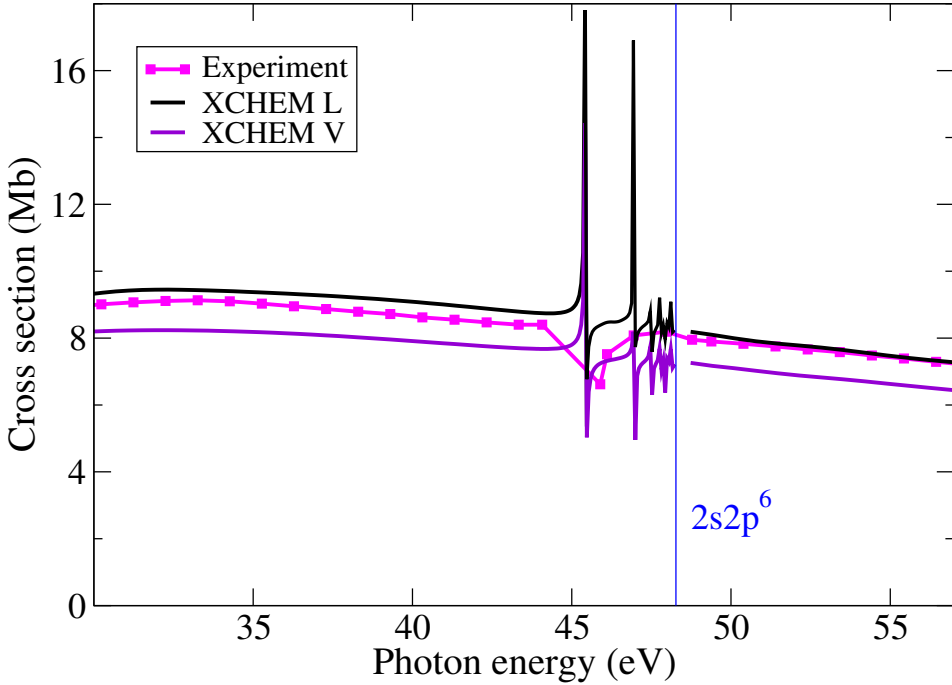


Figure 7.8: Total photoionization cross section from the ground state of Ne, computed using XCHEM (solid lines) at the full CI level, for length (L) and velocity (V) gauges. Absolute cross sections measured by Samson et al [176] are also shown (solid line with squares). The vertical line indicates the position of the $2s2p^6$ ionization threshold.

discrete state in the continuum. Defining the two parameters $\sigma^0 = \sigma_a + \sigma_b$ (total cross section background) and $\rho^2 = \frac{\sigma_a}{\sigma_a + \sigma_b}$ ($0 \leq \rho^2 \leq 1$), Eq. (7.6) becomes:

$$\sigma(\epsilon) = \frac{\sigma^0(\epsilon)}{\epsilon^2 + 1} (\epsilon^2 + 2\rho^2 q \epsilon + \rho^2 q^2 + 1 - \rho^2), \quad (7.7)$$

We have evaluated the resonance parameters by fitting the calculated total cross section to this last formula. Notice that the usual single-channel Fano formula is recovered when $\rho^2 = 1$.

Table 7.6 shows the results obtained from the fit of the cross sections calculated at full CI correlation level. We have extracted the energy E_r , total autoionization width Γ , profile parameter q and correlation parameter ρ^2 for the lowest three $1P^o$ resonances converging to the $2s2p^6$ ionization threshold. For consistency, energies and widths have also been evaluated by fitting the total scattering phases to Eq. (3.25). All parameters have been evaluated by using results obtained in both length and velocity gauge, and are compared with previously reported theoretical and experimental results (we do not compare the values of the total cross section background because all measurements but those of [176] -see Fig. 7.8- were reported in arbitrary units). It is worth noticing that among the four reso-

nance parameters, q is the most sensitive one to the quality of the basis, because it depends both on the coupling between the discrete state embedded in the continuum and the non-resonant continuum components, and on the dipole coupling between the ground and the modified discrete state (perturbed discrete state due to the non-zero coupling with the non-resonant continuum). As can be seen, values of the resonance energies are very close for the different computation schemes (in percent), while ρ^2 , Γ , and q exhibit a higher dispersion.

Table 7.6: Resonance parameters for the lowest three $1P^o$ resonances converging to the $2s2p^6$ threshold. The XCHEM results at the full CI level (highlighted in bold) have been obtained in three different ways: by fitting the total phase shift and by fitting the total cross sections obtained in length and velocity gauges. The results are compared with theoretical and experimental values reported in the literature. Uncertainties, where quoted, are given in parentheses, and experimental values are given in italics for an easy identification.

Resonance	Energy (eV)	Width (meV)	Fano q	$\rho^2 = \frac{\sigma_a}{\sigma_a + \sigma_b}$
$2s2p^63p$	45.431 ^{a,b,c}	15.0 ^{a,b}	-1.47 ^b	0.79 ^b
	45.426 ^d	15.1 ^c	-1.34 ^c	0.77 ^c
	45.5442(50) ^e	13.3 ^d	-1.58(1) ^f	0.75(5) ^f
	45.546(8) ^g	16(2) ^e	-1.6(2) ^g	0.70(7) ^g
	45.53397 ^e	13(2) ^{f,g}	-1.59(1) ^f	0.72 ^f
	45.557 ^f	13 ^h	-1.53(1) ^f	0.73 ^f
	49.725 ^h	18.6(10) ^f	-1.4 ^h	0.77 ^{h,k}
	46.253 ⁱ	34.9 ^e	-3.69 ⁱ	0.514 ⁱ
	45.5655 ^j	13.9 ⁱ	-0.34 ^k	0.93 ^k
	45.538 ^l	11.4 ^j	-1.16 ^k	0.91 ^k
		11.7 ^k	-1.61 ^k	0.76 ^k
		12.1 ^k	-1.30 ^k	
		31.8 ^l	-1.32 ^l	
$2s2p^64p$	46.942 ^{a,b,c}	4.3 ^{a,b,c}	-1.26 ^b	0.84 ^b
	46.945 ^d	3.8 ^d	-1.67 ^c	0.85 ^c
	47.1193(50) ^e	5.7(10) ^f	-1.47(1) ^f	0.78(11) ^f
	47.121(5) ^g	4.5(1.5) ^g	-1.6(3) ^g	0.70(7) ^g
	47.11092 ^e	7 ^h	-1.88 ^f	0.72 ^f
	47.111 ^f	4.3 ^f	-1.82 ^f	0.73 ^f
	51.318 ^h	6.65 ^e	-1.35 ^h	0.63 ^h
	47.397 ⁱ	3.86 ⁱ	-3.95 ⁱ	0.505 ⁱ

Continued on the next page

Continued from the previous page

Resonance	Energy (eV)	Width (meV)	Fano q	$\rho^2 = \frac{\sigma_a}{\sigma_a + \sigma_b}$
$2s2p^65p$	47.1278 ^j	5.28 ^j	−1.75 ^k	0.76 ^k
		3.8 ^k	−1.46 ^k	0.77 ^k
	47.506^a	1.6^{a,d}	−1.35^b	0.86^{b,c}
	47.502^{b,c,d}	1.7^{b,c}	−1.78^c	0.6(2)^f
	47.6952(15) ^e	3.6(18) ^f	−1.46(5) ^f	0.70(14) ^g
	47.692(5) ^g	2(1) ^g	−1.6(5) ^g	0.74 ^f
	51.894 ^h	2.47 ^e	−1.9 ^f	0.75 ^f
	47.687 ^f	1.8 ^f	−1.87 ^f	0.71 ^h
	47.69182 ^e	3 ^h	−1.15 ^h	0.502 ⁱ
	47.814 ⁱ	1.62 ⁱ	−4.05 ^g	
	47.6975 ^j	2.61 ^j		

^a XCHEM: fit of the total phase.

^b XCHEM: fit of the total cross section in length gauge.

^c XCHEM: fit to the total cross section in velocity gauge.

^d XCHEM: eigenvalues of the H_Q (see 3.4.2).

^e Reference [177].

^f Reference [178].

^g Reference [163].

^h Reference [179].

ⁱ Reference [180].

^j Reference [181].

^k Reference [182].

^l Reference [183].

It is worth noticing that the other theoretical results shown in the table were obtained by using very different levels of theory: the relativistic random-phase approximation (RRPA) together with the relativistic multichannel quantum-defect theory (RMQDT) [179], the R-matrix method, sometimes combined with the multichannel quantum-defect theory (MQDT) [177, 178, 181, 182], the time dependent local density approximation (TDLDA) [180], and the time-dependent configuration-interaction singles (TDCIS) [183]. Among all these theoretical studies, the one that resembles the most our level of theory is [182], in which besides some computations with too little correlation, the authors also used the same parent ions we do include in our CC expansion, whose wave functions are obtained within the CISD level (singles and doubles), allowing the excitations from the reference configurations to the pseudo-orbitals: $3s$, $3p$ and $3d$. To this approach correspond in Table 7.6, for the first resonance, the width of 11.7 meV, q param-

ters -1.6 (length gauge) and -1.3 (velocity gauge), and ρ^2 parameters 0.76 (length gauge) and 0.77 (velocity gauge); and for the second resonances, a width of 3.8 meV, q parameters -1.75 (length gauge) and -1.46 (velocity gauge), and the same ρ^2 values than for the first resonance. They don't report the parameters for the third resonance.

Considering the XCHEM results only, the E_r , Γ and ρ^2 parameters obtained from the different fits agree very well to each other. For the Fano q parameter, differences between the results extracted from the length and the velocity gauges are larger. The XCHEM resonance energies are 0.1-0.2 eV lower than the experimental ones, and are comparable or even better than those obtained from other theoretical methods. The agreement with the experimental total widths is also quite good: the computed values are within the experimental error bars or pretty close. For the q parameters, apart from the gauge discrepancy mentioned above, the agreement with the experimental values is quite acceptable.

From the partial cross sections, one can get information about the decay of the resonances to the different open channels. As shown by Starace [184, 185], the photoionization partial cross sections can be written as:

$$\sigma_\mu(\epsilon) = \frac{\sigma_\mu^0(\epsilon)}{\epsilon^2 + 1} \{ \epsilon^2 + 2\epsilon[q\Re(\alpha_\mu) - \Im(\alpha_\mu)] + 1 - 2q\Im(\alpha_\mu) - 2\Re(\alpha_\mu) + (q^2 + 1)|\alpha_\mu|^2 \}, \quad (7.8)$$

where $\sigma_\mu^0(\epsilon)$ is the partial cross section background and $\alpha_\mu = \Re(\alpha_\mu) + i\Im(\alpha_\mu)$ is the Starace parameter [184, 185]. The α_μ parameters are not independent of each other, they fulfill the following relation:

$$\sum_\mu \sigma_\mu^0(\epsilon) |\alpha_\mu|^2 = \sigma^0(\epsilon) \rho^2, \quad (7.9)$$

where $\sigma^0(\epsilon)$ and ρ^2 are the background and the correlation parameters, respectively, appearing in the total cross section. Figure 7.9 shows the $2p^{-1}\epsilon s$ and $2p^{-1}\epsilon d$ partial cross sections around the $2s2p^63p$, $2s2p^64p$ and $2s2p^65p$ resonances. As expected, the $2p^{-1}\epsilon d$ channel clearly dominates the photoionization process. Only when the partial cross section associated with the dominant channel undergoes a very pronounced dip in the vicinity of the resonances, the $2p^{-1}\epsilon s$ partial cross section takes over, but only in very narrow energy intervals.

It is easy to demonstrate that

$$\frac{\Gamma_\nu}{\Gamma_\mu} = \frac{\sigma_\nu^0 |\alpha_\nu|^2}{\sigma_\mu^0 |\alpha_\mu|^2}, \quad (7.10)$$

so, in principle, if we were able to extract the backgrounds σ_μ^0 and the Starace parameters α_μ by fitting the partial cross sections to Eq. (7.8), then we could get the branching ratios from (7.10). The problem lies now on how to perform the fitting. The partial cross sections, like the total one, are nonlinear functions of the

Table 7.7: Starace parameters and branching ratios (Γ_μ/Γ) for the same resonances as in Table 7.6 . The coefficients $C_{1\mu}$ and $C_{2\mu}$ and its error bars (in brackets), obtained through the fitting to the partial cross sections using (7.12), are also shown.

Res.	μ	$C_{1\mu}$	$C_{2\mu}$	$\text{Re}(\alpha_\mu)$	$\text{Im}(\alpha_\mu)$	Γ_μ/Γ
$2s2p^63p$	$2s^22p^5\epsilon s$	2.451(0.009) ^a	4.151(0.014) ^a	-0.770 ^a	-0.097 ^a	0.046 ^c
		1.971(0.008) ^b	3.443(0.010) ^b	-0.677 ^b	-0.079 ^b	0.044 ^d
	$2s^22p^5\epsilon d$					0.049 ^e
		-2.649(0.008) ^a	1.754(0.012) ^a	0.934 ^a	-0.045 ^a	0.954 ^c
		-2.391(0.008) ^b	1.429(0.011) ^b	0.931 ^b	-0.051 ^b	0.956 ^d
						0.951 ^e
$2s2p^64p$	$2s^22p^5\epsilon s$	1.352(0.009) ^a	2.200(0.010) ^a	-0.453 ^a	-0.105 ^a	0.022 ^c
		1.663(0.007) ^b	2.246(0.009) ^b	-0.432 ^b	-0.111 ^b	0.021 ^d
	$2s^22p^5\epsilon d$					0.021 ^e
		-2.301(0.011) ^a	1.392(0.017) ^a	0.846 ^a	0.085 ^a	0.978 ^c
		-3.145(0.013) ^b	2.600(0.024) ^b	0.863 ^b	0.132 ^b	0.979 ^d
						0.979 ^e
$2s2p^65p$	$2s^22p^5\epsilon s$	1.798(0.041) ^a	2.493(0.052) ^a	-0.536 ^a	-0.176 ^a	0.025 ^c
		2.167(0.038) ^b	2.581(0.053) ^b	-0.507 ^b	-0.180 ^b	0.025 ^d
	$2s^22p^5\epsilon d$					0.024 ^e
		-2.544(0.027) ^a	1.618(0.042) ^a	0.963 ^a	-0.028 ^a	0.975 ^c
		-3.395(0.024) ^b	2.882(0.046) ^b	0.964 ^b	-0.018 ^b	0.975 ^d
						0.976 ^e

^a Fit of the partial cross section in length gauge.

^b Fit of the partial cross section in velocity gauge.

^c Using Eq. (7.10) in length gauge.

^d Using Eq. (7.10) in velocity gauge.

^e Using Eq. (7.4).

fitting parameters, but extracting the resonance parameters from the partial ones has two additional complications: (i) there are extra parameters, namely the α_μ and (ii) the α_μ parameters belonging to different channels are not independent (as shown by Eq. (7.9)). For this reason, for each partial cross section, we will fix the parameters already obtained from the fit of the total cross section (E_r , Γ and q) and will only leave three free parameters: $\Re(\alpha_\mu)$, $\Im(\alpha_\mu)$ and σ_μ^0 . The parameters

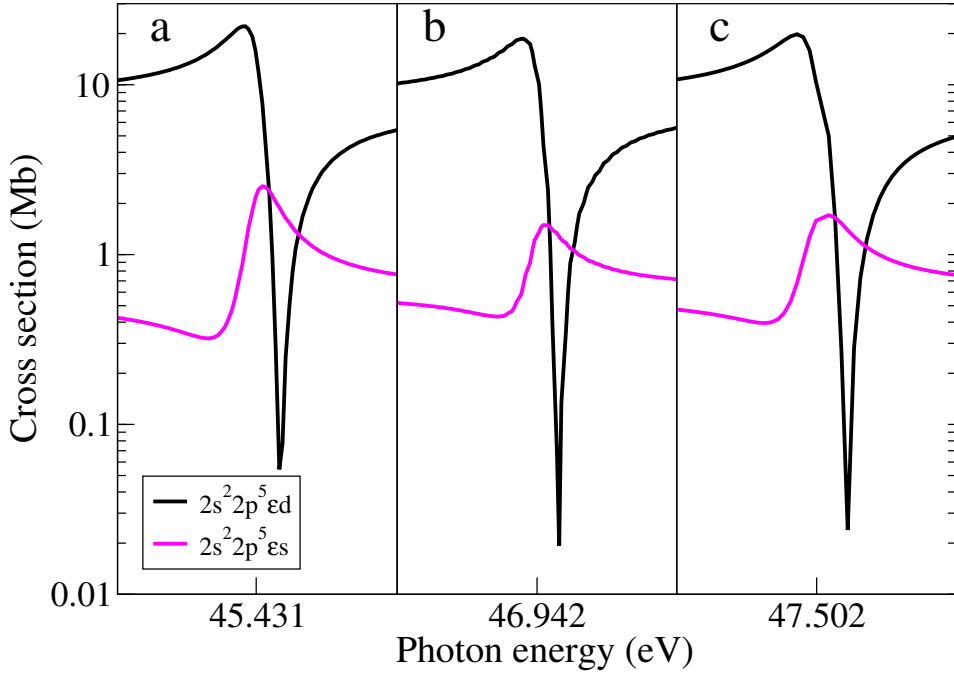


Figure 7.9: Partial photoionization cross sections computed using XCHEM at the full CI level and in velocity gauge. The three panels a, b, c display the energy region around the $2s^2 2p^6 3p$, $2s^2 2p^6 4p$ and $2s^2 2p^6 5p$ resonances, respectively ($[E_r - 4\Gamma, E_r + 4\Gamma]$), which can decay into the $2s^2 2p^5 \epsilon s$ and the $2s^2 2p^5 \epsilon d$ continua.

must be determined by imposing simultaneously the condition given by Eq. (7.9). Due to this additional condition, for many initial values of the α_μ parameters convergence is not reached or leads to absurd values. To double check the results of this fitting procedure, we have also adopted the following procedure. We have linearized Eq. (7.8), by introducing the new parameters $C_{1\mu}$ and $C_{2\mu}$ [186] defined as

$$\begin{aligned} C_{1\mu} &= 2[q\Re(\alpha_\mu) - \Im(\alpha_\mu)], \\ C_{2\mu} &= 1 - 2q\Im(\alpha_\mu) - 2\Re(\alpha_\mu) + (q^2 + 1)|\alpha_\mu|^2, \end{aligned} \quad (7.11)$$

so that Eq. (7.8) results in

$$\sigma_\mu(\epsilon) = \frac{\sigma_\mu^0(\epsilon)}{\epsilon^2 + 1} (\epsilon^2 + C_{1\mu}\epsilon + C_{2\mu}). \quad (7.12)$$

This way, only the positions and widths of the resonances are fixed. There is one last and important thing to be taken into account, which is the boundary

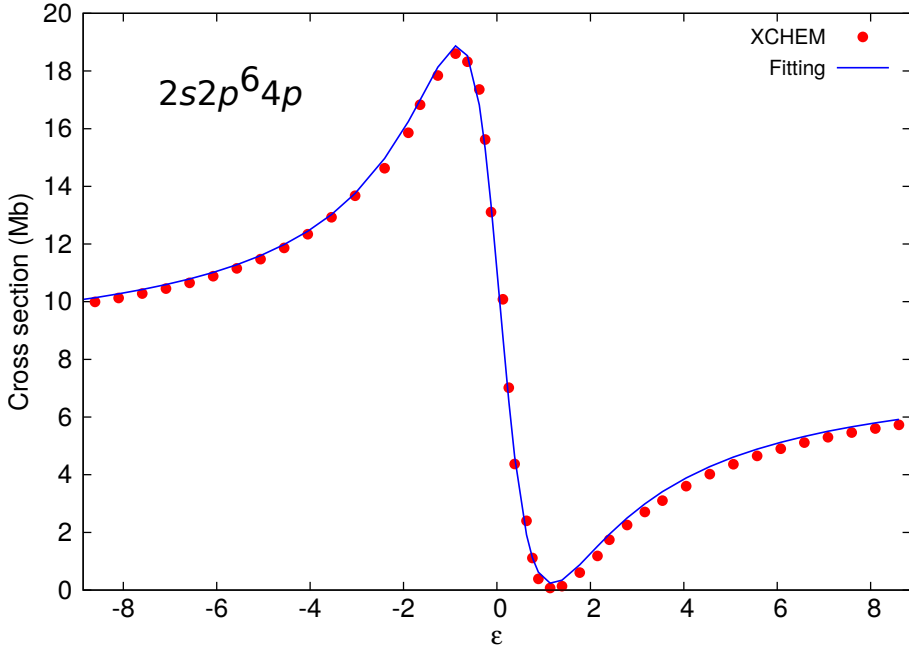


Figure 7.10: Computed and fitted $2s^2 2p^5 \epsilon d$ partial cross section in length gauge, near the $2s^2 2p^6 4p$ resonance. The fitting using (7.8) and (7.12) gives indistinguishable results for the bare eye and only the last one is shown.

conditions for $C_{1\mu}$ and $C_{2\mu}$. From Eq. (7.11), the α_μ parameters are determined from a quadratic equation, so that two roots are obtained:

$$\begin{aligned}\Re(\alpha_\mu) &= \frac{qC_{1\mu} + 2 \pm \sqrt{4C_{2\mu} - C_{1\mu}^2}}{2(1 + q^2)}, \\ \Im(\alpha_\mu) &= \frac{q(2 \pm \sqrt{4C_{2\mu} - C_{1\mu}^2}) - C_{1\mu}}{2(1 + q^2)}.\end{aligned}\quad (7.13)$$

From the fact that $\Re(\alpha_\mu)$ and $\Im(\alpha_\mu)$ must be real numbers, one obtains $4C_{2\mu} \geq C_{1\mu}^2$. This condition must be imposed during the fitting process in order to get meaningful results, in other words, the partial cross sections have to be non-negative. If for some scattering channel there is a very deep window resonance (almost zero partial cross section), the numerical fitted curve could go below zero to minimize the fitting error, giving unphysical values for the parameters. Then one has to select the correct Starace parameter from the two solutions of Eq. (7.13). For this we can use Eq. (7.9) to find the roots that better fulfill this condition. Actually most of the roots rejected following this selection criteria imply a correlation parameter $\rho^2 > 1$, which is outside its validity range. Nevertheless, if there are more than two roots that satisfy reasonably well Eq. (7.9), then we cannot be certain about which one is correct and we need extra information to

remove the ambiguity, for instance, by computing the branching ratios using an independent method.

The results obtained for $C_{1\mu}$, $C_{2\mu}$, α_μ and Γ_μ/Γ using the different methods are shown in Table 7.7. The gauge invariance of the Starace parameters is worse than that of partial widths Γ_μ but better than that of the q parameter. The values of the partial widths obtained with different methods agree very well with each other. These numbers confirm the known qualitative behavior: 95% of the decay of the first resonance goes into the $2p^{-1}\epsilon d$ channel, and 98% of the second and the third resonances.

7.2.3 *Effect of intermediate resonances in the modulation of the SBs in RABITT experiments*

So far, we have discussed one-photon single ionization processes only. However, XCHEM can describe single-ionization states of arbitrary symmetry (up to D_{2h} as mentioned in the previous sections). In particular, the code can be used to reproduce processes in which more than one photon is exchanged, including time-resolved measurements, such as HHG and RABITT interferometric techniques.

In several past works, RABITT has been applied to extract photoemission delays in the non-resonant continuum [187, 116]. Recent experimental efforts [188, 189] however, have extended this technique to regions of the spectrum where resonances are present. These experiments show that the presence of resonances significantly modifies the standard RABITT picture, and in this context, theoretical support can help in the interpretation of the measured spectra.

A straightforward way to theoretically simulate RABITT spectra is to solve the TDSE using pulses that reproduce as closely as possible the experimental conditions (pulses duration, spectral shape, intensity, etc). Most of the experiments however, employ pulses, some of them in the mid IR spectral domain, which make computations unfeasible. On the other hand, due to the moderate intensity of the pulses used in most experiments, which limits absorption to a single XUV and a single IR photon, one can safely rely on perturbation theory.

Taking advantage of this fact, a recently proposed theoretical model [190, 191], in combination with transition matrix elements obtained from ab initio stationary calculations, has been able to reproduce RABITT spectra in He with an accuracy similar to that resulting from solving the TDSE.

Very recently, new RABITT experiments have been carried out on Ne, in which one of the harmonics of the XUV (HH 63) is resonant with the $2s2p^63p$ autoionizing state [192] (see Figure 7.11). The experiment was performed using an IR with an intensity of $3 - 7 \cdot 10^{11} \text{ W/cm}^2$, pulse duration of 60 fs and wavelength in the [1688, 1718] nm range. The XUV harmonics had a FWHM of 350 – 400 meV.

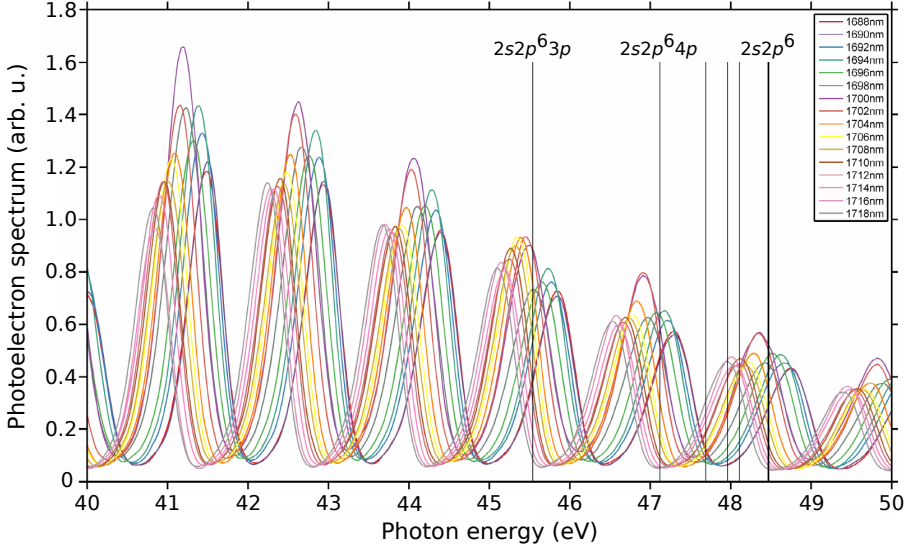


Figure 7.11: Experimental photoelectron spectrum for different wavelengths from 1688 nm to 1718 nm [192].

In this section we use the transition matrix elements computed within XCHEM to feed the perturbative model and reproduce these experimental results.

TWO-PHOTON FINITE-PULSE MODEL FOR RESONANT TRANSITIONS We are interested, in particular, in the process in which there is only one resonance in the intermediate states, and no resonances in the final states. Taking this into account, what is needed is to obtain an approximated analytical expression for the two-photon transition matrix elements:

$$M_{f \leftarrow g}^{2n \pm 1}(E_g + 2n\omega_{IR}) = \sum_{\alpha} \int d\epsilon' \frac{\langle \Psi_{fE} | \mathcal{O} | \Psi_{\alpha E} \rangle \langle \Psi_{\alpha E} | \mathcal{O} | g \rangle}{E_{Ne^+(2p^{-1})} + \epsilon' - [E_g + (2n \pm 1)\omega_{IR}] + i0^+}, \quad (7.14)$$

where g and f are the ground and the final state respectively, and ω_{IR} is the IR central frequency. As pointed in the previous section, when a Ne electron is promoted to the continuum by a photon absorption and below the $2s2p^6$ ionization threshold, two channels of $^1P^o$ symmetry are open: $2s^22p^5\epsilon s$ and $2s^22p^5\epsilon d$. To apply the model, this intermediate channels has to be decoupled into a resonant $|\Psi_{R,E}^{1P^o}\rangle$ and non-resonant $|\Psi_{D,E}^{1P^o}\rangle$ channel:

$$\begin{aligned} |\Psi_{R,E}^{1P^o}\rangle &= C_{s,R} |\Psi_{s,E}^{1P^o}\rangle + C_{d,R} |\Psi_{d,E}^{1P^o}\rangle, \\ |\Psi_{D,E}^{1P^o}\rangle &= C_{s,D} |\Psi_{s,E}^{1P^o}\rangle + C_{d,D} |\Psi_{d,E}^{1P^o}\rangle, \end{aligned} \quad (7.15)$$

where the coefficients $C_{s/d,R/D}$ that makes this transformation possible need to be determined (see below). Once the problem has been separated, Eq. (7.14) can be expressed as:

$$M_{f \leftarrow g}^{2n \pm 1} = M_{f \leftarrow D \leftarrow g}^{2n \pm 1} + M_{f \leftarrow R \leftarrow g'}^{2n \pm 1} \quad (7.16)$$

where the energy dependences have been dropped for the sake of simplicity and (see [190, 191, 193])

$$\begin{aligned} M_{f \leftarrow D \leftarrow g}^{2n \pm 1} &= \mathcal{O}_{fE,DE} \mathcal{O}_{DE,g} w(z_f^\mp), \\ M_{f \leftarrow R \leftarrow g}^{2n \pm 1} &= \mathcal{O}_{fE,RE} \mathcal{O}_{RE,g} [w(z_f^\mp) + (\beta_{Ea} - \epsilon_{Ea}^{-1})(q - i)w(z_a)], \end{aligned} \quad (7.17)$$

where the Faddeeva special functions $w(z) = e^{-z^2} \text{erfc}(-iz)$ incorporate the effect of using pulses of finite duration through its argument. The a subindex stands for the intermediate resonance, with q Fano parameter and reduced energy $\epsilon_{Ea} = 2(E_g + 2n\omega_{IR} - E_r)/\Gamma$. The parameter β_{Ea} measures the relative strength of the transition from the intermediate resonance to the final continuum state. This is a free parameter of the model and typically takes very small values [188]. $\mathcal{O}_{DE,g}$ and $\mathcal{O}_{RE,g}$ are the dipole transition matrix elements that couple the ground state to the non-resonant and the resonant intermediate states, respectively. These matrix elements have been computed using XCHEM (see below for details). $\mathcal{O}_{fE,DE}$ and $\mathcal{O}_{fE,RE}$ are the dipole transition matrix elements between the intermediate and final continuum states. They have been computed by approximating the radial parts of the continuum orbitals to spherical plane-waves and evaluating the result in the on-shell region [191].

There are three possible final states for the Ne two-photon transition from the ground state: $|\Psi_{Ne^+(2p^{-1}) \otimes \epsilon p}^{(-)1S^e}\rangle$, $|\Psi_{Ne^+(2p^{-1}) \otimes \epsilon p}^{(-)1D^e}\rangle$ and $|\Psi_{Ne^+(2p^{-1}) \otimes \epsilon f}^{(-)1D^e}\rangle$. Then the final population of the SB is obtained by adding the probabilities of reaching these three final states. From the profile of the SB population *vs* time-delay, the atomic phases can be extracted (see 4.2.1).

In order to apply the model we need to compute the coefficients $C_{s/d,R/D}$ in Eq. (7.15), to be able to compute the $\mathcal{O}_{D/RE,g}$ dipoles. If the complex dipole transitions from the ground state to the intermediate scattering states $|\Psi_{Ne^+(2p^{-1}) \otimes \epsilon s}^{(-)1P^o}\rangle$ and $|\Psi_{Ne^+(2p^{-1}) \otimes \epsilon s}^{(-)1P^o}\rangle$ near the resonance of interest ($2s2p^63p$), are parameterized as:

$$\mathcal{O}_{\mu E,g}(\epsilon) = A_\mu + B_\mu \frac{(q_\mu + \epsilon)}{\epsilon + i}, \quad (7.18)$$

where q_μ is a channel dependent Fano-like parameter and A_μ, B_μ are in general complex numbers. Then we can define the normalized coefficients

$$\begin{aligned} C_{s,D} &= -\frac{B_d(q_d - i)}{\sqrt{|B_s(q_s - i)|^2 + |B_d(q_d - i)|^2}}, \\ C_{d,D} &= \frac{B_s(q_s - i)}{\sqrt{|B_s(q_s - i)|^2 + |B_d(q_d - i)|^2}}, \\ C_{s,R} &= -C_{d,D}^*, \quad C_{d,R} = C_{s,D}^*, \end{aligned} \quad (7.19)$$

to decouple the intermediate states in the resonant and non-resonant components appearing in Eq. (7.15). Making use of the previous definitions we can express the resonant transition $\mathcal{O}_{RE,g}$ as a Fano-like close form:

$$\mathcal{O}_{RE,g}(\epsilon) = B_R \frac{(q + \epsilon)}{\epsilon + i}, \quad (7.20)$$

where $B_R = \sum_\mu (A_\mu + B_\mu) C_{\mu,R}$. We can also express the Fano q parameter in terms of these coefficients:

$$q = \frac{1}{B_R} [(B_s q_s + i A_s) C_{s,R} + (B_d q_d + i A_d) C_{d,R}], \quad (7.21)$$

for which the imaginary part must cancel out in order to give a real number.

Figure 7.12 shows the results of the fitting using Eq. (7.18) in length gauge near the $2s2p^63p$ autoionizing states, allowing us to obtain the parameters presented in Table 7.8. With these, the resonance Fano parameter computed using Eq. (7.21) is $q = (-1.477, -0.017)$, which have a very small imaginary component that lies within the fitting errors. Comparing the real part with the value reported in Table 7.6 for the same resonance and gauge (-1.47), it is clear that the result is consistent.

It should be noted that, to recover the transition amplitude to continuum states with the definite spherical symmetry character, we must combine several continuum states computed by XCHEM in D_{2h} symmetry. See Appendix (G) for details.

Comparing Eq. (7.18) with the expression provided by Starace [184]

$$\mathcal{O}_{\mu E,g}(\epsilon) = \mathcal{O}_{\mu E,g}^0 [1 + \alpha_\mu^* \frac{(q - i)}{\epsilon + i}], \quad (7.22)$$

Table 7.8: Couplings parameters for the two-photon resonant transition model.

$\mathcal{O}_{DE,g}$	B_R	$C_{s,D}$	$C_{d,D}$
(0.1376, 0.3421)	(0.5784, -0.3982)	(-0.7727, -0.5949)	(-0.1092, -0.1972)

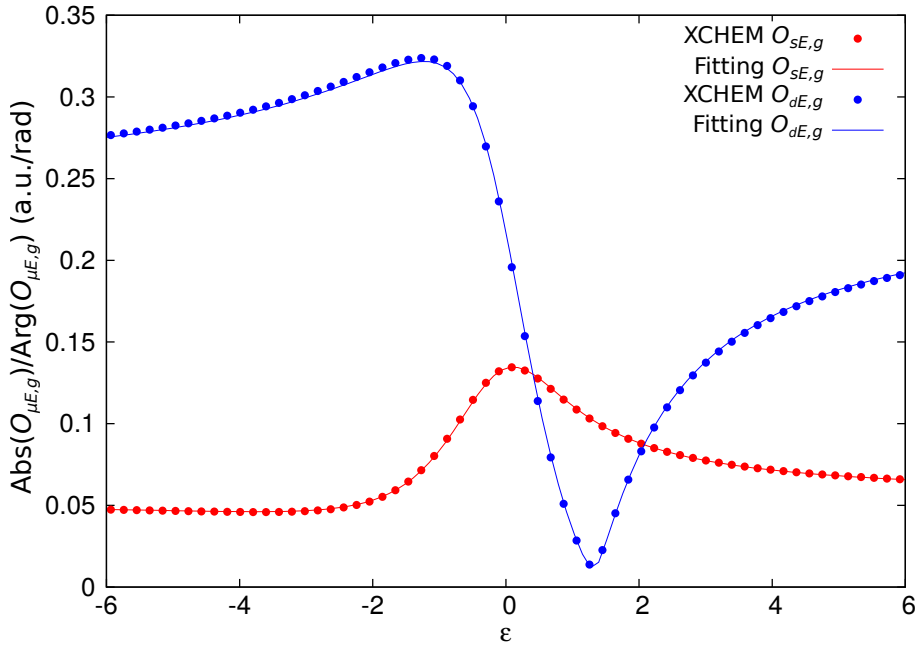


Figure 7.12: Computed and fitted dipole transitions around the $2s2p^63p$ resonance and in length gauge, from the ground state to the $2s2p^6\epsilon s$ and $2s2p^6\epsilon d$ scattering channels.

it is easy to show that the following relations hold:

$$\begin{aligned} \mathcal{O}_{\mu E, g}^0 &= A_\mu + B_\mu, \\ \alpha_\mu &= \frac{B_\mu^*(q_\mu + i)}{(A_\mu + B_\mu)^*(q + i)}. \end{aligned} \quad (7.23)$$

The equation above provides an extra way to compute the Starace parameters, which gives for the two open channels: $\alpha_s = (-0.761, -0.096)$ and $\alpha_d = (0.903, -0.0065)$. This is in very good agreement with the results shown in Table 7.7: $\alpha_s = (-0.770, -0.097)$ and $\alpha_d = (0.934, -0.045)$.

Having checked that the parameters extracted from the fitting provides meaningful results, we can use the model to compute the SB population *vs* time delay, and from it, its phase (see 4.2.1). This results are shown in Figure 7.13, in which the measure phase of SB 62 and SB 64 are shown together with the theoretical calculation using the model (in this case a parameter $\beta_{Ea} = 0.003$ slightly improve the theoretical result). The agreement for the SB 62 is quite good. In the case of SB 64, on the other hand, we observe a big discrepancy, due to the presence of a second intermediate resonance besides $2s2p^63p$. Indeed, HH 65 is in resonance with $2s2p^64p$, as can be seen from Figure 7.11. The two-photon transition model described above only accounts for one intermediate resonance. The same

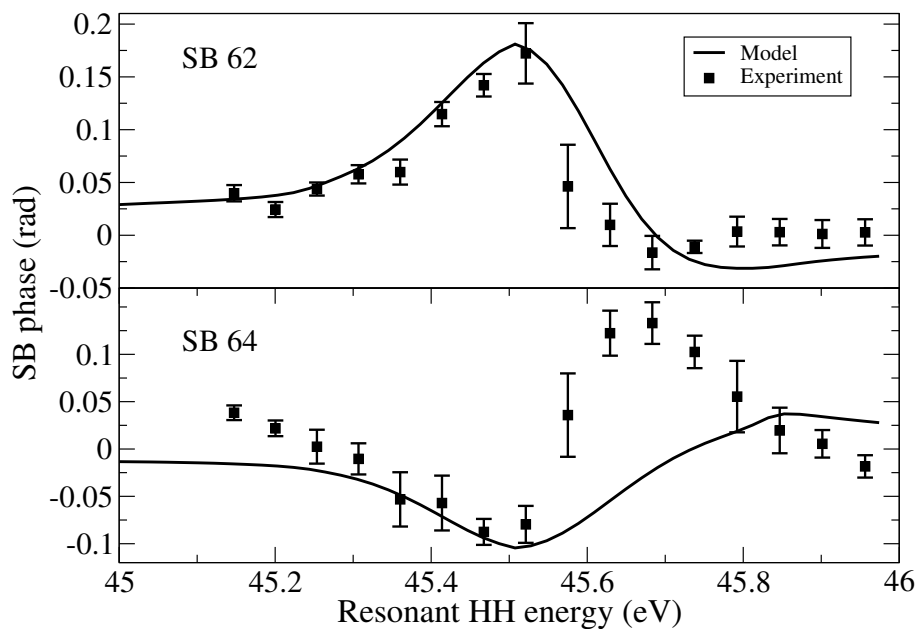


Figure 7.13: Phase of the SB 62 (top panel) and SB 64 (bottom panel) vs the energy of the HH 63. The experimental values (solid squares) are compared with the model (solid line).

model, however, can be generalized to describe the effect of an arbitrary number of ionizing states.

Part IV

CONCLUSIONS & PERSPECTIVES

CONCLUSIONS & PERSPECTIVES

One of the main limitations of existing QCPs is their inability to describe the electronic continuum of molecules, which for many years has limited the study of molecular ionization processes. In this work, we have merged existing QCPs and state-of-the-art numerical scattering methods to overcome this limitation. The new method follows the spirit of earlier close-coupling approaches, in which the scattering wave function is expanded in a basis of channel states representing a molecular cation in a given electronic state and a continuum electron satisfying the appropriate scattering boundary conditions. The electronic configuration space is divided into a short-range region, where electronic configurations are built in terms of Gaussian functions compatible with QCPs, and a long-range region, where a single electron interacts with a finite number of correlated molecular-ion states. The state of this electron is expressed in terms of the hybrid basis GABS, which combines monocentric Gaussian functions with B-splines appropriate to represent the continuum.

Our method takes advantage of existing *ab initio* quantum chemistry packages such as MOLCAS and MOLPRO, putting their advanced machinery at our disposal and facilitating its widespread use by chemical physicists. Other computational approaches combining *ab initio* quantum chemistry and scattering methods are currently under development [100, 101, 102, 30, 94, 99], but at variance with them, our method is able to include electron correlation and exchange in the electronic continuum at the same level of accuracy as quantum chemistry does for bound states. Another important advantage is that increasing the number of electrons for a fixed number of scattering channels does not increase the computational cost of the full dimensional problem significantly. In other words, the effort made to evaluate the electronic continuum in, let's say, H_2 , would be similar to that required for a polyatomic molecule like water or acetylene. Finally, the present method also allows us to describe ionization in many-electron atoms, again taking advantage of many of the features that QCPs incorporate and that are not so often available in atomic computational codes. We want to mention that there is another research group that uses a formalism very similar to ours, merging QCPs with scattering methods [103, 104]. However their basis set, which also comprises B-splines and Gaussian functions, only incorporates standard GTOs, whereas, besides those functions, we include PSGTOs, which help us to reduce the maximum orbital angular momentum, and to avoid the expensive integrals between polycentric Gaussian functions and B-splines.

One of the key ingredients of XCHEM is the basis set that matches the photoelectron short-range radial domain with the long-range. To fulfil this we have introduced a new hybrid Gaussian-B-spline basis (GABS) for the description of the continuum that permits to achieve high electron energies while, at the same time, preserving a purely Gaussian representation of the electronic wave function in a radial region large enough to encompass whole poly-electronic atoms as well as small molecules. We have demonstrated that the hybrid GABS basis can be used to compute with high accuracy all the observables associated with the interaction of a single-active electron atom with external light pulses in a wide energy range. In particular, we have reproduced with the GABS basis the energies and transition amplitudes of the hydrogen atom as well as the fully differential photoelectron distributions that result from the interaction of the atom with strong ultra-short external laser pulses. All the results are in excellent agreement with those obtained numerically from well-established B-spline basis, with data taken from the literature, and with analytical predictions, when available. In the analysis of the results from the solution of the time-dependent Schrödinger equation for the hydrogen atom exposed to external pulses, we have presented and discussed new fully differential photoelectron distributions of the hydrogen ATI spectra obtained in the conditions reported in two recent works [146, 147]. In particular, we contextualize the low-energy multi-peak structure of the ATI spectrum of hydrogen reported by Grum-Grzhimailo and co-workers [147] and the dynamic interference mechanism highlighted recently by Demekhin and Cederbaum [154] within the theoretical framework outlined long ago by Cormier and Lambropoulos [153]. In conclusion, the GABS basis has the benefit of the most flexible numerical basis for the description of the continuum while at the same time being expressed in terms of standard Gaussian functions in a large inner radial region.

As a first step towards more complex systems, we have illustrated the performance of the XCHEM method in the multichannel ionization of He and H₂ by comparing with results from nearly exact *ad hoc* computational methods available in the literature for such simple systems.

Then, we have used the XCHEM approach to study multichannel photoionization of Ne in the vicinity of the autoionizing states lying between the $2s^22p^5$ and $2s2p^6$ ionization thresholds. This is the first application of the XCHEM approach to the case in which the remaining cation is a multi-electron target. Comparison with the results of independent benchmark calculations with the STOCK code, performed at the same level of theory, demonstrates the good performance of our approach. Our calculated total photoionization cross sections, obtained at the XCI level, are also in very good agreement with the absolute ones measured by Samson et al [176]. From these results, we have extracted resonance parameters, namely, resonance positions, total autoionization widths, Fano profile parameters and correlation parameters for the lowest three autoionizing states. These are in good agreement with those reported in earlier theoretical and experimental work.

We have gone a step further and evaluated partial photoionization cross sections, and, from them, partial autoionization widths and Starace parameters for the lowest three resonances. Our results confirm earlier expectations that the resonances of $^1P^o$ symmetry converging to the $2s2p^6$ threshold are much more likely to decay into the $2p^{-1}\epsilon d$ continuum than into the $2p^{-1}\epsilon s$ one [183], but we have now quantified how much likely: 95% vs 5%, respectively, for the lowest resonance, and 98% and 2% for the other two resonances. We have also shown that, in very narrow ranges of the photoelectron energy, in the vicinity of the resonances, the partial $2p^{-1}\epsilon s$ cross section can be larger than the $2p^{-1}\epsilon d$ one, in contrast with the expectation that the latter should amply dominate in the whole energy range.

With the matrix elements obtained within XCHEM, we used the two-photon finite-pulse model for resonant transitions to compute the side bands modulation, and reproduce a very recent RABITT experiment in Ne [192]. For the conditions we considered in the model, only one intermediate resonance, the agreement with the experiment was very good, setting XCHEM as a candidate method to interpret attosecond experiments in novel gases and small molecules.

All these results show the capabilities of the XCHEM code to describe electron correlation in the continuum and hence autoionization decay in multi-electron systems, which is of crucial importance in the case of molecular targets and for which the XCHEM code has been designed. In fact, the description of atomic systems with the XCHEM code is more challenging than that of molecular systems, since one cannot use multi-center Gaussian expansions without compromising spherical symmetry. In particular, it is hard to preserve the degeneracy of thresholds, which implies that rather large powers of the Gaussian pre-exponential factors (K_ℓ) must be used to obtain an accurate representation of continuum states in the short and middle ranges. This gives us confidence that the description of resonant molecular photoionization with the XCHEM code should be rather straightforward.

We are currently studying the ionization of more complicated systems, such as N_2 , H_2O and O_2 using the XCHEM approach. Some preliminary results on this systems show a very good agreement when compare with independent bechmarks.

Several solutions could be adopted to improve the performance of our formalism. One of the most straightforward ones would be to include part of the interaction between the polycentric Gaussian functions describing the parent-ion states and the B-splines. This could be done without computing numerically the whole integral by expanding the asymptotic tail of the polycentric Gaussian molecular orbitals in terms of the monocentric orbitals. In our method, the latter do interact with B-splines, so provided these functions start at a distance at which the polycentric component of the molecular orbitals has only a tail, we would be able to recover part of this neglected interaction.

One other straightforward research line to follow is to use XCHEM to solve the time-dependent Schrödinger equation. For atoms and molecules in the fixed nuclei approximation, a scheme similar to that explained in this thesis for the photoionization of the hydrogen atom can be applied. Actually, we obtained few preliminary results for He and Ne which are in good agreement with independent computations and perturbative calculations. In order to include the nuclear motion in molecules, we would have to implement the Feshbach partitioning method, specially in the case in which the lifetime of the autoionizing states is comparable to the time scale of the nuclear motion, or when in general dissociative channels are energetically available, since one can no longer assume that ionization occurs before the nuclei have time to move significantly. The XCHEM code is able to handle such a partitioning without any major difficulty. However, this should be done in a grid of nuclear geometries, so that the resulting potential energy surfaces can be used to evaluate the wave functions that describe the nuclear motion.

CONCLUSIONES & PERSPECTIVAS

Una de las principales limitaciones de los QCPs existentes, es su incapacidad para describir el continuo electrónico en moléculas, lo cual ha limitado por muchos años el estudio de la ionización molecular. En esta tesis hemos combinados QCPs con métodos numéricos avanzados para calcular los estados del continuo, y así superar las dificultades anteriormente descritas. El nuevo método, XCHEM, se basa en las aproximaciones the close-coupling (CC), en la cual la función de onda del continuo es expandida en una base de funciones de canal, que representan al catión molecular en un dado estado electrónico, donde además, el electrón promovido al continuo satisface con las condiciones apropiadas de contorno para la dispersión. El espacio de configuraciones electrónicas está dividido en una región de corto alcance, donde los electrones son descritos por funciones gaussianas compatibles con los QCPs, y una región de largo alcance, en la cual el electrón interactúa con un número finito de estados iónicos moleculares correlacionados. Este electrón que escapa del sistema es descrito por la base híbrida GABS, que está compuestas por gaussianas centradas den el centro de masas del sistema y B-splines, funciones apropiadas para representar el comportamiento oscilatorio del continuo.

El método XCHEM aprovecha la avanzada maquinaria de la química cuántica que ha sido implementada en los paquetes computacionales MOLCAS y MOLPRO, para así facilitar la utilización de dicho método por parte de una comunidad mucho más amplia de químicos-físicos que no necesariamente esté familiarizada con los métodos de dispersión.

En la literatura existen otros modelos en desarrollo que combinan los métodos *ab initio* de la química cuántica con los de dispersión [100, 101, 102, 30, 94, 99], pero a diferencia de esos, el nuestro es capaz de incluir la correlación electrónica en el continuo, al mismo nivel de precisión con que es tratada en los estados enlazados. Otra ventaja importante de XCHEM es que aumentando el número de electrones para un número fijo de canales de dispersión, no encarece el costo computacional de manera significativa. Nosotros queremos resaltar que existe otro grupo de investigación que usa un formalismo muy parecido al que hemos desarrollado, combinando QCPs con métodos de dispersión y una base de funciones muy parecida la nuestra [103, 104]. A pesar de que también utilizan una combinación de B-spline y gaussianas, para estas últimas solo utilizan las GTOs que de manera estándar aparecen en los QCPs, mientras nosotros además de las GTOs utilizamos las PSGTOs, que ayudan a reducir el máximo momento angu-

lar orbital y evita el cálculo de las costosas integrales entre las B-splines y las gaussianas poly-céntricas.

Las pruebas realizadas para la base GABS, uno de los componentes fundamentales de XCHEM, a través del estudio de la ionización del átomo de hidrógeno en presencia de diferentes pulsos the attosegundo, arrojaron muy buenos resultados al comparar con valores analíticos y cálculos realizados por otros autores utilizando métodos y bases diferentes. En particular, se han reproducido varias distribuciones diferenciales del foto-electrón y espectros ATI.

Como un primer paso en el camino hacia el estudio de sistemas más complejos, ilustramos el desempeño del método XCHEM en la ionización multicanal del átomo de He y la molécula de H₂ con núcleos fijos. El cual resultó ser muy bueno al comparar los resultados obtenidos con otros calculados utilizando códigos independientes y virtualmente exactos.

También hemos utilizado XCHEM para estudiar la fotoionización multicanal del átomo de Ne, en la región donde se encuentran varias resonancias convergentes al $2s2p^6$ umbral de ionización. Esta constituye la primera aplicación del método XCHEM para el caso en el que los cationes que se forman después de la ionización tienen varios electrones. Las comparaciones efectuadas con los cálculos hechos utilizando nuestro modelo y el código STOCK especializado en átomos, demostró las excelentes capacidades de XCHEM. Aumentando el nivel de correlación electrónica, fuimos capaces de obtener la sección eficaz de fotoionización con muy buena precisión comparada con datos experimentales [176]. También extrajimos los principales parámetros que caracterizan los estados autoionizantes: posición, ancho, parámetro de Fano y el parámetro de correlación, y una vez más comparaban muy bien con otros resultados teóricos y experimentales.

Al haber comprobado el buen desempeño de XCHEM, entonces calculamos nuevas magnitudes que no habían sido aún reportadas en la literatura, como son los parámetros de Starace y los anchos parciales de decaimiento para las tres primeras resonancias de simetría $1P^o$ que convergen al $2s2p^6$ umbral de ionización. Con los elementos de matrix calculados, usamos el two-photon finite-pulse model for resonant transitions para calcular la modulación de las bandas laterales en un experimento RABITT muy reciente [192]. Como en el modelo solo consideramos la posibilidad de un estado intermedio resonante, cuando comparamos con el experimento bajo las mismas condiciones, el acuerdo es muy bueno. Por lo que sitúa al método XCHEM como candidato para poder interpretar y reproducir experimentos que se realizan con pulsos de attosegundo en gases nobles y moléculas pequeñas.

Todos los resultados anteriormente expuestos, demuestran el buen desempeño del código XCHEM a la hora de describir la correlación electrónica en el continuo, y por tanto, el decaimiento por autoionización en sistemas polyelectrónicos, que

es de importancia vital para los sistemas moleculares para los cuales XCHEM fue diseñado.

En estos momentos, también estamos estudiando la ionización de otros sistemas más complicados, como N_2 , CO, H_2O y O_2 . Los resultados preliminares que se han obtenido indican un acuerdo muy bueno con resultados experimentales publicados.

Varias cosas pueden aún hacerse para mejorar nuestro formalismo. Uno de los más sencillos sería incluir parte de la interacción entre las gaussianas polycéntricas y las B-splines. Esto podría hacerse, expandiendo la cola de la componente polycéntrica de los orbitales moleculares en función de las gaussianas monocéntricas. De esta manera, si las B-splines empiezan a una distancia tal, que la componente policéntrica de los orbitales ya a empezado a decaer, entonces en principio pudiera utilizarse la aproximación anteriormente expuesta.

Otra extensión del método que es evidente, es utilizarlos para resolver la TDSE. Para átomos y moléculas en la FNA, se puede utilizar un esquema similar al utilizado en la tesis para estudiar la fotoionización del hidrógeno. De manera preliminar ya hemos obtenido varios buenos resultados para el He y el Ne interactuando con pulsos ultracortos. Para poder incluir el movimiento nuclear, habría implementar la partición de Feshbach, especialmente cuando el tiempo de vida media de alguna resonancia relevante en la dinámica sea comparable con los tiempos característicos del movimiento nuclear. También permitiría estudiar otro tipo de fenómenos como la fragmentación molecular.

Part V

APPENDICES

X_{lm} ASSOCIATED TO THE MOLECULAR ABELIAN POINT GROUPS

Point Group Name

Symmetry	SASH	ℓ and m constraints
----------	------	----------------------------

C_1

A	$X_{\ell m}, X_{\ell, -m}$	any ℓ and any m
-----	----------------------------	------------------------

C_s

A'	$X_{\ell m}, X_{\ell, -m}$	$\ell + m$ even
A''	$X_{\ell m}, X_{\ell, -m}$	$\ell + m$ odd

C_2

A	$X_{\ell m}, X_{\ell, -m}$	any ℓ and even m
B	$X_{\ell m}, X_{\ell, -m}$	any ℓ and odd m

C_i

A_g	$X_{\ell m}, X_{\ell, -m}$	even ℓ
A_u	$X_{\ell m}, X_{\ell, -m}$	odd ℓ

C_{2v}

A_1	$X_{\ell m}$	any ℓ and even m
A_2	$X_{\ell, -m}$	any ℓ and even m
B_1	$X_{\ell m}$	any ℓ and odd m
B_2	$X_{\ell, -m}$	any ℓ and odd m

D_2

A	$X_{\ell m}$	even ℓ and even m
	$X_{\ell, -m}$	odd ℓ and even m
B_1	$X_{\ell m}$	odd ℓ and even m
	$X_{\ell, -m}$	even ℓ and even m
B_2	$X_{\ell m}$	even ℓ and odd m
	$X_{\ell, -m}$	odd ℓ and odd m
B_3	$X_{\ell m}$	odd ℓ and odd m
	$X_{\ell, -m}$	even ℓ and odd m

D_{2h}

A_g	$X_{\ell m}$	even ℓ and even m
B_{1g}	$X_{\ell, -m}$	even ℓ and even m
B_{2g}	$X_{\ell m}$	even ℓ and odd m
B_{3g}	$X_{\ell, -m}$	even ℓ and odd m
A_u	$X_{\ell, -m}$	odd ℓ and even m
B_{1u}	$X_{\ell m}$	odd ℓ and even m
B_{2u}	$X_{\ell, -m}$	odd ℓ and odd m
B_{3u}	$X_{\ell m}$	odd ℓ and odd m

Figure A.1: Constraints the symmetry adapted spherical harmonics have to obey in order to describe, angularly, the different irreducible representations of the Abelian point group symmetries.

MATRIX ELEMENTS BETWEEN EXTENDED CHANNEL FUNCTIONS REPRESENTED WITH GABS BASIS FUNCTIONS

The matrix element of a totally symmetric operator \mathcal{O} between extended channel functions is

$$\mathcal{O}_{\alpha i, \beta j} = \langle \bar{Y}_{\alpha i} | \mathcal{O} | \bar{Y}_{\beta j} \rangle = \frac{N_{\alpha i}^* N_{\beta j}}{N_e} \langle Y_{\alpha} \varphi_i | \mathcal{O} \left(1 - \sum_{i=1}^{N_e-1} \mathcal{P}_{i N_e} \right) | Y_{\beta} \varphi_j \rangle, \quad (\text{B.1})$$

where we have made use of the hermiticity and idempotency of the antisymmetrizer ($\hat{A}^\dagger = \hat{A}$, $\hat{A}^2 = \hat{A}$) and of the invariance of the operator \mathcal{O} with respect to permutations ($\forall \mathcal{P} \in \mathcal{S}_{N_e}$, $[\mathcal{O}, \mathcal{P}] = 0 \implies [\mathcal{O}, \hat{A}] = 0$). If either φ_i or φ_j have disjoint support from those of the parent ions, the permutation operators in (B.1) can be dropped

$$\begin{aligned} \mathcal{O}_{\alpha i, \beta j} &= \langle \bar{Y}_{\alpha i} | \mathcal{O} | \bar{Y}_{\beta j} \rangle = \frac{N_{\alpha i}^* N_{\beta j}}{N_e} \langle Y_{\alpha} \varphi_i | \mathcal{O} | Y_{\beta} \varphi_j \rangle, \\ \text{if } \varphi_i(r) &= 0 \vee \varphi_j(r) = 0, \quad \forall r < R_0. \end{aligned} \quad (\text{B.2})$$

In the latter condition, the overlap, mono-electronic and bi-electronic inter-channel matrix elements ($\alpha = (a \ell_{\alpha} m_{\alpha})$, $\beta = (b \ell_{\beta} m_{\beta})$) have simple expressions, as given below.

Overlap matrix elements

$$S_{\alpha i, \beta j} = \langle \bar{Y}_{\alpha i} | \bar{Y}_{\beta j} \rangle = \frac{N_{\alpha i}^* N_{\beta j}}{N_e} \langle Y_{\alpha} | Y_{\beta} \rangle \langle \varphi_i | \varphi_j \rangle = \frac{N_{\alpha i}^* N_{\beta j}}{N_e} \delta_{\alpha \beta} s_{ij} \quad (\text{B.3})$$

where $\delta_{\alpha \beta} = \delta_{ab} \delta_{\ell_{\alpha} \ell_{\beta}} \delta_{m_{\alpha} m_{\beta}}$ and $s_{ij} = \langle \varphi_i | \varphi_j \rangle$.

Mono-electronic operators

These operators can be written as

$$T = \sum_{i=1}^{N_e} t(i), \quad (\text{B.4})$$

and the corresponding matrix elements

$$T_{\alpha i, \beta j} = \frac{N_{\alpha i}^* N_{\beta j}}{N_e} \left(T_{ab} \delta_{\ell_\alpha \ell_\beta} \delta_{m_\alpha m_\beta} s_{ij} + \delta_{ab} t_{\ell_\alpha m_\alpha i, \ell_\beta m_\beta j} \right), \quad (\text{B.5})$$

where $T_{ab} = \langle \Phi_a | T | \Phi_b \rangle$ and $t_{\ell m i, \ell' m' j} = \langle \varphi_i Y_{\ell m} | t | \varphi_j Y_{\ell' m'} \rangle$. The matrix elements T_{ab} can be obtained from the QCPs.

Hamiltonian matrix elements

The total electrostatic hamiltonian is given by

$$H = K + V^{ee} + V^{ne} + V^{nn}, \quad (\text{B.6})$$

where K is the kinetic energy operator, $V^{nn} = \sum_{A, B > A} Z_A Z_B / R_{AB}$ is the nuclear repulsion potential, V^{en} is the electron-nuclei interaction potential,

$$V^{en} = - \sum_{i=1}^{N_e} \sum_{A=1}^{N_n} \frac{Z_A}{r_{iA}}, \quad (\text{B.7})$$

and V^{ee} is the electron-electron repulsion potential,

$$V^{ee} = \sum_{i, j > i} \frac{1}{r_{ij}}. \quad (\text{B.8})$$

The corresponding matrix element has the form

$$\begin{aligned} H_{\alpha i, \beta j} = & \frac{N_{\alpha i}^* N_{\beta j}}{N_e} \left[H_{ab} \delta_{\ell_\alpha \ell_\beta} \delta_{m_\alpha m_\beta} s_{ij} + \delta_{ab} \delta_{\ell_\alpha \ell_\beta} \delta_{m_\alpha m_\beta} k_{i, j}^{(\ell_\alpha)} \right. \\ & \left. + \sum_{\ell m} \langle Y_{\ell_\alpha m_\alpha} Y_{\ell m} | Y_{\ell_\beta m_\beta} \rangle \langle \varphi_i | r^{-\ell-1} | \varphi_j \rangle M_{ab}^{mol, \ell m} \right], \end{aligned} \quad (\text{B.9})$$

where $M_{ab}^{mol, \ell m}$ is the molecular transition multipole given by

$$M_{ab}^{mol, \ell m} = M_{ab}^{el, \ell m} + M_{ab}^{nuc, \ell m}, \quad (\text{B.10})$$

being $M_{ab}^{el, \ell m}$ the electronic transition multipole,

$$M_{ab}^{el, \ell m} = \frac{4\pi}{2\ell+1} \langle \Phi_a | \sum_{i=1}^{N_e-1} r_i^\ell Y_{\ell m}(\hat{r}_i) | \Phi_b \rangle = \frac{4\pi(N_e-1)}{2\ell+1} \langle \Phi_a | r_1^\ell Y_{\ell m}(\hat{r}_1) | \Phi_b \rangle, \quad (\text{B.11})$$

and $M_{ab}^{nuc, \ell m}$ the nuclear transition multipole,

$$M_{ab}^{nuc, \ell m} = - \frac{4\pi}{2\ell+1} \delta_{ab} \sum_{A=1}^{N_n} Z_A R_A^\ell Y_{\ell m}^*(\hat{R}_A). \quad (\text{B.12})$$

The matrix elements H_{ab} and $M_{ab}^{mol,\ell m}$ are obtained from the QCPs. Notice that the monopole term has the simple form

$$M_{ab}^{mol,00} = \sqrt{4\pi}\delta_{ab}Q, \quad (\text{B.13})$$

where Q is the total charge of the parent ion. Notice also that, in order for the scattering theory to be applicable, the channels must be asymptotically decoupled, i.e., the parent-ion states must diagonalize the $N_e - 1$ molecular hamiltonian

$$H_{ab} = E_a\delta_{ab}. \quad (\text{B.14})$$

If we define the hydrogenic mono-electronic operator h as

$$h_{i,j}^{(\ell)} = k_{i,j}^{(\ell)} + Q\langle\varphi_i|r^{-1}|\varphi_j\rangle, \quad (\text{B.15})$$

we can rewrite the expression for the Hamiltonian matrix elements by explicitly indicating the contribution of the multipoles with $\ell > 0$ only

$$\begin{aligned} H_{\alpha i, \beta j} = & \frac{N_{\alpha i}^* N_{\beta j}}{N_e} \left[(E_a s_{ij} + h_{i,j}^{(\ell_\alpha)}) \delta_{ab} \delta_{\ell_\alpha \ell_\beta} \delta_{m_\alpha m_\beta} \right. \\ & \left. + \sum_{\ell > 0, m} \langle Y_{\ell_\alpha m_\alpha} Y_{\ell m} | Y_{\ell_\beta m_\beta} \rangle \langle \varphi_i | r^{-\ell-1} | \varphi_j \rangle M_{ab}^{mol, \ell m} \right]. \end{aligned} \quad (\text{B.16})$$

In the special case in which the target states does not have electrons, it may be necessary to compute the nuclear multipoles explicitly. In the case of a proton displaced by R along the z axis,

$$M^{nuc, \ell m} = -\delta_{m0} \sqrt{\frac{4\pi}{2\ell+1}} R^\ell. \quad (\text{B.17})$$

In the case of the H_2^{2+} parent ion that results from the ionization of the H_2^+ ion, where the two protons are located at $\pm R/2$ along the z axis, only even multipoles differ from zero,

$$M^{nuc, \ell=2j m} = -\delta_{m0} \sqrt{\frac{4\pi}{2\ell+1}} \frac{R^\ell}{2^{\ell-1}}, \quad M^{nuc, \ell=2j+1 m} = 0. \quad (\text{B.18})$$

Other matrix elements

For completeness we also provide the expressions for the matrix elements of the electron-nucleus and electron-electron interactions potentials. For the former, the matrix element is given by

$$V_{\alpha i, \beta j}^{en} = \frac{N_{\alpha i}^* N_{\beta j}}{N_e} \left[V_{ab}^{en} \delta_{\ell_\alpha \ell_\beta} \delta_{m_\alpha m_\beta} s_{ij} + \sum_{\ell m} \langle Y_{\ell_\alpha m_\alpha} Y_{\ell m} | Y_{\ell_\beta m_\beta} \rangle \langle \varphi_i | r^{-\ell-1} | \varphi_j \rangle M_{ab}^{nuc, \ell m} \right], \quad (\text{B.19})$$

where the integral of three harmonics has the following expression

$$\langle Y_{a\alpha} Y_{b\beta} | Y_{c\gamma} \rangle = \sqrt{\frac{(2a+1)(2b+1)}{4\pi(2c+1)}} C_{a0,b0}^{c0} C_{a\alpha,b\beta}^{c\gamma}, \quad (\text{B.20})$$

and for the latter,

$$V_{\alpha i, \beta j}^{ee} = \frac{N_{\alpha i}^* N_{\beta j}}{N_e} \left[V_{ab}^{ee} \delta_{\ell_\alpha \ell_\beta} \delta_{m_\alpha m_\beta} s_{ij} + \sum_{\ell m} \langle Y_{\ell_\alpha m_\alpha} Y_{\ell m} | Y_{\ell_\beta m_\beta} \rangle \langle \varphi_i | r^{-\ell-1} | \varphi_j \rangle M_{ab}^{e\ell, \ell m} \right]. \quad (\text{B.21})$$

DIPOLE TRANSITION GAUGES

In this section we explore in detail how dipole transition matrix elements evaluated between eigenstates of either the unconstrained or the confined hydrogen hamiltonian (*physical* and *confined* eigenstates, respectively, in the nomenclature of Sec. 6.1), computed in different gauges, are related to each other. In the case of the hydrogen hamiltonian,

$$H = \frac{1}{2}p^2 - \frac{Z}{r}, \quad (\text{C.1})$$

the following operator identities hold

$$[H, r_{1\mu}] = \frac{1}{2} [p^2, r_{1\mu}] = -ip_{1\mu}, \quad (\text{C.2})$$

$$[H, p_{1\mu}] = -Z \left[\frac{1}{r}, p_{1\mu} \right] = iZ \frac{r_{1\mu}}{r^3}. \quad (\text{C.3})$$

As a consequence, if we indicate with $\psi_{E\ell m}$ and $\psi_{E'\ell' m'}$ two generic eigenstates of H with eigenvalues E and E' , respectively, we can easily derive the following relations between the *off-shell* ($E \neq E'$) reduced transition matrix elements,

$$i(E - E') \langle \psi_{E\ell} \| \mathcal{O}_1^{(l)} \| \psi_{E'\ell'} \rangle = \langle \psi_{E\ell} \| \mathcal{O}_1^{(v)} \| \psi_{E'\ell'} \rangle, \quad (\text{C.4})$$

$$-i(E - E') \langle \psi_{E\ell} \| \mathcal{O}_1^{(v)} \| \psi_{E'\ell'} \rangle = \langle \psi_{E\ell} \| \mathcal{O}_1^{(a)} \| \psi_{E'\ell'} \rangle. \quad (\text{C.5})$$

These equations have two uses. First, the same *off-shell* transition matrix element (say, the one in velocity gauge) can be computed in three different ways. Since the kernels of the three transition operators (Eq. (6.14)) weighs differently the wave function at short and long range, one can choose the form that weighs more the region where the wave function is known to be computed with better accuracy. Second, Eqs. (C.4,C.5) only hold when evaluated using exact eigenstates of the hamiltonian. The discrepancy between the numerical realization of the RHS and the LHS in (C.4,C.5), therefore, is a measure of the accuracy of the numerical eigenstates.

Three further remarks are in order about the relations (C.4,C.5). First, as it has already been pointed out, these relations permit to convert between each other only *off-shell* matrix elements. In the *on-shell* case, where the two eigenstates are necessarily either both bound or both in the continuum, the relations provide only partial information. For example, they say that the transition matrix elements in velocity and acceleration gauge between degenerate bound states is

exactly zero, but they don't say anything about the finite value of the transition matrix elements in length gauge between degenerate states (e.g., between the $2s$ and the $2p$ states). Second, when evaluated between two continuum generalized eigenstates and expressed in terms of a radial integral, the transition matrix elements in length and velocity gauge must be regularized with the inclusion of an exponential extinction factor for the integral to converge in the first place. As a consequence, Eqs. (C.4,C.5) are to be seen as relations between distributions. The general expression of the velocity-gauge transition matrix element in terms of the acceleration gauge is thus [194, 195, 196]

$$\begin{aligned} \langle \psi_{E\ell} \| \mathcal{O}_1^{(v)} \| \psi_{E'\ell+1} \rangle &= iP \frac{\langle \psi_{E\ell} \| \mathcal{O}_1^{(a)} \| \psi_{E'\ell+1} \rangle}{E - E'} + \\ &+ \mathcal{F}_{\ell E} \delta(E - E'), \end{aligned}$$

where P indicates the principal part and $\mathcal{F}_{\ell E}$ is a function that depends on the asymptotic behavior of the radial part of two functions and must be determined separately. In App. D we derive the explicit expression for $\mathcal{F}_{\ell E}$ for the hydrogen atom as well as in the presence of a short range potential. Third, the use of the term "gauge" for the acceleration operator is admittedly an abuse of language. Indeed, while the velocity and length gauges are related to each other by a unitary transformation (Göppert-Mayer's; see [197]), this is not the case for the acceleration operator. In the present context, the latter should thus be regarded simply as an alternative way to estimate the transition matrix element in velocity gauge.

When computing the transition matrix elements between box eigenstates, the considerations above need to be modified. Indeed, in this case the hamiltonian can be regarded as the limit of the hydrogen hamiltonian plus a step potential at $r = R_{\text{box}}$, with height V , for $V \rightarrow \infty$,

$$H(V) = \frac{p^2}{2} - \frac{Z}{r} + V\theta(r - R_{\text{box}}), \quad (\text{C.6})$$

where we explicitly indicated the parametric dependence of H on V . As long as we are interested in transition matrix elements between eigenstates with eigenvalues smaller than V , the relation (C.4) between velocity and length transition matrix elements continues to apply as it does between bound states of the unconstrained hydrogen hamiltonian. In particular, the equivalence (C.4) holds in the limit $V \rightarrow \infty$, i.e., between box eigenstates. This is because the commutator (C.2) is unaltered by the presence of an additional multiplicative term in the hamiltonian in coordinate representation. Notice, however, that while the positive-energy box eigenstates can be normalized so to coincide, within the box, with the real scattering states with the same energy, the transition matrix elements between box eigenstates (i.e., where the radial integral is truncated at $r = R_{\text{box}}$, where all the box eigenstates vanish) does not coincide with the one evaluated between scattering states; the contribution to the (regularized) transition integral from the radial domain $[R_{\text{box}}, \infty)$ is finite and non-negligible [142]. The picture takes on a

different perspective when the acceleration gauge is considered. In this case, the RHS of (C.3) changes,

$$\begin{aligned} [H, p_{1\mu}] &= -Z \left[\frac{1}{r}, p_{1\mu} \right] + V [\theta(r - R_{\text{box}}), p_{1\mu}] = \\ &= iZ \frac{r_{1\mu}}{r^3} + iV \frac{r_{1\mu}}{r} \delta(r - R_{\text{box}}). \end{aligned} \quad (\text{C.7})$$

This latter equivalence between the LHS and the RHS still holds for arbitrary values of V , but the limit for $V \rightarrow \infty$ of the new term on the RHS evaluated between eigenstates of the hamiltonian that comprises the step potential does not vanish and must be taken into account. If we indicate with $\psi_{E\ell m}(r; V) = r^{-1} u_{\ell E}(r; V) Y_{\ell m}(\hat{r})$ a generic eigenstate of the hamiltonian that includes the step potential, where the parametric dependence on V has explicitly been indicated, and we assume $V \gg E$, then we can immediately write, for $r \geq R_{\text{box}}$,

$$u_{\ell E}(r; V) \simeq N(E, V) e^{-\kappa(r - R_{\text{box}})}, \quad (\text{C.8})$$

$$u'_{\ell E}(r; V) \simeq -\kappa N(E, V) e^{-\kappa(r - R_{\text{box}})}, \quad (\text{C.9})$$

where $\kappa = \sqrt{2(V - E)}$ and $N(E, V)$ is a normalization constant. In the limit $V \rightarrow \infty$, if the wave function is to remain normalized, the wave function at the box boundary must converge to zero while its derivative must converge to a finite value. Therefore, we can choose the normalization so that the wave function derivative coincides with its asymptotic value for any $V \gg E$,

$$u_{\ell E}(r; V) \simeq -\frac{u'_{\ell E}(R_{\text{box}}, \infty)}{\sqrt{2(V - E)}} e^{-\kappa(r - R_{\text{box}})} \simeq \quad (\text{C.10})$$

$$\simeq -\frac{u'_{\ell E}(R_{\text{box}}, \infty)}{\sqrt{2V}} e^{-\kappa(r - R_{\text{box}})}, \quad (\text{C.11})$$

$$u'_{\ell E}(r; V) \simeq u'_{\ell E}(R_{\text{box}}, \infty) e^{-\kappa(r - R_{\text{box}})}. \quad (\text{C.12})$$

Now we can compute the limit of the matrix element of the second term on the RHS of eq. (C.7) (we assume radial wave functions to be real),

$$\begin{aligned} \langle \psi_{E\ell m} | iV \frac{r_{1\mu}}{r} \delta(r - R_{\text{box}}) | \psi_{E'\ell' m'} \rangle &= \\ &= i \langle Y_{\ell m} | \frac{r_{1\mu}}{r} | Y_{\ell' m'} \rangle \times \\ &\times V u_{\ell E}(R_{\text{box}}; V) u_{E'\ell'}(R_{\text{box}}; V) \simeq \quad (\text{C.13}) \\ &\simeq \frac{C_{\ell' m', 1\mu}^{\ell m}}{\sqrt{2\ell + 1}} \frac{i}{2} \sqrt{2\ell' + 1} C_{\ell' 0, 10}^{\ell 0} \times \\ &\times u'_{\ell E}(R_{\text{box}}; \infty) u'_{\ell' E'}(R_{\text{box}}; \infty). \end{aligned}$$

The increase of the barrier height, therefore, exactly compensates the decrease of the wave function at the boundary. In the limit $V \rightarrow \infty$, the last approximate equality becomes an identity. In conclusion, even if the transition matrix elements

in velocity and acceleration gauges, defined as in (6.14), do not satisfy the relation (C.5) when computed between box eigenstates unless the radial derivative of at least one of them is vanishingly small at the box boundary, the conversion from one gauge to the other can still be performed provided that the correction (C.13) is taken into account,

$$\begin{aligned}
(E - E') \langle \psi_{E\ell} \| \mathcal{O}_1^{(v)} \| \psi_{E'\ell'} \rangle_{r \in [0, R_{\text{box}}]} &= \\
= i \langle \psi_{E\ell} \| \mathcal{O}_1^{(a)} \| \psi_{E'\ell'} \rangle_{r \in [0, R_{\text{box}}]} &+ \\
+ \frac{i}{2} \sqrt{2\ell' + 1} C_{\ell'0,10}^{\ell 0} u'_{E\ell}(R_{\text{box}}) u'_{E'\ell'}(R_{\text{box}}). &
\end{aligned} \tag{C.14}$$

Finally, if the box size is large enough, thanks to the r^{-2} behavior of the acceleration kernel, the acceleration matrix element between any two box eigenstates does converge to those between the real eigenstates of the unconstrained hamiltonian,

$$\lim_{R_{\text{box}} \rightarrow \infty} \langle \psi_{E\ell} \| \mathcal{O}_1^{(a)} \| \psi_{E'\ell'} \rangle_{r \in [R_{\text{box}}, \infty)} = 0 \tag{C.15}$$

As a consequence, the contribution to the regularized velocity transition integral from the $[R_{\text{box}}, \infty)$ radial domain, evaluated between the analytic extensions of the box eigenfunctions, can be obtained, for large values of R_{box} , from the correction in (C.13),

$$\begin{aligned}
(E - E') \langle \psi_{E\ell} \| \mathcal{O}_1^{(v)} \| \psi_{E'\ell'} \rangle_{r \in [R_{\text{box}}, \infty)} &= \\
= -\frac{i}{2} \sqrt{2\ell' + 1} C_{\ell'0,10}^{\ell 0} u'_{E\ell}(R_{\text{box}}) u'_{E'\ell'}(R_{\text{box}}). &
\end{aligned} \tag{C.16}$$

This last equation has two distinctive features that set it apart from similar corrections available in the literature. First, it is a closed expression which, together with the transition integral truncated to R_{box} , provides a transition matrix element which is as accurate as the one that can be obtained in the same box using the acceleration gauge instead. This means that Eq (C.16) offers the opportunity to extend to continuum-continuum transitions the stringent gauge-invariance test employed for transitions from or to bound states, and thus provides an independent way to assess the accuracy of the discretized continuum functions computed numerically. Second, Eq (C.16) is only applicable to the fixed energies, for both ℓ and ℓ' angular momenta, that result from imposing box boundary conditions. Cormier *et al.* [142] derived a perturbative expansion for the contribution to the transition radial integral from the $[R_{\text{box}}, \infty]$ domain in the case of arbitrary initial and final continuous energies. In App. F we derive a different approximate expression for the transition matrix element correction between arbitrary energies based on a perturbative expansion of the integral alternative to the one used in [142].

SINGULAR PART OF THE DIPOLE MATRIX ELEMENTS BETWEEN CONTINUUM STATES

As mentioned in App. C, the relation between continuum-continuum dipole transition matrix elements in velocity and acceleration gauges includes a singular *on-shell* contribution,

$$\langle \psi_{E\ell} | \mathcal{O}_1^{(v)} | \psi_{E'\ell+1} \rangle = i \frac{\langle \psi_{E\ell} | \mathcal{O}_1^{(a)} | \psi_{E'\ell+1} \rangle}{E - E' + i0^+} + \mathcal{F}_{\ell E} \delta(E - E'),$$

To evaluate the factor $\mathcal{F}_{\ell E}$, we start from the following well known formula [140]:

$$\begin{aligned} \langle \psi_{E\ell} | \nabla_1 | \psi_{E',\ell+1} \rangle &= -\sqrt{\ell+1} \times \\ &\times \int_0^\infty dr u_{\ell E}^*(r) \left(\frac{d}{dr} + \frac{\ell+1}{r} \right) u_{\ell+1,E'}(r) \end{aligned} \quad (\text{D.1})$$

Where $u_{\ell E}(r)$ is a reduced radial function. Since we are interested in the singular part of the integral, we can disregard the contribution to the integral from any finite interval $[0, R]$. As a consequence, we can replace $u_{\ell E}(r)$ with its asymptotic expression [139],

$$u_{\ell E}(r) \simeq \sqrt{\frac{2}{\pi k}} \sin \theta_{\ell k}(r), \quad (\text{D.2})$$

$$\theta_{\ell k}(r) = kr - \gamma \ln 2kr - \frac{\ell\pi}{2} + \sigma_\ell + \delta_\ell, \quad (\text{D.3})$$

and disregard entirely the term that comes from the operator r^{-1} . As usual, in Eq. (D.2), $k = \sqrt{2E}$, $\gamma = -Z/k$, $\sigma_\ell = \arg \Gamma(\ell+1 + i\gamma)$ is the Coulomb phase, and δ_ℓ is the additional phase due to a possible short-range potential. For hydrogen $Z = 1$ and $\delta_\ell = 0$. What matters to evaluating the singular part of the integral (D.1) is that the oscillations of the degenerate initial and final states are in a fixed phase relation across the whole radial range. This is true independently of the presence or not of the asymptotic logarithmic term in (D.2). Indeed, it is sufficient to perform the change of variable $r \mapsto r'(r) = r - \gamma/k \ln 2kr$, $dr' = [1 - \gamma/(2k^2r)]dr$ to realize that the logarithmic term can be safely ignored. On the basis of these considerations, the factor $\mathcal{F}_{\ell E}$ can be computed as

$$\begin{aligned} \mathcal{F}_{\ell E} &= \int_{E-\epsilon}^{E+\epsilon} dE' \langle \psi_{E\ell} | \mathcal{O}_1^{(v)} | \psi_{E',\ell+1} \rangle = \\ &= \frac{2i\sqrt{\ell+1}}{\pi k} \int_{E-\epsilon}^{E+\epsilon} dE' \int_R^\infty dr \sin \theta_{\ell k}(r) \frac{d}{dr} \sin \theta_{\ell+1,k'}(r), \end{aligned} \quad (\text{D.4})$$

in the limit of $\epsilon \rightarrow 0^+$ and $R \rightarrow \infty$. To the purpose of evaluating its singular part, the radial integral on the RHS in the last equation is equivalent to the following expression

$$k \int_0^\infty dr \sin(kr + \sigma_\ell + \delta_\ell - \ell\pi/2) \times \\ \times \cos(k'r + \sigma_{\ell+1} + \delta_{\ell+1} - (\ell+1)\pi/2). \quad (D.5)$$

It takes only few passages to show that the singular component of this last integral is

$$\frac{k\pi}{2} \delta(k - k') \cos(\sigma_{\ell+1} + \delta_{\ell+1} - \sigma_\ell - \delta_\ell), \quad (D.6)$$

and, in conclusion,

$$\mathcal{F}_{\ell E} = i\sqrt{\ell+1} k \cos(\sigma_{\ell+1} + \delta_{\ell+1} - \sigma_\ell - \delta_\ell). \quad (D.7)$$

In the case of the hydrogen atom, $\delta_\ell = 0 \forall \ell$, and we can write

$$\begin{aligned} \mathcal{F}_{\ell E} &= i \frac{\sqrt{\ell+1}}{2} k \left[\frac{\Gamma(\ell+2+i\gamma)}{\Gamma(\ell+1+i\gamma)} \left| \frac{\Gamma(\ell+1+i\gamma)}{\Gamma(\ell+2+i\gamma)} \right| + c.c. \right] = \\ &= i \frac{(\ell+1)^{3/2} k}{|\ell+1+i\gamma|}, \end{aligned} \quad (D.8)$$

where in the last passage we made use of the relation $\Gamma(s) = (s-1)\Gamma(s-1)$.

ANALYTICAL DIPOLE MATRIX ELEMENTS IN HYDROGEN

The equation for the reduced radial Coulomb problem of an electron in interaction with a point charge Z is

$$\psi_{k\ell m}(\vec{r}) = \frac{u_{\ell k}(r)}{r} Y_{\ell m}(\hat{r}) \quad (\text{E.1})$$

$$\left[\frac{d^2}{dr^2} + k^2 - \frac{\ell(\ell+1)}{r^2} + \frac{2Z}{r} \right] u_{\ell k}(r) = 0. \quad (\text{E.2})$$

For negative energies, we can set $k = i\sqrt{2|E|}$ and obtain

$$\left[\frac{d^2}{d\rho^2} + \frac{2\gamma}{\rho} - \frac{\ell(\ell+1)}{\rho^2} - 1 \right] y_{\ell k}(\rho) = 0, \quad (\text{E.3})$$

where we have defined $\gamma = Z/|k|$, $\rho = |k|r$, and $y_{\ell k}(\rho) = u_{\ell k}(r)$. The solution to the latter equation that is regular at $r \rightarrow \infty$ can be expressed as

$$y_{\ell k}(\rho) \propto e^{-\rho} (2\rho)^{\ell+1} U(\ell+1-\gamma, 2\ell+2, 2\rho), \quad (\text{E.4})$$

where $U(a, b, z)$ is the confluent hypergeometric function of the second kind [134],

$$\begin{aligned} U(a, b, z) &= \frac{\Gamma(1-b)}{\Gamma(a-b+1)} {}_1F_1(a; b; z) + \\ &+ \frac{\Gamma(b-1)}{\Gamma(a)} z^{1-b} {}_1F_1(a-b+1; 2-b; z), \end{aligned} \quad (\text{E.5})$$

${}_1F_1(\alpha; \beta; z)$ being the ordinary confluent hypergeometric function

$$\begin{aligned} {}_1F_1(\alpha; \beta; z) &= \sum_{j=0}^{\infty} \frac{(\alpha)_j z^j}{(\beta)_j j!}, \\ (\alpha)_0 &= 1, \quad (\alpha)_n = \prod_{j=0}^{n-1} (\alpha + j). \end{aligned} \quad (\text{E.6})$$

Even in the presence of short-range potentials, (E.4) expresses the general asymptotic form that must be fulfilled by the bound states of the system. To determine the acceptable bound-state energies, the logarithmic derivative of (E.4) must match, at a radius R beyond which the short-range potential is negligible, that

of the degenerate solution that is regular at the origin. This is how we obtained Eq. (6.11) in Sec. 6.1. The function $U(\ell + 1 - \gamma, 2\ell + 2, 2\rho)$ is irregular at the origin except for integer values of γ , $\gamma = n > \ell$. In this latter case, U is proportional to a Laguerre polynomial (Eq. 13.6.27 in [134])

$$U(-k, 2\ell + 2, z) = (-1)^k k! L_k^{(2\ell+1)}(z), \quad k \in \mathbb{N}_0, \quad (\text{E.7})$$

and (E.4) thus identifies with an admissible bound state of the hydrogen-like system. The reduced radial component $u_{n\ell}$ of the normalized hydrogen bound states $\psi_{n\ell m}$, with energy $E_n = -1/2n^2$, angular momentum ℓ and projection m , have the following expression [139]

$$u_{n\ell}(r) = N_{n\ell} r^{\ell+1} e^{-\frac{r}{n}} {}_1F_1(\ell - n + 1; 2\ell + 2; 2r/n) \quad (\text{E.8})$$

where the normalization factor $N_{n\ell}$ is

$$N_{n\ell} = \frac{1}{(2\ell + 1)!} \sqrt{\frac{(n + \ell)!}{2n(n - \ell - 1)!}} \left(\frac{2}{n}\right)^{\ell + \frac{3}{2}}. \quad (\text{E.9})$$

In the case of the continuum states, the reduced radial part of the wave function $\psi_{E\ell m}$, normalized as $\langle \psi_{E\ell m} | \psi_{E'\ell m} \rangle = \delta(E - E')$, is [139]:

$$u_{\ell E}(r) = C_{\ell E} (2i\rho)^{\ell+1} e^{-i\rho} {}_1F_1(\ell + 1 - i\gamma; 2\ell + 2; 2i\rho) \quad (\text{E.10})$$

where

$$C_{\ell E} = \frac{e^{-\frac{\pi}{2}\gamma}}{i\sqrt{2\pi k}} \frac{\Gamma(\ell + 1 - i\gamma)}{(2\ell + 1)!} \quad (\text{E.11})$$

$k = \sqrt{2E}$, $\gamma = -1/k$, $\rho = kr$.

In the following, we will derive the analytical expressions for the reduced dipole transition matrix elements, in length gauge, between arbitrary hydrogen eigenstates

$$\langle \psi_{a\ell'} || r_1 || \psi_{b\ell} \rangle = \prod_{\ell} C_{\ell 0, 10}^{\ell' 0} \int_0^\infty u_{\ell' a}^* r u_{\ell b} dr, \quad (\text{E.12})$$

where $\prod_{\ell_1 \ell_2 \dots} = \sqrt{(2\ell_1 + 1)(2\ell_2 + 1) \dots}$ and $C_{\ell_1 m_1, \ell_2 m_2}^{\ell_3 m_3}$ is a Clebsch-Gordan coefficient. The expression for the corresponding quantities in the other two gauges can be readily obtained using relations (C.4, C.5). We focus the attention on the radial integral

$$\mathcal{O}_{\ell' a, \ell b} = \int_0^\infty u_{\ell' a}^* r u_{\ell b} dr, \quad (\text{E.13})$$

and consider the bound-bound ($a, b = n', n$), continuum-bound ($a, b = E, n$) and continuum-continuum ($a, b = E', E$) cases separately. Thanks to the exponential

decay with r of the bound-state wave functions, the first two cases do not pose any regularization problem, so we cover those first,

$$\begin{aligned}\mathcal{O}_{\ell'n',\ell n} &= N_{n'\ell'} N_{n\ell} \int_0^\infty dr r^{\ell+\ell'+3} e^{-r(\frac{1}{n}+\frac{1}{n'})} \times \\ &\times {}_1F_1(\ell'+1-n'; 2\ell'+2; \frac{2r}{n'}) \times \\ &\times {}_1F_1(\ell+1-n; 2\ell+2; \frac{2r}{n}),\end{aligned}\quad (\text{E.14})$$

$$\begin{aligned}\mathcal{O}_{\ell'E,\ell n} &= C_{\ell'E}^* N_{n\ell} (2ik)^{\ell'+1} \int_0^\infty dr r^{\ell+\ell'+3} e^{ikr-r/n} \times \\ &\times {}_1F_1(\ell'+1+i\gamma; 2\ell'+2; -2ikr) \times \\ &\times {}_1F_1(\ell+1-n; 2\ell+2; 2r/n).\end{aligned}\quad (\text{E.15})$$

The integrals in Eqs. (E.14,E.15) are of the form [198]:

$$\begin{aligned}J_\beta^{s,p}(\alpha, \alpha') &= \int_0^\infty dr e^{-(h+h')\frac{r}{2}} r^{\beta-1+s} {}_1F_1(\alpha; \beta; hr) \\ &\times {}_1F_1(\alpha'; \beta-p; h'r),\end{aligned}\quad (\text{E.16})$$

which can be solved by applying repeatedly the well-known recurrence relations

$$J_\beta^{s,p}(\alpha, \alpha') = \frac{(\beta-1)}{h} \left[J_{\beta-1}^{s,p-1}(\alpha, \alpha') - J_{\beta-1}^{s,p-1}(\alpha-1, \alpha') \right] \quad (\text{E.17})$$

$$\begin{aligned}J_\beta^{s+1,0}(\alpha, \alpha') &= \frac{4}{h^2-h'^2} \left\{ 2\alpha' s J_\beta^{s-1,0}(\alpha, \alpha'+1) + \right. \\ &+ \left[\frac{1}{2}\beta(h-h') - h\alpha + h'(\alpha'-s) \right] J_\beta^{s,0}(\alpha, \alpha') + \\ &+ s(\beta-1+s-2\alpha') J_\beta^{s-1,0}(\alpha, \alpha') \left. \right\}\end{aligned}\quad (\text{E.18})$$

until the initial expression is entirely given in terms of $J_\beta^{0,0}$ integrals, and finally compute :

$$\begin{aligned}J_\beta^{0,0}(\alpha, \alpha') &= 2^\beta \Gamma(\beta) (h+h')^{\alpha+\alpha'-\beta} (h'-h)^{-\alpha} \\ &\times (h-h')^{-\alpha'} {}_2F_1\left[\alpha, \alpha'; \beta; -\frac{4hh'}{(h'-h)^2}\right]\end{aligned}\quad (\text{E.19})$$

where ${}_2F_1(\alpha, \beta; \gamma; z)$ is the Hypergeometric Function,

$${}_2F_1(\alpha, \beta; \gamma; z) = \sum_{j=0}^{\infty} \frac{(\alpha)_j (\beta)_j z^j}{(\gamma)_j j!} \quad (\text{E.20})$$

Doing this we arrive to the following result:

$$\begin{aligned}
\mathcal{O}_{\ell+1n',\ell n} = & \frac{(-1)^{\ell-n'} n' (n \cdot n')^{2\ell+4} (2\ell+3)! N_{n',\ell+1} N_{n\ell}}{2(n^2 - n'^2) (n' + n)^{n'+n+1} (n - n')^{2\ell+3-n'-n}} \\
& \times \left[(n' - n)^2 {}_2F_1(\ell - n', \ell - n + 1; 2\ell + 2; \right. \\
& - \frac{4n \cdot n'}{(n' - n)^2}) - (n' + n)^2 {}_2F_1(\ell - n' + 2, \\
& \left. \ell - n + 1; 2\ell + 2; - \frac{4n \cdot n'}{(n' - n)^2}) \right] \quad (E.21)
\end{aligned}$$

It is not necessary to compute $\mathcal{O}_{\ell n',\ell+1n}$ because all the bound-bound transitions can be expressed only using $\mathcal{O}_{\ell+1n',\ell n}$. For the continuum-bound transitions

$$\begin{aligned}
\mathcal{O}_{\ell+1E,\ell n} = & \frac{i(-1)^{\ell-n} n^{2\ell+4} (2\ell+3)! k^\ell C_{\ell+1}^* N_{n\ell}}{2(1 + k^2 n^2)^{n+2-i\gamma} (1 + ikn)^{2(\ell+2-n+i\gamma)}} \\
& \times \left[(1 + ikn)^4 {}_2F_1(\ell + i\gamma, \ell + 1 - n; 2\ell + 2; \right. \\
& \frac{4ikn}{(1 + ikn)^2}) - (1 + k^2 n^2)^2 {}_2F_1(\ell + 2 + i\gamma, \\
& \left. \ell + 1 - n; 2\ell + 2; \frac{4ikn}{(1 + ikn)^2}) \right] \quad (E.22)
\end{aligned}$$

$$\begin{aligned}
\mathcal{O}_{\ell-1E,\ell n} = & \frac{(-1)^{\ell+1-n} n^{2\ell+3} (2\ell+1)! k^{\ell-1} C_{\ell-1}^* N_{n\ell}}{2(1 + k^2 n^2)^{n+2-i\gamma} (1 + ikn)^{2(\ell+1-n+i\gamma)}} \\
& \times \left[(1 + ikn)^4 {}_2F_1(\ell - 1 - n, \ell + i\gamma; 2\ell; \frac{4ikn}{(1 + ikn)^2}) - \right. \\
& \left. (1 + k^2 n^2)^2 {}_2F_1(\ell + 1 - n, \ell + i\gamma; 2\ell; \frac{4ikn}{(1 + ikn)^2}) \right] \quad (E.23)
\end{aligned}$$

Due to the intrinsic relationship between the quantum numbers n and ℓ : $n \geq \ell + 1$, at least one of the parameters α, β in the hypergeometric functions ${}_2F_1(\alpha, \beta; \gamma; z)$, is equal to $-q$; $q = 0, 1, 2, \dots$. Then from the definition (E.20), for this particular case ${}_2F_1(\alpha, \beta; \gamma; z)$ is transformed into a polynomial of degree q , which makes it much more easy to compute.

For the case of continuum-continuum transitions we use the result given in [141]:

$$\begin{aligned}
\mathcal{O}_{\ell E, \ell' E'} &= -C_{k\ell} C_{k'\ell'} \times \\
&\times \frac{(-1)^{\lambda_i} (2\lambda_s + 1)!}{2x_s (x_i - x_s)^{2\lambda_s + 2}} \left(\frac{k - k'}{k + k'} \right)^{\frac{i}{k'}} \left(\frac{k' - k}{k + k'} \right)^{\frac{i}{k}} \times \\
&\times \left[{}_2F_1 \left(\lambda_s + 1 - \frac{1}{x_s}, \lambda_i + 1 - \frac{1}{x_i}; 2\lambda_s; \frac{-4kk'}{(k - k')^2} \right) - \right. \\
&- \left(\frac{k - k'}{k + k'} \right)^2 \times \\
&\times \left. {}_2F_1 \left(\lambda_s - 1 - \frac{1}{x_s}, \lambda_i + 1 - \frac{1}{x_i}; 2\lambda_s; \frac{-4kk'}{(k - k')^2} \right) \right]
\end{aligned} \tag{E.24}$$

where $\lambda_s = \sup(\ell, \ell')$, $\lambda_i = \inf(\ell, \ell')$, $x_s = -ik$ and $x_i = -ik'$ if $\lambda_s = \ell$, $x_s = -ik'$ and $x_i = -ik$ if $\lambda_s = \ell'$. The normalization constant $C_{k\ell}$ is:

$$C_{k\ell} = \frac{2^{\ell+1}}{(2\ell + 1)!} k^{\ell - \frac{1}{2}} \left[\frac{\prod_{s=1}^{\ell} (s^2 + k^{-2})}{1 - \exp(-\frac{2\pi}{k})} \right]. \tag{E.25}$$

ANALYTICAL APPROXIMATION TO THE OUTER CONTINUUM-CONTINUUM TRANSITION INTEGRAL

As was mentioned in the text, the computation of the continuum-continuum reduced dipole matrix elements, using the radial basis, is done in a truncated interval $[0, R]$. For the calculation using the velocity and length gauges, the lacking interval $[R, \infty)$ makes a non-negligible contribution. This contribution can be estimated analytically from the expression:

$$\begin{aligned} \mathcal{O}_{\ell E, \ell' E'}|_R^\infty &= C_{k\ell} C_{k'\ell'} \int_R^\infty r^{\ell+\ell'+3} e^{ir(k+k')} \\ &\quad \times {}_1F_1\left(\ell+1-\frac{i}{k}; 2\ell+2; -2ikr\right) \\ &\quad \times {}_1F_1\left(\ell'+1-\frac{i}{k'}; 2\ell'+2; -2ik'r\right) \end{aligned} \quad (\text{F.1})$$

The Confluent Hypergeometric functions can be expanded for $|z| \rightarrow \infty$ and for the case $-\frac{3\pi}{2} + \delta \leq \arg z \leq \frac{\pi}{2} - \delta$, where $0 < \delta \ll 1$, as [199]:

$$\begin{aligned} {}_1F_1(a; b; z) &\approx \Gamma(b) \left[\frac{e^z z^{a-b}}{\Gamma(a)} \sum_{j=0}^{\infty} \frac{(b-a)_j (1-a)_j z^{-j}}{j!} + \right. \\ &\quad \left. \frac{e^{-i\pi a} z^{-a}}{\Gamma(b-a)} \sum_{j=0}^{\infty} \frac{(a)_j (1+a-b)_j (-z)^{-j}}{j!} \right] \end{aligned} \quad (\text{F.2})$$

We truncate the previous summations for $j = 2$. Then using (F.2) in (F.1), if the integral is regularized introducing in the subintegral part the parametric function $e^{-\xi r}$, and computing the limit when $\xi \rightarrow 0^+$ once the integration is done, a closed-form analytical correction can be obtained:

$$\begin{aligned} \mathcal{O}_{\ell+1 E, \ell' E'}|_R^\infty &\approx \frac{C_{k, \ell+1} C_{k', \ell} (2\ell+3)! (2\ell+1)!}{(-2i)^{2\ell+3} k^{\ell+2} k'^{\ell+1}} \\ &\quad \times [I_\ell(k, k') + I_\ell(k, -k') + \\ &\quad I_\ell(-k, k') + I_\ell(-k, -k')], \end{aligned} \quad (\text{F.3})$$

where the function $I_\ell(x, y)$ is

$$I_\ell(x, y) = -\frac{2\left(\frac{1}{x} + \frac{1}{y}\right) D_\ell(x, y)}{i(x+y)} [G_1(x, y) + G_2(x, y)] \times \\ \times \frac{e^{-i\left(xR + \frac{1}{x} \ln|x|R\right)}}{\Gamma\left(\ell + 2 - \frac{i}{x}\right)} \frac{e^{-i\left(yR + \frac{1}{y} \ln|y|R\right)}}{\Gamma\left(\ell + 1 - \frac{i}{y}\right)}, \quad (\text{F.4})$$

the $G_i(x, y)$ functions are:

$$G_1(x, y) = R + \frac{1 - i\left(\frac{1}{x} + \frac{1}{y}\right)}{i(x+y)} + \\ + i\left(\frac{1}{x} + \frac{1}{y}\right) \frac{1 - i\left(\frac{1}{x} + \frac{1}{y}\right)}{R(x+y)^2} \quad (\text{F.5})$$

$$G_2(x, y) = H_1(x, y) \left[1 - \frac{\frac{1}{x} + \frac{1}{y}}{R(x+y)} \right] + \frac{H_2(x, y)}{R} \quad (\text{F.6})$$

and

$$D_\ell(x, y) = e^{-i\pi\left[\left(\ell+1-\frac{i}{|y|}\right)[1-\theta(y)] + \left(\ell+2-\frac{i}{|x|}\right)[1-\theta(x)]\right]} \quad (\text{F.7})$$

Defining:

$$a = \ell + 2 - \frac{i}{|x|}; \quad b = 2\ell + 4; \quad d = -2i|x| \\ a' = \ell + 1 - \frac{i}{|y|}; \quad b' = 2\ell + 2; \quad d' = -2i|y|$$

then

$$H_1(x, y) = \begin{cases} \frac{(b-a)(1-a)}{d} + \frac{(b'-a')(1-a')}{d'} & x > 0 \wedge y > 0 \\ \frac{(b-a)(1-a)}{d} - \frac{a'(1+a'-b')}{d'} & x > 0 \wedge y < 0 \\ \frac{ba-a^2-a}{d} + \frac{(b'-a')(1-a')}{d'} & x < 0 \wedge y > 0 \\ -\left(\frac{a'(1+a'-b')}{d'} + \frac{a(1+a-b)}{d}\right) & x < 0 \wedge y < 0 \end{cases}$$

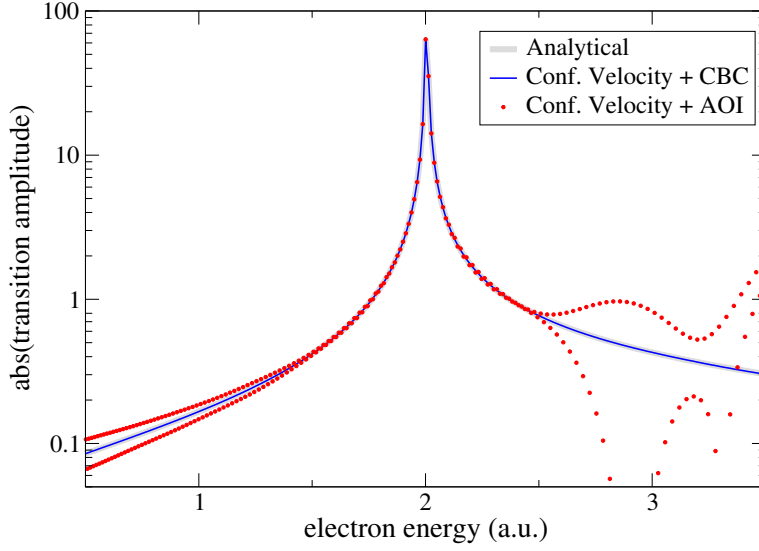


Figure F.1: Absolute value of the reduced velocity-gauge hydrogen dipole matrix element $\langle \psi_{E_p} \| \mathcal{O}_1^v \| \psi_{E_s} \rangle$ from the s scattering state with $E = 2$ a.u. to several p scattering states evaluated as the sum of two contributions: the first contribution is the numerical radial integral shown in Fig. 6.9, which is computed with the GABS basis and truncated at R_{box} , and the second contribution is, in the case of the full circles, an analytical approximation to outer integral (AOI) in the radial domain $[R_{\text{box}}, \infty)$, as detailed in this appendix, and in the case of the thin solid line, the confined boundary correction (CBC) derived in App. C. The agreement between the numerical result corrected using CBC for the out-of-the-box contribution and the exact analytical result (thick solid line) is excellent. The deviations for the very off-shell transition using the AOI correction are attributed to the approximations made.

$$H_2(x, y) = \begin{cases} \frac{(b'-a')_2(1-a')_2}{2d'^2} + \frac{(b-a)_2(1-a)_2}{2d^2} + \frac{(b'-a')(1-a')(b-a)(1-a)}{d \cdot d'} & x > 0 \wedge y > 0 \\ \frac{(b-a)_2(1-a)_2}{2d^2} + \frac{(a')_2(1+a'-b')_2}{2d'^2} - \frac{(b-a)(1-a)a'(1+a'-b')}{d \cdot d'} & x > 0 \wedge y < 0 \\ \frac{(b'-a')_2(1-a')_2}{2d'^2} + \frac{(a)_2(1+a-b)_2}{2d^2} - \frac{(b'-a')(1-a')a(1+a-b)}{d \cdot d'} & x < 0 \wedge y > 0 \\ \frac{(a)_2(1+a-b)_2}{2d^2} + \frac{(a')_2(1+a'-b')_2}{2d'^2} + \frac{a(1+a-b)a'(1+a'-b')}{d \cdot d'} & x < 0 \wedge y < 0 \end{cases}$$

RELATION BETWEEN D_{2h} AND SPHERICAL SCATTERING CHANNELS IN THE PHOTOIONIZATION OF NE

The dipole operator couples the Ne ground state, which has $^1S^e$ symmetry, with the $^1P^o$ continuum. Due to the spherical symmetry of the atoms, these scattering states are triply degenerate with respect to the total magnetic quantum number M : $(^1P^o)_M$, $M = -1, 0, 1$, and the photoionization cross sections from the ground state along any of the directions: \hat{x} , \hat{y} and \hat{z} are the same. Therefore we can focus on one of these direction, let's say \hat{z} , that couples the ground state with those of the continuum having $(^1P^o)_0$ symmetry.

The highest symmetry we are able to represent in the XCHEM formalism is that corresponding to the D_{2h} point group. In this representation the Ne ground state has A_g symmetry meanwhile the countinuum states that are couple through the dipole along the \hat{z} direction have B_{1u} symmetry. So if we are interested in obtaining the correct spherical scattering channels, we need to add appropriately those coming from the D_{2h} representation. For the total cross section this difference in symmetry representation is not important, because it is an invariant, but for a partial cross section analysis for instance, we need to disentangle all the contributions in terms of the 'physical channels': spherical channels in the atoms perspective, or $C_{\infty v}$ channels for homonuclear diatomic molecules. In the Ne case, we need to express the $(^1P^o)_0$ scattering states in terms of the channels defined in our CC expansion having B_{1u} symmetry. Below the $N = 2$ threshold there are two channels with $^1P^o$ total symmetry: $2p^{-1}\epsilon s$ and $2p^{-1}\epsilon d$, while for the D_{2h} point group, the B_{1u} channels are:

$$\begin{aligned} (2p^{-1})_z \otimes \{X_{00}, X_{20}, X_{22}\} &\rightarrow [B_{1u} \otimes A_g], \\ (2p^{-1})_y \otimes X_{2-1} &\rightarrow [B_{2u} \otimes B_{3g}], \\ (2p^{-1})_x \otimes X_{21} &\rightarrow [B_{3u} \otimes B_{2g}] \end{aligned} \quad (G.1)$$

where $X_{\ell m}$ are the symmetry adapted spherical harmonics and represent the spherical component of the asymptotic electron. The corresponding symmetry product is given between brackets. From Eq. (G.1), the physical channel $(2p^{-1}\epsilon s)_0$ is easy to identify, because there is only one channel with an s -wave electron: $(2p^{-1})_z \otimes X_{00}$. Nevertheless, to build the $(2p^{-1}\epsilon d)_0$ channel, we have to find the correct linear combination:

$$(2p^{-1}\epsilon d)_0 = \sum_m C_{1m,2m}^{10} (2p^{-1})_m Y_{2m}, \quad (G.2)$$

where Y_{2m} are the standard spherical harmonics associated with $\ell = 2$, $C_{1m,2m}^{10}$ the Clebsh-Gordan coefficients and $(2p^{-1})_m$ the parent-ion wave function in spherical components. The parent ions in the CC expansion are expressed in terms of the cartesian components, they are related with the spherical ones by the expressions:

$$\begin{aligned}(2p^{-1})_1 &= -\frac{1}{\sqrt{2}}[(2p^{-1})_x + i(2p^{-1})_y], \\ (2p^{-1})_0 &= (2p^{-1})_z, \\ (2p^{-1})_{-1} &= \frac{1}{\sqrt{2}}[(2p^{-1})_x - i(2p^{-1})_y].\end{aligned}\tag{G.3}$$

Substituting Eq. (G.3) and our definition of the X_{lm} functions in terms of the Y_{lm} in Eq. (5.11), into Eq. (G.2), we get:

$$(2p^{-1}\epsilon d)_0 = \sqrt{\frac{3}{10}}[(2p^{-1})_y X_{2-1} + (2p^{-1})_x X_{21}] - \sqrt{\frac{2}{5}}(2p^{-1})_z X_{20}.\tag{G.4}$$

BIBLIOGRAPHY

- [1] M.S. Schöffler, J. Titze, N. Petridis, T. Jahnke, K. Cole, L. Ph. H. Schmidt, A. Czasch, D. Akoury, O. Jagutzki, J. B. Williams, N. A. Cherepkov, S. K. Semenov, C. W. McCurdy, T. N. Rescigno, C. L. Cocke, T. Osipov, S. Lee, M. H. Prior, A. Belkacem, A. L. Landers, H. Schmidt-Böcking, Th. Weber, and R. Dörner. Ultrafast Probing of Core Hole Localization in N₂. *Science*, 320(5878):920–923, 2008. ISSN 0036-8075. doi: 10.1126/science.1154989. URL <http://science.sciencemag.org/content/320/5878/920>.
- [2] Till Jahnke, Hendrik Sann, Tilo Havermeier, K Kreidi, C Stuck, M Meckel, Markus Schöffler, N Neumann, R Wallauer, S Voss, A Czasch, O Jagutzki, A Malakzadeh, F Afaneh, Th. Weber, and Reinhard D Dörner. Ultrafast energy transfer between water molecules. *Nat. Phys.*, 6: 139–142, 2010. ISSN 1745-2473. doi: 10.1038/nphys1498. URL <http://dx.doi.org/10.1038/nphys1498>.
- [3] M. Dell’Angela, T. Anniyev, M. Beye, R. Coffee, A Föhlisch, J. Gladh, T. Katayama, S. Kaya, O. Krupin, J. LaRue, A Mø gelhøj, D. Nordlund, J K Nø rskov, H. Oberg, H. Ogasawara, H Oström, L. G. M. Pettersson, W. F. Schlotter, J. A. Sellberg, F. Sorgenfrei, J. J. Turner, M. Wolf, W. Wurth, and A. Nilsson. Real-time observation of surface bond breaking with an x-ray laser. *Science*, 339(6125):1302–5, March 2013. ISSN 1095-9203. doi: 10.1126/science.1231711. URL <http://www.sciencemag.org/cgi/doi/10.1126/science.1231711><http://www.ncbi.nlm.nih.gov/pubmed/23493709>.
- [4] F Calegari, D Ayuso, A Trabattoni, L Belshaw, S De Camillis, S Anumula, F Frassetto, L Poletto, A Palacios, P Decleva, J B Greenwood, F Martín, and M Nisoli. Ultrafast electron dynamics in phenylalanine initiated by attosecond pulses. *Science*, 346(6207):336–339, oct 2014. ISSN 0036-8075. doi: 10.1126/science.1254061. URL <http://science.sciencemag.org/content/346/6207/336>.
- [5] Christian Ott, Andreas Kaldun, Luca Argenti, Philipp Raith, Kristina Meyer, Martin Laux, Yizhu Zhang, Alexander Blättermann, Steffen Hagstotz, Thomas Ding, Robert Heck, Javier Madroñero, Fernando Martín, and Thomas Pfeifer. Reconstruction and control of a time-dependent two-electron wave packet. *Nature*, 516(7531):374–378, 2014. ISSN 0028-0836. doi: 10.1038/nature14026. URL <http://www.nature.com/doi/10.1038/nature14026>.
- [6] Erik P Månsson, Diego Guénou, Cord L Arnold, David Kroon, Susan Kasper, J Marcus Dahlström, Eva Lindroth, Anatoli S Kheifets, Anne L’Huillier, Stacey L Sorensen, and Mathieu Gisselbrecht. Double ionization probed on the attosecond timescale. *Nat. Phys.*, 10(3):207–211, 2014. ISSN 1745-2473. doi: 10.1038/nphys2880. URL <http://dx.doi.org/10.1038/nphys2880>.
- [7] P M Kraus, B Mignolet, D Baykusheva, A Rupenyan, L Horný, E F Penka, G Grassi, O I Tolstikhin, J Schneider, F Jensen, L B Madsen, A D Bandrauk, F Remacle, and H J Wörner. Measurement and laser control of attosecond charge migration in ionized iodoacetylene. *Science*, 350(6262):790–795, 2015. ISSN 0036-8075. doi: 10.1126/science.aab2160. URL <http://science.sciencemag.org/content/350/6262/790>.
- [8] M. Nisoli, F. Calegari, A. Palacios, P. Decleva, and F Martín. Attosecond electron dynamics in molecules. *Chem. Rev.* (in press), 2016.
- [9] Brian W. J. McNeil and Neil R. Thompson. X-ray free-electron lasers. *Nature Photonics*, 4(12):814–821, November 2010. ISSN 1749-4885. doi: 10.1038/nphoton.2010.239. URL <http://www.nature.com/doi/10.1038/nphoton.2010.239>.

- [10] Ferenc Krausz. Attosecond physics. *Rev. Mod. Phys.*, 81(1):163–234, February 2009. ISSN 0034-6861. doi: 10.1103/RevModPhys.81.163. URL <http://link.aps.org/doi/10.1103/RevModPhys.81.163>.
- [11] Michael Chini, Kun Zhao, and Zenghu Chang. The generation, characterization and applications of broadband isolated attosecond pulses. *Nature Photonics*, 8(3):178–186, February 2014. ISSN 1749-4885. doi: 10.1038/nphoton.2013.362. URL <http://www.nature.com/doi/10.1038/nphoton.2013.362>.
- [12] G Lambert, T Hara, D Garzella, T Tanikawa, M Labat, B Carre, H Kitamura, T Shintake, M Bougeard, S Inoue, Y Tanaka, P Salieres, H Merdji, O Chubar, O Gobert, K Tahara, and M.-E. Couprie. Injection of harmonics generated in gas in a free-electron laser providing intense and coherent extreme-ultraviolet light. *Nat. Phys.*, 4(4):296–300, apr 2008. ISSN 1745-2473. URL <http://dx.doi.org/10.1038/nphys889>.
- [13] E. Allaria, R. Appio, L. Badano, W.A. Barletta, S. Bassanese, S.G. Biedron, A. Borgia, E. Busetto, D. Castronovo, P. Cinquegrana, S. Cleva, D. Cocco, M. Cornacchia, P. Craievich, I. Cudin, G. D’Auria, M. Dal Forno, M.B. Danailov, R. De Monte, G. De Ninno, P. Delgiusto, Alexander Demidovich, S. Di Mitri, B. Diviacco, A. Fabris, R. Fabris, W. Fawley, M. Ferianis, E. Ferrari, S. Ferry, L. Froehlich, P. Furlan, G. Gaio, F. Gelmetti, L. Giannessi, M. Giannini, R. Gobessi, R. Ivanov, E. Karantzoulis, M. Lonza, A. Lutman, B. Mahieu, M. Milloch, S.V. Milton, M. Musardo, I. Nikolov, S. Noe, F. Parmigiani, Giuseppe Penco, M. Petronio, L. Pivetta, M. Predonzani, F. Rossi, L. Rumiz, A. Salom, C. Scafuri, C. Serpico, P. Sigalotti, S. Spampinati, C. Spezzani, M. Svandrlik, C. Svetina, S. Tazzari, M. Trovo, R. Umer, A. Vascotto, M. Veronese, R. Visintini, M. Zaccaria, D. Zangrando, and M. Zangrando. Highly coherent and stable pulses from the FERMI seeded free-electron laser in the extreme ultraviolet. *Nature Photonics*, 6(10):699–704, September 2012. ISSN 1749-4885. doi: 10.1038/nphoton.2012.233. URL <http://dx.doi.org/10.1038/nphoton.2012.233>.
- [14] David Gauthier, Primož Rebernik Ribič, Giovanni De Ninno, Enrico Allaria, Paolo Cinquegrana, Miltcho Bojanov Danailov, Alexander Demidovich, Eugenio Ferrari, Luca Giannessi, Benoît Mahieu, and Giuseppe Penco. Spectrotemporal Shaping of Seeded Free-Electron Laser Pulses. *Phys. Rev. Lett.*, 115(11):114801, September 2015. ISSN 0031-9007. doi: 10.1103/PhysRevLett.115.114801. URL <http://link.aps.org/doi/10.1103/PhysRevLett.115.114801>.
- [15] M. Žitnik, A. Mihelič, K. Bučar, M. Kavčič, J.-E. Rubensson, M. Svanquist, J. Söderström, R. Feifel, C. Saathe, Y. Ovcharenko, V. Lyamayev, T. Mazza, M. Meyer, M. Simon, L. Journel, J. Lüning, O. Plekan, M. Coreno, M. Devetta, M. Di Fraia, P. Finetti, R. Richter, C. Grazioli, K. C. Prince, and C. Callegari. High resolution multiphoton spectroscopy by a tunable Free-Electron-Laser light. *Phys. Rev. Lett.*, 113(19):193201, November 2014. ISSN 0031-9007. doi: 10.1103/PhysRevLett.113.193201. URL <http://link.aps.org/doi/10.1103/PhysRevLett.113.193201>.
- [16] Francisco Silva, Stephan M Teichmann, Seth L Cousin, Michael Hemmer, and Jens Biegert. Spatiotemporal isolation of attosecond soft X-ray pulses in the water window. *Nat. Commun.*, 6:6611, mar 2015. ISSN 2041-1723. doi: 10.1038/ncomms7611. URL <http://www.nature.com/ncomms/2015/150319/ncomms7611/full/ncomms7611.html#{#}affil-auth>.
- [17] Wilmer Arbelo-González, Rachel Crespo-Otero, and Mario Barbatti. Steady and time-resolved photoelectron spectra based on nuclear ensembles. *J. Chem. Theory Comput.*, 12(10):5037–5049, 2016. ISSN 1549-9618. doi: 10.1021/acs.jctc.6b00704. URL <http://pubs.acs.org/doi/abs/10.1021/acs.jctc.6b00704>.
- [18] Samer Gozem, Anastasia O Gunina, Takatoshi Ichino, David L Osborn, John F Stanton, and Anna I Krylov. Photoelectron Wave Function in Photoionization: Plane Wave or Coulomb Wave? *J. Phys. Chem. Lett.*, 6(22):4532–4540, 2015. ISSN 19487185. doi: 10.1021/acs.jpclett.5b01891. URL <http://dx.doi.org/10.1021/acs.jpclett.5b01891>.

- [19] M E Corrales, J González-Vázquez, G Balerdi, I R Solá, R de Nalda, and L Bañares. Control of ultrafast molecular photodissociation by laser-field-induced potentials. *Nat. Chem.*, 6(9): 785–790, sep 2014. ISSN 1755-4330. doi: 10.1038/nchem.2006. URL <http://www.nature.com/doi/10.1038/nchem.2006>.
- [20] Megan L Shelby, Patrick J Lestrangé, Nicholas E Jackson, Kristoffer Haldrup, Michael W Mara, Andrew B Stickrath, Diling Zhu, Henrik Lemke, Matthieu Chollet, Brian M Hoffman, Xiaosong Li, and Lin X Chen. Ultrafast Excited State Relaxation of a Metalloporphyrin Revealed by Femtosecond X-ray Absorption Spectroscopy. *J. Am. Chem. Soc.*, 138(28):8752–8764, 2016. ISSN 0002-7863. doi: 10.1021/jacs.6b02176. URL <http://pubs.acs.org/doi/abs/10.1021/jacs.6b02176>.
- [21] Philip George Burke. *R-Matrix Theory of Atomic Collisions*, volume 61 of *Springer Series on Atomic, Optical, and Plasma Physics*. Springer Berlin Heidelberg, Berlin, Heidelberg, 2011. ISBN 978-3-642-15930-5. doi: 10.1007/978-3-642-15931-2. URL <http://www.springer.com/physics/atomic,+molecular,+optical+%26+plasma+physics/book/978-3-642-15930-5><http://link.springer.com/10.1007/978-3-642-15931-2>.
- [22] Jonathan Tennyson. Electron–molecule collision calculations using the R-matrix method. *Phys. Rep.*, 491(2-3):29–76, June 2010. ISSN 03701573. doi: 10.1016/j.physrep.2010.02.001. URL <http://linkinghub.elsevier.com/retrieve/pii/S0370157310000451>.
- [23] Oleg Zatsarinny and Klaus Bartschat. The B-spline R-matrix method for atomic processes: application to atomic structure, electron collisions and photoionization. *J. Phys. B: At. Mol. Opt. Phys.*, 46(11):112001, June 2013. ISSN 0953-4075. doi: 10.1088/0953-4075/46/11/112001. URL <http://stacks.iop.org/0953-4075/46/i=11/a=112001?key=crossref.73520ee34d41ba97aca0972d8c6c0166>.
- [24] Luca Argenti, Renate Pazourek, Johannes Feist, Stefan Nagele, Matthias Liertzer, Emil Persson, Joachim Burgdörfer, and Eva Lindroth. Photoionization of helium by attosecond pulses: Extraction of spectra from correlated wave functions. *Phys. Rev. A*, 87(5):053405, May 2013. ISSN 1050-2947. doi: 10.1103/PhysRevA.87.053405. URL <http://link.aps.org/doi/10.1103/PhysRevA.87.053405>.
- [25] T. Carette, J. M. Dahlström, L. Argenti, and E. Lindroth. Multiconfigurational hartree-fock close-coupling ansatz: Application to the argon photoionization cross section and delays. *Phys. Rev. A*, 87:023420, Feb 2013. doi: 10.1103/PhysRevA.87.023420. URL <http://link.aps.org/doi/10.1103/PhysRevA.87.023420>.
- [26] Manohar Awasthi, Yulian V Vanne, Alejandro Saenz, Alberto Castro, and Piero Decleva. Single-active-electron approximation for describing molecules in ultrashort laser pulses and its application to molecular hydrogen. *Phys. Rev. A*, 77(6):63403, jun 2008. doi: 10.1103/PhysRevA.77.063403. URL <http://link.aps.org/doi/10.1103/PhysRevA.77.063403>.
- [27] E Kukk, D Ayuso, T D Thomas, P Decleva, M Patanen, Luca Argenti, E. Plésiat, A Palacios, K Kooser, O Travníkova, S Mondal, M Kimura, K Sakai, C Miron, F. Martín, and K. Ueda. Effects of molecular potential and geometry on atomic core-level photoemission over an extended energy range: The case study of the CO molecule. *Phys. Rev. A*, 88(3):033412, September 2013. ISSN 1050-2947. doi: 10.1103/PhysRevA.88.033412. URL <http://link.aps.org/doi/10.1103/PhysRevA.88.033412>.
- [28] D Ayuso, A Palacios, P Decleva, and F Martín. Dissociative and non-dissociative photoionization of molecular fluorine from inner and valence shells. *J. Electron Spectrosc. Relat. Phenom.*, 195:320–326, 2014. ISSN 03682048. doi: 10.1016/j.jelspec.2013.11.014. URL <http://linkinghub.elsevier.com/retrieve/pii/S0368204813002338>.
- [29] Christof Hättig, Wim Klopper, Andreas Köhn, and David P. Tew. Explicitly Correlated Electrons in Molecules. *Chem. Rev.*, 112(1):4, January 2012. ISSN 1520-6890. doi: 10.1021/cr200168z. URL <http://www.ncbi.nlm.nih.gov/pubmed/22206503>.

- [30] Thanh-Tung Nguyen-Dang, Étienne Couture-Bienvenue, Jérémy Viau-Trudel, and Amaury Sainjon. Time-dependent quantum chemistry of laser driven many-electron molecules. *J. Chem. Phys.*, 141(24):244116, 2014. ISSN 0021-9606. doi: 10.1063/1.4904102. URL <http://scitation.aip.org/content/aip/journal/jcp/141/24/10.1063/1.4904102>.
- [31] Motomichi Tashiro, Kiyoshi Ueda, and Masahiro Ehara. Auger decay of molecular double core-hole state. *J. Chem. Phys.*, 135(15):154307, oct 2011. ISSN 00219606. doi: 10.1063/1.3651082. URL <http://www.ncbi.nlm.nih.gov/pubmed/22029313><http://link.aip.org/link/JCPSA6/v135/i15/p154307/s1f&Agg=doi>.
- [32] Helena Aksela and Seppo Aksela. Photoionization and Auger decay in free atoms, molecules and small clusters. *Radiation Physics and Chemistry*, 76:370–374, 2007. doi: 10.1016/j.radphyschem.2005.10.043.
- [33] Ji Cai Liu, Christophe Nicolas, Yu Ping Sun, Roberto Flammini, Patrick O’Keeffe, Lorenzo Avaldi, Paul Morin, Victor Kimberg, Nobuhiro Kosugi, Faris Gel’mukhanov, and Catalin Miron. Multimode resonant auger scattering from the ethene molecule. *J. Phys. Chem. B*, 115(18):5103–5112, 2011. ISSN 15205207. doi: 10.1021/jp104228x.
- [34] I. Sañchez and F. Martín. The doubly excited states of the H₂ molecule. *J. Chem. Phys.*, 106(18):7720, 1997. ISSN 00219606. doi: 10.1063/1.473773. URL <http://scitation.aip.org/content/aip/journal/jcp/106/18/10.1063/1.473773>.
- [35] S Kopelke, K Gokhberg, Lorenz S Cederbaum, and V Averbukh. Calculation of resonant interatomic Coulombic decay widths of inner-valence-excited states delocalized due to inversion symmetry. *J. Chem. Phys.*, 130(14):144103, 2009. ISSN 1089-7690. doi: 10.1063/1.3109988. URL <http://www.ncbi.nlm.nih.gov/pubmed/19368425>.
- [36] U. Fano. Effects of configuration interaction on intensities and phase shifts. *Phys. Rev.*, 124(6):1866–1878, 1961. ISSN 0031899X. doi: 10.1103/PhysRev.124.1866. URL <https://link.aps.org/doi/10.1103/PhysRev.124.1866>.
- [37] Vincenzo Carravetta, H. Ågren, O. Vahtras, and H. J. Aa. Jensen. Ab initio calculations of molecular resonant photoemission spectra. *J. Chem. Phys.*, 113(18):7790, 2000. ISSN 00219606. doi: 10.1063/1.1316046. URL <http://link.aip.org/link/JCPSA6/v113/i18/p7790/s1&Agg=doi>.
- [38] Motomichi Tashiro, Kiyoshi Ueda, and Masahiro Ehara. Double core-hole correlation satellite spectra of N₂ and CO molecules. *Chem. Phys. Lett.*, 521:45–51, 2012. ISSN 00092614. doi: 10.1016/j.cplett.2011.11.062. URL <http://linkinghub.elsevier.com/retrieve/pii/S0009261411014576>.
- [39] QiGuo Tian, Jing Yang, YuFeng Shi, Xu Shan, and XiangJun Chen. Outer- and inner-valence satellites of carbon dioxide: Electron momentum spectroscopy compared with symmetry-adapted-cluster configuration interaction general-R calculations. *J. Chem. Phys.*, 136(9):94306, 2012. doi: <http://dx.doi.org/10.1063/1.3691103>. URL <http://scitation.aip.org/content/aip/journal/jcp/136/9/10.1063/1.3691103>.
- [40] Suren Sukiasyan, Serguei Patchkovskii, Olga Smirnova, Thomas Brabec, and Misha Yu. Ivanov. Exchange and polarization effect in high-order harmonic imaging of molecular structures. *Phys. Rev. A*, 82(4):043414, October 2010. ISSN 1050-2947. doi: 10.1103/PhysRevA.82.043414. URL <http://link.aps.org/doi/10.1103/PhysRevA.82.043414>.
- [41] Emilio Pisanty and Misha Ivanov. Momentum transfers in correlation-assisted tunneling. *Phys. Rev. A*, 89(4):043416, April 2014. ISSN 1050-2947. doi: 10.1103/PhysRevA.89.043416. URL <http://link.aps.org/doi/10.1103/PhysRevA.89.043416>.
- [42] N. R. Badnell, M. A. Bautista, K. Butler, F. Delahaye, C. Mendoza, P. Palmeri, C. J. Zeippen, and M. J. Seaton. Updated opacities from the Opacity Project. *Mon. Not. R. Astron. Soc.*, 360(2): 458–464, 2005. ISSN 00358711. doi: 10.1111/j.1365-2966.2005.08991.x.

- [43] B Boudaïffa, P Cloutier, D D Hunting, M A Huels, and Sanche L. Resonant Formation of DNA Strand Breaks by Low-Energy (3 to 20 eV) Electrons. *Science*, 287(5458):1658–1660, 2000. ISSN 00368075. doi: 10.1126/science.287.5458.1658. URL <http://www.sciencemag.org/cgi/doi/10.1126/science.287.5458.1658>.
- [44] R. Dörner, V. Mergel, O. Jagutzki, L. Spielberger, Joachim Ullrich, Robert Moshhammer, and H. Schmidt-Böcking. Cold Target Recoil Ion Momentum Spectroscopy: a ÅÅmomentum microscopeÅÅ to view atomic collision dynamics. *Phys. Rep.*, 330(2-3):95–192, June 2000. ISSN 03701573. doi: 10.1016/S0370-1573(99)00109-X. URL <http://linkinghub.elsevier.com/retrieve/pii/S037015739900109X>.
- [45] André T J B Eppink, David H Parker, and I Introduction. Velocity map imaging of ions and electrons using electrostatic lenses: Application in photoelectron and photofragment ion imaging of molecular oxygen. *Rev. Sci. Instrum.*, 68(September):3477–3484, 1997.
- [46] D W Lindle and O A Hemmers. Time-of-flight photoelectron spectroscopy of atoms and molecules. *J. Alloys Compd.*, 328(1-2):27–34, 2001. ISSN 09258388. doi: 10.1016/S0925-8388(01)01326-3.
- [47] E. Goulielmakis, Z-H Loh, A. Wirth, R. Santra, N. Rohringer, V. S. Yakovlev, S. Zherebtsov, T. Pfeifer, A. M. Azzeer, M. F. Kling, S. R. Leone, and F. Krausz. Real-time observation of valence electron motion. *Nature*, 466(7307):739–743, August 2010. ISSN 0028-0836. doi: 10.1038/nature09212. URL <http://www.nature.com/doi/finder/10.1038/nature09212>.
- [48] Volker Schmidt. Photoionization of atoms using synchrotron radiation. *Rep. Prog. Phys.*, 55: 1483–1659, 1992. ISSN 0034-4885. doi: 10.1088/0034-4885/55/9/003. URL <http://iopscience.iop.org/0034-4885/55/9/003>.
- [49] Donald H Bilderback, Pascal Elleaume, and Edgar Weckert. Review of third and next generation synchrotron light sources. *J. Phys. B: At. Mol. Opt. Phys.*, 38(9):S773—S797, may 2005. ISSN 0953-4075. doi: 10.1088/0953-4075/38/9/022. URL <http://stacks.iop.org/0953-4075/38/i=9/a=022?key=crossref.fff50e96d91376df49e03a0a29977070>.
- [50] Sophie E Canton, Etienne Plésiat, John D Bozek, Bruce S Rude, Piero Decleva, and Fernando Martín. Direct observation of Young’s double-slit interferences in vibrationally resolved photoionization of diatomic molecules. *PNAS*, 108(18):7302–6, May 2011. ISSN 1091-6490. doi: 10.1073/pnas.1018534108. URL <http://www.ncbi.nlm.nih.gov/pubmed/21498686>.
- [51] K. Ueda, C. Miron, E Plésiat, Luca Argenti, M. Patanen, K. Kooser, D. Ayuso, S. Mondal, M. Kimura, K. Sakai, O. Travnikova, A. Palacios, P. Decleva, E. Kukuk, and F Martín. Intramolecular photoelectron diffraction in the gas phase. *J. Chem. Phys.*, 139(12):124306, September 2013. ISSN 1089-7690. doi: 10.1063/1.4820814. URL <http://link.aip.org/link/JCPSA6/v139/i12/p124306/s1&Agg=doihttp://www.ncbi.nlm.nih.gov/pubmed/24089766>.
- [52] F. J. Wuilleumier and M. Meyer. Pump-probe experiments in atoms involving laser and synchrotron radiation: an overview. *J. Phys. B: At. Mol. Opt. Phys.*, 39(23):R425–R477, 2006. ISSN 0953-4075. doi: 10.1088/0953-4075/39/23/R01.
- [53] Francesco Aquilante, Jochen Autschbach, Rebecca K. Carlson, Liviu F. Chibotaru, Mickaël G. Delcey, Luca De Vico, Ignacio Fdez. Galván, Nicolas Ferré, Luis Manuel Frutos, Laura Gagliardi, Marco Garavelli, Angelo Giussani, Chad E. Hoyer, Giovanni Li Manni, Hans Lischka, Dongxia Ma, Per Åke Malmqvist, Thomas Müller, Artur Nenov, Massimo Olivucci, Thomas Bondo Pedersen, Daoling Peng, Felix Plasser, Ben Pritchard, Markus Reiher, Ivan Rivalta, Igor Schapiro, Javier Segarra-Martí, Michael Stenrup, Donald G. Truhlar, Liviu Ungur, Alessio Valentini, Steven Vancocillie, Valera Veryazov, Victor P. Vysotskiy, Oliver Weingart, Felipe Zapata, and Roland Lindh. Molcas 8: New capabilities for multiconfigurational quantum chemical calculations across the periodic table. *J. Comput. Chem.*, 37(5):506–541, 2016. ISSN 1096-987X. doi: 10.1002/jcc.24221. URL <http://dx.doi.org/10.1002/jcc.24221>.

- [54] H.-J. Werner, P J Knowles, G Knizia, F R Manby, and M Schütz. Molpro: a general-purpose quantum chemistry program package. *WIREs Comput. Mol. Sci.*, 2(2):242–253, 2012. ISSN 1759-0884. doi: 10.1002/wcms.82. URL <http://dx.doi.org/10.1002/wcms.82>.
- [55] Hans Lischka, Ron Shepard, Russell M Pitzer, Isaiah Shavitt, Michal Dallos, Thomas Muller, Peter G Szalay, Michael Seth, Gary S Kedziora, Satoshi Yabushita, and Zhiyong Zhang. High-level multireference methods in the quantum-chemistry program system COLUMBUS: Analytic MR-CISD and MR-AQCC gradients and MR-AQCC-LRT for excited states, GUGA spin-orbit CI and parallel CI density. *Phys. Chem. Chem. Phys.*, 3(5):664–673, 2001. doi: 10.1039/B008063M. URL <http://dx.doi.org/10.1039/B008063M>.
- [56] Hans Lischka, Thomas Müller, Péter G Szalay, Isaiah Shavitt, Russell M Pitzer, and Ron Shepard. Columbus program system for advanced multireference theory calculations. *WIREs Comput. Mol. Sci.*, 1(2):191–199, 2011. ISSN 1759-0884. doi: 10.1002/wcms.25. URL <http://dx.doi.org/10.1002/wcms.25>.
- [57] Kestutis Aidas, Celestino Angeli, Keld L Bak, Vejbjørn Bakken, Radovan Bast, Linus Boman, Ove Christiansen, Renzo Cimiraglia, Sonia Coriani, Pål Dahle, Erik K Dalskov, Ulf Ekström, Thomas Enevoldsen, Janus J Eriksen, Patrick Ettenhuber, Berta Fernández, Lara Ferrighi, Heike Fliegl, Luca Frediani, Kasper Hald, Asger Halkier, Christof Hättig, Hanne Heiberg, Trygve Helgaker, Alf Christian Hennum, Hinne Hettrema, Eirik Hjertenæs, Stinne Høst, Ida-Marie Høyvik, Maria Francesca Iozzi, Branislav Jansík, Hans Jørgen Aa. Jensen, Dan Jonsson, Poul Jørgensen, Joanna Kauczor, Sheela Kirpekar, Thomas Kjærgaard, Wim Klopper, Stefan Knecht, Rika Kobayashi, Henrik Koch, Jacob Kongsted, Andreas Krapp, Kasper Kristensen, Andrea Ligabue, Ola B Lutnæs, Juan I Melo, Kurt V Mikkelsen, Rolf H Myhre, Christian Neiss, Christian B Nielsen, Patrick Norman, Jeppe Olsen, Jógvan Magnus H Olsen, Anders Osted, Martin J Packer, Filip Pawłowski, Thomas B Pedersen, Patricio F Provasi, Simen Reine, Zilvinas Rinkevicius, Torgeir A Ruden, Kenneth Ruud, Vladimir V Rybkin, Pawel Sałek, Claire C M Samson, Alfredo Sánchez de Merás, Trond Saue, Stephan P A Sauer, Bernd Schimmelpfennig, Kristian Sneskov, Arnfinn H Steindal, Kristian O Sylvester-Hvid, Peter R Taylor, Andrew M Teale, Erik I Tellgren, David P Tew, Andreas J Thorvaldsen, Lea Thøgersen, Olav Vahtras, Mark A Watson, David J D Wilson, Marcin Ziolkowski, and Hans Ågren. The Dalton quantum chemistry program system. *WIREs Comput. Mol. Sci.*, 4(3):269–284, 2014. ISSN 1759-0884. doi: 10.1002/wcms.1172. URL <http://dx.doi.org/10.1002/wcms.1172>.
- [58] M W Schmidt, K K Baldridge, J A Boatz, S T Elbert, M S Gordon, J H Jensen, S K N Matsunaga, K Nguyen, S Su, T L Windus, M Dupuis, and J A Montgomery Jr. General atomic and molecular electronic structure system. *J. Comput. Chem.*, 14(11):1347–1363, nov 1993. ISSN 1096-987X. doi: 10.1002/jcc.540141112. URL <http://onlinelibrary.wiley.com/doi/10.1002/jcc.540141112/abstract>.
- [59] M J Frisch, G W Trucks, H B Schlegel, G E Scuseria, M A Robb, J R Cheeseman, G Scalmani, V Barone, B Mennucci, G A Petersson, H Nakatsuji, M Caricato, X Li, H P Hratchian, A F Izmaylov, J Bloino, G Zheng, J L Sonnenberg, M Hada, M Ehara, K Toyota, R Fukuda, J Hasegawa, M Ishida, T Nakajima, Y Honda, O Kitao, H Nakai, T Vreven, J A Montgomery Jr., J E Peralta, F Ogliaro, M Bearpark, J J Heyd, E Brothers, K N Kudin, V N Staroverov, R Kobayashi, J Normand, K Raghavachari, A Rendell, J C Burant, S S Iyengar, J Tomasi, M Cossi, N Rega, J M Millam, M Klene, J E Knox, J B Cross, V Bakken, C Adamo, J Jaramillo, R Gomperts, R E Stratmann, O Yazyev, A J Austin, R Cammi, C Pomelli, J W Ochterski, R L Martin, K Morokuma, V G Zakrzewski, G A Voth, P Salvador, J J Dannenberg, S Dapprich, A D Daniels, Ö Farkas, J B Foresman, J V Ortiz, J Cioslowski, and D J Fox. *Gaussian 09 Revision D.01*. Gaussian Inc, Wallingford, England, 2009.
- [60] Hans Jørgen, Aa. Jensen, Poul Jørgensen, and Hans Ågren. Efficient optimization of large scale mcsf wave functions with a restricted step algorithm. *J. Chem. Phys.*, 87(1):451–466, 1987. doi: 10.1063/1.453590. URL <http://dx.doi.org/10.1063/1.453590>.
- [61] Andrew T. B. Gilbert, Nicholas A. Besley, and Peter M. W. Gill. Self-consistent field calculations of excited states using the maximum overlap method (mom). *J. Phys. Chem. A*, 112(50):13164–

- 13171, 2008. doi: 10.1021/jp801738f. URL <http://dx.doi.org/10.1021/jp801738f>. PMID: 18729344.
- [62] Alexandre B. Rocha. Potential curves for inner-shell states of co calculated at multiconfigurational self-consistent field level. *J. Chem. Phys.*, 134(2):024107, 2011. doi: 10.1063/1.3528725. URL <http://dx.doi.org/10.1063/1.3528725>.
- [63] Inés Corral, Jesús González-Vázquez, and Fernando Martín. Potential Energy Surfaces of Core-Hole and Shake-Up States for Dissociative Ionization Studies. *J. Chem. Theory Comput.*, 13(4): 1723–1736, 2017. ISSN 1549-9618. doi: 10.1021/acs.jctc.6b01214. URL <http://pubs.acs.org/doi/abs/10.1021/acs.jctc.6b01214>.
- [64] A. Macías, F. Martín, A. Riera, and M. Yáñez. Simple discretization method for autoionization widths. i. theory. *Phys. Rev. A*, 36:4179–4186, Nov 1987. doi: 10.1103/PhysRevA.36.4179. URL <https://link.aps.org/doi/10.1103/PhysRevA.36.4179>.
- [65] A. Macías, F. Martín, A. Riera, and M. Yáñez. Simple discretization method for autoionization widths. ii. atoms. *Phys. Rev. A*, 36:4187–4202, Nov 1987. doi: 10.1103/PhysRevA.36.4187. URL <https://link.aps.org/doi/10.1103/PhysRevA.36.4187>.
- [66] A. Macías, F. Martín, A. Riera, and M. Yáñez. Simple discretization method for autoionization widths. iii. molecules. *Phys. Rev. A*, 36:4203–4211, Nov 1987. doi: 10.1103/PhysRevA.36.4203. URL <https://link.aps.org/doi/10.1103/PhysRevA.36.4203>.
- [67] A. Macías, F. Martín, A. Riera, and M. Yáñez. A practical solution to the "unknown normalization" problem. *Int. J. Quantum Chem.*, 33(4):279–300, 1988. ISSN 1097-461X. doi: 10.1002/qua.560330404. URL <http://dx.doi.org/10.1002/qua.560330404>.
- [68] I. Sánchez and F. Martín. Representation of the electronic continuum of H₂ with B-spline basis. *J. Phys. B At. Mol. Opt. Phys.*, 30(3):679–692, 1997. ISSN 0953-4075. doi: 10.1088/0953-4075/30/3/021. URL <http://stacks.iop.org/0953-4075/30/i=3/a=021>.
- [69] Fernando Martín. Ionization and dissociation using B-splines: photoionization of the hydrogen molecule. *J. Phys. B At. Mol. Opt. Phys.*, 32(16):R197–R231, 1999. ISSN 0953-4075. doi: 10.1088/0953-4075/32/16/201. URL <http://stacks.iop.org/0953-4075/32/i=16/a=201>.
- [70] Yulian V Vanne, Alejandro Saenz, Alex Dalgarno, Robert C Forrey, Piotr Froelich, and Svante Jonsell. Doubly excited autoionizing states of $\{<\math display="inline">\{<\mrow>\{<\msub>\{<\mi mathvariant="normal">H\{</mi>\{<\mn>\{<\mn>\{</msub>\{</mrow>\{</math>\} converging to the $\{<\math display="inline">\{<\mrow>\{<\mi mathvaria$. *Phys. Rev. A*, 73(6):62706, jun 2006. ISSN 1050-2947. doi: 10.1103/PhysRevA.73.062706. URL <http://link.aps.org/doi/10.1103/PhysRevA.73.062706>.$
- [71] Wim Vanroose, D. Horner, Fernando Martín, T. Rescigno, and C. McCurdy. Double photoionization of aligned molecular hydrogen. *Phys. Rev. A*, 74(5):052702, November 2006. ISSN 1050-2947. doi: 10.1103/PhysRevA.74.052702. URL <http://link.aps.org/doi/10.1103/PhysRevA.74.052702>.
- [72] Liang Tao, C. W. McCurdy, and Thomas N. Rescigno. Grid-based methods for diatomic quantum scattering problems. III. Double photoionization of molecular hydrogen in prolate spheroidal coordinates. *Phys. Rev. A*, 82(2):023423, August 2010. ISSN 1050-2947. doi: 10.1103/PhysRevA.82.023423. URL <http://link.aps.org/doi/10.1103/PhysRevA.82.023423>.
- [73] Carl de Boor. *A Practical Guide to Splines (Applied Mathematical Sciences)*. Springer, 2001. ISBN 0387953663.
- [74] Henri Bachau, Eric Cormier, Piero Decleva, J E Hansen, and Fernando Martín. Applications of B-splines in atomic and molecular physics. *Rep. Prog. Phys.*, 64(12):1815–1943, December 2001. ISSN 0034-4885. doi: 10.1088/0034-4885/64/12/205. URL <http://stacks.iop.org/0034-4885/64/i=12/a=205?key=crossref.2257eec0e5040fc21410a9ef6e58af89>.

- [75] T. Rescigno and C. McCurdy. Numerical grid methods for quantum-mechanical scattering problems. *Phys. Rev. A*, 62(3):032706, August 2000. ISSN 1050-2947. doi: 10.1103/PhysRevA.62.032706. URL <http://link.aps.org/doi/10.1103/PhysRevA.62.032706>.
- [76] Péter G Szalay, Thomas Müller, Gergely Gidofalvi, Hans Lischka, and Ron Shepard. Multiconfiguration Self-Consistent Field and Multireference Configuration Interaction Methods and Applications. *Chem. Rev.*, 112(1):108–181, 2012. ISSN 0009-2665. doi: 10.1021/cr200137a. URL <http://dx.doi.org/10.1021/cr200137ahttp://pubs.acs.org/doi/abs/10.1021/cr200137a>.
- [77] N Saito, D Toffoli, R R Lucchese, M Nagoshi, A De Fanis, Y Tamenori, M Oura, H Yamaoka, M Kitajima, H Tanaka, U Hergenhahn, and K Ueda. Symmetry- And multiplet-resolved N 1s photoionization cross sections of the NO₂ molecule. *Phys. Rev. A*, 70(6):62724, 2004. ISSN 10502947. doi: 10.1103/PhysRevA.70.062724. URL <http://link.aps.org/doi/10.1103/PhysRevA.70.062724>.
- [78] Etienne Plésiat, P Declava, and Fernando Martín. Vibrationally resolved photoelectron angular distributions from randomly oriented and fixed-in-space N₂ and CO molecules. *J. Phys. B: At. Mol. Opt. Phys.*, 45(19):194008, October 2012. ISSN 0953-4075. doi: 10.1088/0953-4075/45/19/194008. URL <http://stacks.iop.org/0953-4075/45/i=19/a=194008?key=crossref.91c2ff0bb5f43160aba39644dc249240>.
- [79] N Padial, G Csanak, B V McKoy, and P W Langhoff. Photoexcitation and ionization in carbon dioxide: Theoretical studies in the separated-channel static-exchange approximation. *Phys. Rev. A*, 23(1):218–235, 1981. doi: 10.1103/PhysRevA.23.218. URL <http://link.aps.org/doi/10.1103/PhysRevA.23.218>.
- [80] V McKoy, T A Carlson, and R R Lucchese. Photoelectron dynamics of molecules. *J. Phys. Chem.*, 88(15):3188–3196, 1984. doi: 10.1021/j150659a011. URL <http://dx.doi.org/10.1021/j150659a011>.
- [81] Philip George Burke and Harry M Schey. Elastic Scattering of Low-Energy Electrons by Atomic Hydrogen. *Phys. Rev.*, 126(1):147–162, 1962. ISSN 0031-899X. doi: 10.1103/PhysRev.126.147. URL <http://link.aps.org/doi/10.1103/PhysRev.126.147>.
- [82] Ivo Cacelli, Roberto Moccia, and Antonio Rizzo. Gaussian-type orbitals basis sets for the calculation of continuum properties in molecules: The differential photoionization cross section of Li₂ and LiH. *J. Chem. Phys.*, 102(18):7131–7141, 1995. ISSN 00219606. doi: 10.1063/1.469107. URL <http://scitation.aip.org/content/aip/journal/jcp/102/18/10.1063/1.469107>.
- [83] I. Cacelli, R. Moccia, and A. Rizzo. Gaussian type orbitals basis sets for the calculation of continuum properties in molecules: the differential photoionization cross section of acetylene. *Chemical Physics*, 252(1-2):67–81, January 2000. ISSN 03010104. doi: 10.1016/S0301-0104(99)00325-0. URL <http://linkinghub.elsevier.com/retrieve/pii/S0301010499003250http://link.aps.org/link/JCPSA6/v102/i18/p7131/s1&Agg=doi>.
- [84] Xiao-Min Tong and Shih-I Chu. Density-functional theory with optimized effective potential and self-interaction correction for ground states and autoionizing resonances. *Phys. Rev. A*, 55(5):3406–3416, 1997. ISSN 1050-2947. doi: 10.1103/PhysRevA.55.3406. URL <http://journals.aps.org/pr/abstract/10.1103/PhysRevA.55.3406>.
- [85] Mahmoud Abu-samha and Lars Bojer Madsen. Single-active-electron potentials for molecules in intense laser fields. *Phys. Rev. A*, 81(3):033416, March 2010. ISSN 1050-2947. doi: 10.1103/PhysRevA.81.033416. URL <http://link.aps.org/doi/10.1103/PhysRevA.81.033416>.
- [86] M Beck. The multiconfiguration time-dependent Hartree (MCTDH) method: a highly efficient algorithm for propagating wavepackets. *Phys. Rep.*, 324(1):1–105, 2000. ISSN 03701573. doi: 10.1016/S0370-1573(99)00047-2. URL <http://www.sciencedirect.com/science/article/pii/S0370157399000472>.

- [87] Kenneth Kulander. Multiphoton ionization of hydrogen: A time-dependent theory. *Phys. Rev. A*, 35(1):445–447, January 1987. ISSN 0556-2791. doi: 10.1103/PhysRevA.35.445. URL <http://link.aps.org/doi/10.1103/PhysRevA.35.445>.
- [88] J Schirmer, M Braunstein, and V McKoy. Molecular K-shell photoionization cross sections in the relaxed-core Hartree-Fock approximation. *Phys. Rev. A*, 41(1):283–300, 1990. ISSN 10502947. doi: 10.1103/PhysRevA.41.283.
- [89] Robert R Lucchese and Robert W Zuraes. Comparison of the random-phase approximation with the multichannel frozen-core Hartree-Fock approximation for the photoionization of N₂. *Phys. Rev. A*, 44(1):291–303, 1991. ISSN 10502947. doi: 10.1103/PhysRevA.44.291.
- [90] Jérémie Caillat, J. Zanghellini, M. Kitzler, O. Koch, W. Kreuzer, and Armin Scrinzi. Correlated multielectron systems in strong laser fields: A multiconfiguration time-dependent Hartree-Fock approach. *Phys. Rev. A*, 71(1):012712, January 2005. ISSN 1050-2947. doi: 10.1103/PhysRevA.71.012712. URL <http://link.aps.org/doi/10.1103/PhysRevA.71.012712>.
- [91] D Toffoli, M Stener, G Fronzoni, and P Decleva. Convergence of the multicenter B-spline DFT approach for the continuum. *Chem. Phys.*, 276(1):25–43, January 2002. ISSN 03010104. doi: 10.1016/S0301-0104(01)00549-3. URL <http://linkinghub.elsevier.com/retrieve/pii/S0301010401005493>.
- [92] Daniele Toffoli and Piero Decleva. Multiphoton core ionization dynamics of polyatomic molecules. *J. Phys. B: At. Mol. Opt. Phys.*, 46(14):145101, July 2013. ISSN 0953-4075. doi: 10.1088/0953-4075/46/14/145101. URL <http://stacks.iop.org/0953-4075/46/i=14/a=145101?key=crossref.a373685a80383b783a66306bb86e89c6>.
- [93] M Stener and P Decleva. Photoionization of first and second row hydrides by the B-spline one-centre expansion density functional method. *J. Electron Spectrosc. Relat. Phenom.*, 94(1-2):195–209, June 1998. ISSN 03682048. doi: 10.1016/S0368-2048(98)00186-8. URL <http://linkinghub.elsevier.com/retrieve/pii/S0368204898001868>.
- [94] Vinay Pramod Majety and Armin Scrinzi. Dynamic Exchange in the Strong Field Ionization of Molecules. *Phys. Rev. Lett.*, 115(10):103002, sep 2015. ISSN 10797114. doi: 10.1103/PhysRevLett.115.103002. URL <http://link.aps.org/doi/10.1103/PhysRevLett.115.103002>.
- [95] I. Lindgren and Morrison J. *Atomic Many-Body Theory (2nd Edition)*, volume 13 of *Springer Series in Chemical Physics*. Springer-Verlag Berlin Heidelberg, Berlin, Heidelberg, 1982. ISBN 978-3-642-96616-3. doi: 10.1007/978-3-642-96614-9.
- [96] Charlotte Froese Fischer, Tomas Brage, and Per Jönsson. *Computational Atomic Structure: An MCHF Approach (1st Edition)*. IOP Publishing Ltd, Bristol, UK, 1997. ISBN 0-7503-0466-9.
- [97] Walter R. Johnson. *Atomic Structure Theory (1st Edition)*. Springer-Verlag Berlin Heidelberg, Berlin, Heidelberg, 2007. ISBN 978-3-540-68010-9. doi: 10.1007/978-3-540-68013-0.
- [98] Carlos Marante, Luca Argenti, and Fernando Martín. Hybrid Gaussian–B-spline basis for the electronic continuum: Photoionization of atomic hydrogen. *Phys. Rev. A*, 90(1):12506, jul 2014. ISSN 1050-2947. doi: 10.1103/PhysRevA.90.012506. URL <http://link.aps.org/doi/10.1103/PhysRevA.90.012506>.
- [99] Vinay Pramod Majety and Armin Scrinzi. Photo-Ionization of Noble Gases: A Demonstration of Hybrid Coupled Channels Approach. *Photonics*, 2(1):93–103, 2015. ISSN 2304-6732. doi: 10.3390/photonics2010093. URL <http://www.mdpi.com/2304-6732/2/1/93/>.
- [100] T. Rescigno, D. Horner, F. Yip, and C. McCurdy. Hybrid approach to molecular continuum processes combining Gaussian basis functions and the discrete variable representation. *Phys. Rev. A*, 72(5):052709, November 2005. ISSN 1050-2947. doi: 10.1103/PhysRevA.72.052709. URL <http://link.aps.org/doi/10.1103/PhysRevA.72.052709>.

- [101] F. Yip, C. McCurdy, and T. Rescigno. Hybrid Gaussian–discrete-variable representation approach to molecular continuum processes: Application to photoionization of diatomic Li_2^+ . *Phys. Rev. A*, 78(2):023405, August 2008. ISSN 1050-2947. doi: 10.1103/PhysRevA.78.023405. URL <http://link.aps.org/doi/10.1103/PhysRevA.78.023405>.
- [102] F L Yip, C W McCurdy, and T N Rescigno. Hybrid Gaussian–discrete-variable representation for one- and two-active-electron continuum calculations in molecules. *Phys. Rev. A*, 90(6):63421, 2014. ISSN 1050-2947. doi: 10.1103/PhysRevA.90.063421. URL <http://link.aps.org/doi/10.1103/PhysRevA.90.063421>.
- [103] Zdeněk Maňáček and Jimena D Gorfinkiel. Towards an accurate representation of the continuum in calculations of electron, positron and laser field interactions with molecules. *J. Phys. Conf. Ser.*, 490(1):012090, 2014. URL <http://stacks.iop.org/1742-6596/490/i=1/a=012090>.
- [104] Khrystyna Regeta, Michael Allan, Zdeněk Maňáček, and Jimena D. Gorfinkiel. Absolute cross sections for electronic excitation of pyrimidine by electron impact. *J. Chem. Phys.*, 144(2): 024302, 2016. doi: 10.1063/1.4939077. URL <http://dx.doi.org/10.1063/1.4939077>.
- [105] Philip. G. Burke. *R-Matrix Theory of Atomic Collisions*. Springer Berlin Heidelberg, 2011. doi: 10.1007/978-3-642-15931-2.
- [106] B. H. Lengsfeld and T. N. Rescigno. Electron-molecule close coupling with correlated target wave functions: Application to impact dissociation of f_2 . *Phys. Rev. A*, 44:2913–2920, Sep 1991. doi: 10.1103/PhysRevA.44.2913. URL <https://link.aps.org/doi/10.1103/PhysRevA.44.2913>.
- [107] R. G. Newton. *Scattering theory of waves and particles*. Dover Publications, 1982. ISBN 978-0486425351.
- [108] W. Kohn. Variational methods in nuclear collision problems. *Phys. Rev.*, 74:1763–1772, Dec 1948. doi: 10.1103/PhysRev.74.1763. URL <https://link.aps.org/doi/10.1103/PhysRev.74.1763>.
- [109] Leonard S. Rodberg and R. M. Thaler. The S Matrix and the K Matrix. *Introduction to the Quantum Theory of Scattering*. Academic Press, New York, first edition, 1967.
- [110] Harald Friedrich. Elastic Scattering by a Conservative Potential. *Scattering Theory*, volume 872 of *Lecture Notes in Physics*. Springer, Heidelberg, Germany, first edition, 2013.
- [111] H.A. Weidenmüller. Resonances and eigenphases of the s-matrix. *Phys. Lett. B*, 24(9):441 – 442, 1967. ISSN 0370-2693. doi: [http://dx.doi.org/10.1016/0370-2693\(67\)90264-X](http://dx.doi.org/10.1016/0370-2693(67)90264-X). URL <http://www.sciencedirect.com/science/article/pii/037026936790264X>.
- [112] Joesph Macek. Behavior of eigenphases near a resonance. *Phys. Rev. A*, 2(3):1101–1103, 1970. ISSN 10502947. doi: 10.1103/PhysRevA.2.1101. URL <https://link.aps.org/doi/10.1103/PhysRevA.2.1101>.
- [113] A. U. Hazi. Behavior of the eigenphase sum near a resonance. *Phys. Rev. A*, 19(2):920–922, 1979. ISSN 10502947. doi: 10.1103/PhysRevA.19.920. URL <https://link.aps.org/doi/10.1103/PhysRevA.19.920>.
- [114] M J Seaton. Quantum defect theory i. general formulation. *Proceedings of the Physical Society*, 88 (4):801, 1966. URL <http://stacks.iop.org/0370-1328/88/i=4/a=302>.
- [115] Leonard Rosenberg. Levinson-seaton theorem for potentials with an attractive coulomb tail. *Phys. Rev. A*, 52:3824–3826, Nov 1995. doi: 10.1103/PhysRevA.52.3824. URL <https://link.aps.org/doi/10.1103/PhysRevA.52.3824>.
- [116] Sebastian Heuser, Álvaro Jiménez Galán, Claudio Cirelli, Carlos Marante, Mazyar Sabbar, Robert Boge, Matteo Lucchini, Lukas Gallmann, Igor Ivanov, Anatoli S. Kheifets, J. Marcus Dahlström, Eva Lindroth, Luca Argenti, Fernando Martín, and Ursula Keller. Angular dependence of photoemission time delay in helium. *Phys. Rev. A*, 94:063409, Dec 2016. doi: 10.1103/PhysRevA.94.063409. URL <https://link.aps.org/doi/10.1103/PhysRevA.94.063409>.

- [117] L. Argenti and R. Moccia. K-matrix method with B-splines : σ_n , β_n and resonances in He photoionization below $N = 4$ threshold. *J. Phys. B: At. Mol. Opt. Phys.*, 39(12):2773, June 2006. ISSN 0953-4075. doi: 10.1088/0953-4075/39/12/012. URL <http://stacks.iop.org/0953-4075/39/i=12/a=012?key=crossref.3a6e24a308963caa42efedb59838a425>.
- [118] A. J. F. Siegert. On the derivation of the dispersion formula for nuclear reactions. *Phys. Rev.*, 56:750–752, Oct 1939. doi: 10.1103/PhysRev.56.750. URL <http://link.aps.org/doi/10.1103/PhysRev.56.750>.
- [119] Richard M More and Edward Gerjuoy. Properties of resonance wave functions. *Phys. Rev. A*, 7:1288–1303, Apr 1973. doi: 10.1103/PhysRevA.7.1288. URL <https://link.aps.org/doi/10.1103/PhysRevA.7.1288>.
- [120] Barry Simon. The definition of molecular resonance curves by the method of exterior complex scaling. *Phys. Lett. A*, 71(2):211–214, 1979. ISSN 03759601. doi: 10.1016/0375-9601(79)90165-8. URL <http://www.sciencedirect.com/science/article/pii/0375960179901658>.
- [121] W P Reinhardt. Complex Coordinates in the Theory of Atomic and Molecular Structure and Dynamics. *Annual Review of Physical Chemistry*, 33(1):223–255, 1982. ISSN 0066-426X. doi: 10.1146/annurev.pc.33.100182.001255.
- [122] U V Riss and H D Meyer. Calculation of resonance energies and widths using the complex absorbing potential method. *J. Phys. B: At. Mol. Opt. Phys.*, 26(23):4503, 1993. URL <http://stacks.iop.org/0953-4075/26/i=23/a=021>.
- [123] J.G. Muga, J.P. Palao, B. Navarro, and I.L. Egusquiza. Complex absorbing potentials. *Physics Reports*, 395(6):357 – 426, 2004. ISSN 0370-1573. doi: <http://dx.doi.org/10.1016/j.physrep.2004.03.002>. URL <http://www.sciencedirect.com/science/article/pii/S0370157304001218>.
- [124] R. Santra. Why complex absorbing potentials work: A discrete-variable-representation perspective. *Phys. Rev. A*, 74(3):034701, September 2006. ISSN 1050-2947. doi: 10.1103/PhysRevA.74.034701. URL <http://link.aps.org/doi/10.1103/PhysRevA.74.034701>.
- [125] U V Riss and H D Meyer. Reflection-free complex absorbing potentials. *J. Phys. B: At. Mol. Opt. Phys.*, 28(8):1475, 1995. URL <http://stacks.iop.org/0953-4075/28/i=8/a=012>.
- [126] U. Fano and J. W. Cooper. Line profiles in the far-uv absorption spectra of the rare gases. *Phys. Rev.*, 137:A1364–A1379, 1965. ISSN 0031899X. doi: 10.1103/PhysRev.137.A1364. URL <https://link.aps.org/doi/10.1103/PhysRev.137.A1364>.
- [127] C D H Chisholm. *Group theoretical techniques in quantum chemistry*. Academic Press, 1976.
- [128] A. Macías, F. Martín, A Riera, and M. Yañez. Simple discretization method for autoionization widths. I. Theory. *Phys. Rev. A*, 36(9):4179–4186, November 1987. ISSN 0556-2791. doi: 10.1103/PhysRevA.36.4179. URL <http://link.aps.org/doi/10.1103/PhysRevA.36.4179>.
- [129] L. Argenti and R. Colle. On the B-splines effective completeness. *Comput. Phys. Commun.*, 180(9): 1442, September 2009. ISSN 00104655. doi: 10.1016/j.cpc.2009.03.002. URL <http://linkinghub.elsevier.com/retrieve/pii/S0010465509000848>.
- [130] Jürgen Hinze, editor. The Graphical Unitary Group Approach and its Application to Direct Configuration Interaction Calculations. *The Unitary Group for the Evaluation of Electronic Energy Matrix Elements*. Lecture Notes in Chemistry. Springer-Verlag, Heidelberg, Germany, first edition, 1981. ISBN 9788578110796. doi: 10.1017/CBO9781107415324.004.
- [131] Björn O Roos. The Complete Active Space Self-Consistent Field Method and its Applications in Electronic Structure Calculations. In *Ab Initio Methods in Quantum Chemistry Part 2*, volume 69 of Lawley, K. P., Ed.; *Advances in Chemical Physics*. John Wiley & Sons, Ltd., Chichester, England, first edition, 1987. ISBN 9780470142943. doi: 10.1002/9780470142943.ch7. URL <http://dx.doi.org/10.1002/9780470142943.ch7>.

- [132] Björn O Roos, G. Karlström, P. Å. Malmqvist, and A. J. Sadlej. MOLCAS: A General Purpose Quantum Chemistry Program System for Correlated Wavefunctions. In *Modern techniques in computational chemistry: MOTECC-91*. Clementi, E., Ed.; ESCOM Science Publishers B.V., New York, 1991.
- [133] Sven Feuerbacher and Robin Santra. Calculating molecular Rydberg states using the one-particle Green's function: application to HCO and C(NH₂)₃. *J. Chem. Phys.*, 123(19):194310, nov 2005. ISSN 0021-9606. doi: 10.1063/1.2122687. URL <http://www.ncbi.nlm.nih.gov/pubmed/16321091>.
- [134] Milton Abramowitz and Irene A. Stegun. *Handbook of Mathematical Functions: with Formulas, Graphs, and Mathematical Tables* (Dover Books on Mathematics). Dover Publications, 1965. ISBN 0486612724. URL <http://www.amazon.com/Handbook-Mathematical-Functions-Formulas-Mathematics/dp/0486612724>.
- [135] H.A. Weidenmüller. Resonances and eigenphases of the S-Matrix. *Physics Letters*, 24(9):441–442, 1967.
- [136] A. U. Hazi. Behavior of the eigenphase sum near a resonance. *Phys. Rev. A*, 19(2):920–922, 1979. ISSN 10502947. doi: 10.1103/PhysRevA.19.920.
- [137] L. Nikolopoulos. Electromagnetic transitions between states satisfying free-boundary conditions. *Phys. Rev. A*, 73(4):043408, April 2006. ISSN 1050-2947. doi: 10.1103/PhysRevA.73.043408. URL <http://link.aps.org/doi/10.1103/PhysRevA.73.043408>.
- [138] Roger G. Newton. *Scattering theory of waves and particles*. Texts and Monographs in Physics. Springer-Verlag, New York, second edition, 1982.
- [139] Albert Messiah. *Quantum Mechanics. Two volumes*. North-Holland / NY: John Wiley & Sons, 1966.
- [140] D A Varshalovich, A N Moskalev, and V K Khersonskii. *Quantum Theory of Angular Momentum*. World Scientific Publishing Co. Pte. Ltd., Singapore, 1988. ISBN 978-9971509965.
- [141] Valérie Vénier and Bernard Piraux. Continuum-continuum dipole transitions in femtosecond-laser-pulse excitation of atomic hydrogen. *Phys. Rev. A*, 41(7):4019–4034, April 1990. ISSN 1050-2947. doi: 10.1103/PhysRevA.41.4019. URL <http://link.aps.org/doi/10.1103/PhysRevA.41.4019>.
- [142] Eric Cormier, H Bachau, and J Zhang. Discretization techniques applied to the study of multiphoton excitation of resonances in helium. *J. Phys. B: At. Mol. Opt. Phys.*, 26(23):4449–4463, December 1993. ISSN 0953-4075. doi: 10.1088/0953-4075/26/23/016. URL <http://stacks.iop.org/0953-4075/26/i=23/a=016?key=crossref.c15f36f5237959bb63d5f0d0c897c4a8>.
- [143] S. J. van Enk, Jian Zhang, and P. Lambropoulos. On the free-free dipole moment. *J. Phys. B: At. Mol. Opt. Phys.*, 30:L17, 1997.
- [144] P. Agostini, F. Fabre, G. Mainfray, G. Petite, and N. Rahman. Free-Free Transitions Following Six-Photon Ionization of Xenon Atoms. *Phys. Rev. Lett.*, 42(17):1127–1130, April 1979. ISSN 0031-9007. doi: 10.1103/PhysRevLett.42.1127. URL <http://link.aps.org/doi/10.1103/PhysRevLett.42.1127>.
- [145] Eric Cormier and P. Lambropoulos. Above-threshold ionization spectrum of hydrogen using B-spline functions. *J. Phys. B: At. Mol. Opt. Phys.*, 30:77, 1997.
- [146] V D Rodríguez, Diego G. Arbó, and P a Macri. Above-threshold ionization of atoms by resonant XUV laser pulses. *J. Phys. B: At. Mol. Opt. Phys.*, 44(12):125603, June 2011. ISSN 0953-4075. doi: 10.1088/0953-4075/44/12/125603. URL <http://stacks.iop.org/0953-4075/44/i=12/a=125603?key=crossref.85006cc8e592b00e7fe2fa1a808cca11>.

- [147] Alexei N. Grum-Grzhimailo, Brant Abeln, Klaus Bartschat, Daniel Weflen, and Timothy Urness. Ionization of atomic hydrogen in strong infrared laser fields. *Phys. Rev. A*, 81(4):043408, April 2010. ISSN 1050-2947. doi: 10.1103/PhysRevA.81.043408. URL <http://link.aps.org/doi/10.1103/PhysRevA.81.043408>.
- [148] Lars Madsen. Gauge invariance in the interaction between atoms and few-cycle laser pulses. *Phys. Rev. A*, 65(5):053417, May 2002. ISSN 1050-2947. doi: 10.1103/PhysRevA.65.053417. URL <http://link.aps.org/doi/10.1103/PhysRevA.65.053417>.
- [149] Eric Cormier and P. Lambropoulos. Effect of the initial phase of the field in ionization by ultrashort laser pulses. *Eur. Phys. J. D*, 2(1):15–20, May 1998. ISSN 1434-6060. doi: 10.1007/s100530050104. URL <http://www.springerlink.com/openurl.asp?genre=article&id=doi:10.1007/s100530050104>.
- [150] J N Bardsley, A Szoke, and M J Comella. Multiphoton ionisation from a short-range potential by short-pulse lasers. *J. Phys. B: At. Mol. Opt. Phys.*, 21(23):3899–3916, December 1988. ISSN 0953-4075. doi: 10.1088/0953-4075/21/23/010. URL <http://stacks.iop.org/0953-4075/28/i=12/a=010?key=crossref.ebe3ef5570f8aae684670f6b42c22d35http://stacks.iop.org/0953-4075/21/i=23/a=010?key=crossref.937b41d762957eac5a6006f500ce5bf3>.
- [151] JIAN ZHANG and P. LAMBROPOULOS. NONPERTURBATIVE TIME-DEPENDENT THEORY OF TWO-ELECTRON ATOMS IN STRONG LASER FIELDS. *J. Nonlinear Optic. Phys. Mat.*, 04(03):633–646, July 1995. ISSN 0218-8635. doi: 10.1142/S0218863595000276. URL <http://www.worldscientific.com/doi/abs/10.1142/S0218863595000276>.
- [152] D A Telnov and S I Chu. Multiphoton above-threshold detachment by intense laser pulses: a new adiabatic approach. *J. Phys. B: At. Mol. Opt. Phys.*, 28(12):2407–2423, June 1995. ISSN 0953-4075. doi: 10.1088/0953-4075/28/12/010. URL <http://stacks.iop.org/0953-4075/28/i=12/a=010?key=crossref.ebe3ef5570f8aae684670f6b42c22d35>.
- [153] Eric Cormier and P. Lambropoulos. Optimal gauge and gauge invariance in non-perturbative time-dependent calculation of above-threshold ionization. *J. Phys. B: At. Mol. Opt. Phys.*, 29: 1667–1680, 1996.
- [154] Philipp V. Demekhin and Lorenz S. Cederbaum. Dynamic Interference of Photoelectrons Produced by High-Frequency Laser Pulses. *Phys. Rev. Lett.*, 108(25):253001, June 2012. ISSN 0031-9007. doi: 10.1103/PhysRevLett.108.253001. URL <http://link.aps.org/doi/10.1103/PhysRevLett.108.253001>.
- [155] Farhad H.M. Faisal. *Theory of Multiphoton Processes (Physics of Atoms and Molecules)*. Springer, 1987. ISBN 0306423170.
- [156] Tanja Van Mourik, Angela K Wilson, and Thom H Dunning JR. Benchmark calculations with correlated molecular wavefunctions. XIII. Potential energy curves for He₂, Ne₂ and Ar₂ using correlation consistent basis sets through augmented sextuple zeta. *Molecular Physics*, 96(4):529–547, 1999. doi: 10.1080/00268979909482990. URL <http://dx.doi.org/10.1080/00268979909482990>.
- [157] David R. Herrick. Doubly Excited Two-Electron Atoms. In *New Symmetry Properties of Atoms and Molecules*, volume 52 of *Prigogine, I. and Rice, Stuart A., Eds.; Advances in Chemical Physics*. John Wiley & Sons, New York, 1983. ISBN 1118949714. doi: 10.1002/9780470175422. URL <http://books.google.com/books?hl=en&lr=&id=bV6FBQAAQBAJ&pgis=1>.
- [158] Thom H Dunning. Gaussian basis sets for use in correlated molecular calculations. I. The atoms boron through neon and hydrogen. *J. Chem. Phys.*, 90(2):1007, 1989. ISSN 00219606. doi: 10.1063/1.456153. URL <http://link.aip.org/link/JCPSA6/v90/i2/p1007/s1&Agg=doi>.
- [159] O. a Fojón, Jorge Fernández, Alicia Palacios, R. D. Rivarola, and Fernando Martín. Interference effects in H₂ photoionization at high energies. *J. Phys. B: At. Mol. Opt. Phys.*, 37(15):3035–3042, August 2004. ISSN 0953-4075. doi: 10.1088/0953-4075/37/15/003. URL <http://stacks.iop.org/0953-4075/37/i=15/a=003?key=crossref.cd548df0d848e1a8b115b06f16edde49>.

- [160] R. P. Madden and K. Codling. New Autoionizing Atomic Energy Levels in He, Ne and Ar. *Phys. Rev. Lett.*, 10(12):516–518, 1963. doi: 10.1103/PhysRevLett.10.516. URL <https://link.aps.org/doi/10.1103/PhysRevLett.10.516>.
- [161] R. P. Madden and K. Codling. Recently Discovered Auto-Ionizing States of Krypton and Xenon in the $\lambda 380\text{\AA}$ – 600\AA Region. *J. Opt. Soc. Am.*, 54(2):268–269, 1964. ISSN 0030-3941. doi: 10.1364/JOSA.54.000268. URL <http://www.opticsinfobase.org/abstract.cfm?URI=josa-54-2-268>.
- [162] R. P. Madden and K. Codling. Two-electron excitation states in helium. *AJ*, 141:364–375, 1965. doi: 10.1086/148132. URL <http://adsabs.harvard.edu/abs/1965ApJ...141..364M>.
- [163] K. Codling, R. P. Madden, and D. L. Ederer. Resonances in the photo-ionization continuum of ne i (20-150 ev). *Phys. Rev.*, 155:26–37, Mar 1967. doi: 10.1103/PhysRev.155.26. URL <http://link.aps.org/doi/10.1103/PhysRev.155.26>.
- [164] O. Hassouneh, A. C. Brown, and H. W. van der Hart. Multichannel interference in high-order-harmonic generation from ne^+ driven by an ultrashort intense laser pulse. *Phys. Rev. A*, 89: 033409, Mar 2014. doi: 10.1103/PhysRevA.89.033409. URL <https://link.aps.org/doi/10.1103/PhysRevA.89.033409>.
- [165] A. C. Brown and H. W. van der Hart. Extreme-ultraviolet-initiated high-order harmonic generation: Driving inner-valence electrons using below-threshold-energy extreme-ultraviolet light. *Phys. Rev. Lett.*, 117:093201, Aug 2016. doi: 10.1103/PhysRevLett.117.093201. URL <https://link.aps.org/doi/10.1103/PhysRevLett.117.093201>.
- [166] Nicolas Douguet, Elena V. Gryzlova, Ekaterina I. Staroselskaya, Klaus Bartschat, and Alexei N. Grum-Grzhimailo. Photoelectron angular distribution in two-pathway ionization of neon with femtosecond XUV pulses. *arXiv:1611.01878*, 2016. URL <http://arxiv.org/abs/1611.01878>.
- [167] Nicolas Douguet, Alexei N Grum-Grzhimailo, and Klaus Bartschat. Above-threshold ionization in neon produced by combining optical and bichromatic XUV femtosecond pulses. *Phys. Rev. A*, 95:013407, 2017. ISSN 10941622. doi: 10.1103/PhysRevA.95.013407. URL <https://link.aps.org/doi/10.1103/PhysRevA.95.013407>.
- [168] D. You, H. Fukuzawa, Y. Sakakibara, T. Takanashi, Y. Ito, G. G. Maliyar, K. Motomura, K. Nagaya, T. Nishiyama, K. Asa, Y. Sato, N. Saito, M. Oura, M. Schöffler, G. Kastirke, U. Hergen-hahn, V. Stumpf, K. Gokhberg, A. I. Kuleff, L. S. Cederbaum, K. Ueda, W. Bambynek, B. Boudaiffa, P. Cloutier, D. Hunting, M. A. Huels, L. Sanche, R. W. Howell, L. S. Cederbaum, J. Zobeley, F. Tarantelli, V. Averbukh, T. Jahnke, T. Jahnke, M. Mucke, R. Santra, L. S. Cederbaum, Y. Morishita, T. Ouchi, K. Gokhberg, P. Kolorenč, A. Kuleff, L. S. Cederbaum, F. Trinter, V. Stumpf, P. Kolorenč, K. Gokhberg, L. S. Cederbaum, J. Zobeley, R. Santra, L. S. Cederbaum, K. Sakai, M. Förstel, M. Mucke, T. Arion, A. M. Bradshaw, U. Hergen-hahn, V. Stumpf, K. Gokhberg, L. S. Cederbaum, J. J. Yeh, I. Lindau, K. Kreidi, B. Kanngießer, T. Ouchi, M. Oura, U. Buck, R. Krohne, A. Albiez, M. Thoma, W. Weber, W. Mehlhorn, R. Dörner, J. Ullrich, and K. Ueda. Charge transfer to ground-state ions produces free electrons. *Nat. Commun.*, 8:14277, 2017. ISSN 2041-1723. doi: 10.1038/ncomms14277. URL <http://www.nature.com/doifinder/10.1038/ncomms14277>.
- [169] C. A. Nicolaides and D. R. Beck. The variational calculation of energies and widths of resonances. *Phys. Lett. A*, 65(1):11–12, 1978. ISSN 03759601. doi: 10.1016/0375-9601(78)90116-0. URL <http://www.sciencedirect.com/science/article/pii/0375960178901160>.
- [170] Charlotte Froese Fischer, Georgio Tachiev, Gediminas Gaigalas, and Michel R. Godefroid. An MCHF atomic-structure package for large-scale calculations. *Comput. Phys. Commun.*, 176(8):559–579, 2007. ISSN 0010-4655. doi: 10.1016/j.cpc.2007.01.006. URL <http://www.sciencedirect.com/science/article/pii/S0010465507000446>.
- [171] David Feller. The role of databases in support of computational chemistry calculations. *J. Comput. Chem.*, 17(13):1571–1586, 1996. ISSN 1096-987X. doi: 10.1002/(SICI)1096-987X(199610)17:13<1571::AID-JCC9>3.0.CO;2-P. URL [http://dx.doi.org/10.1002/\(SICI\)1096-987X\(199610\)17:13<1571::AID-JCC9>3.0.CO;2-P](http://dx.doi.org/10.1002/(SICI)1096-987X(199610)17:13<1571::AID-JCC9>3.0.CO;2-P).

- [172] Karen L Schuchardt, Brett T Didier, Todd Elsethagen, Lisong Sun, Vidhya Gurumoorthi, Jared Chase, Jun Li, and Theresa L Windus. Basis set exchange: a community database for computational sciences. *J. Chem. Inf. Model.*, 47(3):1045–1052, 2007. doi: 10.1021/ci600510j. URL <http://dx.doi.org/10.1021/ci600510j>. PMID: 17428029.
- [173] Carlos Marante, Markus Klinker, InÃs Corral, JesÃs Gonzlez-Vzquez, Luca Argenti, and Fernando Martn. Hybrid-basis close-coupling interface to quantum chemistry packages for the treatment of ionization problems. *J. Chem. Theory Comput.*, 13(2):499–514, 2017. doi: 10.1021/acs.jctc.6b00907. URL <http://dx.doi.org/10.1021/acs.jctc.6b00907>.
- [174] U. Fano and J. W. Cooper. Spectral distribution of atomic oscillator strengths. *Rev. Mod. Phys.*, 40(3):441–507, 1968. ISSN 00346861. doi: 10.1103/RevModPhys.40.441. URL <https://link.aps.org/doi/10.1103/RevModPhys.40.441>.
- [175] Daniele Toffoli and Piero Decleva. A Multichannel Least-Squares B-Spline Approach to Molecular Photoionization: Theory, Implementation, and Applications within the Configuration-Interaction Singles Approximation. *J. Chem. Theory Comput.*, 12(10):4996–5008, 2016. doi: 10.1021/acs.jctc.6b00627. URL <http://dx.doi.org/10.1021/acs.jctc.6b00627>.
- [176] J.a.R. Samson and W.C. Stolte. Precision measurements of the total photoionization cross-sections of He, Ne, Ar, Kr, and Xe. *J. Elect. Spect. Rel. Phen.*, 123(2-3):265–276, 2002. ISSN 03682048. doi: 10.1016/S0368-2048(02)00026-9. URL <http://www.sciencedirect.com/science/article/pii/S0368204802000269>.
- [177] Konrad Schulz, Michael Domke, Ralph Pttner, Alejandro Gutirrez, Gnter Kaindl, Gregory Miecznik, and Chris Greene. High-resolution experimental and theoretical study of singly and doubly excited resonances in ground-state photoionization of neon. *Phys. Rev. A*, 54(4):3095–3112, 1996. ISSN 1050-2947. doi: 10.1103/PhysRevA.54.3095. URL <https://link.aps.org/doi/10.1103/PhysRevA.54.3095>.
- [178] B Langer, N Berrah, R Wehlitz, T W Gorczyca, J Bozek, and a Farhat. Angular distribution of the Ne autoionization resonances: experimental and theoretical study. *J. Phys. B At. Mol. Opt. Phys.*, 30(3):593–607, 1999. ISSN 0953-4075. doi: 10.1088/0953-4075/30/3/015. URL <http://stacks.iop.org/0953-4075/30/i=3/a=015>.
- [179] M. Nrisimhamurthy, G. Aravind, P. C. Deshmukh, and S. T. Manson. Autoionization resonances in the neon isoelectronic sequence using relativistic multichannel quantum-defect theory. *Phys. Rev. A*, 91(1):013404, 2015. ISSN 10941622. doi: 10.1103/PhysRevA.91.013404. URL <https://link.aps.org/doi/10.1103/PhysRevA.91.013404>.
- [180] M Stener, P Decleva, and a Lisini. Density functional-time-dependent local density approximation calculations of autoionization resonances in noble gases. *J. Phys. B: At. Mol. Opt. Phys.*, 28(23):4973–4999, 1999. ISSN 0953-4075. doi: 10.1088/0953-4075/28/23/009. URL <http://stacks.iop.org/0953-4075/28/i=23/a=009>.
- [181] Liang Liang, Y. C. Wang, and Zhou Chao. The theoretical study of singly and doubly resonances of photoionization of neon. *Phys. Lett. A*, 360(4-5):599–602, 2007. ISSN 0375-9601. doi: 10.1016/j.physleta.2006.09.010. URL <http://www.sciencedirect.com/science/article/pii/S0375960106014162>.
- [182] P G Burke and K T Taylor. R-matrix theory of photoionization. Application to neon and argon. *J. Phys. B At. Mol. Opt. Phys.*, 8(16):2620–2639, 1975. ISSN 0022-3700. doi: 10.1088/0022-3700/8/16/020. URL <http://stacks.iop.org/0022-3700/8/i=16/a=020>.
- [183] Elisabeth Heinrich-Josties, Stefan Pabst, and Robin Santra. Controlling the 2p hole alignment in neon via the 2s-3p Fano resonance. *Phys. Rev. A*, 89(4):043415, April 2014. ISSN 1050-2947. doi: 10.1103/PhysRevA.89.043415. URL <http://link.aps.org/doi/10.1103/PhysRevA.89.043415>.

- [184] Anthony F. Starace. Behavior of partial cross sections and branching ratios in the neighborhood of a resonance. *Phys. Rev. A*, 16:231–242, Jul 1977. doi: 10.1103/PhysRevA.16.231. URL <https://link.aps.org/doi/10.1103/PhysRevA.16.231>.
- [185] Anthony F. Starace. *Atomic Photoionization*, pages 69–110. Springer US, Boston, MA, 1983. ISBN 978-1-4613-3781-2. doi: 10.1007/978-1-4613-3781-2_3. URL http://dx.doi.org/10.1007/978-1-4613-3781-2_3.
- [186] L. Journal, B. Rouvellou, D. Cubaynes, J. Bizau, F. Wuilleumier, M. Richter, P. Sladeczek, K.-H. Selbmann, P. Zimmermann, and H. Bergeron. First observation of a Fano profile following one step autoionization into a double photoionization continuum. *J. Phys. IV*, 03(C6): C6–217–C6–226, 1993. doi: 10.1051/jp4:1993621. URL <https://hal.archives-ouvertes.fr/jpa-00251706>.
- [187] D. GuÁrnot, D. Kroon, E. Balogh, E. W. Larsen, M. Kotur, M. Miranda, T. Fordell, P. Johnson, J. Mauritsson, M. Gisselbrecht, K. VarjÁz, C. L. Arnold, T. Carette, A. S. Kheifets, E. Lindroth, A. LÉijHuillier, and J. M. DahlstrÁúm. Measurements of relative photoemission time delays in noble gas atoms. *J. Phys. B: At. Mol. Opt. Phys.*, 47(24):245602, 2014. URL <http://stacks.iop.org/0953-4075/47/i=24/a=245602>.
- [188] Marija Kotur, D. Guenot, Á. Jiménez-Galán, David Kroon, E. W. Larsen, M. Louisy, M. Bengtsson, M. Miranda, J. Mauritsson, C. L. Arnold, S. E. Canton, M. Gisselbrecht, T. Carette, Marcus J. Dahlström, Eva Lindroth, Alfred Maquet, Luca Argenti, Fernando Martín, and Anne L’Huillier. Phase measurement of a Fano window resonance using tunable attosecond pulses Át. *Nat. Commun.*, 7:10566, 2015. URL <https://www.nature.com/articles/ncomms10566>.
- [189] V. Gruson, L. Barreau, Á. Jiménez-Galan, F. Risoud, J. Caillat, A. Maquet, B. Carré, F. Lepetit, J.-F. Hergott, T. Ruchon, L. Argenti, R. Taïeb, F. Martín, and P. Salières. Attosecond dynamics through a fano resonance: Monitoring the birth of a photoelectron. *Science*, 354(6313):734–738, 2016. ISSN 0036-8075. doi: 10.1126/science.aah5188. URL <http://science.sciencemag.org/content/354/6313/734>.
- [190] Á. Jiménez Galán, L. Argenti, and F. Martín. Modulation of attosecond beating in resonant two-photon ionization. *Phys. Rev. Lett.*, 113(26):263001, December 2014. ISSN 0031-9007. doi: 10.1103/PhysRevLett.113.263001. URL <http://link.aps.org/doi/10.1103/PhysRevLett.113.263001>.
- [191] Á. Jiménez-Galán, Fernando Martín, and Luca Argenti. Two-photon finite-pulse model for resonant transitions in attosecond experiments. *Phys. Rev. A*, 93:023429, Feb 2016. doi: 10.1103/PhysRevA.93.023429. URL <https://link.aps.org/doi/10.1103/PhysRevA.93.023429>.
- [192] Private communication with the Pascal Salieres’ group at CEA Saclay (joint paper in preparation).
- [193] Á. Jiménez Galán. *Attosecond Spectroscopy of Autoionizing States*. PhD thesis, Universidad Autónoma de Madrid, 2015.
- [194] Th. Mercouris, Y. Komninos, S. Dionissopoulou, and C. Nicolaides. Computation of strong-field multiphoton processes in polyelectronic atoms: State-specific method and applications to H and Li⁺. *Phys. Rev. A*, 50(5):4109–4121, November 1994. ISSN 1050-2947. doi: 10.1103/PhysRevA.50.4109. URL <http://link.aps.org/doi/10.1103/PhysRevA.50.4109>.
- [195] Theodoros Mercouris, Yannis Komninos, Stavroula Dionissopoulou, and Cleanthes A. Nicolaides. Effects on observables of the singularity in the multiphoton freeÁfree dipole matrix elements. *J. Phys. B: At. Mol. Opt. Phys.*, 29:L13, 1996.
- [196] Yannis Komninos, Theodoros Mercouris, and Cleanthes a. Nicolaides. Structure and calculation of field-induced free-free transition matrix elements in many-electron atoms. *Phys. Rev. A*, 86(2):023420, August 2012. ISSN 1050-2947. doi: 10.1103/PhysRevA.86.023420. URL <http://link.aps.org/doi/10.1103/PhysRevA.86.023420>.

- [197] B.H. Bransden and C.J. Joachain. *Physics of Atoms and Molecules (2nd Edition)*. Addison-Wesley, 2003. ISBN 058235692X. URL <http://www.amazon.com/Physics-Atoms-Molecules-2nd-Edition/dp/058235692X>.
- [198] L. D. Landau and L. M. Lifshitz. *Quantum Mechanics Non-Relativistic Theory, Third Edition: Volume 3*. Butterworth-Heinemann, 1976. ISBN 0750635398.
- [199] John Pearson. *Computation of Hypergeometric Functions*. Master thesis, University of Oxford, 2009.